About Journal

The University of Sistan and Baluchestan entered into strategic partnership with Iranian Association of Electrical and Electronic Engineers (IAEEE) to publish the **International Journal of Industrial Electronics Control and Optimization (IECO)**. The IECO is a refereed international journal which presents to the international scientific community important results of work in these fields, whether in the form of modeling, simulation, analysis, fundamental research, development, application, design or real-time implementation. The scope of IECO is broad, encompassing all aspects of Industrial Electronics, Control and Optimization.
Note: International Journal of Industrial Electronics, Control and Optimization (IECO) has qualified to **ACADEMIC RESEARCH JOURNAL (ELMI-PAJOHESHI)** status certified by the Ministry of Science, Research and Technology of Iran (No. 231566/3/18 dated 1396/10/09), and is published by the University of Sistan and Baluchestan through a formal partnership (No. 952/2/1500 dated 1395/11/04) with Iranian Association of Electrical and Electronic Engineers (IAEEE) in order to develop scientific and research cooperation.

Aims and Scope

International Journal of Industrial Electronics, Control and Optimization (IECO) is a peer reviewed journal of advances and state-of-the-art in the science and engineering of Industrial Electronics, Control and Optimization. Its scope encompasses the applications of industrial electronics, power systems, control, optimization and computational intelligence for the enhancement of industrial and manufacturing systems and processes. The scope of the journal includes the following:

I. Industrial Electronics

- *Low and high power converters*
- *Renewable energy*
- *Drive control techniques*
- *Techniques for advanced power semiconductor devices*
- *Power quality and utility applications*
- *Communications*
- *Flexible AC Transmission Systems (FACTS)*
- *Control in power electronics*
- *Electromagnetic and thermal performance of electronic power converters*
- *Motion control, robotics, sensors and actuators*
- *Fault detection and diagnosis*
- *Power systems*
- *Factory automation, communication, and computer networks*

II. Control

- *Adaptive control*
- *Control of process systems*
- *Control theory*
- *Data processing*
- *Design of control systems*
- *Hybrid systems*
- *Identification and observation*
- *Intelligent systems*
- *Model-predictive control*
- *Optimal control*
- *Robust control*
- *Fractional order systems*

III. Optimization

- *Ant Colony*
- *Chaos Theory*
- *Evolutionary Computing*
- *Fuzzy Computing*
- *Hybrid Methods*
- *Immunological Computing*
- *Neuro Computing*
- *Particle Swarm*
- *Probabilistic Computing*
- *Rough Sets*
- *Wavelet*

International Journal of Industrial Electronics, Control and Optimization © 2020 IECO
Vol. 3, No. 4, pp. 393-406, Sep (2020)

A New Whale Optimization Algorithm-Based Fault Location Method by Focusing on Dispersed Model of the Transmission Line

Hossein Faramarzi[1], Navid Ghaffarzadeh[2,†]

[1,2] Faculty of Technical and Engineering, Imam Khomeini International University, Qazvin, Iran.

ABSTRACT

In this paper, a fault location approach is presented by using the Whale Optimization Algorithm (WOA) strategy in two terminal transmission feeders. Also, the Grey Wolf Optimization (GWO) method is discussed. Voltage and current are measured in both ends to collect the data required for the proposed strategy. The paper considers several types of faults and simulations, and the objective function identifies the fault location with a high accuracy in a short time. In addition, based on distributed model of the line, the fault location is defined and the optimization algorithm does not utilize the compressed model of the line, and the calculations are highly accurate. The WOA-based optimization method results in a notable reduction in the computational time. As the benefit of the proposed technique, accurate and timely location of the source of the fault is highly helpful to the repair crew. Almost in all cases, the accuracy of the proposed procedure is very high, and the error is kept below 1%.

Article Info

Keywords:
Bergeron model in time domain, Dispersed model of the line, Fault location technique, Grey wolf optimization algorithm, Whale optimization algorithm.

Article History:
Received 2019-10-17
Accepted 2020-02-28

I. INTRODUCTION

Basic goal of power system is to continuously provide electrical energy to the users. Like any other system, failures may occur in a power system. After detecting fault condition and location, it is critical to apply correct remedial actions. Accurate determination of fault location and its condition are important. Since the visual search of faulted lines are costly and sometimes inconclusive, fast and precise designation of fault location is necessary for prompt restoration of power, particularly on transmission lines, which would lead to saving on time and resources for the electric utilities. This will help field personnel to figure out the fault locations from transmission line maps and drawings. As a result, power system operators can identify and isolate faulted sections by opening circuit breakers or switches correctly and timely.
Subsequently, the power is restored to healthy transmission sections, and the customers are supplied reliably because long outages on the customer side are prevented and quick detection of faults helps beneficiaries to tackle them as fast as possible. It is worth noting that to increase the accuracy of calculations, line modeling plays a key role in the fault location process. Using distributed model of the line is one of the prevalent approaches in fault location optimization problems. Various methods have been proposed in the literature and have extensively been used to improve the solution of an optimal fault location problem. Linear programming (LP), nonlinear programming (NLP) mixed nonlinear techniques are just some examples. These methods have been classified and their advantages, limitations and requirements have been discussed in detail. One essential aspect of these methods is how to model the transmission line because it changes the accuracy of the calculations. Some

†Corresponding Author: ghaffarzadeh@eng.ikiu.ac.ir
Tel: +98(28)-33901120, Fax: +98(28)-33780073, Faculty of Technical and Engineering, Imam Khomeini International University

researches have focused on modeling lines with a compressed model, which reduces the accuracy of the calculations. So, to improve the precision of calculations, it is inevitable to use more comprehensive models of the transmission line. One of these accurate models is the distributed model of lines. According to the distributed time domain model of the lines, Ghiafeh Davoudi and Sadeh [1] proposed a method to detect the fault location using post-fault voltage and current samples at both terminals in which the objective was minimized by the genetic algorithm. Kezunovic and Mrkic [2] introduced a new fault location method based on the information of two end systems. It considers two different algorithm constructions utilizing two line models, and simulation performance is achieved by using EMTP software. It uses time sampling method for the proposed approach and it is concluded as the proposed method is cost-effective. Also, an algorithm is introduced by Sadeh [3] that uses time domain line model which is compensated with series connected FACTS device. It improves accuracy. An application of this technique can be developed to any series FACTS compensated line. Due to the calculation of the location and resistance of the fault, samples of voltage and current at both ends of the line are used synchronously. Ghazizadeh [4] suggested a novel arcing faults location technique for multi-segment combined transmission lines, which uses unsynchronized measurements from two terminals of the line. Also, Junzhang and Zhonghui [5] showed that fault location accuracy has been reduced by ignoring the line distributed capacitance. In document Ahmed and Attia [6], some optimization algorithms like teaching-learning-based optimization and harmony search algorithms are used. Also, some methods such as genetic algorithm, artificial bee colony, artificial neural networks and cause and effect are discused along with the advantages and disadvantages of all methods. In Youssef [7], an accurate method is discussed about the calculations needed to find the exact fault location on transmission lines. It used travelling wave-based method. The method is unaffected by noise or spurious changes in line. Salehi [8] presents a closed-form solution for fault location that does not need the GPS-synchronized sampling of wide-area measurements. Sparse intelligence is used to record the unsynchronized measurement. Also, the Schur-Banachiewicz inversion formula is utilized to obtain a solution for fault location.

From the previous efforts, we can conclude that these approaches have many contrasts, especially as to points such as the model of transmission line, measured variables from one side or both sides, and the optimization strategies employed to get the best results. Since the fault location is not derived directly from equations related to the currents and voltages, more smart methods are used to detect fault location in transmission systems.

Based on the goal, the present paper focuses on the operational use and application of a pre-existing approach, which has been already described in the literature. In this paper, some structures like the model of the transmission line, optimization algorithm, and cost function are updated and all information about the model used in locating the fault are fully described. Here, our approach to find the fault location is as follows. First, the objective function along time interval is defined. Second, to perform the fault location (FL) calculations, samples of currents and voltages are taken. Then, the optimal solution of the problem is found. We also vary the accurate fault location to measure the advantages of the proposed approach, The results are compared with the results obtained by the GWO algorithm. The main objective of this paper is to find out the best solution for the problem using WOA. The results show that by using a distributed model of the line and information which are sent from PMUs, under the dynamic operation, online employment of the approach is feasible. In this paper, we calculate the location of different types of faults in the category shown in Fig. 1.

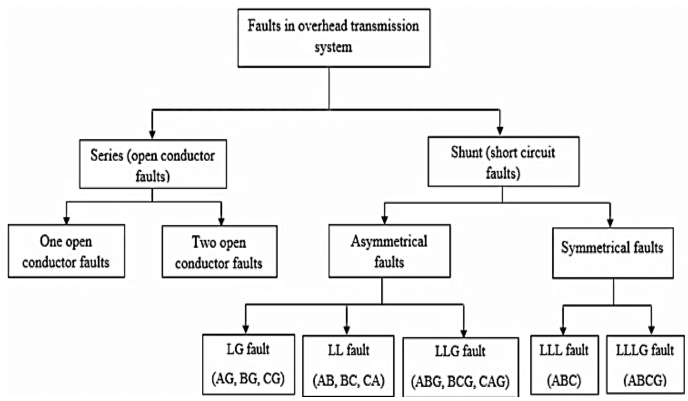

Fig. 1. Classification of faults.

II. DISPERSED MODEL OF TRANSMISSION LINE

A single-phase diagram of a three-phase transmission line with distributed parameters is shown in Fig. 2 where *S* and *R* denote the sending and receiving ends, respectively, and *F* shows the location of a free fault. Point F with a distance x from S end is located along the transmission line. As a rule, lumped RLC elements are usually utilized for short transmission lines whereas the dispersed model is for long lines [9]. To select an appropriate transmission line model, a decision is made based on a tree shown in Fig. 3 where traveling time is equal to length of line/speed of light and δt is the solution time step.

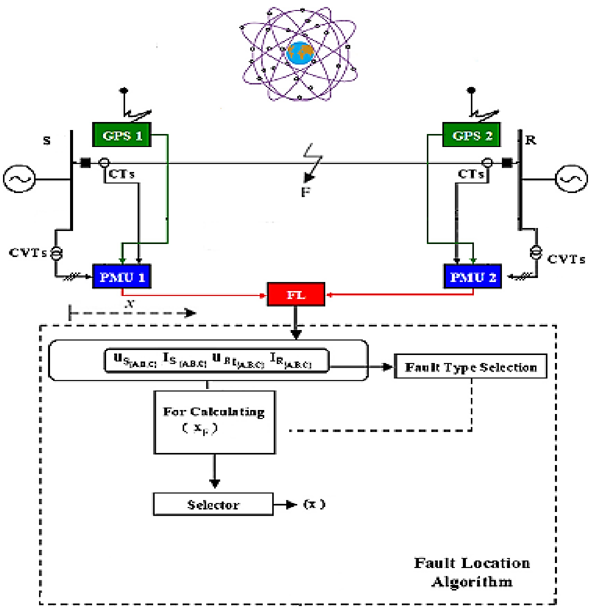

Fig. 2. A single-line diagram of the transmission line.

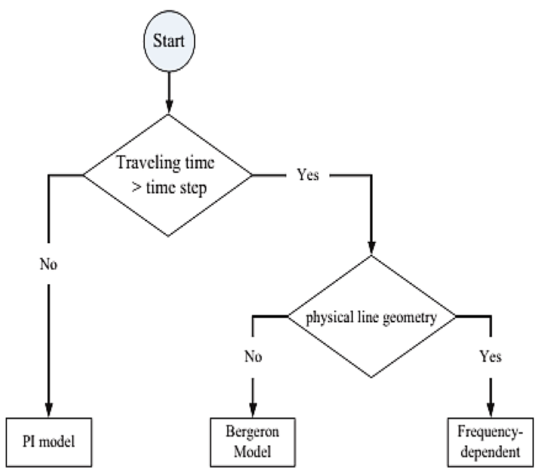

Fig. 3. The decision tree for selecting the transmission line model [16].

A distributed model of transmission line (segments S to F) is shown in Figs. 4-5. A set of equations depict the relevance between voltages and currents to send and receive end buses as follows (Bergeron's equations) [9; 10]:

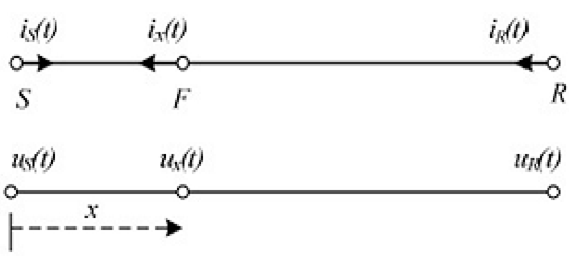

Fig. 4. The single phase diagram of a three-phase transmission line.

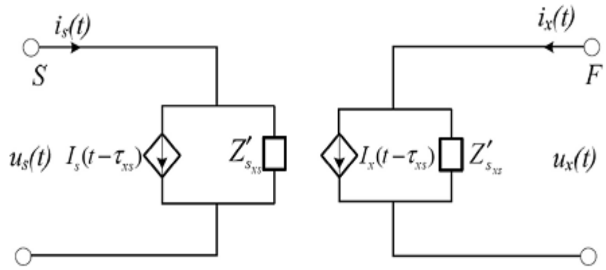

Fig. 5. The distributed model of the transmission line (segments S to F).

$$i_S(t) = \frac{1}{Z'_{sxs}} u_S(t) + I_S(t - \tau_{XS}) \tag{1}$$

$$i_X(t) = \frac{1}{Z'_{sxs}} u_X(t) + I_X(t - \tau_{XS}) \tag{2}$$

where the dependent source currents can be described by Eq. (3)- (4).

$$I_S(t-\tau_{XS}) = \frac{\frac{R_{XS}}{4}}{Z'^{2}_{SXS}} u_S(t-\tau_{XS}) + Z''_{SXS} i_S(t-\tau_{XS}) - \frac{Z_S}{Z'^{2}_{SXS}} u_X(t-\tau_{XS}) + Z''_{SXS} i_X(t-\tau_{XS}) \tag{3}$$

$$I_X(t-\tau_{XS}) = \frac{\frac{R_{XS}}{4}}{Z'^{2}_{sxs}} u_X(t-\tau_{XS}) + Z''_{SXS} i_X(t-\tau_{XS}) - \frac{Z_S}{Z'^{2}_{sxs}} u_S(t-\tau_{XS}) + Z''_{SXS} i_S(t-\tau_{XS}) \tag{4}$$

where Z_S is the surge impedance of the line and R_{XS} is the resistance of the SF section.

$$Z'_{S_{XS}} = Z_S + \frac{R_{XS}}{4} \tag{5}$$

$$Z''_{S_{XS}} = Z_S - \frac{R_{XS}}{4} \tag{6}$$

Where τ_{XS} is the time required for the wave to traverse from S to F.

T is the time required for the wave to traverse from S to R. In a single-phase Bergeron transmission line of two buses, if the fault takes place at point F, from above equation we can conclude that as a function of measured quantities at terminals S and R, the voltage at fault point can be extracted where R_{XR} is the resistance of the RF section.

$$Z'_{S_{XR}} = Z_S + \frac{R_{XR}}{4} \tag{7}$$

$$Z''_{S_{XR}} = Z_S - \frac{R_{XR}}{4} \tag{8}$$

The part of transmission line from receive end to fault (F) point is named RF section. At the fault point, the voltage can be calculated using the quantities measured at terminals S and R. The following equations describe it.

$$u_{XS}(t)=\{\frac{1}{2Z_s^{\ 2}}Z'_{S_{XS}}{}^2[u_S(t+\tau_{XS})-Z'_{S_{SX}}i_S(t+\tau_{XS})] \tag{9}$$
$$+Z'_{sxs}{}^2[u_S(t-\tau_{XS})-Z''_{S_{XS}}i_S(t-\tau_{XS})]$$
$$-\frac{R_{XS}{}^2}{8}u_S(t)-\frac{R_{XS}}{2}Z'_{sxs}Z''_{S_{XS}}i_S(t)\}$$

$$u_{XR}(t)=\{\frac{1}{2Z_s^{\ 2}}Z'_{S_{XR}}{}^2[u_R(t+(T-\tau_{XS}))-Z'_{S_{XR}}i_R(t+(T-\tau_{XS}))] \tag{10}$$
$$+Z''_{S_{XR}}{}^2[u_R(t-(T-\tau_{XS}))+Z''_{S_{XR}}i_R(t-(T-\tau_{XS}))]$$
$$-\frac{R_{XS}{}^2}{8}u_R(t)-\frac{R_{XR}}{2}Z'_{S_{XR}}Z''_{S_{XR}}i_R(t)\}$$

Based on the Bergeron model, the distributed parameters are characterized by the surge impedance and phase velocity. In this study, we can define the objective function based on the fact that, at fault point, voltage is the same as whatever calculated from sending or receiving end.

III. Optimal Fault location approach

This section formulates an optimization model to determine the solution of fault location problem. To get the solution of the optimization problem, it is necessary to determine an objective function which deals with decision variable. The goal is to obtain the distance between fault point and sending end. It is necessary to use an optimization technique to solve the fault allocation problem in such a way that the objective function is minimized. The formulation of the objective function is based on the voltage difference, considering *nxs* and *k* as discrete variable.

A. Objective Function

The objective function is based on partial differential equations of the transmission line model which has two variables: : position and time. By placing the measured voltage and current as boundary conditions in those functions, fault location can be calculated. To find the fault location, the key idea of this work is based on minimizing the voltage differential at fault point.

1) Minimization of Voltage differential at Fault Point

With the measured quantities at S and R terminals and using Eq. (1) and (2), we can conclude the following equation. Since the voltage of the fault point should be singular, the voltage differential at point F should be held at zero.

$$F(us,is,ur,ir,t,\tau_{xs})=\left|u_{xs}(t,\tau_{xs})-u_{xr}(t,\tau_{xs})\right| \tag{11}$$

Eq. (11) must be reached to its least value. It should be noted that the discretization of the measured voltage and current at discrete moments must be considered.

$$F(k,x)=\left|u_{xs}(k,x)-u_{xr}(k,x)\right| \tag{12}$$

The fault point X_F is estimated by scanning the minimum value of the absolute difference between the fault voltage seen by both end. The scanning of F(k,x) for each Δt starts at $t_{Start}=K_0\,\Delta t$ and proceeds until the protection system pick-up at $t_{Stop}=K_1\,\Delta t$.

The mean value over time of F(k,x) leads to a better understanding of fault voltage behavior during the whole fault period. Its calculation is as follows:

$$\text{Min (obj)}=\min\left(\frac{1}{\Delta t(k_1-k_0)}\sum_{k=k_0}^{k=k_1}F(k,x)\right) \tag{13}$$

$$k=\frac{t}{\Delta t} \tag{14}$$

$$n_{XS}=\frac{\tau_{XS}}{\Delta t} \tag{15}$$

$$x=C\times\tau_{XS} \tag{16}$$

$$C=3*10^{\wedge}8\ \ m/s$$

Δt: Sampling step.

n_{XS} , k arbitrary integers.

In this paper, the objective function is set at its minimum value using the WOA and GWO algorithms and the results are compared with each other. These algorithms are described in Section 5.

2) Constraint

In this paper, the inequality constraint for distance, x, is given by Eq. (17) in which *x* is the distance from sending end to the fault point.

$$0\le x\le L \tag{17}$$

IV. Modal transformation

The coupled direct equations in the three-phase transmission line are as below:

$$\frac{\partial v(x,t)}{\partial x}=-L\frac{\partial i(x,t)}{\partial t} \tag{18}$$

$$\frac{\partial i(x,t)}{\partial x}=-C\frac{\partial v(x,t)}{\partial t} \tag{19}$$

To get rid of the mutual effects, a transformation should be used to eliminate the foresaid mutual effects. Modal transformation can decompose the coupled equations into decoupled ones. By determining the equation in modal domain that is similar to the equation for a single-phase transmission line, decoupling process is terminated. A commonly used modal transformation matrix is defined as:

$$M=\begin{bmatrix}1 & 1 & 1\\ 1 & -2 & 1\\ 1 & 1 & -2\end{bmatrix} \tag{20}$$

The phase quantities will be transformed to each other by using M matrix.

$$[I_{ph}]=M\times[I_M] \tag{21}$$

$$[I_M]=M^{-1}\times[I_{ph}] \tag{22}$$

Eq. (23) can be extracted by Eq. (22).

$$\begin{bmatrix} I_0 \\ I_1 \\ I_2 \end{bmatrix} = \frac{1}{3}\begin{bmatrix} 1 & 1 & 1 \\ 1 & -1 & 0 \\ 1 & 0 & -1 \end{bmatrix}\begin{bmatrix} Ia \\ Ib \\ Ic \end{bmatrix} \tag{23}$$

in which I_0 is ground mode current and I_1 and I_2 are the aerial mode. Aerial mode 1 will be used in the fault location procedure if the aerial modes have non-zero values in all fault types. Similarly, the voltages can be derived in modal domain. The equations governing the system were derived based on these equations, and finally, the first aerial mode is used to determine the fault location in three phase transmission line. In this paper, since fault location is determined by minimizing the objective function, two different optimization algorithms are considered. The objective function is defined in Eq. (13). To assess fault location, there is a need to use an optimization algorithm with some features such as having fewer control parameters and shorter computational time, being simple and fast to converge, and having an ability to explore wider search area. In the present work, the WOA and GWO algorithms are initially used to optimally locate the fault. The use of these algorithms is based on the following reasons. First, the algorithm is universal for problem-solving and does not need to transform the problem as a linear and mix-integer model. Second, we define some constraints to the problem. These algorithms are swarm-based methods which are driven from the collective behavior of social creatures. The implementation of swarm-based algorithms is easier than the evolutionary-based algorithms because they include fewer operators (i.e., selection, crossover, mutation). Also, these algorithms have lower input parameters as compared to evolutionary-based algorithms, like genetic algorithm. These methods use time domain representation of the signal and distributed-parameter model of the transmission line. Two approaches solve partial equations using optimization algorithm methods. They require the solution of partial differential equations.

A. Whale Optimization Algorithm (WOA)

In 2016, Mirjalili and Lewis developed an optimization algorithm which named Whale Optimization Algorithm (WOA). It is inspired by the hunting behavior of humpback whales in response to the search for food in the nature [11]. The main interesting point of these whales is how they hunt humpbacks. In WOA, each solution is thought to be a whale. In this solution, a whale tries to replete a new place in the search space considered as a reference the best element of the group. Two mechanisms are used by the whales to locate their prey and attack it. In the first one, the preys are encircled and the second creates bubble nets. Regarding optimization, when the whales look for a prey, the search space is explored and the exploitation occurs during the attack behavior. Random search and local search are two main characteristics of WOA. They play an important role to get the highest capability in solving the optimization problem. WOA has some good features, like simplicity, reliability, robustness, and flexibility. As already mentioned, the operational steps of this algorithm include the following ones: encircling the target, bubble-net attacking method, and searching for the target. Ashraf Darwish [12] and Xiaofei Wang and Hui Zhao [13] have described it in details.

B. Grey wolf Optimization (GWO)

The GWO algorithm is one of the recent meta-heuristic algorithms which is based on hunting and social leadership of grey wolves (Ashraf Darwish [12]). It was proposed by Iranian scholar Mirjalili in 2014. Gray wolves usually live in groups, and under the leadership of a head grey wolf, the wolves capture the prey through a series of processes, such as surrounding, hunting and attacking. In this algorithm, attaining the results is centered on three best grey wolves. The leader of the group is called alpha and is responsible for some activities such as making decisions about sleeping place and hunting [12, 13]. The second wolf is called beta, and he helps the wolf alpha in making decisions. The third grey wolf is called omega and is responsible for providing information to all the other wolves. All the other remaining gray wolves are called delta. They are responsible for dominating the omega. The main phases of the GWO algorithm are based on the following steps [12]:

- Tracking, chasing and approaching the prey.
- Pursuing, encircling and harassing the prey.
- Attacking the prey.

More details on this algorithm is available in [13]. In this paper the performance of our approach is evaluated by the GWO algorithm.

C. Flowchart

More details about the proposed approach is depicted in Fig. 6. In this paper, Eq. (13) is selected as the fitness function.

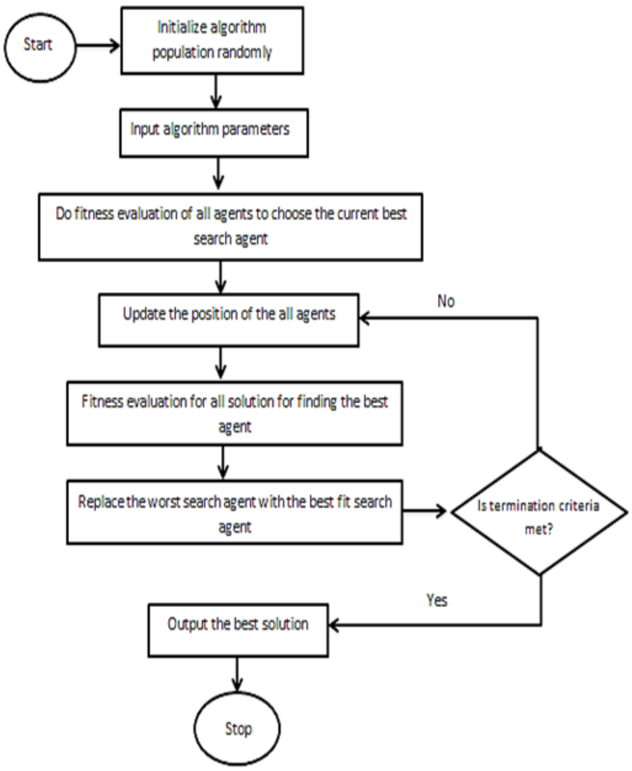

Fig. 6. The WOA methodology.

It is shown that in the optimization procedure, whenever the initial solutions are generated, the fitness function is evaluated for each solution. The solution that has the best fitness function (lower value of Eq. (13)) is used to update the current solutions. This step is repeated until the breaking rule is met. Finally, among all the solutions, the one with the best value of the fitness function is selected as the optimum solution of the problem

V. Simulated Case Study

In order to get the exact fault location, two different optimization algorithms are considered in this paper. It should be noted that there is an effective factor for any method to attain the location of the fault. This is mis-locality in the consequences, which is defined by Eq. (24).

$$E_{FL} = \frac{X_{measured} - X_{real}}{L_{sr}} \times 100 \qquad (24)$$

where $X_{measured}$ is the measured location of a fault, X_{real} is the real location of the fault, and L_{sr} is the totality of line length. This equation provides a metric to analyze the accuracy of the proposed fault location methods.

VI. Results and Discussion

A series of simulation studies were conducted to evaluate the performance of the approach using MATLAB/Simulink. The test system is shown in Fig. 7. The voltage of the system was 400 kV and the length of line was 120 km. The variables of this line are presented in Table 1. A fault occurs at point F with an distance of X km from the end bus (S) after the simulating results are obtained. Optimization would be done by using the WOA and GWO algorithms. The maximum number of iterations and initial population size were set at 500 and 100, respectively. In order to avoid the fluctuations of the performance, we repeated the algorithm for 20 times. After finding the voltage and current waveforms in the modal domain, optimization algorithm was utilized to locate the fault. The results were illustrated for comparison. A three-phase fault to ground has occurred on section SR without any resistance to ground.

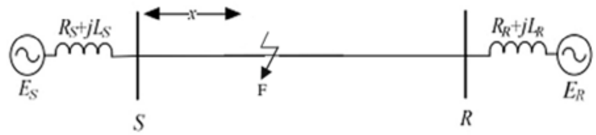

Fig. 7. The studied system.

TABLE I
Transmission Line Parameters

$R^{+}_{Line} = 0.0275 \quad \Omega/km$	$R^{0}_{Line} = 0.0275 \quad \Omega/km$
$L^{+}_{Line} = 1.00268 \quad mH/km$	$L^{0}_{Line} = 3.26798 \quad mH/km$
$C^{+}_{Line} = 0.013 \quad \mu F/km$	$C^{0}_{Line} = 0.0085 \quad \mu F/km$

The fault occurrence time was 0.02 s and its clearance time was .04 s. The voltage and current waveforms were achieved at buses S and R as shown in Figs. 9-12, respectively. Also, their adaptive waveforms in the modal domain are depicted in Figs. 13-16. These figures illustrate the voltage and current change during the time interval between 0-2 s. The average operation time of the WOA and GWO algorithms were 10.125 min and 1.957 min, respectively. So, based on the time value to achieve the result for all types, WOA took more time to optimize the objective function. It may be regarded as a bad attainment. A comparison between WOA and GWO was done to verifying which algorithm was better than the other.

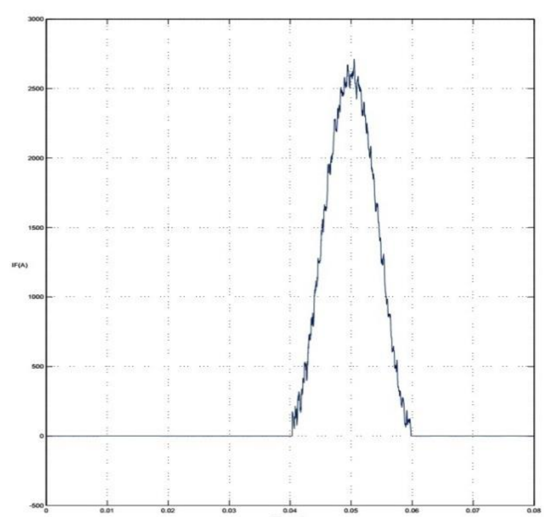

Fig. 8. The fault current waveform.

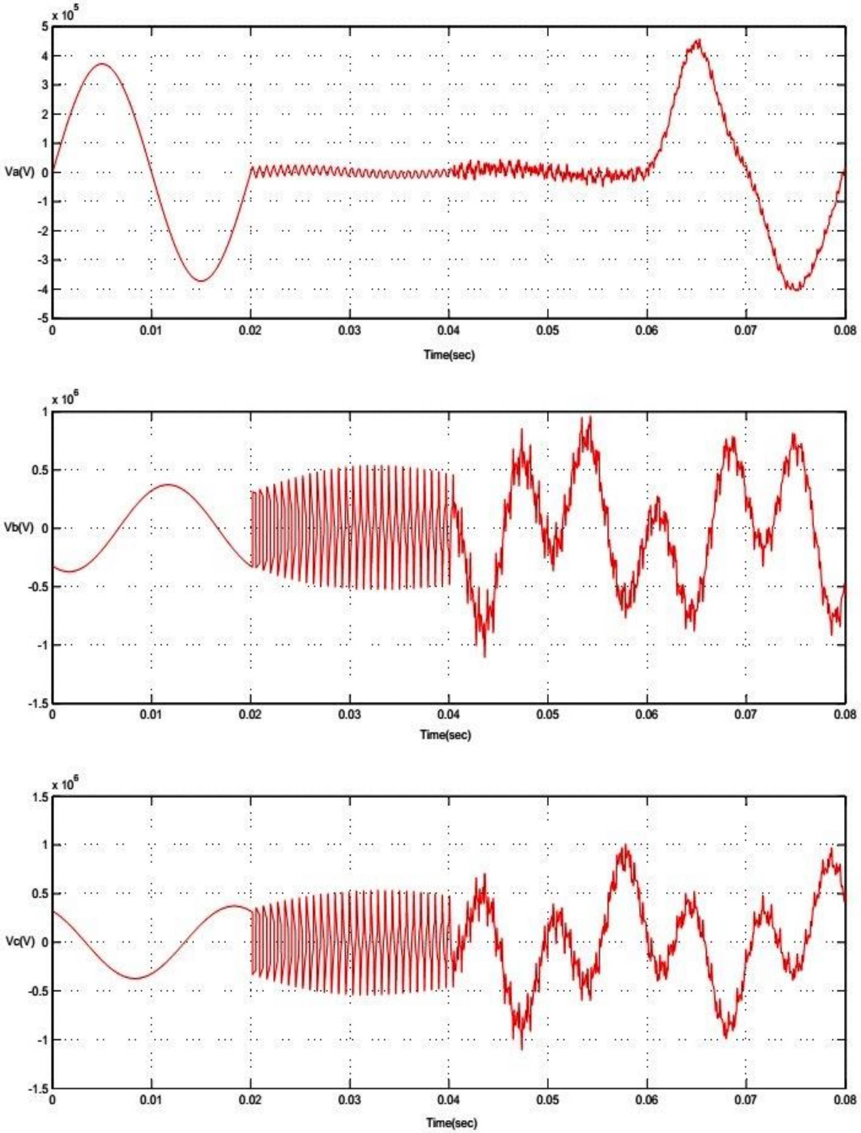

Fig. 9. Three-phase voltage waveforms of terminal S.

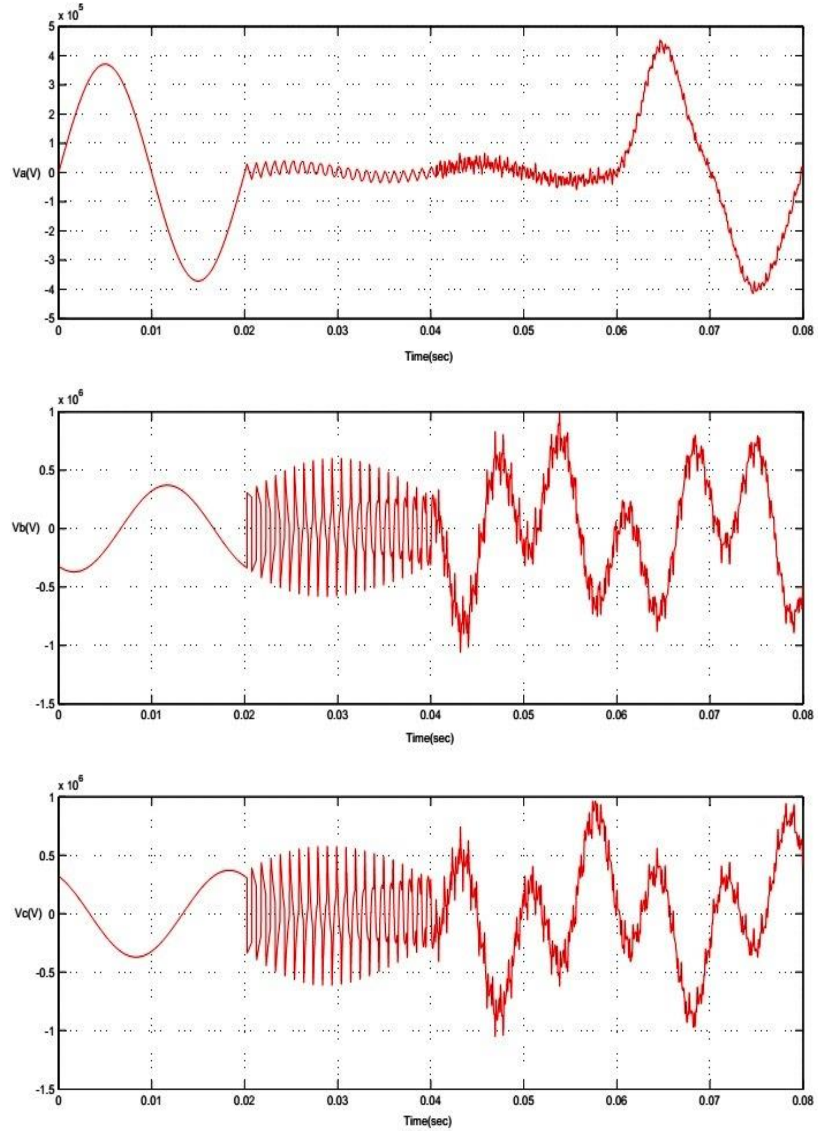

Fig. 10. Three-phase voltage waveforms of terminal R.

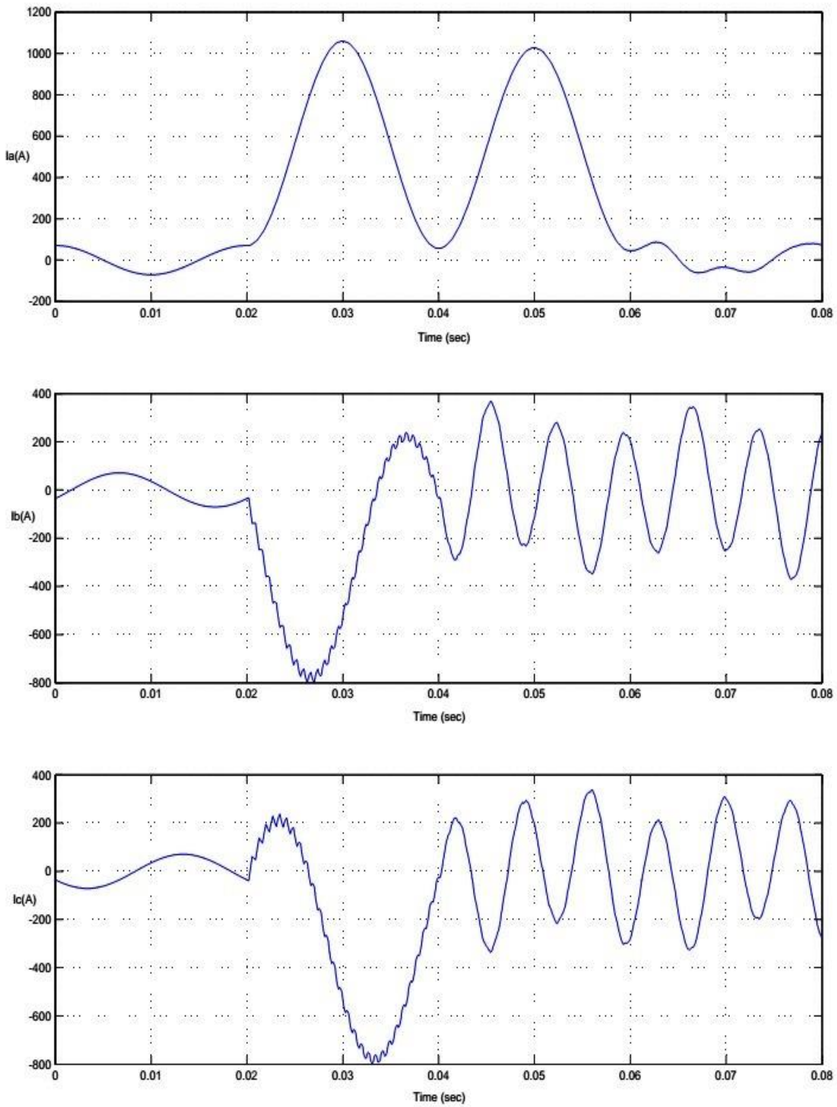

Fig. 11. Line current waveforms with measurement at terminal S.

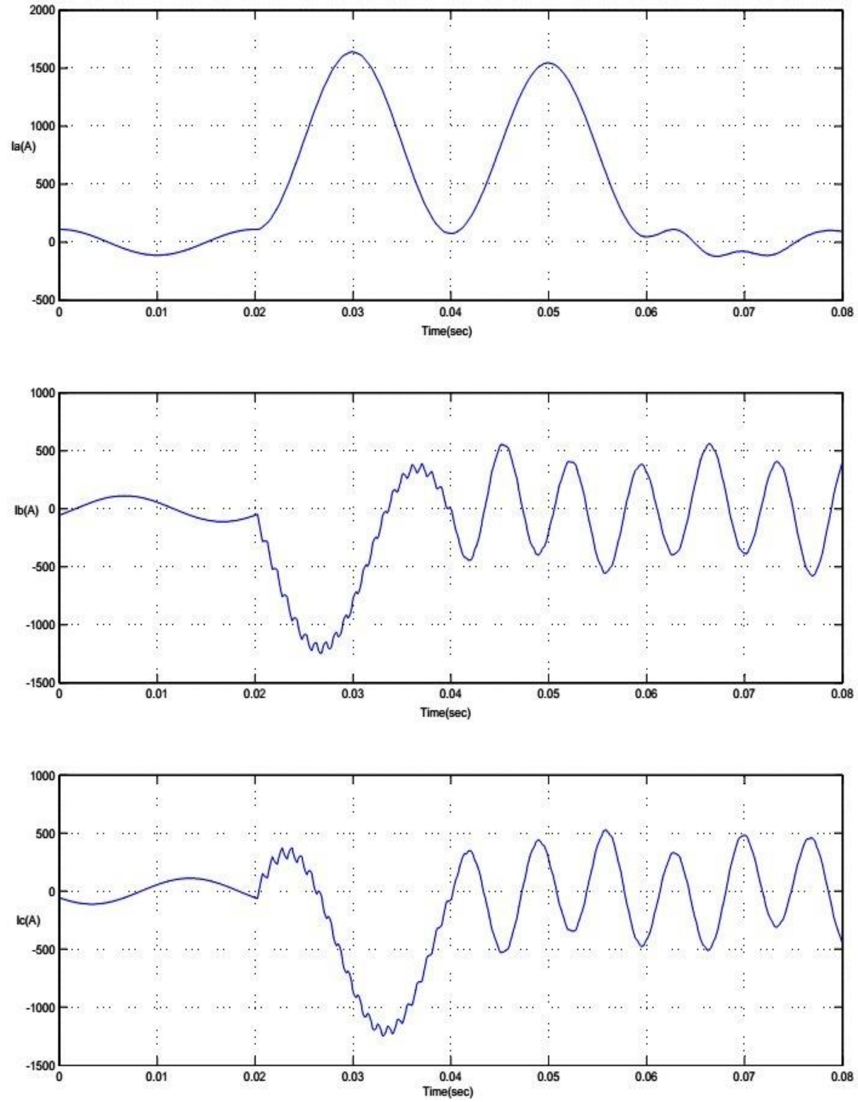

Fig. 12. Line current waveforms with measurement at terminal R.

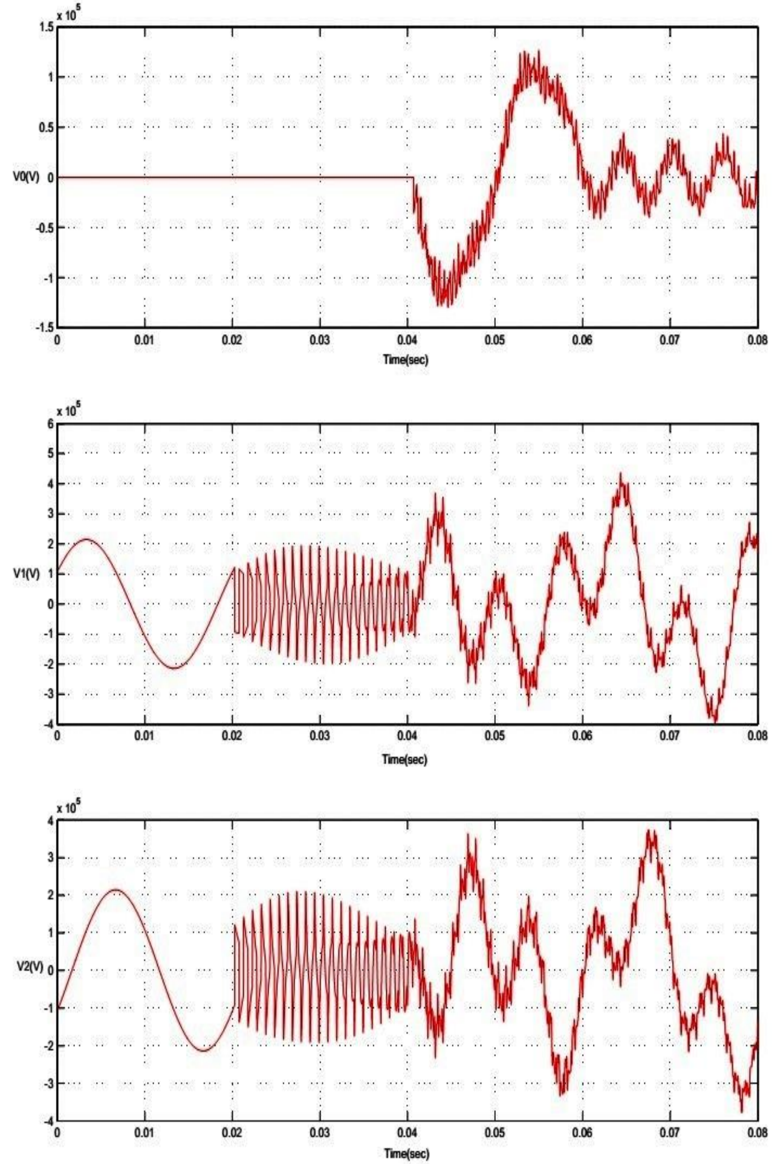

Fig. 13.Three-phase voltage waveforms in modal domain for terminal S.

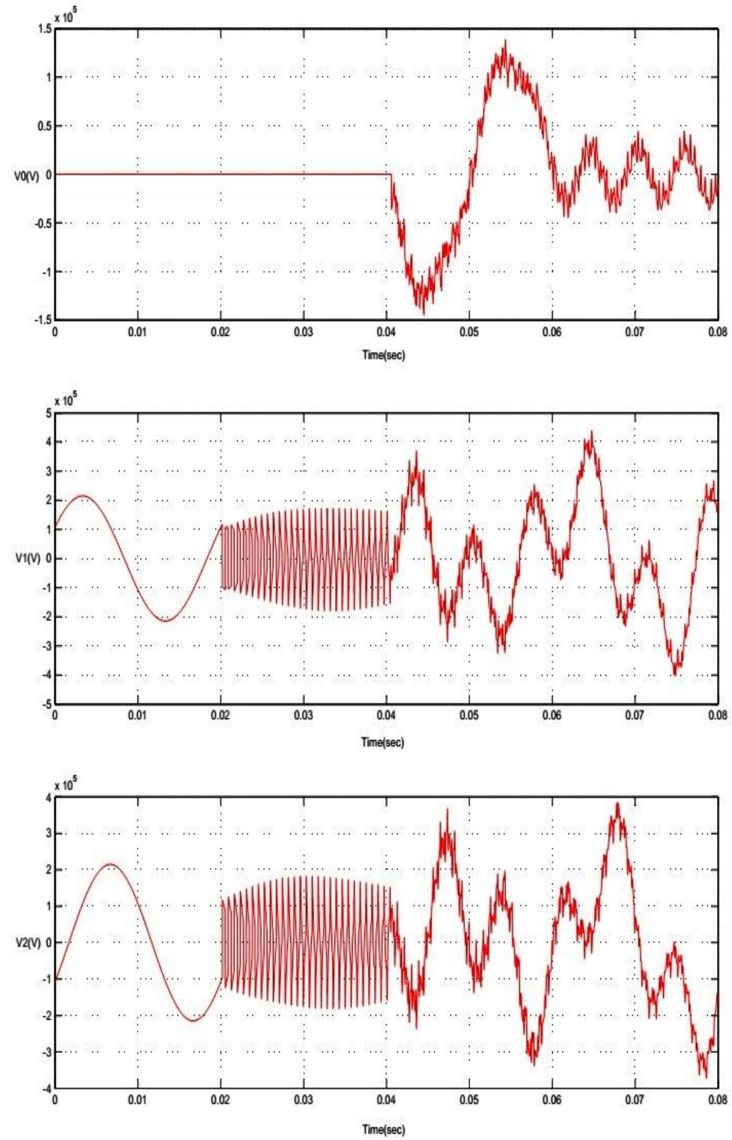

Fig. 14.Three-phase voltage waveforms in modal domain for terminal R.

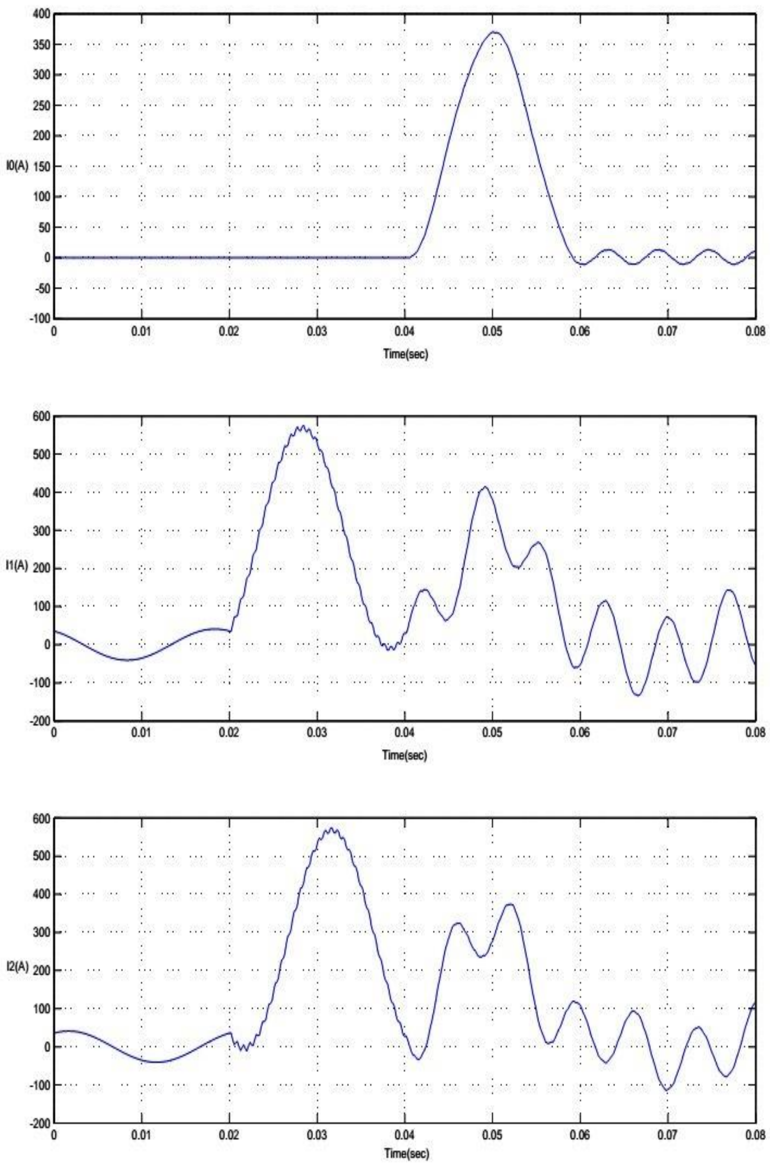

Fig. 15.Line current waveforms in modal domain with measurement at terminal S.

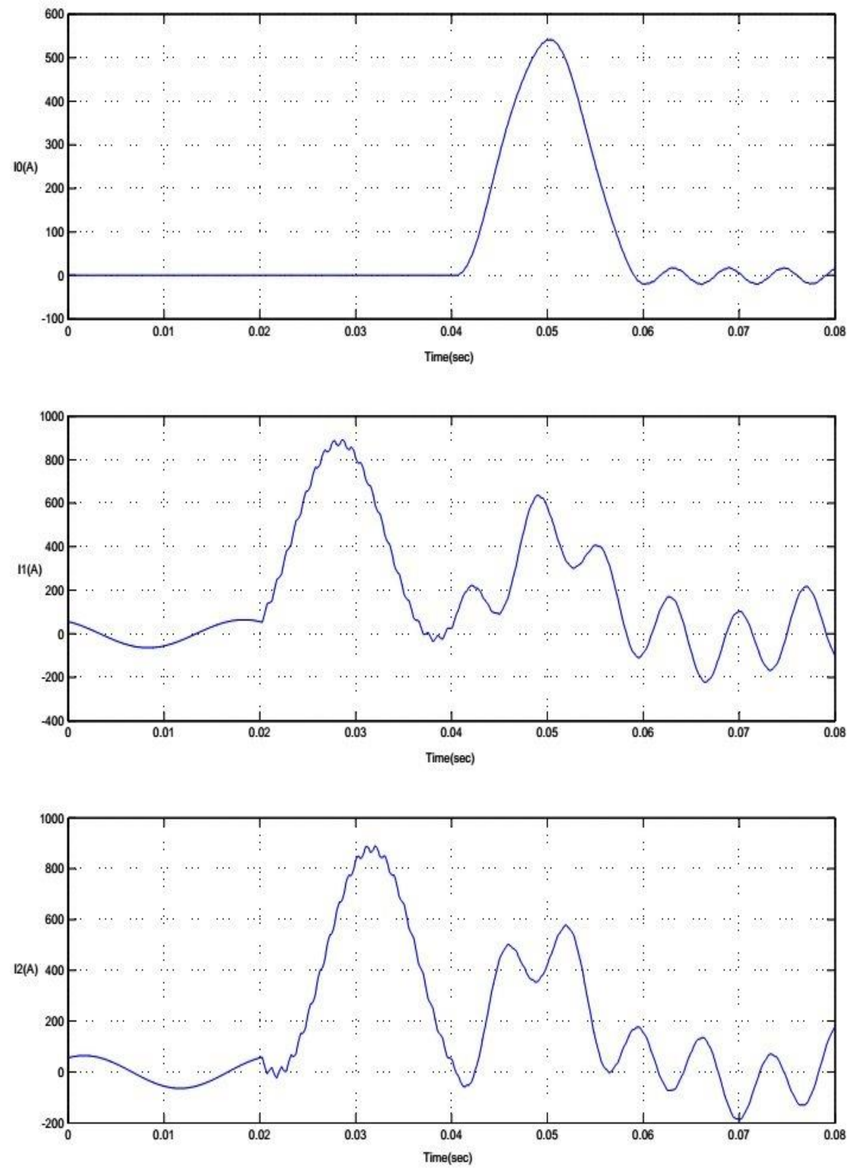

Fig. 16.Line current waveforms in modal domain with measurement at terminal R

TABLE II

ATTAINED SOLUTIONS FOR WOA AT DIFFERENT LOCATIONS AND RESISTANCES OF FAULT =0 OHM.

Fault type	Fault real location	Fault location measured by WOA	Fault location by GWO	Error % in WOA	Error % in GWO
ABCG	5	4.9736	4.967	-0.0220	-0.0275
	50	49.4301	49.41	-0.4749	-0.4917
	100	99.937	98.9034	-0.0525	-0.9138
	115	114.906	114.831	-0.0783	-0.1408
AG	5	4.9728	4.9638	-0.0227	-0.0302
	50	49.458	49.4031	-0.4517	-0.4974
	100	99.941	98.906	-0.0492	-0.9117
	115	114.911	114.794	-0.0742	-0.1717
ABG	5	4.9731	4.9686	-0.0224	-0.0262
	50	49.461	49.4058	-0.4492	-0.4952
	100	99.954	98.886	-0.0383	-0.9283
	115	114.908	114.842	-0.0767	-0.1317
AB	5	4.9801	4.973	-0.0166	-0.0225
	50	49.851	49.7056	-0.1242	-0.2453
	100	99.952	98.9171	-0.0400	-0.9024
	115	114.941	114.889	-0.0492	-0.0925

TABLE III

ATTAINED SOLUTIONS FOR WOA AT DIFFERENT LOCATIONS AND RESISTANCES OF FAULT =5 OHM.

Fault type	Fault real location	Fault location measured by WOA	Fault location by GWO	Error % in WOA	Error % in GWO
ABCG	5	5.0632	5.136	0.0527	0.1133
	50	50.487	50.497	0.4058	0.4142
	100	99.799	99.698	-0.1675	-0.2517
	115	115.207	115.226	0.1725	0.1883
AG	5	5.2005	5.290	0.1671	0.2417
	50	50.307	50.474	0.2558	0.3950
	100	99.834	99.588	-0.1383	-0.3433
	115	115.709	115.798	0.5908	0.6650
ABG	5	5.1837	5.1989	0.1531	0.1658
	50	50. 615	50.863	0.5125	0.7192
	100	99.981	98.895	-0.0158	-0.9208
	115	115.967	115.981	0.8058	0.8175
AB	5	4.951	4.869	-0.0408	-0.1092
	50	50.361	50.6101	0.3008	0.5084
	100	100.83	100.977	0.6917	0.8142
	115	114.583	114.497	-0.3475	-0.4192

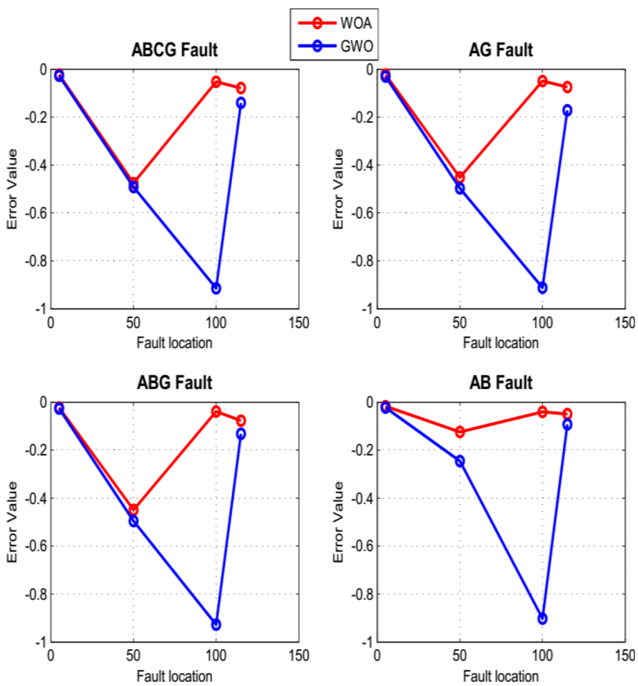

Fig. 17. Error profile at different fault location with resistance of fault =0 ohm.

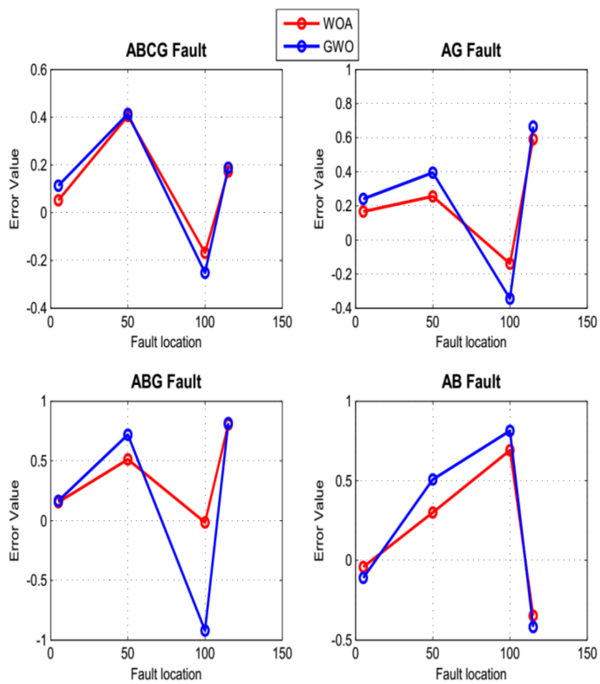

Fig. 18. Error profile at different fault location with resistance of fault =5 ohm.

TABLE IV

ATTAINED SOLUTIONS FOR WOA AT DIFFERENT LOCATIONS AND RESISTANCES OF FAULT =15 OHM.

Fault type	Fault real location	Fault measured location by WOA	Fault measured location by GWO	Error % in WOA	Error % in GWO
ABCG	5	5.2641	5.2798	0.2201	0.2332
	50	50.135	50.261	0.1125	0.2175
	100	99.893	99.6029	-0.0892	-0.3309
	115	115.14	115.301	0.1167	0.2508
AG	5	5.0370	5.1470	0.0308	0.1225
	50	50.218	50.4011	0.1817	0.3342
	100	100.063	100.264	0.0525	0.2200
	115	115.271	115.740	0.2258	0.6167
ABG	5	5.1837	5.1989	0.1531	0.1658
	50	50. 615	50.863	0.5125	0.7192
	100	99.981	98.795	-0.0158	-1.0042
	115	115.567	115.605	0.4725	0.5042
AB	5	4.6821	4.3979	-0.2649	-0.5018
	50	50.539	50.581	0.4492	0.4842
	100	100.795	100.890	0.6625	0.7417
	115	114.476	114.364	-0.4367	-0.5300

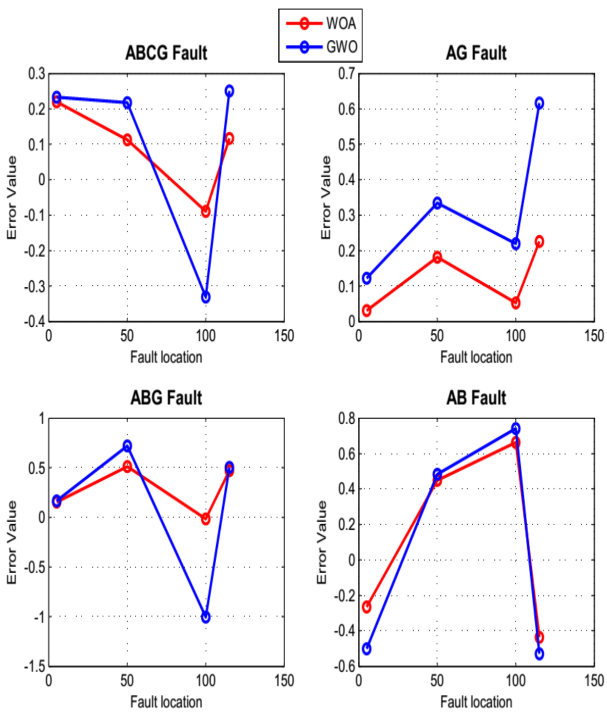

Fig. 19. Error profile at different fault locations with resistance of fault =15 ohm.

Tables II-IV show the comparison between the WOA and GWO algorithms. Based on different locations and fault resistance, the results of all fault types are illustrated in these tables. It is clear that WOA and GOW show the results accurately in spite of the fault type and fault resistance.

Figs. 17-19 show the error profile of the used algorithms at different fault locations. The analysis revealed a strong capability of the proposed approach (%error<1). It can be seen that the WOA algorithm has a higher capability than the other one. Also, Figs. 20-23 illustrate the effect of fault resistance on error value in different fault locations. As is shown, the fault resistance affects detection accuracy and %error. Although it is true for all fault types wherever the fault is, fault location is detected with minimal error values. The same has been included in Tables I-IV.

VII. CONCLUSIONS

A new correct fault location algorithm was used to compute the correct location of fault based on the Bergeron model of transmission line. In order to clarify the idea about the proposed method used in this paper, some factors such as simulation time, number of inputs, and rules are considered. Based on these factors, the complexity level is determined. In this article, some simulations were performed in different conditions, and the performance of the proposed method was compared with the GWO method. The aforesaid conditions are as follows: symmetrical and unsymmetrical faults, different fault locations, and different fault resistance. The results indicated the superiority of the proposed method in all cases. The main advantages of the proposed method are as follows:

- High accuracy of calculations
- High operating speed and low computational time
- Suitable to search for the solutions
- Low complexity of implementation
- Correct operation in different conditions of fault

Based on these advantages, the concerns on utilities about the service interruptions and down times are minimized by the proposed method. In this work, it is supposed that the location of PMU is known. In future works, the allocation of PMUs is recommended in the process of the problem definition.

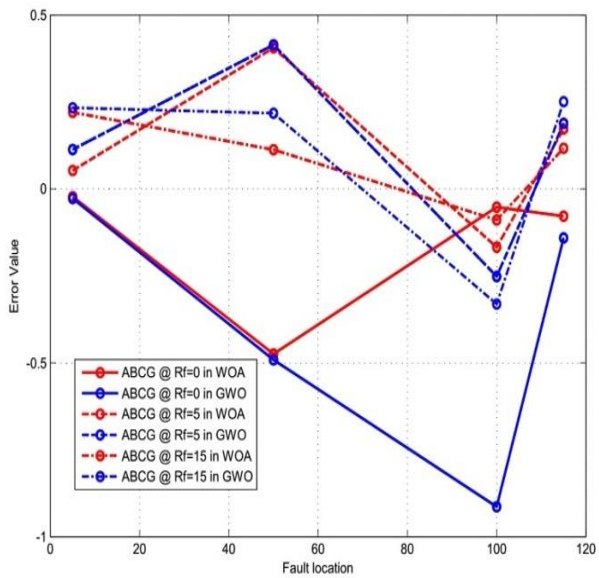

Fig. 20.Error value at different fault resistance for ABCG fault

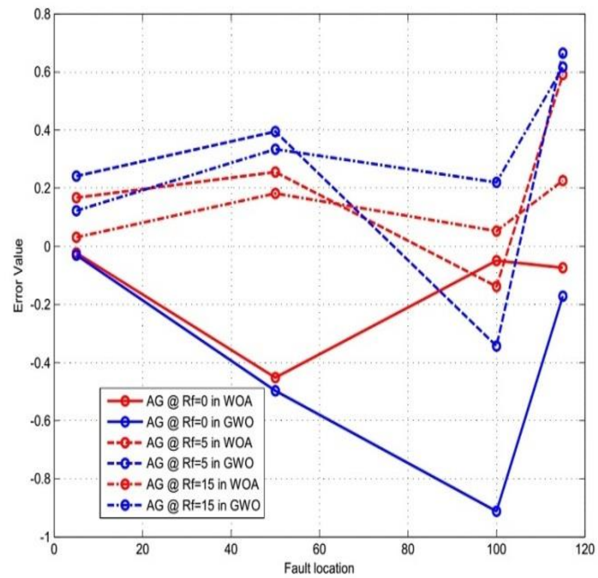

Fig. 21.Error value at different fault resistance for AG fault

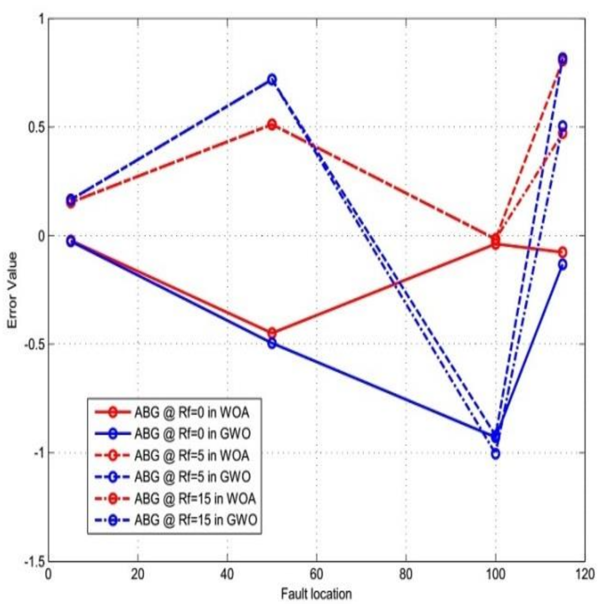

Fig. 22.Error value at different fault resistance for ABG fault.

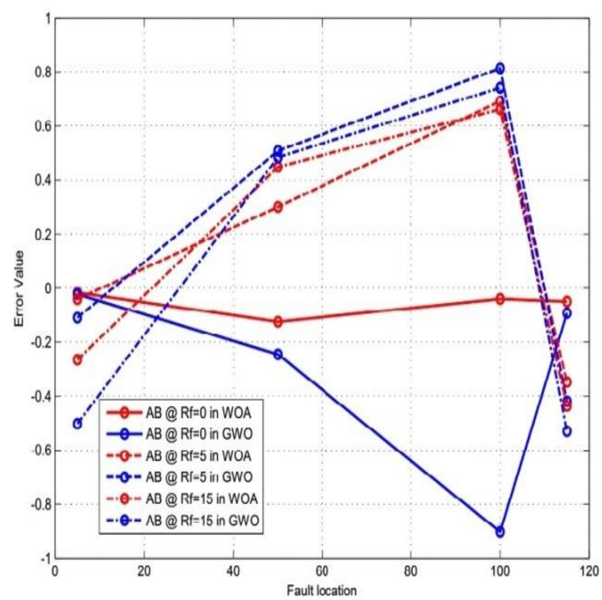

Fig. 23.Error value at different fault resistance for AB fault.

REFERENCES

[1] M.Ghiafeh Davoudi., & J. Sadeh," Time Domain Fault Location on Transmission Lines Using Genetic Algorithm". *11th International Conference on Environment and Electrical Engineering*, May, 2012.

[2] M.Kezunovic. ,& J. Mrkic,"An accurate fault location algorithm using synchronized sampling".*Electric Power Systems Research*, 161-169, 1993.

[3] J. Sadeh,"Accurate fault location algorithm for transmission line in the presence of series connected FACTS devices". *Electrical Power and Energy Systems*, 323–328, 2009.

[4] M.Ghazizadeh," Two-terminal AF location scheme for multi-segment combined transmission lines using unsynchronized measurements" *Electrical Power and Energy Systems*, 104 101–109, 2019.

[5] Ou Junzhang, & Z. Zhonghui,"The Research of Fault Location of Transmission Line Based on Bergeron Model", *3rd International Conference on Advanced Computer Theory and Engineering(ICACTE)*, August, 2010.

[6] A.S. Ahmed., & M. A. Attia," Modern optimization algorithms for fault location estimation in power systems". *Engineering Science and Technology, an International Journal*, 20, 1475–1485,2017.

[7] Omar A. S. Youssef," Fault classification based on wavelet transforms". *Transmission and Distribution" Conference and Exposition*, November,2001

[8] A.Salehi Dobakhshari," Fast accurate fault location on transmission system utilizing wide-area unsynchronized measurements". *Electrical Power and Energy Systems*, 234–242, 2018.

[9] Gabriel Pino," Fault location in transmission line using time domain equations", M.S. Thesis, Sao Paulo University, 2018.

[10] Maja Knezev, & Dipl.Ing,"Optimal Fault Location",M.S. Thesis, Texas A&M University,2007.

[11] Farhad Soleimanian., & Gharehchopogh,"A comprehensive survey: Whale Optimization Algorithm and its applications*",Swarm and Evolutionary Computation BASE DATA*, S2210-6502(18)30935-0, 2019.

[12] Ashraf Darwish," Bio-Inspired Computing: Algorithms Review, Deep Analysis, and the Scope of Applications", *Future Computing and Informatics Journal*, S2314-7288(18)30063-1, 2018.

[13] Xiaofei Wang., & Hui Zhao," A grey wolf optimizer using Gaussian estimation of distribution and its application in the multi-UAV multi-target urban tracking problem",A*pplied Soft Computing Journal*, S1568-4946(19)30101-2, 2019.

[14] M.Mirzaei., & M.Z.A.AbKadi," Review of Fault Location Meth od s for Distribution Power System", *Australian Journal of Basic and Applied Sciences*, 3(3), 2670-2676,2009.

[15] A. Bahmanyar., & S. Jamali," A comparison framework for distribution system outage and fault location methods", *Electric Power Systems Research*, 145,19–34,2017

[16] Avagaddi Prasad., & J. Belwin Edward,"A Review on Fault Classification Methodologies in Power Transmission Systems",*Journal of electrical systems and information technology*, S2314-7172(17)30006-5,2017.

[17] Alireza Siadatan, & Narges Fatahi, & Mahsa Sedaghat, "Optimum Designed Multilayer Switched Reluctance Motors for use in Electric Vehicles to Increase Efficiency", *International Symposium on Power Electronics, Electrical Drives, Automation and Motion (SPEEDAM)*, 2018.

[18] H. Torkaman & M. Fakhari & H. Karimi & B. Taheri, " New Frequency Modulation Strategy with SHE for H-bridge Multilevel Inverters*", 4th International Conference on Electrical Energy Systems (ICEES)*, 2018.

[19] Shokoufeh Sharifi & Mahsa Sedaghat & etc, " Environmental economic dispatch using improved artificial bee colony algorithm", *Evolving Systems*, 8, pages233–242, 2017.

Hossein Faramarzi received his B.Sc. degree in Electrical Engineering from Shahed University, Tehran, Iran in 2009 and his M.Sc. degree in Electrical Engineering from Imam Khomeini International University, Qazvin, Iran in 2012. He is currently a Ph.D. candidate in Electrical Engineering at Imam Khomeini International University. His research interests cover power system optimization, energy hub management, power system protection, and renewable energy systems.

Navid Ghaffarzadeh is an associate professor in Department of Electrical Engineering at Imam Khomeini International University, Qazvin, Iran. His main areas of research interest are smart grid, intelligent systems, optimization applications in power systems, power system protection, renewable energy, and power quality. He has over 100 technical publications and has written seven books on power systems.

International Journal of Industrial Electronics, Control and Optimization © 2020 IECO
Vol. 3, No. 4, pp. 407-414, Sep (2020)

A Semi-Analytic Method for Solving a Class of Non-Linear Optimal Control Problems

Pooneh Omidiniya[1,] and Maryam Alipour[2,†]

[1,2] Department of Mathematics, Statistics and Computer Science, University of Sistan and Baluchestan, Zahedan, Iran.

ABSTRACT

This paper, proposes an approximate analytical method to solve a class of optimal control problems. This method is an enhancement of the variational iteration method (VIM) that named modified variational iteration method (MVIM) and eliminates all additional calculations in VIM, thus requires less time to do the calculations. In this approach, first, the optimal control problem is converted into a nonlinear two-point boundary value problem via the Pontryagins maximum principle, and then we applied the MVIM method to solve this boundary value problem. This suggested method is suitable for a large class of nonlinear optimal control problems that for the non-linear part of the problem, we used the Taylor series expansion. In the end, three examples are provided to demonstrate the simplicity and efficiency of the method. Numerical results of the proposed method versus other methods is presented in tables. All calculations were carried out using Mathematica software.

Article Info

Keywords:
Differential equations, Modified variational iteration method (MVIM),Numerical solution, Optimal control problems

Article History:
Received 2019-11-20
Accepted 2020-02-03

I. Introduction

Recently, non-linear optimal control problems (NOCPs) have been applied in different fields such as aircraft systems [1, 2], biomedicine [3] and robotics [4]. Because of the importance of this type of problem and its impact on science and engineering, researchers have shown considerable interest in this issue. Indeed, numerical approaches are usually applied to solve the problems In direct methods, the problem can be converted into a linear or non-linear programming by using the discretization or parametrization techniques [5]. Indirect methods, on the other hand, are based on the Pontryagin's maximum principle [6]. Various kinds of techniques have been proposed to solve NOCP's. Shirazian et al. [7] suggested the application of the variational iteration method along with a shooting method in order to solve the extreme conditions resulting from the Pontryagin's maximu principle. Kafash et al. [8] offered a numerical approach for solving optimal control problems (OCP) using the Boubaker polynomials expansion scheme. This approach is based on state parametrization. Indeed, the state variable is approximated by Boubaker polynomials with unknown coefficients and then performance index and boundary conditions are transformed into some algebraic equations. A new analytic technique based on VIM and some modifications was suggested to solve NOCPs in [9]. Jafari et al. [10] has been shown that the method proposed in [9] is exactly the same iterative formula as the ADM and HPM for solving NOCPs. Alipour et al. [11] introduced an approach for NOCPs which makes use of homotopy analysis and parametrization methods. Actually an appropriate parametrization of control is applied and state variables are computed using homotopy analysis method. Jajarmi et al. [12] came up with a novel analytical technique, called OHPM, to solve a class of NOCPs. In this paper, the authors argue that the proposed algorithm method has low computational complexity and fast convergence rate. A numerical technique based on the linear B-spline polynomials offered to solve OCP [13]. In this process, state and control functions are approximated in terms of B-spline functions. Also, in [14], OCPs were solved through the spectral homotopy analysis method (SHAM). SHAM is combination of

†Corresponding Author :m.alipour@math.usb.ac.ir
Tell: 09113130460
Faculty of Mathematics, Statistics and Computer Science, University of Sistan and Baluchestan, Zahedan, Iran.

the hybrid spectral collocation technique and the homotopy analysis method. This article points out that SHAM is stronger than HAM due to it removes restrictions of the HAM such as the requirement for the solution to conform to the so-called rule of solution expression and the rule of coefficient ergodicity. In addition, more numerical methods in this area can be found in [15, 16, 17, 18, 19].

Ji-Huan He adevised a method to solve non-linear differential equations using VIM [20, 21]. VIM also features a number of disadvantages which decrease its power. These are mainly associated with repetitive calculations and the introduction of excessive unnecessary terms. To overcome these downsides, Abassy et al. [22] proposed the modified variational iteration method (MVIM). Besides, MVIM improved the rate of convergence. This paper uses MVIM as a semi-analytical method to solve NOCPs. The proposed method is an indirect method and does not require discretization, linearization or transformation. In this approach, first, the optimal control problem is converted into a nonlinear two-point boundary value problem via the Pontryagin's maximum principle, and then we applied the MVIM method to solve this boundary value problem. The examples show that our proposed method is rewarding thanks to its simplicity and small computation costs. The paper is organized as follows: Section 2, introduces NOCPs; MVIM for NOCPs is discussed in Section 3; Section4 simulates the numerical examples to check the efficiency of the method; and Section 5 draws a number of conclusions based on the results.

II. NONLINEAR OPTIMAL CONTROL PROBLEMS

Consider the following nonlinear dynamical system:

$$x'(t) = f\big(t, x(t)\big) + g\big(t, x(t)\big)u(t), t \in [t_0, t_f] \quad (1)$$
$$x(t_0) = x_0\,,\ x(t_f) = x_f,$$

Where $x(t) \in R^n$ denotes the state variable, $u(t) \in R^m$ is the control variable, and x_0 and x_f are the given initial and final states at t_0 and t_f respectively. Moreover, $f\big(t, x(t)\big) \in R^n$ and $g\big(t, x(t)\big)u(t) \in R^{n\times m}$ are two continuously differentiable functions in all arguments. Our purpose is to minimize the quadratic objective function.

$$J[x, u] = \frac{1}{2}\int_{t_0}^{t_f}(x^T(t)Qx(t) + u^T(t)R\,u(t)\,)\,dt \quad (2)$$

subject to the non-linear system (1), where $Q \in R^{n\times n}$ and $R \in R^{m\times m}$ are positive semi-definite and positive definite matrices, respectively. Since the performance index (2) is convex, the following extreme necessary conditions are also sufficient for optimality:

$$x' = f(t, x) + g(t, x)u^*$$
$$\lambda' = -H_x(x, u^*, \lambda),$$
$$u^* = argmin_u\, H(x, u, \lambda) \quad (3)$$
$$x(t_0) = x_0\,,\ x(t_f) = x_f,$$

where

$$H(x, u, \lambda) = \frac{1}{2}[x^TQx + u^TRu] + \lambda^T\,[f(t, x) + g(t, x)u]$$

is the Hamiltonian function. Similarly (3) can be written in the form of:

$$x' = f(t, x) + g(t, x)[-R^{-1}\,g^T(t, x)\lambda],$$
$$\lambda' = -(Qx + \left(\frac{\partial f(t,x)}{\partial x}\right)^T\lambda + \sum_{i=1}^{n}\lambda_i[-R^{-1}\,g^T(t, x)\lambda]^T\frac{\partial g_i(t,x)}{\partial x})$$
$$x(t_0) = x_0\,,\ x(t_f) = x_f \quad (4)$$

where , $\lambda(t) \in R^n$ is the co-state vector with the ith component $\lambda_i(t), i = 1, \dots, n,$ and $g(t, x) = [g_1(t, x), \dots, g_n(t, x)]^T$ with $g_i(t, x) \in R^n$, $i = 1, \dots, n.$ Also, the optimal control law is obtained by

$$u^* = -R^{-1}\,g^T(t, x)\lambda \quad (5)$$

There is no analytical solution for solving such a two-point boundary-value problem (TPBVP) in (4). Therefore, it is highly recommended to calculate analytic approximate or numerical solutions for it. We shall apply MVIM to solve the following initial value problem. Taylor series expansion is used here for the non-linear part of the problem.

III. THE MODIFIED VARIATIONA ITERATION METHOD

In this section, consider the following differential equations,

$$LV(t) + RV(t) + NV(t) = g(t)$$
$$V(0) = f(t), \quad (6)$$

where L = $\frac{d}{dt}$, R is a linear operator, N is a non-linear term and $g(t)$ is an inhomogeneous term. Using VIM [20, 21] to solve the non-linear differential equation (6), the following variational iteration formula can be obtained:

$$V_{n+1}(t) = V_n(t) - \int_0^t\{L\big(V_n(\tau)\big) + R\big(V_n(\tau)\big) + N\big(V_n(\tau)\big) - g(\tau)\}\,d\tau. \quad (7)$$

It has been shown [22] that equation (7) is equivalent to the following equation:

$$V_{n+1}(t) = V_n(t) - \int_0^t\{R\big(V_n(\tau) - V_{n-1}(\tau)\big) + \big(G_n(\tau) - G_{n-1}(\tau)\big) - g(\tau)\}\,d\tau, \quad (8)$$

where $V_{-1} = 0$, $V_0 = f(t)$, $V_1 = V_0 - \int_0^t\{\,R(V_0 - V_{-1}) + (G_0 - G_{-1}) - g\}d\tau$ and $G_n(t)$ is obtained from $NV_n(t) = G_n(t) + O(t^{n+1})$. The Maclaurin series expansion is employed here for the non-linear part of the problem. Eq. (8) can be solved iteratively to obtain an approximate solution that takes the form $V(t) \simeq V_n(t)$, where n is the final iteration step.

Theorem 1. Suppose that $V_0(t) = V_0$ and the iterative sequence $\{V_n(t)\}$ obtained from (7) converges to $V(t)$; then $V(t)$ is the solution of Eq. (6).

Proof. Considering the limits in the iterative formula (7), it follows that

$$\lim_{n\to\infty} V_{n+1} = \lim_{n\to\infty} V_n - \int_0^t \lim_{n\to\infty}[\,L\,(V_n(\tau)) + R(V_n(\tau)) + N(V_n(\tau))]\,d\tau.$$

By considering $\lim_{n\to\infty} V_n = V$ and the continuity of N operator, we will have

$$\int_0^t [L(V(\tau)) + R(V(\tau)) + N(V(\tau))]d\tau = 0.$$

Then, differentiation of both sides concerning t yields

$$LV(t) + RV(t) + NV(t) = 0. \quad (9)$$

Clearly, $V(t)$ satisfies (6). Moreover, if$t = 0$, then form (7), $V_{n+1}(0) = V_n(0)$, for every $n \geq 0$. Thus $V_0(0) = V_n(0) = V_0$. Hence, $V(t)$ is the solution of Eq. (6) and the proof is complete. Since the Maclaurin series is convergent, equation (8) also converges.

The Modified Variational Iteration Method for Nocp's

We consider equation (4) as follows:

$$x'(t) + L\,x(t) + Nx(t) = 0,$$
$$\lambda'(t) + L\,\lambda(t) + N\,\lambda(t) = 0,$$
$$x(t_0) = x_0\,,\ x(t_f) = x_f, \quad (10)$$

where L is a linear operator and N is a non-linear operator. To solve system (10) with MVIM, we should answer the following system:

$$x'(t) + L\,x(t) + Nx(t) = 0,$$
$$\lambda'(t) + L\,\lambda(t) + N\,\lambda(t) = 0,$$
$$x(t_0) = x_0\,,\ \lambda(t_0) = \alpha. \quad (11)$$

In equation (11)

$$Lx(t) + Nx(t) = -(f(t,x) + g(t,x)[-R^{-1}\,g^T(t,x)\lambda]),$$
$$L\lambda(t) + N\lambda(t) = \quad (Qx + \left(\frac{\partial f(t,x)}{\partial x}\right)^T \lambda + \sum_{i=1}^{n} \lambda_i[-R^{-1}\,g^T(t,x)\lambda]^T \frac{\partial g_i(t,x)}{\partial x}). \quad (12)$$

To solve equation (11) with MVIM, we construct the below iterations formula according to equation (8):

$$x_{n+1}(t) = x_n(t) - \int_0^t \{R\big(x_n(\tau) - x_{n-1}(\tau)\big) + \big(G_n(\tau) - G_{n-1}(\tau)\big)\}\,d\tau, \quad (13)$$

$$\lambda_{n+1}(t) = \lambda_n(t) - \int_0^t \{R\big(\lambda_n(\tau) - \lambda_{n-1}(\tau)\big) + \big(K_n(\tau) - K_{n-1}(\tau)\big)\}\,d\tau, \quad (14)$$

where $\mathrm{x}_{-1}(t) = 0$, $\lambda_{-1}(t) = 0, x(0) = \mathrm{x}_0$ and $\lambda(0) = \alpha$. We have:

$$x_1(t) = x_0(t) - \int_0^t \{R\big(x_0(\tau) - x_{-1}(\tau)\big) + \big(G_0(\tau) - G_{-1}(\tau)\big)\}\,d\tau,$$

$$\lambda_1(t) = \lambda_0(t) - \int_0^t \{R\big(\lambda_0(\tau) - \lambda_{-1}(\tau)\big) + \big(K_0(\tau) - K_{-1}(\tau)\big)\}\,d\tau,$$

and $G_n(t)$ *and* $K_n(t)$ are obtained from

$Nx_n(t) = G_n(t) + O(t^{n+1})$ and $N\lambda_n(t) = k_n(t) + O(t^{n+1})$.

Eqs. (13) and (14) can be solved iteratively to obtain an approximate solution that takes the form $x(t) \simeq x_n(t)$ and $\lambda(t) \simeq \lambda_n(t)$, where n is the final iteration step. The optimal control law is obtained by

$$u^* = -R^{-1}g^T(t,x)\lambda. \quad (15)$$

For stopping criterion, we consider the following criterion: $\left|\frac{J_{n+1} - J_n}{J_{n+1}}\right| < \varepsilon$, where $\varepsilon > 0$ should be chosen according to the desirable accuracy.

Numerically Example

In this section, we have solved three examples to illustrate the simplicity and efficiency of the proposed method.

Example 1. Consider the following nonlinear optimal control problem

$$minimize J = \int_0^1 u^2(t)dt,$$

Subject to:

$$x' = \frac{1}{2}\,x^2(t)sinx(t) + u(t), \qquad t \in [0,1],$$
$$x(0) = 0, \qquad x(1) = 0.5, \quad (16)$$

The necessary equations for the optimal control are given as:

$$x' = \frac{1}{2}\,x^2(t)sinx(t) - \frac{1}{2}\lambda(t), \qquad t \in [0,1],$$
$$\lambda' = -\lambda(t)x(t)sinx(t) - \frac{1}{2}\lambda(t)x^2(t)cosx(t),$$
$$x(0) = 0, \qquad \lambda(0) = \alpha, \quad (17)$$

that

$$u(t) = -\frac{1}{2}\lambda(t).$$

In this example, applying the following iteration formula

$$x_{n+1} = x_n - \int_0^t \{R(x_n - x_{n-1}) + (G_n - G_{n-1})\}d\tau,$$
$$\lambda_{n+1} = \lambda_n - \int_0^t \{R(\lambda_n - \lambda_{n-1}) + (G_n - G_{n-1})\}d\tau,$$

we consider

$$R\big(x(t)\big) = \frac{1}{2}\lambda(t),$$
$$G\big(x(t)\big) = -\,\frac{1}{2}\,x^2(t)sinx(t),$$
$$R\big(\lambda(t)\big) = 0,$$
$$G\big(\lambda(t)\big) = \lambda(t)x(t)sinx(t) + \frac{1}{2}\lambda(t)x^2(t)cosx(t), \quad (18)$$

by applying Mathematica software, five-term approximations for x and λ were obtained as follows:

$$x_5(t) = -\frac{t\alpha}{2},$$
$$\lambda_5(t) = \alpha - \frac{t^3\alpha^3}{8} + \frac{t^5\alpha^5}{192}.$$

In this case, we should have

$$x_5(1) = -\frac{\alpha}{2},$$

whereα is an unknown parameter which, will be obtained from the final state condition $x(t_f) = x_f$. Here, the value of α is derived from

$$x_5(1) = -\frac{\alpha}{2} = 0.5,$$

that is $\alpha = -1$. The optimal control is as follows:

$$u(t) \simeq u_5(t) = -\frac{1}{2}\lambda_5(t) = \frac{1}{2}\left(1 - \frac{t^3}{8} + \frac{t^5}{192}\right).$$

We consider $\varepsilon = 10^{-3}$. Once the proposed method is applied, the numerical results for J_i and stopping criterion are as given in Table I. The maximum absolute error of the proposed method, modal series method [23], and measure theory method [24] are presented in Table II, which shows the proposed method has achieved similar results with modal series method. In addition, it should be noted that the basic VIM can not be calculated more than two iterations for example above. Also, the obtained numerical solution for $x(t)$ and $u(t)$ in five iterative are depicted in Fig 1.

Table I: Numerical results for different iteration, Example 1

i	J_i	$\left\lvert\frac{J_i - J_{i-1}}{J_i}\right\rvert$
1	0.25000	-
2	0.25000	0
3	0.23493	6.4146767×10^{-2}
4	0.23493	0
5	0.23533	1.6997408×10^{-3}

Table II: Numerical results for the proposed method versus other methods, Example 1

Method	Objective value	Max state error	CPU time
Proposed Method (N=5)	0.2353	3.2×10^{-5}	0.01562
Modal series method (n=5)	0.2353	2.8×10^{-5}	-
Measure theory method	0.2425	4.3×10^{-3}	-

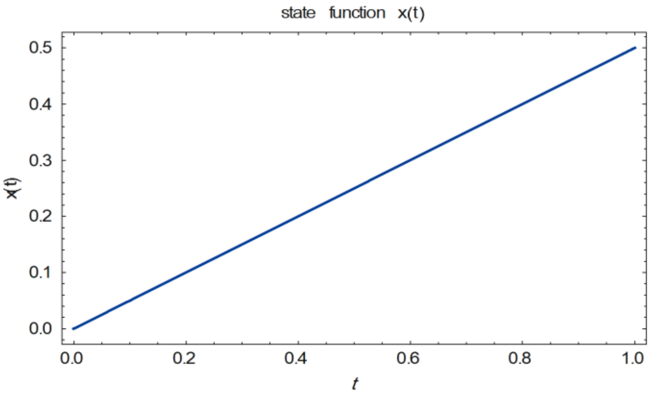

Fig. 1(a): Suboptimal state and control $x(t)$Example 1.

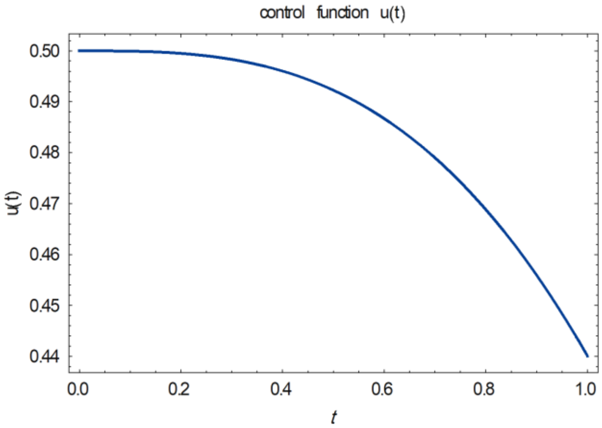

Fig. 1(b): Suboptimal state and control $u(t)$, Example 1.

Example 2. We consider the optimal maneuvers of a rigid asymmetric space craft [2]. The Euler's equations for the angular velocities of the spacecraft are given by:

$$x' = \begin{bmatrix} x'_1(t) \\ x'_2(t) \\ x'_3(t) \end{bmatrix} = \begin{bmatrix} -\frac{I_3 - I_2}{I_1} x_2(t)x_3(t) \\ -\frac{I_1 - I_3}{I_2} x_1(t)x_3(t) \\ -\frac{I_2 - I_1}{I_3} x_1(t)x_2(t) \end{bmatrix} + \begin{bmatrix} \frac{1}{I_1} & 0 & 0 \\ 0 & \frac{1}{I_2} & 0 \\ 0 & 0 & \frac{1}{I_3} \end{bmatrix} \begin{bmatrix} u_1(t) \\ u_2(t) \\ u_3(t) \end{bmatrix},$$

where x_1, x_2 and x_3 are the angular velocities of the spacecraft, u_1, u_2 and u_3 are the control torques, and $I_1 = 86.24$, $I_2 = 85.07$, and $I_3 = 113.59 \text{ kg } m^2$ are the spacecraft principle inertia. The optimal control is to find the control $u(t)$ ($t \in [o, T]$) that minimize the cost function

$$J[x,u] = \frac{1}{2}\int_0^{100} (x^T(t)Qx(t) + u^T(t)Ru(t))dt,$$

Where: $Q = \begin{bmatrix} 0 & 0 & 0 \\ 0 & 0 & 0 \\ 0 & 0 & 0 \end{bmatrix}, R = \begin{bmatrix} 1 & 0 & 0 \\ 0 & 1 & 0 \\ 0 & 0 & 1 \end{bmatrix}.$

In addition, the following boundary conditions should be satisfied:

$x_1(0) = 0.01\, {}^{r}/_{s}, x_2(0) = 0.005\, {}^{r}/_{s},\ x_3(0) = 0.001\, {}^{r}/_{s},$
$x_1(100) = x_2(100) = x_3(100) = 0\, {}^{r}/_{s}.$

According to the Pontryagin's maximum principle, the following non-linear TPBVP should be solved:

$$x_1'(t) = -\frac{\lambda_1(t)}{{I_1}^2} - \frac{I_3 - I_2}{I_1} x_2(t)x_3(t),$$

$$x_2'(t) = -\frac{\lambda_2(t)}{{I_2}^2} - \frac{I_1 - I_3}{I_2} x_1(t)x_3(t),$$

$$x_3'(t) = -\frac{\lambda_3(t)}{{I_3}^2} - \frac{I_2 - I_1}{I_3} x_1(t)x_2(t),$$

$$\lambda'_1(t)=\frac{I_1-I_3}{I_2}x_3(t)\lambda_2(t)+\frac{I_2-I_1}{I_3}x_2(t)\lambda_3(t),$$
$$\lambda'_2(t)=\frac{I_3-I_2}{I_1}x_3(t)\lambda_1(t)+\frac{I_2-I_1}{I_3}x_1(t)\lambda_3(t),$$
$$\lambda'_3(t)=\frac{I_3-I_2}{I_1}x_2(t)\lambda_1(t)+\frac{I_1-I_3}{I_2}x_1(t)\lambda_2(t),$$
$x_1(0)=0.01\, {}^{r}/_{s}, x_2(0)=0.005\, {}^{r}/_{s},\ x_3(0)=0.001\, {}^{r}/_{s},$
$x_1(100)=x_2(100)=x_3(100)=0\, {}^{r}/_{s}.$
and the optimal control law is given by:

$$\begin{cases} u_1(t)=-\dfrac{\lambda_1(t)}{I_1} \\ u_2(t)=-\dfrac{\lambda_2(t)}{I_2} & \mathrm{t}\in[0,100], \\ u_3(t)=-\dfrac{\lambda_3(t)}{I_3} \end{cases}$$

To solve the above problem by means of MVIM, we choose the initial approximations $\mathrm{x}_{1,0}(t)=0.01$, $\mathrm{x}_{2,0}(t)=0.005$, $\mathrm{x}_{3,0}(t)=0.001$, $\lambda_{1,0}(t)=\alpha_1$, $\lambda_{2,0}(t)=\alpha_2$, $\lambda_{3,0}(t)=\alpha_3$ Four-term approximations for $\lambda_1,\lambda_2,\lambda_3,\mathrm{x}_1,\mathrm{x}_2$ and x_3, were obtained as follows:

$x_{14}(t)=0.01-9.57399*10^{-10}\,t^2-3.80068*10^{-13}\,t^3-8.41885*10^{-17}\,t^4-t(1.65353*10^{-6}+0.000134457\alpha_1)+4.83265*10^{-11}\,t^3\,\alpha_1+\cdots$

$x_{24}(t)=0.005+5.62075*10^{-10}\,t^2+6.97602*10^{-14}\,t^3-9.74227*10^{-17}\,t^4-4.44624*10^{-8}\,t^2\,\alpha_1-8.35108*10^{-11}\,t^3\,\alpha_1+1.00806*10^{-14}\,t^4\,\alpha_1+\cdots$

$x_{34}(t)=0.001+2.45993*10^{-10}\,t^2-1.59378*10^{-17}\,t^4-7.10014*10^{-8}\,t^2\,\alpha_1+2.73532*10^{-27}\,t^3\,\alpha_1-2.77608*10^{-15}\,t^4\,\alpha_1+1.80313*10^{-14}\,t^4\,{\alpha_1}^2+\cdots,$

$\lambda_{14}(t)=\alpha_1-9.57399*10^{-8}\,t^2\alpha_1-3.65045*10^{-11}\,t^3\,\alpha_1-1.08007*10^{-14}\,t^4\,\alpha_1+2.61537*10^{-12}\,t^4\,{\alpha_1}^2-2.92101*10^{-12}\,t^3\,\alpha_2+4.63115*10^{-15}\,t^4\,\alpha_2+\cdots,$

$\lambda_{24}(t)=2.59506*10^{-11}\,t^3\alpha_1-4.76375*10^{-15}\,t^4\,\alpha_1-7.0635*10^{-9}\,t^3\,{\alpha_1}^2+3.50454*10^{-15}\,t^4\,{\alpha_1}^2+\alpha_2+1.12415*10^{-7}\,t^2\,\alpha_2-3.65045*10^{-11}\,t^3\,\alpha_2-1.02222*10^{-14}t^4\alpha_2+\cdots,$

$\lambda_{34}(t)=-1.05879*10^{-22}\,t^2\alpha_1+6.77927*10^{-11}\,t^3\,\alpha_1-3.01805*10^{-14}\,t^4\,\alpha_1-1.36096*10^{-10}\,t^3\,{\alpha_1}^2-1.22707*10^{-12}\,t^4\,{\alpha_1}^2-\mathrm{t}(-0.00165353\alpha_1+0.003215\alpha_2)-1.31811*10^{-10}\,t^3\,\alpha_2+\cdots$

That

$u_1(t)=-\frac{\lambda_{14}(t)}{I_1}=-0.0115955(0.743687-0.00012251\,t+5.03449*10^{-7}t^2+8.58655*10^{-10}t^3-7.81513*10^{-13}t^4),$

$u_2(t)=-\frac{\lambda_{24}(t)}{I_2}=-0.011755(0.361736+0.000233517\,t-1.04679*10^{-6}t^2-8.36735*10^{-10}t^3+2.54377*10^{-13}t^4),$

$u_3(t)=-\frac{\lambda_{34}(t)}{I_3}=-0.00880359(0.120619+0.000066725\,t-3.17293*10^{-7}t^2-1.53805*10^{-10}t^3+3.94016*10^{-13}t^4),$

with the final state condition $\mathrm{x}_{14}(100)=0, \mathrm{x}_{24}(100)=0$, $\mathrm{x}_{34}(100)=0$, we have gained:

$\alpha_1=0.7436866718467056,$
$\alpha_2=0.36173553498082317,$
$\alpha_3=\ 0.12061935192581671.$

We consider$\varepsilon=10^{-4}$. By applying the proposed method, the numerical results for J_i and stopping criterion are as given in Table III. The maximum absolute error of the proposed method, SHAM Chebyshev [14], SHAM Legendre [14] and HPM are as given in Table IV. It is noteworthy that the given method improves the maximum absolute error which indicates the efficiency of the method. Also, the obtained numerical solution for $x(t)$and $u(t)$ in four iterative are depicted in Figures 2, 3 and 4.

Table III: Numerical results for different iteration, Example 2

i	1	2	3	4
J_i	0.00468052	0.00467797	0.00467903	0.00467886
$\left\lvert\frac{J_i-J_{i-1}}{J_i}\right\rvert$	-	5.451082 × 10^{-4}	2.265426× 10^{-4}	3.63336× 10^{-5}

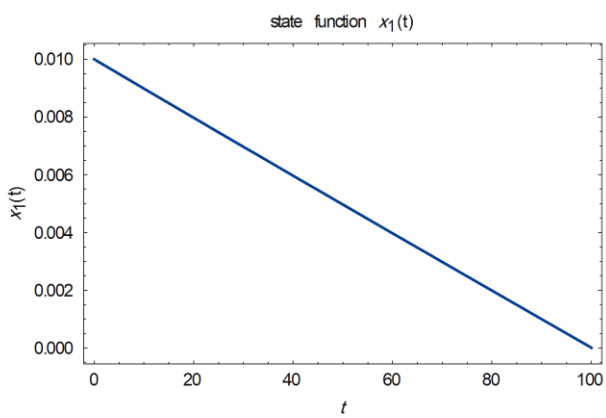

Fig. 2(a). Suboptimal state $\mathrm{x}_1(\mathrm{t})$,Example 2.

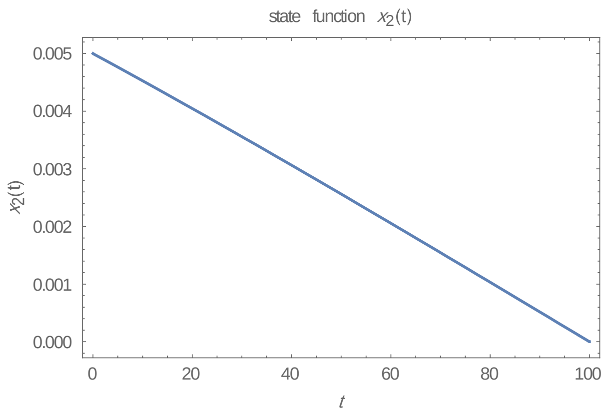

Fig. 2: Suboptimal state $x_2(t)$, Example 2.

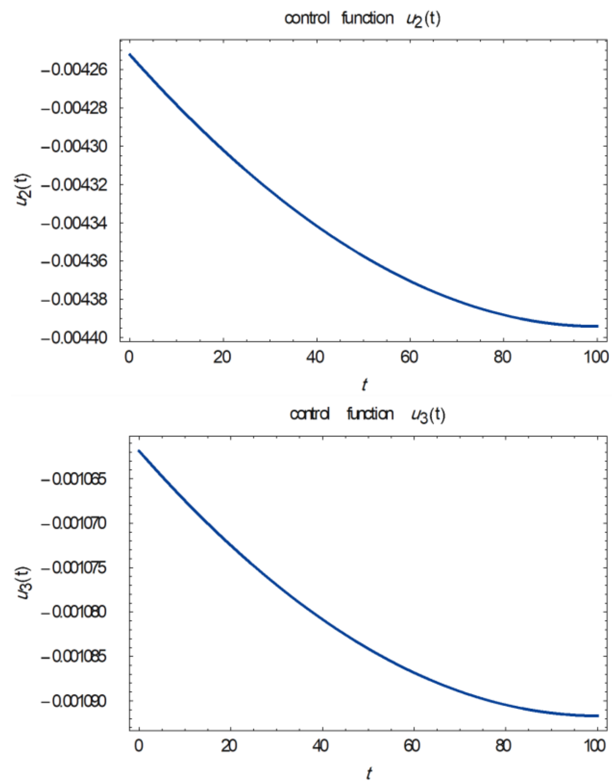

Fig. 4: Suboptimal control $u_2(t)$ and $u_3(t)$, Example 2.

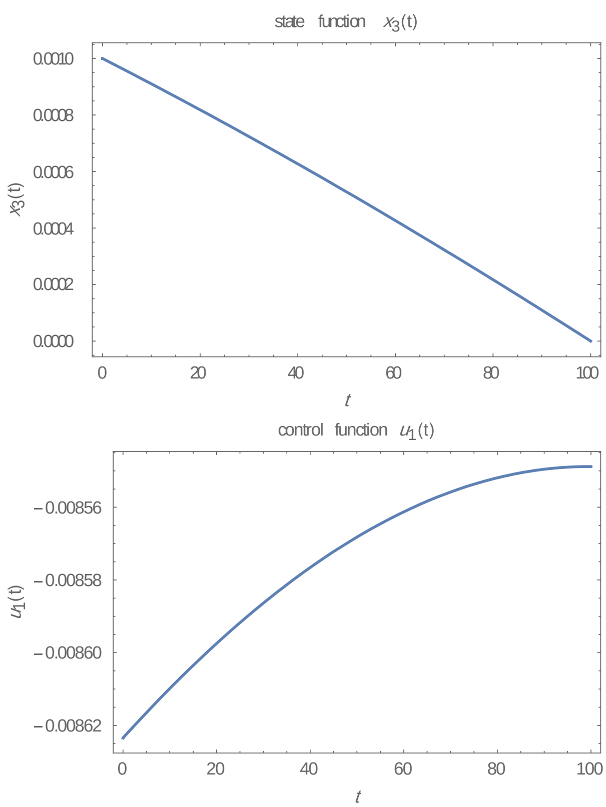

Fig. 3: Suboptimal control $x_3(t)$ and $u_1(t)$, Example2.

Table IV: Numerical results for the proposed method versus other methods, Example 2

METHOD	Objective value	Max state error	CPU time
PROPOSED METHOD	0.004678	2.40484×10^{-14}	0.046875
SHAM CHEBICHEV (M=6, N=50, H= -1.2)	0.004687	1.0586×10^{-9}	-
SHAM LEGENDER (M=6, N=50, H= -1.2)	0.004687	1.0589×10^{-9}	-
HPM (M=6)	0.004687795533	3.1420×10^{-8}	-

Example 3. Consider the non-linear system described by

$x_1{}' = x_2 + x_1 x_2$,

$x_2{}' = -x_1 + x_2 + x_2{}^2 + u$,

$x_1(0) = -0.8, \qquad x_2(0) = 0,$

and the functional

$$minimize\ J = \frac{1}{2}\int_0^1 ({x_1}^2 + {x_2}^2 + u^2)dt.$$

The extreme conditions are

$\lambda_1{}' = -(x_1 + \lambda_1 x_2 - \lambda_2)$,

$\lambda_2{}' = -(x_2 + \lambda_1(1 + x_1) + \lambda_2(1 + 2x_2))$,

$x_1{}' = x_2 + x_1 x_2$,

$x_2{}' = -x_1 + x_2 + {x_2}^2 - \lambda_2$,

that

$x_1(0) = -0.8, x_2(0) = 0,\ \ \lambda_1(1) = \lambda_2(1) = 0,$

and the optimal control is $u = -\lambda_2$. By using Mathematica software, two- term approximations for λ_1, λ_2, x_1 and x_2, were obtained as follows:

$x_{12}(t) = -0.8 + 0.08\, t^2 - 0.1\, t^2\alpha_1$,

$x_{22}(t) = 0.4\, t^2 + 0.1\, t^2\alpha_1 - t(-0.8 + \alpha_2),$

$$\lambda_{12}(t) = \alpha_1 - 0.5t^2\,\alpha_1 - t(-0.8 - \alpha_2) - \frac{t^2\alpha_2}{2} + \frac{1}{2}t^2\alpha_1\alpha_2\,,$$

$\lambda_{22}(t) = -0.48t^2 + 0.1t^2\alpha_1 + \alpha_2 + 0.1t^2\alpha_2 + t^2\,{\alpha_2}^2 - t(0.2\alpha_1 + \alpha_2),$

That

$u(t) \simeq u_{22}(t) = -\lambda_{22} = -\,0.536036 + 0.257913t + 0.278123t^2.$

We consider $\varepsilon = 3 \times 10^{-2}$. Once the proposed method is applied, the numerical results for J_i and stopping criterion are as given in Table 6. The obtained numerical solution for $x(t)$and $u(t)$ in three iterative are depicted in Fig 5 and 6.

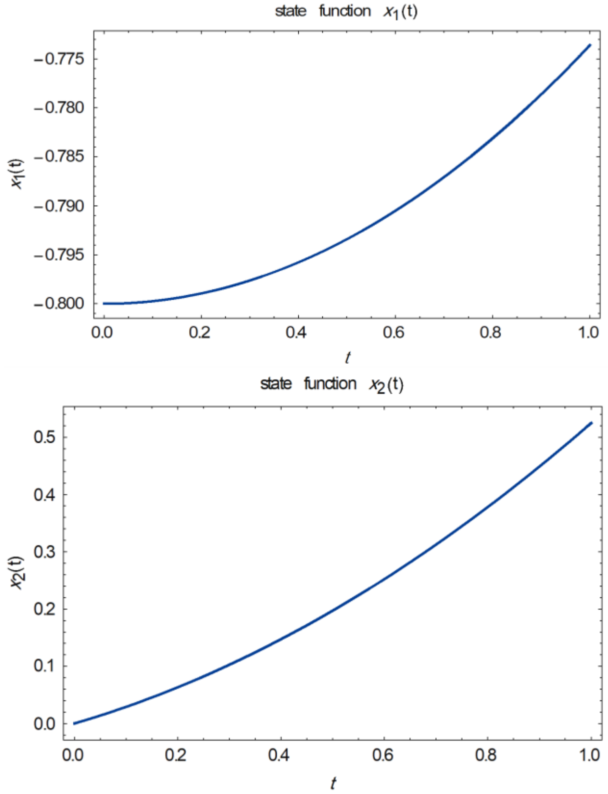

Fig 5: Suboptimal state $x_1(t)$ and $x_2(t)$, Example 3.

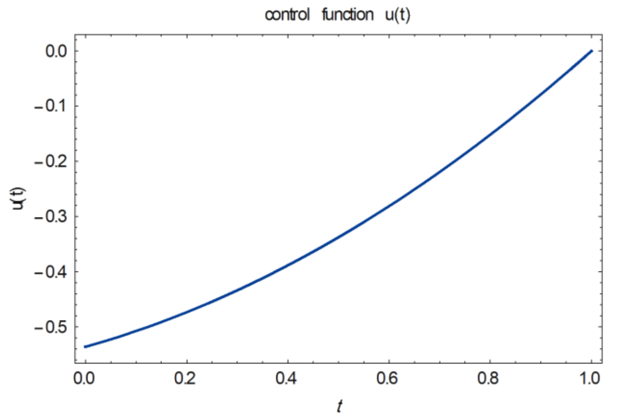

Fig. 6: Suboptimal control $u(t)$, Example 3.

Table V: Calculation of α for $N = 2$, Example 3

α_1	α_2	j
-1.39061579	0.536036193	0.410274

Table VI: Numerical results for different iteration, Example 3

i	J_i	$\lvert\frac{J_i - J_{i-1}}{J_i}\rvert$
1	0.417241	-
2	0.410274	1.6981×10^{-2}
3	0.427145	3.9497×10^{-2}
4	0.431156	9.3028×10^{-3}

Table VII: Minimum of objective value for the proposed method, Example 3

Method	Objective value	CPU time (sec)
Proposed method (N=3)	0. 410274	0. 015625
VIM (N=3) [18]	0.4102	-

Conclusions

Due to its high computing demands, VIM cannot solve some non-linear optimal control problems. Hence, we proposed the modified variational iteration method to find a solution for this type of optimal control problems. The suggested method eliminates all additional calculations in VIM thus requires less time to do the computations. As stated, in Example1, the VIM cannot be counted more than two iterations due to additional calculations, but the proposed method is applicable in the high iteration. In addition, as seen in Table IV, the better max state error is obtained compared to other methods. As a future research direction, we can apply this method for solving optimal control problems ruled by partial differential equations and integral equations.

REFERENCES

[1] W. L. Garrard, J. M. Jordan, "Design of nonlinear automatic flight control systems," *Automatica*, 13, 497 - 505, 1977.

[2] J. L. Junkins and J. D. Turner, "Optimal Spacecraft Rotational Maneuvers," *Elsevier, Amsterdam*, 1986.

[3] M. Itik, M. U. Salamci, S. P. Banksa, "Optimal control of drug therapy in cancer treatment," *Nonlinear Analysis*, 71 (12), 1473 - 1486, 2009.

[4] S. Wei, M. Zefran, R. A. Decarlo, "Optimal control of the robotic system with logical constraints., application to UAV path planning," *Proceeding(s) of the IEEE International Conference on Robotics and Automation, Pasadena*, CA, USA, (2008).

[5] M. Alipour, M. A. Vali, A. H. Borzabadi, "A direct approach for approximate optimal control of integro-differential equations based on homotopy analysis and parametrization method," *IMA Journal of Mathematical Control and Information*, 34, 611 - 630, 2017.

[6] E. Tohidi, O. R. N. Samadi, "Legendre spectral collocation method for approximating the solution of shortest path problems," *Syst. Sci. Control Eng*, 3, 62 - 68, 2014.

[7] M. Shirazian, and S. Effati, "Solving a Class of Nonlinear Optimal Control Problems via He's Variational Iteration Method,"*International Journal of Control, Automation, and Systems*, 10, 249 - 256, 2012.

[8] B. Kafash, A. Delavarkhalafi, S. MKarbassi, K. Boubaker. "A Numerical Approach for Solving Optimal Control Problems Using the Boubaker Polynomials Expansion Scheme," *Journal of Interpolation and Approximation in Scientific Computing*, 2014, 1 - 18, 2014.

[9] M. Matinfar, and M. Saeidy, "A new analytical method for solving a class of nonlinear optimal control problems," *Optimal Control Applications and Methods*, 35, 286 - 302, 2014.

[10] H. Jafari, S. Ghasempour, D. Baleanu, "On comparison between iterative methods for solving nonlinear optimal control problems," *Journal of Vibration and Control*, 22, 2281 - 2287, 2016.

[11] M. Alipour, M. A. Vali, A. H. Borzabadi, "A hybrid parametrization approach for a class of nonlinear optimal control problems," *Numerical Algebra, Control and Optimization*, 9, 493 - 506, 2019.

[12] A. Jajarmi, N. Pariz, A. Vahidian Kamyad, S. Effati. "A highly computational efficient method to solve nonlinear optimal control problems," *Scientia Iranica*, 19, 759 - 766, 2012.

[13] Z. Shabani, H. Tajadodi, "A numerical scheme for constrained optimal control problems," *International Journal of Industrial Electronics, Control and Optimization*, 2, 233 - 238, 2019.

[14] H. Saberi Nik, S. Effati, S. S. Motsa, M. Shirazian, "Spectral homotopy analysis method and its convergence for solving a class of nonlinear optimal control problems," *Numer Algor*, 65, 171 - 194, 2014.

[15] M. Akbarian, N. Eghbal2, N. Pariz, "A Novel Method for Optimal Control of Piecewise Affine Systems Using Semi-Definite Programming," *International Journal of Industrial Electronics, Control and Optimization*, 3, 59 - 68, 2020.

[16] M. Dehghan, M. Abbaszadeh, "The solution of nonlinear Green - Naghdi equation arising in water sciences via a meshless method which combines moving kriging interpolation shape functions with the weighted essentially non - oscillatory method," *Communications in Nonlinear Science and Numerical Simulation*, 68, 220 - 239, 2019.

[17] E. Zakeri, S. Farahat, S. A. Moezi, A. Zare, "Path planning for unmanned underwater vehicle in 3d space with obstacles using spline-imperialist competitive algorithm and optimal interval type-2 fuzzy logic controller," *Latin American Journal of Solids and Structures*, 13, 1054 - 1085, 2016.

[18] E. Zakeri, S. A. Moezi, M. Eghtesad, "Tracking control of ball on sphere system using tuned fuzzy sliding mode controller based on artificial bee colony algorithm," *International Journal of Fuzzy Systems*, 20, 295 - 308, 2018.

[19] E. Zakeri, S. A. Moezi, M. Eghtesad, "Optimal interval type-2 fuzzy fractional order super twisting algorithm: A second order sliding mode controller for fully-actuated and under-actuated nonlinear systems," *ISA transactions*, 85, 13 - 32, 2019.

[20] J.H. He, "A new approach to nonlinear partial differential equations," *Commun. Nonlinear Sci. Numer. Simulation.*, 2 (4), 230 - 235, 1997.

[21] J.H. He, "Variational iteration method - A kind of non-linear analytical technique: Some examples," *International Journal of Non-Linear Mechanics*, 34, 699 - 708, 1999.

[22] T. A. Abassy, M. A. El-Tawil, H. El-Zoheiry, "Modified variational iteration method for Boussinesq equation," *Computers, and Mathematics with Applications*, 54 (7 - 8), 955 - 965, 2007.

[23] A. Jajarmi, N. Pariz, A. V. Kamyad, and S. Effati, "A novel modal series representation approach to solve a class of nonlinear optimal control problems," *International Journal of Innovative Computing, Information and Control*, 7, 1413 - 1425, 2011.

[24] J. E. Rubio, "Control and Optimization, the Linear Treatment of Nonlinear Problems," *Manchester University Press, Manchester*, UK, 1986.

Pooneh Omidiniya received her MSc degree from Sistan and Baluchestan University. Her research interests include optimal control, iterative method.

Maryam Alipour received her MSc degree from Mazandaran University and Ph.D. degree from Shahid Bahonar University of Kerman in applied mathematics. She is currently an Assistant Professor with university of Sistan and Baluchestan, Zahedan, Iran. Her research interests include optimal control, iterative method and fractional calculu

International Journal of Industrial Electronics, Control and Optimization © 2020 IECO
Vol. 3, No. 4, pp. 415-429, Sep (2020)

Application of Improved Salp Swarm Algorithm Based on MPPT for PV Systems Under Partial Shading Conditions

Javad Farzaneh[1], Ali Karsaz[2,†]

[1] Department of Electrical and Computer Engineering Faculty, Semnan University, Semnan, Iran
[2,†] Department of Electrical and Electronic Engineering, Khorasan Institute of Higher Education. Mashhad, Iran

ABSTRACT

Maximum Power Point Tracking (MPPT) is an important concept for both uniform solar irradiance and Partial Shading Conditions (PSCs). The paper presents an Improved Salp Swarm Algorithm (ISSA) for MPPT under PSCs. The proposed method benefits a fast convergence speed in tracking the Maximum Power Point (MPP), in addition to overcoming the problems of conventional MPPT methods, such as failure to detect the Global MPP (GMPP) under PSCs, getting trapped in the local optima, and oscillations around the MPP. The proposed method is compared with original algorithms such as Perturbation and Observation (P&O) method (which is widely employed in MPPT applications), Differential Evolutionary (DE) algorithm, Particle Swarm Optimization (PSO), and Firefly Algorithm (FA). The obtained results show that the proposed method can detect and track the MPP in a very short time, and its accuracy outperforms the other methods in terms of detecting the GMPP. The proposed ISSA algorithm has a higher speed and the convergence rate than the other traditional algorithms.

Article Info

Keywords:
Improved Salp swarm algorithm, Photovoltaic systems, Maximum power point tracking, Partial shading condition.

Article History:
Received 2019-08-16
Accepted 2020-06-30

I. INTRODUCTION

On account of restrictions on fuel resources, increased fossil fuel price, effects of fossil fuel sources on the environment and increased energy consumption, employing Renewable Energy Sources (RESs) has significantly increased during the last decades [1]. Among RESs, solar energy and Photovoltaic (PV) systems have greatly been utilized as they generate reliable electrical energy without producing emissions [2-3].

PV systems are considered as a reliable source of electrical energy generation thanks to the following reasons: they can be utilized widely all over the globe, they do not require fuel for energy generation, and their maintenance cost is very low [4]. Specific features, such as no depreciation and the minimum number of moving parts, have resulted in exclusive advantages for PV systems, including durability and increased lifelong up to roughly 20 years. Another advantage of PV systems is that they can be used in different capacities. Therefore, it is possible to supply the required energy of a residential home in small dimensions or even supply the needs of a town. Furthermore, the application of PV systems is economically feasible for supplying electrical energy in places where it is either impossible to transfer the electricity from the grid or when high amounts of time and cost should be invested. One major hurdle in employing PV systems is the high installation cost and low energy transformation efficiency, where the latter is somehow due to the nonlinear characteristics and

†Corresponding Author: karsaz@khorasan.ac.ir
† Department of Electrical and Electronic Engineering, Khorasan Institute of Higher Education. Mashhad, Iran

dependency of I-V and P-V characteristics on temperature and solar irradiance. Solar irradiance and temperature have direct bearings on the generated current and voltage of the PV system, respectively. Therefore, it is incumbent on us to employ MPPT technology in PV systems to extract the maximum power under different irradiance and temperature conditions [5]. Up to date, different methods have been introduced for MPPT under uniform insolation conditions, such as Perturbation and Observation (P&O) [6], Incremental Conductance (IC) [7], Fuzzy Logic-based methods [8], Artificial Neural Network (ANN) [9], Fractional Open-Circuit Voltage or Short-Circuit Current methods [10], and Hill Climbing (HC) [11]. The mentioned methods have great ability in MPPT applications under uniform insolation conditions. Among these methods, P&O and IC have the most extensive applications in comparison with the other mentioned methods [12]. In addition to temperature and irradiance, the other effective factor on the generated power of PV systems is the Partial Shading Condition (PSC). When PSC occurs due to the presence of clouds, shadings by trees, and or other objects in the neighborhood of the PV system, the output power of a PV system dramatically decreases. Normally, bypass diodes are used for reducing the PSC effect. If the bypass diodes are used in the case of PSC, the P-V characteristics curve of a PV system will have several peaks instead of one single peak. In this situation, conventional methods are unable to detect the GMPP and normally trap in the local optima [13].

Many different methods have already been introduced for MPPT under PSCs, all of which have their advantages and disadvantages. Among the available MPP tracking methods, optimization algorithm-based methods such as Firefly Algorithm (FA) [20], Particle Swarm Optimization (PSO) algorithm [14], Cuckoo Search (CS) algorithm [15], Ant Colony Optimization (ACO) algorithm [16], Grey Wolf Optimization (GWO) algorithm [17], Artificial Bee Colony (ABC) [18], Bat Algorithm (BA) [19], evolutionary algorithms [20], and Gravitational Search Algorithm (GSA) [21] are widely used. The reason behind this is that these types of techniques have many features, including the ability to detect the GMPP under any conditions, very small probability of trapping in the local optima, no oscillation around the MPP, and easy implementation in comparison to other methods.

Ref. [22] used the FA method for MPPT under PSCs, where a boost converter was utilized for connecting the load to the PV system. The method was compared with PSO and P&O methods, and it has been observed that the FA method has faster speed and higher accuracy in detecting the GMPP compared to the other two methods. A combined method was introduced in [16] for the MPPT application. In the first step, using an ACO algorithm, the proposed method reaches the neighborhood of the MPP and then tracks it by using the P&O method. GWO algorithm was employed in [23] for MPPT under PSCs. The author has compared the proposed method with P&O and other improved PSO methods and showed that the proposed method has a higher convergence speed without oscillations around the MPP. The average efficiency of the method is 99.85%. Fibonacci series was employed as a method of tracking the GMPP [24], where it was utilized as a mathematical basis for dividing the P-V curve. Since the method works based on a mathematical basis, it has very suitable accuracy, although its implementation cost is high. In [25], a method similar to the two-step search approach was used for MPPT under PSC. In this method, at first, the P-V curve is completely swept and the local optimum points are stored. Then, by perturbing the voltage and observing the power variations, the GMPP is tracked. The speed of this method is acceptable and has suitable tracking accuracy. An Adaptive Neuro-Fuzzy Inference System (ANFIS) was used for MPPT under uniform solar irradiance [26]. The suggested method has a very high convergence speed, and the accuracy of the MPPT depends on the learning quality of the ANFIS system such that if it is trained with enough data, it will have good accuracy. A new MPPT method based on the PSO algorithm was presented in [27], where extra coefficients are added to the PSO equations to reduce the computational effort of the algorithm. Nonetheless, it cannot be surely said whether the algorithm succeeds in continuously tracking the MPP. The reason is that when the particles are close to the MPP, the speed of the algorithm becomes significantly low or even is zero. One of the most common problems with the PSO algorithm is that when there is a small difference in the solar irradiances, the changes in the duty cycle should be small enough to be able to perform MPPT more accurately.

Ref. [28] makes use of the PSO algorithm for MPPT under PSC. In this paper, a boost converter is utilized for increasing the efficiency of the system for each solar panel, but this leads to the increased capital cost. Additionally, [29] used PSO for MPPT under PSCs. The author defined linear equations for parameters of the PSO algorithm to increase the speed and accuracy of the MPPT. The equations were tuned so that the system would have higher exploration and diversity at the beginning of running the algorithm, and the exploration value is decreased through running the algorithm so that the solutions converge. In [30], the ACO algorithm was used for MPPT. ACO is an inspiration by ant behaviors in the colony and the foraging path. The population size was assumed to be four. The proposed method was compared with PSO, P&O, and fractional open-circuit voltage methods. The simulation results were obtained for four different case studies of PSCs, highlighting the superiority of the ACO-based method over the other three methods. The authors in [31] combined the P&O algorithm with the genetic algorithm (GA) structure. This resulted in a reduction in the population size of the algorithm. Due to the reduction in the number of iterations (NOI), the MPPT's speed increased significantly. In [32], a combined method was used for MPPT under PSCs. Noting that the P&O

method is unable to detect the global optimum and the probability of trapping in the local optima is high, the author used it in conjunction with the PSO algorithm. In this method, at first, the P&O method starts the search process and once it reaches the local optimum point, the PSO method takes action. Since the P&O method is used in the first stage, it reduces the search space for the PSO method; thus, the system converges in a short time. A combination of PSO and P&O methods was employed in [33] for MPPT applications, where the P&O method is used under uniform solar irradiance and the PSO algorithm for tracking the MPP only at the beginning of PSCs. In ref. [34], by mixing the GWO and P&O methods, the author made an effort to extract the MPP under PSCs. Initially, the range of GMPP is determined by the GWO algorithm, and then the MPP is tracked using the P&O method. The speed of this approach is acceptable. In [35], the author has made some modifications in the FA method to reduce the convergence time while increasing the tracking speed of the MPPT. In this paper, using the average coordination of all fireflies as a representative point, the desired firefly moves only towards their average, instead of moving towards each of the brighter fireflies. In this method, by reducing the number of firefly movements, the tracking speed is increased. Nonetheless, the probability of not detecting the global optimum by the system is increased because the variety of fireflies' movements has dramatically reduced.

Li, Hong, et al. have proposed an overall distribution PSO and MPPT algorithm for a PV power system to track the GMPP under PSCs [36]. The main difference between our methodology and this new published paper is that in our algorithm the new proposed metaheuristic method SSA is used. The SSA is able to explore the most promising regions of the search space, move salps abruptly in the initial steps along with move gradually in the final steps of iterations compared to the standard and improved versions of the PSO methods. Moreover our proposed algorithm based on SSA method ensures and improves the average fitness of all salps, and enhance that best solution found so far over the course of optimization.

Recently, Yang, Bo, et al. proposed a new hybrid algorithm based on memetic algorithm and salp swarm optimization, named as MSSA [37]. The Memetic algorithm has developed into a broad class of algorithm and can properly hybrid a population based global search and heuristic local search. So the new ideal in this paper is to adopt the memetic computing framework to enhance the search ability of SSA, which mainly contains two operations, “local search in each chain” and “global coordination in virtual population”. Therefore, this paper is also proposed a new method to improve the standard SSA as well as our methodology. In our proposed algorithm with a simple manner, contribution of previous position of salp to update new positions have increased. So our proposed algorithm is an alternative algorithm to Yang, Bo’s idea in a simple manner.

The present work aims to use an improved salp swarm algorithm (ISSA) for the MPPT under PSCs in PV systems. The proposed method is compared with its counterparts, including the SSA method; the P&O method, which is a common method for MPPT; the DE method, which is one of the mostly-used evolutionary algorithms in engineering sciences and MPPT applications; and FA, and PSO methods, which work based on swarm intelligence and have suitable efficacy in tracking the MPP. It is worth mentioning that the optimization methods at the start of the algorithm are initialized randomly and the probability of trapping in the local optima is very high. Another challenge that should be investigated is the ability to detect the global optimum, which cannot be perceived or detected in only one or two times of executing of the simulation software. Thus, the suggested method is compared with DE, FA, PSO, and SSA methods by running the software for many times and the obtained results verify the superiority of the proposed method over its counterparts. The advantages of our proposed scheme make it different from some other works are:

1- The proposed ISSA benefits from many interesting features, making it a highly reliable method for accurate track of the MPP within a short time.

2- The ability to detect the global optimum, which cannot be perceived or detected in only one or two times of executing of the simulation software.

3- The proposed ISSA algorithm has a higher speed and converges very fast.

In the rest of the paper, the model of the solar cell, the effects of temperature and solar irradiance, as well as the effect of shading conditions on PV systems are given in Section II. In Section III, the objective function and the P&O method are described. SSA and ISSA methods are explained in Section IV, and their applications in MPPT are described. The simulation results are thoroughly presented in Section V and finally, conclusions are included in Section VI.

II. CHARACTERISTIC OF THE PV SYSTEM AND THE EFFECTS OF PSCS

A. *Modeling of the PV module*

A current source connected in shunt to a diode can be used to represent the equivalent circuit of an ideal PV cell. A resistor (R_p) is connected in parallel to the equivalent circuit to limit the leakage current flow. Similarly, a series resistor (R_s) is employed to measure the losses. There are two types of modeling for the PV cell: (i) single-diode model, and (ii) double-diode mode [38]. Between these two models, the later is more accurate, but more parameters are required to accurately model the PV cell. As a result, a single-diode model is used in this paper for simplification. Fig. 1 illustrates the schematic of the single-diode model.

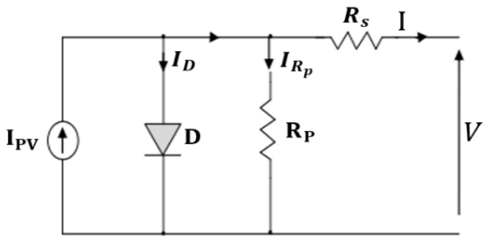

Fig. 1. Equivalent circuit of the single-diode model.

In general, equations of the output voltage and current of a solar cell are expressed as (1).

$$I = I_{PV} - I_O\left[exp\left(\frac{V+R_SI}{V_ta}\right)-1\right]-\frac{V+R_SI}{R_P} \quad (1)$$

Where I_{PV} is the PV current and I_0 is the reverse saturation current. I_{PV} is defined based on the following equation:

$$I_{PV} = \left(I_{PV,n} - K_I\Delta T\right)\frac{G}{G_n} \quad (2)$$

The generated current due to solar irradiance at standard conditions (temperature of 25℃ and irradiance of 1000W/m^2) is $I_{PV,n}$. In addition, ΔT is the temperature difference between the actual temperature (T) and the ambient standard temperature (T_n). K_I indicates the temperature coefficient of the short-circuit current. G is the irradiance and G_n denotes the irradiance at nominal conditions. Furthermore, for the inverse saturation current, we have:

$$I_o = \frac{I_{sc,n}+K_I\Delta T}{exp\left(\frac{V_{oc,n}+K_V\Delta T}{aV_t}\right)-1} \quad (3)$$

The short-circuit current and open-circuit voltage at nominal conditions are expressed by $I_{sc,n}$, $V_{oc,n}$,, and the voltage factor of the open-circuit is defined as K_V. The heating voltage of a panel with N_s number of solar cells connected in series is stated as (4).

$$V_t = \left(\frac{N_SKT}{q}\right) \quad (4)$$

q is the electron charge ($q = 1.6\,exp(-19)c$), k is the Boltzmann factor ($k = 1.3805\,\exp(-23)\,\frac{j}{k}$), and T is cell's temperature in Kelvin.

B. *Effects of temperature and irradiance on the PV panel*

Characteristics of the assumed PV panel for this study at standard conditions (temperature = *25°C*, air mass = *1.5*, irradiance =1000 W/m^2) are given in Table.1. One of the effective factors of the produced power by PV systems is irradiance. By increasing solar irradiance, the produced power is proportionally increased, and vice versa. Fig. 2(a) depicts I-V and P-V curves of the PV panel under-study (MSX-60). As it is obvious from the figure, in the temperature of 25℃, when the irradiance is increased from 400 W/m^2 to 1000 W/m^2 with steps of 200, the generated current is increased and this entails the increase in the produced power. Besides, the temperature is also effective on the generated power by PV systems. By increasing temperature the output power is decreased, and vice versa. Fig. 2(b) illustrates that when the temperature is increased from 25℃ to 55℃ in the steps of 10℃, the open-circuit voltage is decreased, and as a result, the output power of the solar panel will decrease. Solar irradiance in graphs of Fig. 2(b) is assumed to be constant, equal to 1000 W/m^2.

Table. 1

Parameters of the MSX-60 PV module at STC

Maximum power (W), P_{MPP}	*60*
Nominal open-circuit voltage (V), V_{ocn}	*21.1*
Maximum power voltage (V), V_{MPP}	*17.1*
Nominal short-circuit current (A), I_{scn}	*3.8*
Maximum power current (A), I_{MPP}	*3.5*
Number of series cells, N_s	*36*

C. *Effects of PSCs on PV systems*

The produced power by a PV system depends on temperature and irradiance, and these two factors have direct impacts on the output power produced by the PV system. Another effective event on PV systems is PSCs. When a PV system is used in urban environments, PSC is not negligible. In most cases, the reason for the occurrence of PSC is the presence of trees, buildings, and other objects around PV systems. Hence, the impact of PSCs on the PV system should be investigated. When a part of a module or even the whole module of a PV system is under shading conditions, the output power reduces. In Fig. 3, the PV module has n cells. And a cell separated from the other cells is shown, which has current I and voltage V.

a)

b)

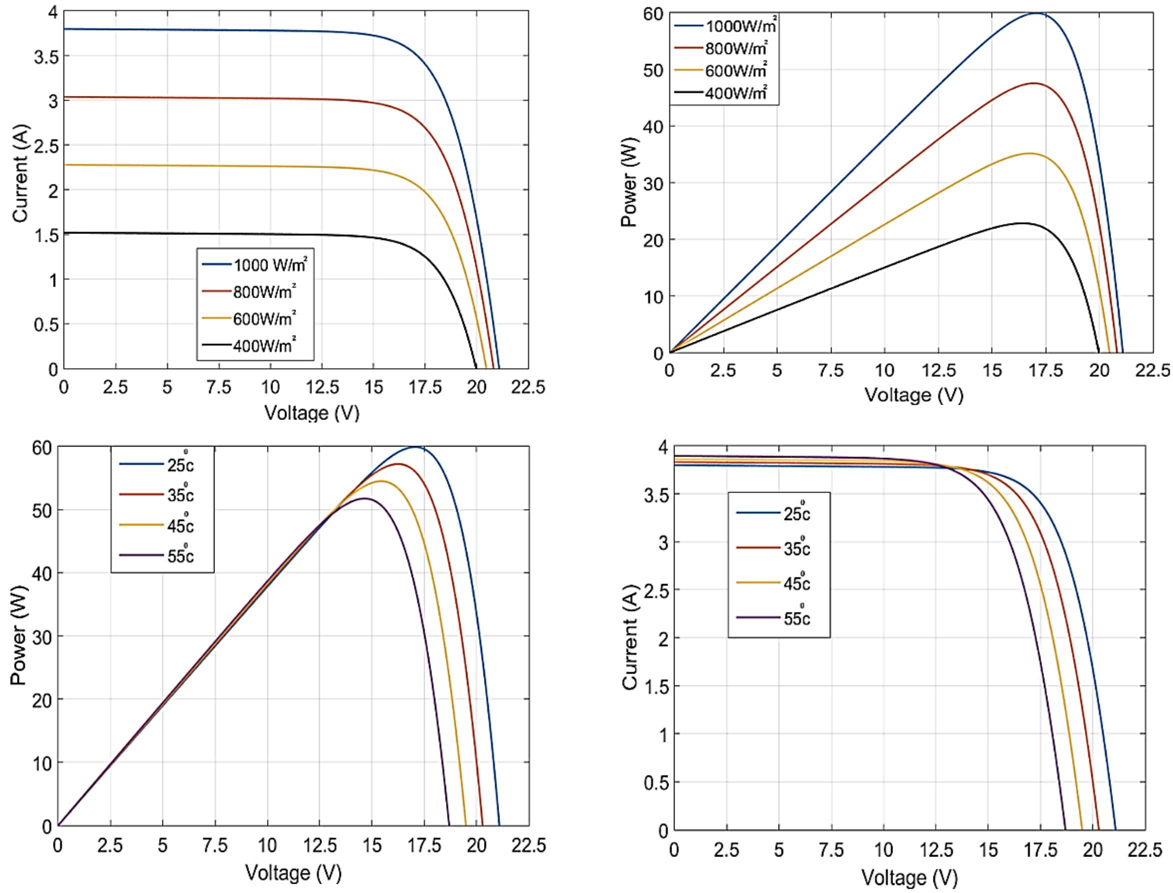

Fig. 2. The P-V and I-V curves under varying irradiation (b) The P-V and I-V curves under variable temperature

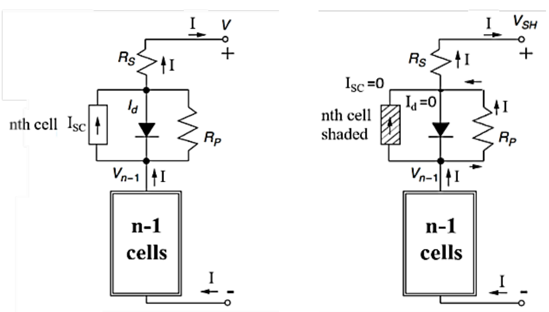

(a) (b)

Fig. 3. The PV module with n cells (a) all the cells are under solar irradiation, and (b) a cell under shading and n-1 cells under solar irradiation.

In Fig. 3 (a), all cells are under direct solar irradiation and are connected in series. Thus, the same current I is flowing through them. In Fig. 3(b), the upper cell is under shading condition and its produced current is zero. The remaining n – 1 cells are under solar irradiation. As a result, the whole current produced by n – 1 cells must flow through resistors R_p and R_s, and this reduces the output power. In the cases the PV modules are connected in series or shunt to increase the output power, bypass diodes are used to reduce the impact of PSCs. For instance, when PSC occurs and a module is under shading condition, diodes prevent the loss of power produced by other modules and impede the creation of a hotspot. Consequently, only the module under shading condition produces less power. P-V characteristics of PV systems differ in the presence and absence of the bypass diodes. Under shading conditions, different currents flow through the modules, therefore the P-V curve has several peaks. In Fig. 4, four PV panels are connected in series, wherein Fig. 4(a) the irradiance is the same for all panels and is equal to 1000 W/m^2. In Fig. 4(b), it is assumed that the PSC has occurred and irradiance is 1000 W/m^2, 850 W/m^2, 700 W/m^2, and 300 W/m^2, respectively. Fig. 5 depicts P-V and P-I curves in the presence of bypass diodes in the PV system of Fig. 4. As it is evident from Fig. 5, the uniform irradiance is equal to 1000 W/m^2, the produced power is 240 W. Moreover, when the PSC occurs, there are several peaks in the P-V curve and the produced power is decreased as well.

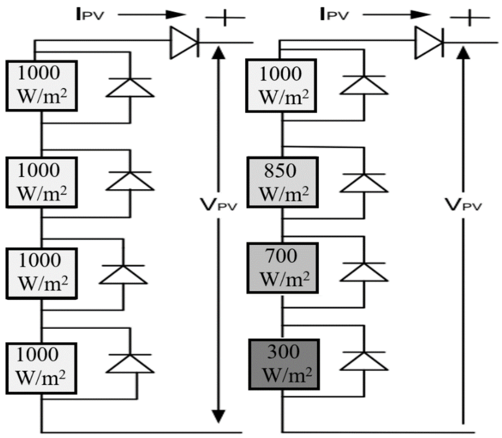

Fig. 4. A PV system with two different patterns.

(a)
(b)

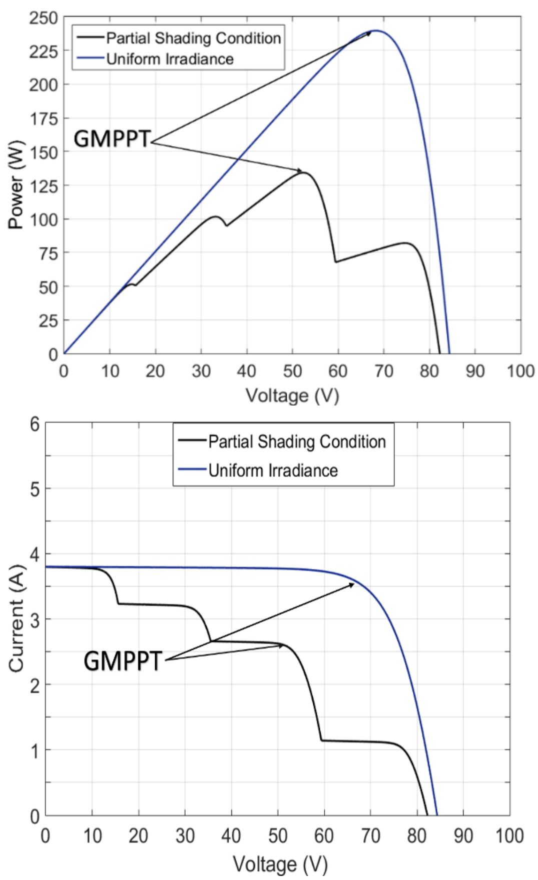

Fig. 5. The (a) P-V and (b) I-V curves of a PV system under uniform irradiance and PSCs.

III. OBJECTIVE FUNCTION AND P&O METHOD

The formulation of the MPPT as an optimization problem is as follows:

$$\begin{aligned} &Maximize\ P_{pv}\,(d) \\ &Subject\ to \begin{cases} d_{min} \le d \le d_{max} \\ V_{min} < V_{pv} < V_{max} \end{cases} \end{aligned} \tag{5}$$

In Eq. (5), P_{PV} is the output power, d is the duty cycle of the DC-DC buck-boost converter, and d_{min} and d_{max} define the minimum and maximum duty cycles of the DC-DC converter. In this work, the latter two parameters are set *0.1* and *0.9*, respectively.

A. PERTURBATION AND OBSERVATION METHOD

The P&O method is a widely-used conventional method for MPPT under uniform irradiance as it has easy implementation and low cost compared with other MPPT methods [39]. In some papers, the P&O method is combined with other MPPT methods to increase the tracking speed [40]. The performance of the P&O method is such that, at first, a small controlled disturbance is established in the initial operating voltage of the PV system based on the tracking criteria. This is performed in such a manner that its value increases in case the produced power of the PV system is increased, i.e., the operating point moves toward the MPP. As a result, in the next disturbance, the operation voltage is established in the same direction exactly similar to the previous disturbance. This is continued until the MPP is reached. However, if the produced power by the PV system is reduced, it means that it has moved further away from the MPP. Therefore, the direction of the disturbance must be changed [41]. The efficacy of the P&O method is reduced by quick changes in environmental conditions and under PSCs because it is unable to track the GMPP under PSCs [42].

IV. SALP SWARM ALGORITHM

A. Inspiration and the proposed mathematical model

Salp swarm algorithm was introduced by Seyed Ali Mirjalli et al. in 2017 [42]. A swarm formed by a group of salps is known as a salp chain. The population of salps is divided into two groups to mathematically model salp chains: leader salp and follower salps. The leader salp is the one at the front end of the salp chain, and other salps are considered as followers. It is clear from the naming that the leader has the task of leading and guiding the followers. Like other population-based algorithms, an n-dimensional search space is assigned to define the positions of the salps, where n indicates the number of variables for a specific problem. A two-dimensional matrix, x, is used for storing the positions of the salps. Moreover, it is taken for granted that there is a food source, F, in the search space and the salp is trying to reach that. The following equation is used for updating the position of the leader salp:

$$x_j^1 = \begin{cases} F_j + c_1\left(\left(ub_j - lb_j\right)c_2 + lb_j\right) & c_3 \ge 0 \\ F_j - c_1\left(\left(ub_j - lb_j\right)c_2 + lb_j\right) & c_3 < 0 \end{cases} \tag{6}$$

It can be understood that the position of the leader is updated only corresponding to F as the food source. In the above equation, x_j^1 is the position of the leader in the j^{th} dimension, F_j represents the food source in the j^{th} dimension, and ub_j and lb_j are the upper and lower boundaries of the j^{th} dimension. The most important parameter to be considered in the SSA is coefficient c_1 because this coefficient makes a random balance between exploration and exploitation. Furthermore, c_2 and c_3 are two random numbers generated uniformly in the interval [0, 1]. These two numbers determine the movement of the next position in the j^{th} dimension, either towards positive or negative infinity. Moreover, the size of the steps is defined by c_2 and c_3. The equation to update the position of the followers is:

$$x_j^i = \frac{1}{2}\left(x_j^i + x_j^{i-1}\right) \tag{7}$$

where $i \geq 2$ and x_j^i indicates the position of the i^{th} follower salp in the j^{th} dimension.

B. Improved SSA algorithm

In the SSA algorithm, the positions of the follower salps are updated based on (7). For the system to have a high convergence speed and converge within a shorter time, equation (7) is changed so that the previous positions of the follower salps have more contribution to updating new positions of the salps. This leads the salps to have smaller displacements with respect to their previous positions. According to (7) and assuming that x_j^i and $x_j^{i-1}$are positive values, (7) can be rewritten as:

$$\begin{aligned} x_j^i &= \frac{1}{2}\left(x_j^i + x_j^{i-1}\right) = \frac{1}{2}\left(\left(x_j^i + x_j^{i-1}\right)^2\right)^{\frac{1}{2}} \\ &= \frac{1}{2}\left((x_j^i)^2 + (x_j^{i-1})^2 + 2x_j^i x_j^{i-1}\right)^{\frac{1}{2}} \end{aligned} \tag{8}$$

In the above equation, for the contributions of previous positions of the salps have more effects on updating new positions, the value of $2(x_j^{i-1})^2$ is taken into account, not $2(x_j^i\ x_j^{i-1})$. As a result of this, the salps move less than their previous positions and finally, this increases the convergence speed. By simplifying (8), we have:

$$x_j^i = \frac{1}{2}\left((x_j^i)^2 + 3(x_j^{i-1})^2\right)^{\frac{1}{2}} \tag{9}$$

As it is clear from the above equation, contributions of previous positions of the salp to updating new positions have increased. Due to this, when the system will not experience large variations and have more inertia when reaches the optimal point, leading to increase convergence speed.

C. Application of the ISSA method to MPPT

In this section, the ISSA method is used for MPPT Fig. 6 shows the block diagram of the proposed system. The system under-study consists of four PV modules connected in series. Also, a buck-boost DC-DC converter is used as a link between the load and the PV system. In the following, the steps of the ISSA method for MPP tracking are illustrated in detail. Fig. 7 exhibits the flowchart of the proposed method.

Step 1: Adjusting the parameter c_1 of the ISSA and determining the population size, N. In this algorithm, the position of each salp is considered as the duty cycle of the buck-boost DC-DC converter. The power generated by the PV system is assumed as the fitness of each salp, which is corresponding to the position of each salp.

Step 2: Initialization of the salps. This step initializes the population of the salps in an acceptable solution space respect to the lower bound, d_{min}, and the upper bound, d_{max}. The position of a salp shows the duty cycle of the DC-DC converter. As was mentioned in the previous section, if the size of the population size large, the calculation time will increase; otherwise, the algorithm might be trapped in local optima. Therefore, the population size is assumed four, meaning that one salp for each panel.

Step 3: Fitness evaluation. In this step, the buck-boost converter operates sequentially corresponding to the position of each salp. For each duty cycle, the output power of the PV system is taken into account as the fitness of the corresponding salp. This step is repeated for positions of all of the salps available in the population.

Step 4: Updating salps' positions. The position of the leader salp is updated according to (6), and positions of the follower salps are updated based on (9).

Step 5: The termination criterion, similar to other optimization methods, is the number of iterations. Once it is reached, the algorithm stops, and the system operates based on the optimal duty cycle.

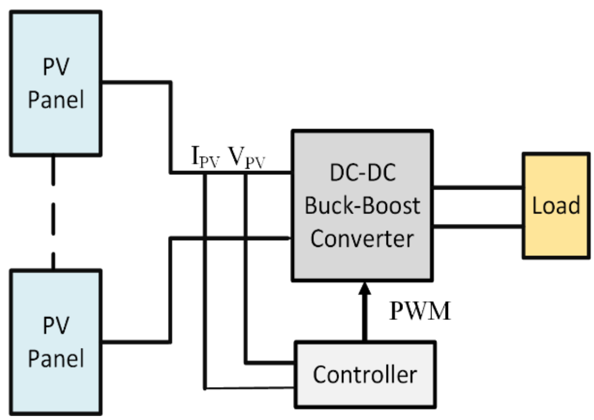

Fig. 6. Block diagram of the proposed system

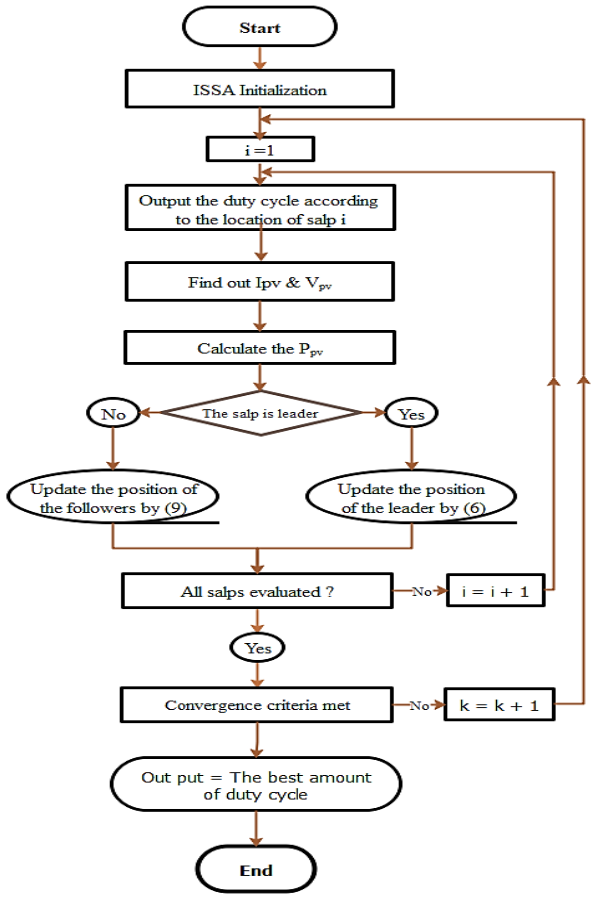

Fig. 7. Flowchart of the ISSA based MPPT

V. SIMULATION RESULTS

To analyze the global MPP tracking using the ISSA method, a thorough comparison is made between SSA; FA; and PSO methods; which work based on swarm intelligence; DE; and P&O methods, respectively. Extensive studies have been performed on MATLAB/Simulink software under different patterns of PSCs. The input inductance of the buck-boost DC-DC converter is 1 mH, the output capacitor is 220 µF, the input capacitor is 470 µF, and the switching frequency is 50 kHz. To ensure that the system will experience steady-state conditions before the start of the next particle to track the MPP, the sampling time interval is set 0.04 s. For the PSO method, $C_1=1.2$, $C_2=1.6$, and $W=0.4$ are taken into account, as in [28]. The number of iterations (NOI) is also set 10. The values of the FA parameter for (β_0, α, γ) are obtained by the trial and error method using simulations. Finally, the parameter values are given as $\beta_0=2$, $\alpha=0.6$ and $\gamma=1$. Since each firefly moves towards the brighter ones, the NOI is set equal to 6 in the algorithm, yielding to shorter convergence time. Coefficients of the DE method are obtained by trial and error and using the FA parameters. To increase the convergence speed, parameter F is chosen randomly between 0.2 and 0.8, and CR=0.3. The NOI for this method is set 10.

For the P&O method, T_a=0.005 (sampling interval), Δd=0.005 (magnitude of the disturbance on the duty cycle). For the SSA method, the constants of parameter c_1 are obtained by a trial and error method, and the new included coefficients are as follows:

$$c_1 = 3.2e^{-(\frac{3.5l}{L})^2} \tag{10}$$

Where l shows the present iteration and L represents the maximum NOI. For the ISSA method:

$$c_1 = 2.3e^{-(\frac{3.2l}{L})^2} \tag{11}$$

The values of NOIs in these two methods are set 10. The above-mentioned parameters are summarized in Table. 2.

Table. II

Parameters of the different methods used in this paper

PSO	C_1	1.2
	C_2	1.6
	W	0.4
	NOI	10
FA	β_0	2
	α	0.6
	γ	1
	NOI	6
DE	F_{Min}	0.2
	F_{Max}	0.8
	CR	0.3
	NOI	10
P&O	T_a	0.005
	Δd	0.005
SSA	c_1	$3.2e^{-(\frac{3.5l}{L})^2}$
	NOI	10
ISSA	c_1	$2.3e^{-(\frac{3.2l}{L})^2}$
	NOI	10

MPPT techniques have been used as controllers to supply the buck-boost converter with a desired duty cycle to study and compare dynamic responses of the PV system under PSCs. MPPT methods were investigated from the following perspectives: tracking time, convergence speed, oscillations around the MPP, and the efficiency of MPP tracking under PSCs. Two PSC patterns were utilized to evaluate the efficacy of the methods used in this paper in tracking the MPP. In the first PSC pattern, the irradiance on each module is 1000 W/m^2, 800 W/m^2, 600 W/m^2, and 400 W/m^2, respectively, and the temperature is set 25°C. P-I and P-V curves for the first PSC pattern and uniform irradiance (1000 W/m^2) are given in Fig. 8(a) and (b), respectively. In the first PSC pattern, there are four peaks, in which the GMPP is 116.468 W and is located on the P-I curve on the second peak. Details of the simulation results obtained for the PV system (power and duty cycle of the buck-boost converter) are provided in Fig. 9 for different MPPT techniques under the first PSC pattern.

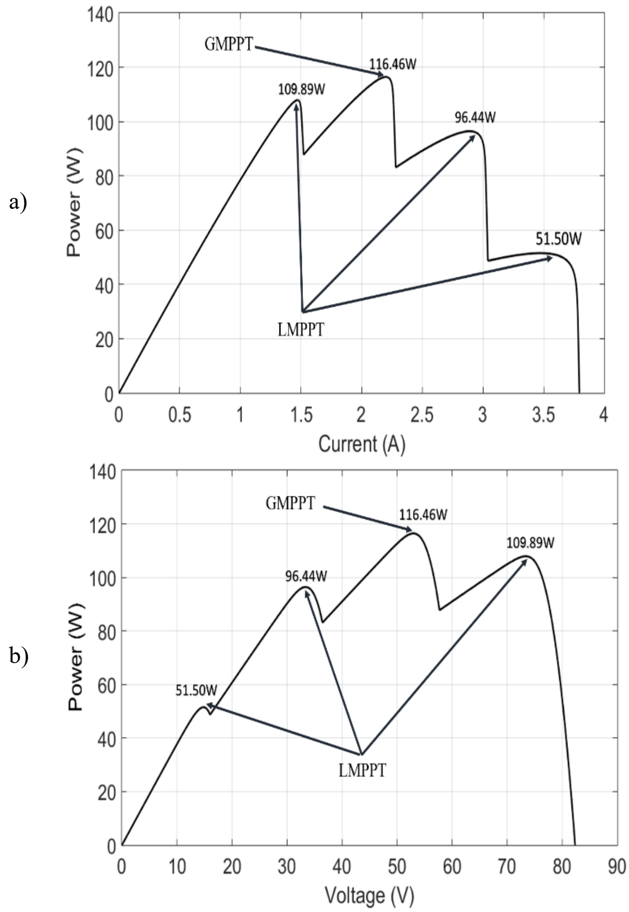

Fig. 8. (a) P−I curve (b) P−V curve under the first PSC

According to Fig. 9, the P&O method has reached a power of 108.5 W in less than 0.7 s. In terms of speed, the P&O method has acceptable speed but cannot detect the global MPP and is trapped in local optima. Further, power and duty cycle curves given in the corresponding curves of the P&O method are presented in smaller intervals to clearly show the changes in power and duty cycle. As is observed from the figure, duty cycle continuously changes in the P&O method and the output power has limited oscillation, which results in power loss. The FA method has succeeded to track the global MPP in less than 3 s and reach a power of 115.52 W. As is seen in the figure, the algorithm has tracked the global point in the last iterations and had changes when searching for the accurate point in the neighborhood of the optimal duty cycle. The algorithm continues its operation with the optimal duty cycle after the iterations are finished. Power and duty cycle curves in smaller intervals clearly show the convergence of the FA method. As is seen, the particles in the last iterations are seeking for the accurate MPP in the duty cycle range of 0.55. PSO, DE, and SSA methods track the GMPP within 1.76 s, 1.6 s, and 1.56 s, respectively. However,

the ISSA method does it in a shorter time, within almost 1.2s. Compared to other methods, as is seen in Fig. 9, the ISSA method has successfully detected the GMPP in a very short time and extracted the maximum power. As the system tends to maintain its position in the proposed system, it converges with a high speed after detecting the considered point. Moreover, the suggested method benefits a significantly high accuracy. Simulation results are summarized in Table. 3. Also, to illustrate the impact of data uncertainties on the obtained solution, this table shows the results under 15 percent fluctuations in input data including temperature and irradiance for each panel.

Table. III

Performance comparison of P&O, PSO, and FA methods

Shading pattern	Technique	Power (W)	Tracking speed (s)	Power at the GMPP (W)	Voltage at the GMPP (V)	Current at the GMPP (A)	Tracking efficiency (%)
First case	P&O	108.5	0.76	116.46	53.95	2.16	92.44
	FA	115.52	2.92				99.01
	PSO	115.56	1.53				99.04
	DE	115.45	1.76				98.89
	SSA	115.58	1.35				99.12
	ISSA	115.59	1.22				99.13

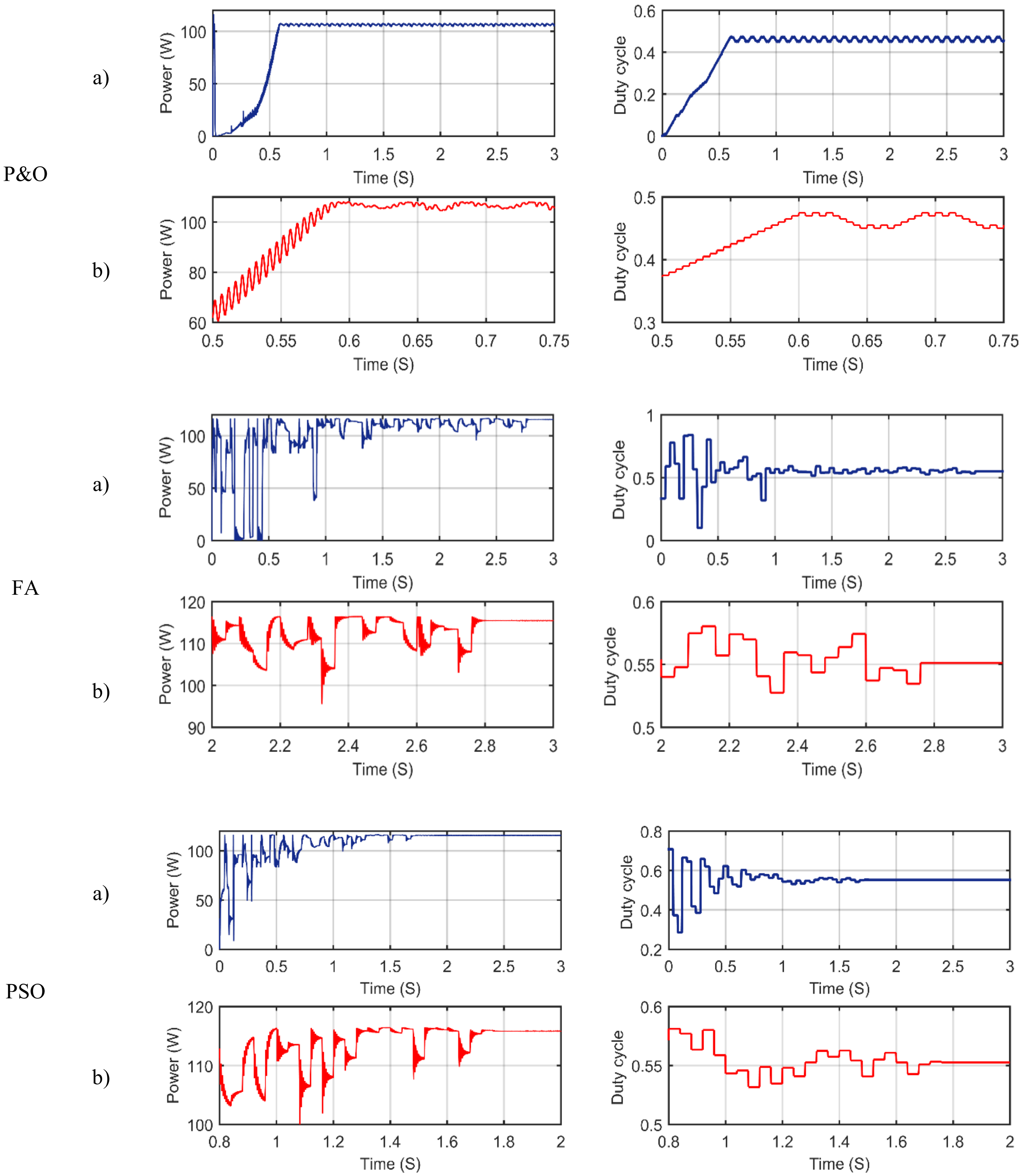
P&O
FA
PSO
a)
b)
Power (W)
Duty cycle
Time (S)

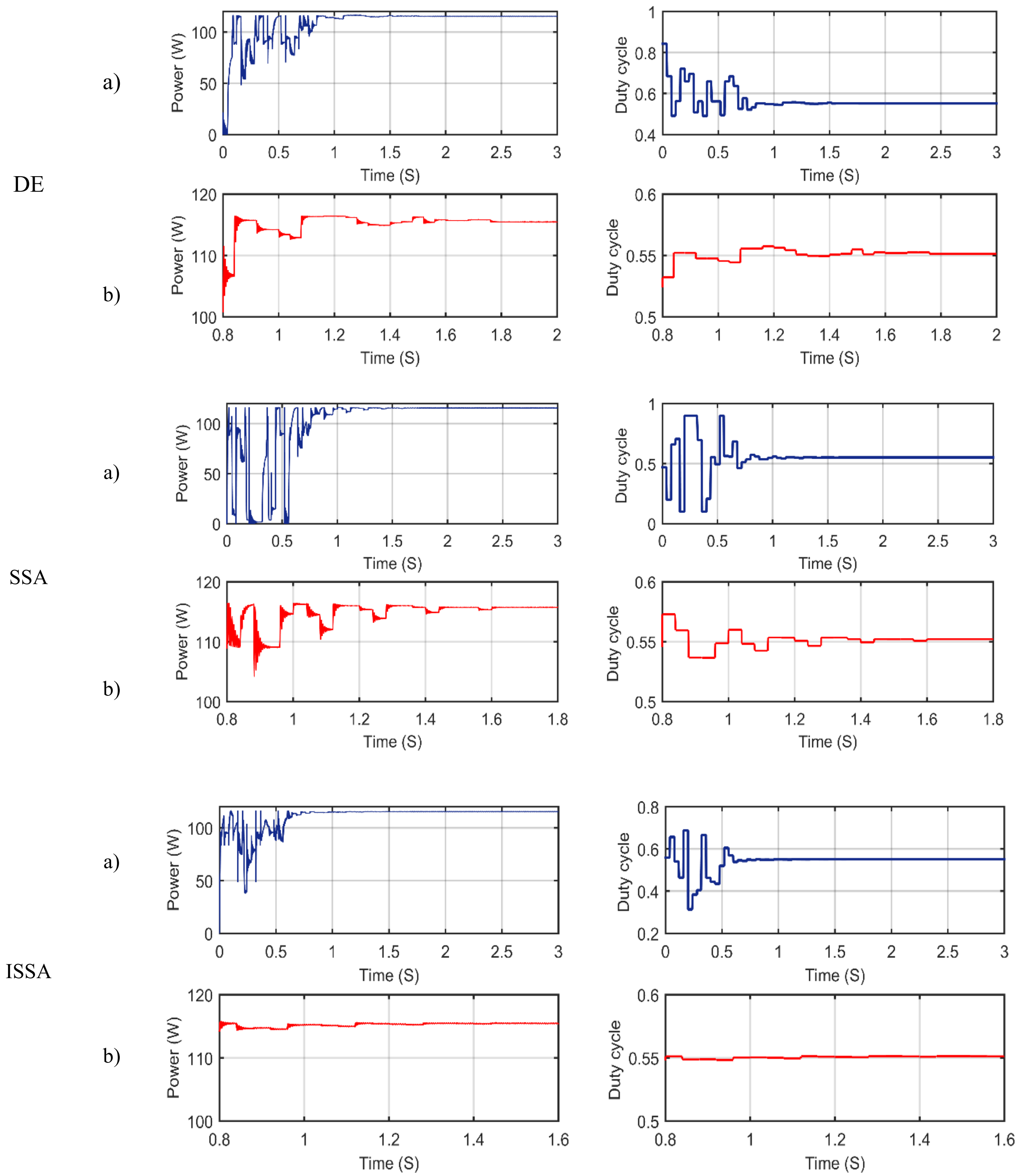

Fig. 9. Simulation results for the PV system under the first PSC, a) power and duty cycle curves, b) a with higher magnification

For further study, the second PSC pattern was also studied, in which the power difference between the global optimal point and one of the local optima is small to better show the efficiency of the algorithms. The irradiance for each panel is considered 1000 W/m^2, 800 W/m^2, 500 W/m^2, and 300 W/m^2, respectively, and the temperature is set 25℃. Another point that is worth noting here is that the efficacy of meta-heuristic algorithms cannot be proved only by one single run. Therefore, for the second PSC pattern, each algorithm was run 40 times to find the most efficient and superior MPP tracking method under PSCs. P-I and P-V curves for the second PSC case are given in Figs. 10 (a) and (b), respectively. As observed in the P-V curve, the difference between the GMPP and one of the local optima is significantly small, making it difficult to detect the GMPP. The GMPP value is 98.21 W and the local optimal value with a small difference to the GMPP is 96.14W. It can be concluded from the obtained results of the first PSC case that the P&O method fails to detect the GMPP, and that is why it was not compared with other methods in the second PSC case. Details of simulation results obtained for the PV system from different MPPT methods under the second PSC case are shown in Fig. 11.

a)
b)

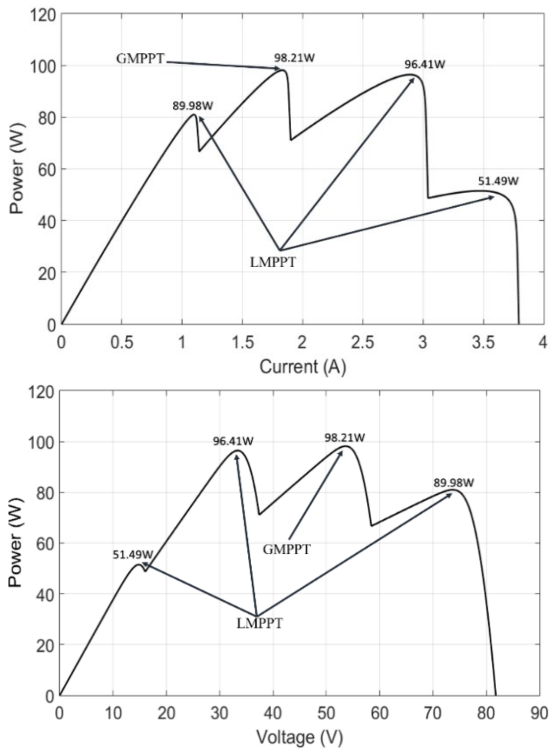

Fig. 10. (a) P−I curve (b) P−V curve under the second PSC

FA
PSO

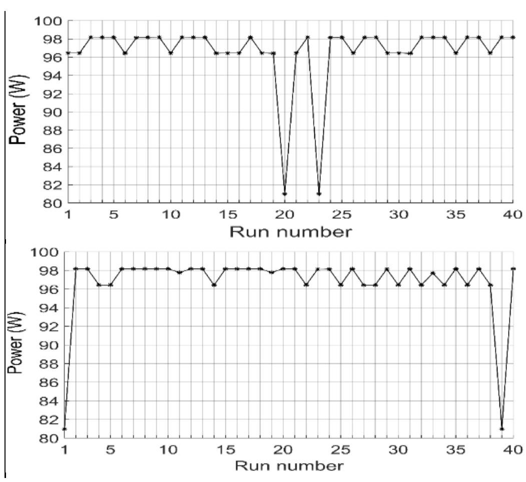

DE
SSA
ISSA

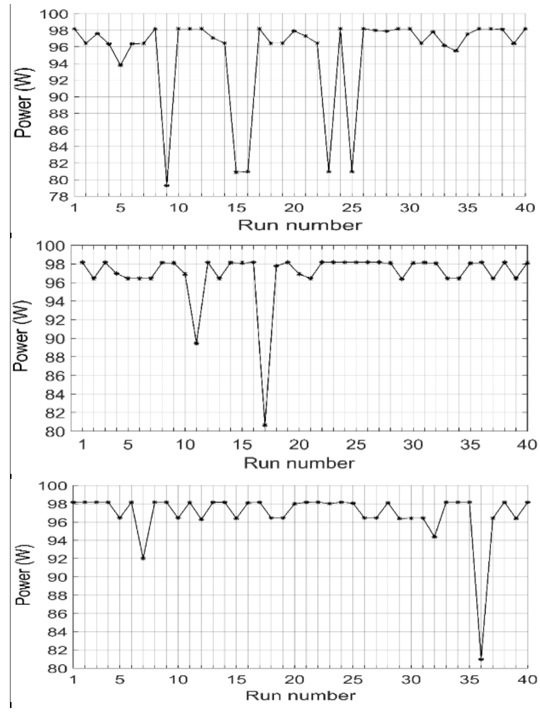

Fig. 11. Details of the PV system simulation results under the second PSC case.

In Fig. 11, meta-heuristic methods were compared from the MPPT ability point of view. As is evident in Fig. 11, the FA method was successful in tracking the GMPP for 22 out of 40 times, was trapped in a local optimum with a small difference to the GMPP for 16 times, and was trapped in other local optima for 2 times. These numbers for the PSO, DE, SSA, and ISSA methods were 23, 15, 2; 15, 20, 5; 24, 15, 1; and 24, 15, 1, respectively. Finally, from the first pattern of the PSC, it can be concluded that the ISSA method has a high convergence speed and is a suitable method for tracking the GMPP. According to the results obtained from the second PSC run for a high number of repetitions, notable conclusions can be drawn. The results of the second pattern show that the DE method is trapped in the local optima, so it cannot be considered as a reliable method. FA and PSO methods are more reliable than the DE method, and in most cases, they can detect the global optimum with satisfactory accuracy. Nevertheless, their convergence times are longer. Additionally, simulation results illustrate that SSA and ISSA methods have acceptable accuracy in detecting the GMPP. Table.4 describes a quality comparison between different proposed methods.

Table. IV
Qualitative comparison of different methods

Criteria	ISSA	SSA	PSO	FA	DE	P&O
Periodic Tuning	Not Required	Not Required	Not Required	Not Required	Not Required	Not Required
Tracking Accuracy	Highly Accurate	Highly Accurate	Highly Accurate	Highly Accurate	Accurate	Low (may locate local peak)
Steady state oscillation	Zero	Zero	Zero	Zero	Zero	High
Tracking Speed (without PSC condition)	Fast	Medium	Medium	Medium	Medium	Very Fast
Ability to track under PSCs	High	High	High	High	Average	Poor
Algorithm complexity	Medium	Medium	Medium	Medium	Medium	Simple
Efficiency	High	High	High	High	Average	Poor in PSCs

VI. CONCLUSION

The original SSA algorithm is amongst the most recently introduced algorithms. In this paper, a new method based on the improved SSA is proposed for the MPPT under PSCs in PV systems. In this study, the method of updating the follower salps' positions is improved to increase the tracking speed of the MPP in the SSA algorithm. The ISSA method was compared with the original algorithm; the P&O method as a conventional method for MPPT; the DE method, which is included in evolutionary algorithms; and FA, and PSO methods as swarm intelligence algorithms, under PSCs. The simulation results obtained from MATLAB/Simulink software show that the proposed method, SSA, FA, PSO, and DE can track the GMPP under PSCs. In addition, ISSA and SSA methods have a noticeable capability in detecting the global MPP, even when the difference between the global optimum and the local optima is very small. Moreover, the speed of the ISSA method in tracking the GMPP under PSCs is higher than other methods. High efficiency and speed are the main advantages of the proposed method.

REFERENCES

[1] J. Zhao, X. Zhou, Z. Gao, Y. Ma, and Z. Qin, "A novel global maximum power point tracking strategy (GMPPT) based on optimal current control for photovoltaic systems adaptive to variable environmental and partial shading conditions," *Solar Energy*. Vol. 144 pp. 767–779, Mar. 2017.

[2] H. Rezk, M. Al-oran, M.R. Gomaa, M.A. Tolba, A. Fathy, M. Ali, A.G. Olabi, A.H.M. El-sayed, W. Addawaser, P. Sattam, B. Abdulaziz, and S. Arabia, *"A novel statistical performance evaluation of most modern optimization- based global MPPT techniques for partially shaded PV system,"* Renewable and Sustainable Energy Reviews, Vol. 115, Nov. 2019.

[3] J. Farzaneh, R. Keypour, and A. Karsaz, "A novel fast maximum power point tracking for a PV system using hybrid PSO-ANFIS algorithm under partial shading conditions," *International Journal of Industrial Electronics, Control and Optimization*, Vol. 2, No. 1, pp. 47-58, Nov. 2019.

[4] J. Farzaneh, R. Keypour, and M. Ahmadieh, *"A New Maximum Power Point Tracking Based on Modified Firefly Algorithm for PV System Under Partial Shading Conditions," Technology and Economics of Smart Grids and Sustainable Energy*, Vol. 3, No. 1, Jun. 2018.

[5] S. Titri, C. Larbes, K.Y. Toumi, and K. Benatchba, "A new MPPT controller based on the ant colony optimization algorithm for photovoltaic systems under partial shading conditions*," Applied Soft Computing,* Vol. 58, pp. 465–479. Sep. 2017.

[6] N. Femia, G. Petrone, G. Spagnuolo, and M. Vitelli, "Optimization of perturb and observe maximum power point tracking method, Power Electron*," IEEE transactions on power electronics,* Vol. 20, no. 4, pp. 963–973, Jul. 2005.

[7] Y. C. Kuo, T. J. Liang, and J. F. Chen, "Novel maximum-power-point-tracking controller for photovoltaic energy conversion system," *IEEE transactions on industrial electronics*. Vol. 48, no. 3, pp. 594–601, Jun. 2001.

[8] A. El Khateb, N.A. Rahim, and S. Member, "Fuzzy-logic-controller-based SEPIC converter for maximum power point tracking," *IEEE Transactions on Industry Applications*, Vol. 50, no. 4, pp. 2349–2358, Jan 2014.

[9] S. Saravanan, and N. R. Babu, *"RBFN based MPPT algorithm for PV system with high step up converter, Energy conversion and Management*," Vol. 122. pp. 239–251. Aug. 2016.

[10] M. a. S. Masoum, H. Dehbonei, and E.F. Fuchs, "Theoretical and experimental analyses of photovoltaic systems with voltage and current-based maximum power-point tracking," *IEEE Transactions on energy conversion,* Vol. 17, No. 4, Dec. 2002.

[11] E. Koutroulis, K. Kalaitzakis, and N.C. Voulgaris, "Development of a microcontroller-based, photovoltaic maximum power point tracking control system*," IEEE Transactions on power electronics*. Vol. 16, No. 1, PP. 46–54, Jan. 2001.

[12] A. Belkaid, I. Colak, and O. Isik, "Photovoltaic maximum power point tracking under fast varying of solar radiation," *Applied energy*. Vol.179, PP. 523–530, Oct. 2016.

[13] M. Farhat, O. Barambones, and L. Sbita, "A new maximum power point method based on a sliding mode approach for solar energy harvesting," *Applied energy*, Vol. 185, pp. 1185–1198, Jan. 2017.

[14] R. Aboelsaud, and S. Obukhov, "Improved particle swarm optimization for global maximum power point tracking of partially shaded PV array*," Electrical Engineering,* Vol. 101 NO. 2, pp. 443–455, Jun. 2019.

[15] J. Ahmed, and Z. Salam, "A maximum power point tracking (MPPT) for PV system using cuckoo search with partial shading capability*," Applied Energy*, Vol. 119, pp. 118–130, Apr. 2014.

[16] K. Sundareswaran, V. Vigneshkumar, P. Sankar, S.P. Simon, P. Srinivasa Rao Nayak, and S. Palani, *"Development of an improved P&O algorithm assisted* through a colony of foraging ants for MPPT in PV system," *IEEE Transactions on Industrial Informatics*, Vol. 12, No. 1, pp. 187–200, Nov. 2015.

[17] S. Mohanty, B. Subudhi, S. Member, and P.K. Ray, "A new MPPT design using grey wolf optimization technique for photovoltaic system under partial shading conditions*," IEEE Transactions on Sustainable Energy*, Vol. 7, No. 1, pp. 181-188, Oct. 2015.

[18] K. Sundareswaran, P. Sankar, P.S.R. Nayak, S.P. Simon, and S. Palani, "Enhanced energy output From a PV system under partial shaded conditions through artificial bee colony*," IEEE transactions on sustainable energy*, Vol. 6, No. 1, pp. 198-209, Nov. 2014.

[19] Z. Wu, and D. Yu, "Application of improved bat algorithm for solar PV maximum power point tracking under partially shaded condition," Applied Soft Computing, Vol. 62, pp. 101–109, Jan. 2018.

[20] M. Faridun, N. Tajuddin, and S. Ayob, "Evolutionary based maximum power point tracking technique using differential evolution algorithm," Energy and Buildings, Vol. 67, pp. 245–252, Dec. 2013.

[21] L. L. Li, G. Q. Lin, M. L. Tseng, K. Tan, and M. K. Lim, "A maximum power point tracking method for PV system with improved gravitational search algorithm," *Applied Soft Computing*, Vol. 65, pp. 333–348, Apr. 2018.

[22] K. Sundareswaran, S. Peddapati, and S. Palani, "MPPT of PV systems under partial shaded conditions through a colony of flashing fireflies," *IEEE transactions on energy conversion,* Vol. 29, pp. 463–472, Jan. 2014.

[23] S. Mohanty, B. Subudhi, and P.K. Ray, "A new MPPT design using grey wolf optimization technique for photovoltaic system under partial shading conditions," *IEEE Transactions on Sustainable Energy*, Vol. 7 No. 1, pp. 181–188. Oct. 2015.

[24] N.A. Ahmed, and M. Miyatake, "A novel maximum power point tracking for photovoltaic applications under partially shaded insolation conditions," *Electric Power Systems Research*, Vol. 78, No.5, pp. 777–784, May. 2008.

[25] B.N. Alajmi, K.H. Ahmed, S.J. Finney, B.W. Williams, and B. Wayne Williams, "A maximum power point tracking technique for partially shaded photovoltaic systems in microgrids," *IEEE Transactions on Industrial Electronics,* Vol. 60, No. 4, pp. 1596–1606, Sep. 2011.

[26] R.K. Kharb, S.L. Shimi, S. Chatterji, and M.F. Ansari, "Modeling of solar PV module and maximum power point tracking using ANFIS," *Renewable and Sustainable Energy Reviews,* Vol. 33, pp. 602–612, May. 2014,

[27] V. Phimmasone, T. Endo, Y. Kondo, and M. Miyatake, "Improvement of the maximum power point tracker for photovoltaic generators with particle swarm optimization technique by adding repulsive force among agents," *International conference on electrical machines and systems*, pp. 1-6, Nov. 2009.

[28] M. Miyatake, M. Veerachary, F. Toriumi, N. Fujii, and H. Ko, "Maximum power point tracking of multiple photovoltaic arrays: A PSO approach," *IEEE Transactions on Aerospace and Electronic Systems*, Vol. 47, No. 1, pp. 367–380, Jan. 2011.

[29] Y. Liu, S. Huang, J. Huang, and W. Liang, "A particle swarm optimization-based maximum power point tracking algorithm for PV systems operating under partially shaded conditions," *IEEE Transactions on Energy Conversion*, Vol. 27, No. 4, pp. 1027-1035. Oct.

2012.

[30] L.L. Jiang, D.L. Maskell, and J.C. Patra, "A novel ant colony optimization-based maximum power point tracking for photovoltaic systems under partially shaded conditions*," Energy and Buildings*, Vol. 58, pp. 227–236, Mar. 2013.

[31] S. Daraban, D. Petreus, and C. Morel, "A novel MPPT (maximum power point tracking) algorithm based on a modified genetic algorithm specialized on tracking the global maximum power point in photovoltaic systems affected by partial shading," *Energy*. Vol.74, pp. 374–388, Sep. 2014.

[32] K.L. Lian, J.H. Jhang, and I.S. Tian, "A maximum power point tracking method based on perturb-and-observe combined with particle swarm optimization," *IEEE journal of photovoltaics*, Vol.4, No. 2, pp. 626–633, Jan. 2014.

[33] C. Manickam, G.R. Raman, G.P. Raman, S.I. Ganesan, C. Nagamani, A hybrid algorithm for tracking of GMPP based on P&O and PSO with reduced power oscillation in string inverters*, IEEE Transactions on Industrial Electronics*, Vol. 63, No. 10, pp. 6097–6106. Jul. 2016

[34] S. Mohanty, B. Subudhi, and P.K. Ray, "A grey wolf assisted perturb & observe MPPT algorithm for a photovoltaic power system," *IEEE Transactions on Energy Conversion,* Vol. 32, No. 1, pp. 340–347, Dec. 2016.

[35] D.F. Teshome, C.H. Lee, Y.W. Lin, and K.L. Lian, "A modified firefly algorithm for photovoltaic maximum power point tracking control under partial shading," *IEEE Journal of Emerging and Selected Topics in Power Electronics*, Vol. 5, No. 2, pp. 661–671, Jun. 2016.

[36] H. Li, S. Member, D. Yang, and W. Su, "An Overall Distribution Particle Swarm Optimization MPPT Algorithm for Photovoltaic System under Partial Shading," *IEEE Transactions on Industrial Electronics*, Vol. 66, No.1, pp. 265-275, Apr. 2018.

[37] B. Yang, L. Zhong, X. Zhang, H. Shu, T. Yu, H. Li, L. Jiang, and L. Sun, "Novel bio-inspired memetic salp swarm algorithm and application to MPPT for *PV systems considering partial shading condition," Journal of cleaner production*, Vol. 215, pp. 1203–1222, Apr. 2019.

[38] J.P. Ram, T.S. Babu, T. Dragicevic, and N. Rajasekar, "A new hybrid bee pollinator flower pollination algorithm for solar PV parameter estimation," *Energy conversion and management*, Vol. 135, pp. 463–476, Mar. 2017.

[39] V.R. Kota, and M.N. Bhukya, A novel linear tangents based P & O scheme for MPPT of a PV system, *Renewable and Sustainable Energy Reviews*. Vol. 71, pp. 257–267, May. 2017.

[40] K. Sundareswaran, V. Vignesh kumar, and S. Palani, "Application of a combined particle swarm optimization and perturb and observe method for MPPT in PV systems under partial shading conditions," *Renewable Energy*, Vol. 75, pp. 308–317, Mar. 2015.

[41] S. Lyden, and M.E. Haque, "A simulated annealing global maximum power point tracking approach for PV Modules under Partial Shading Conditions," *IEEE Transactions on Power Electronics*, Vol. 31, pp. 4171-4181, Aug. 2015.

[42] S. Mirjalili, A.H. Gandomi, S.Z. Mirjalili, S. Saremi, H. Faris, and S.M. Mirjalili, "Salp swarm algorithm: a bio-inspired optimizer for engineering design problems," *Advances in Engineering Software*, Vol. 114, pp. 163-191, Dec. 2017.

Javad Farzaneh was born in Mashhad, Iran, in 1991. He received the B.Sc. degree from the Bahar Institute of Higher Education, Mashhad, Iran, in 2014, the M.Sc. degree in electrical engineering from the Semnan University, Semnan, Iran, in 2017. His research interests are Artificial Neural Networks, Adaptive Neuro-Fuzzy Inference Systems (ANFIS), Stochastic Modeling and Estimation, System Identification, Soft Computing, Metaheuristic Optimization, Renewable Energy, Power Electronics.

Ali Karsaz received his B.S. degree in Electrical Engineering from the Amirkabir University of Technology (*Tehran Polytechnic*), Tehran, Iran, in 1999. He received his M.Sc. and Ph.D. degrees in Control Engineering both form Ferdowsi University of Mashhad, Iran, in 2004 and 2008, respectively. Since 2008, he has been Assistant Professor of control and biomedical engineering at Khorasan Institute of Higher Education and he was Chair of the Division of Control Department from 2012 until now. His current research interests include the development of mathematical models for analysis and control of Biological Systems, Pharmacodynamics, System Biology Mathematical Modeling, Artificial Neural Networks, Stochastic Modeling and Estimation, System Identification, Time Series Analysis and Prediction, Renewable Energy, Power Electronics, Inertial Navigation Systems, Multi-sensory Multi-target Tracking. He has published over 130 peer-reviewed articles in these and related research fields

IECO
This page intentionally left blank

.

International Journal of Industrial Electronics, Control and Optimization © 2020 IECO
Vol. 3, No. 4, pp. 431-438, Sep (2020)

Model-Free Tracking Control via Adaptive Dynamic Sliding Mode Control With Application To Robotic Systems

Mohammad Reza Shokoohinia[1,†], Mohammad Mehdi Fateh[2]

[1,2] Department of Electrical and Robotic Engineering, Shahrood University of Technology, 3619995161 Shahrood, Iran.

ABSTRACT

In this paper, a novel model-free control scheme is developed to enhance the tracking performance of robotic systems based on an adaptive dynamic sliding mode control and voltage control strategy. In the voltage control strategy, actuator dynamics have not been excluded. In other words, instead of the applied torques to the robot joints, motor voltages are computed by the control law. First, a dynamic sliding mode control is designed for the robotic system. Then, to enhance the tracking performance of the system, an adaptive mechanism is developed and integrated with the dynamic sliding mode control. Since the lumped uncertainty is unknown in practical applications, the uncertainty upper bound is necessary in the design of the dynamic sliding mode controller. Hence, the lumped uncertainty is estimated by an adaptive law. The stability of the closed-loop system is proved based on the Lyapunov stability theorem. The simulation results demonstrate the superior performance of the proposed adaptive dynamic sliding mode control strategy.

Article Info

Keywords:
Adaptive Dynamic Sliding Mode Control, Model-Free Tracking Control, Robotic Systems, Voltage Control Strategy.

Article History:
Received 2019-09-10
Accepted 2020-06-14

I. INTRODUCTION

Since robotic systems are always affected by the environmental disturbances, it is necessary to develop robust and adaptive controllers to suppress the effects of them [1-6]. Sliding mode control (SMC) is a well-known robust control technique that has good tracking performance due to its robustness against the uncertainties and disturbances.

However, this control strategy suffers from the chattering problem, due to the discontinuous control law [7-9]. A common method adopted to improve the chattering is to replace the switching function by the saturation function. Since the chattering is reduced by this method, an indefinite steady-state error is also caused depending on the selection of the boundary layer. Thus, the chattering and accuracy become a tradeoff problem in this design [10,11]. Another technique is to reduce the switching gain in the controller. However, if the controller is not powerful enough to confront the uncertainties, the robustness of SMC becomes poor.

Dynamic sliding mode control (DSMC) is an effective scheme to reduce the control chattering. The time derivative of the control signal is considered as the new control variable for the augmented system in which the augmented system includes the original system and the integrator. In DSMC, the chattering problem can be effectively reduced due to the integration method in obtaining the control signal [12-14]. However, similar to SMC, the uncertainty bound should be known in the design of DSMC. In this paper, to overcome this problem, the uncertainty is estimated using an adaptive mechanism. In [15-19], the Fourier series expansion is used for the controller design. These methods require more computation, whereas the proposed method is simpler and

[†]Corresponding Author: mshokoohinia@yahoo.com
Department of Electrical and Robotic Engineering, Shahrood University of Technology, Shahrood, Iran

can alleviate the computation burden. Many studies focused on the torque control strategy (TCS) of robotic systems. In this strategy, the control law computes the torques which should be produced by the motors. The system actuators should be excited, so that they produce the desired torques. However, the actuator dynamics are not considered in the TCS and its input is not calculated in this strategy. To solve the aforementioned problem, voltage control strategy (VCS) has been developed which is more effective and requires less computation [20-23]. As a result, voltage-based approaches are superior. Therefore, in this paper, using VCS, an adaptive DSMC is developed for robust control of robotic systems.

The purpose of this paper is developing an adaptive dynamic sliding mode controller for tracking control of robotic systems. The proposed method is model-free and does not require the robot dynamics. The proposed method does not need the uncertainty upper bound. In fact, the lumped uncertainty is estimated using an adaptive rule. Using Lyapunov direct method, it is guaranteed that the tracking errors converge to zero.

The remainder of the paper is organized as follows. Section 2 introduces the robotic problem formulation. In Section 3, the proposed adaptive dynamic sliding mode controller is designed. Stability analysis is presented in Section 4. Simulation results are discussed in Section 5. Our conclusions are given in Section 6.

II. Problem Formulation

The dynamics of a robotic system can be described as [24]

$$D(q)\ddot{q} + C(q,\dot{q})\dot{q} + G(q) = \tau_l \quad (1)$$

$$J_m r^{-1}\ddot{q} + B_m r^{-1}\dot{q} + r\tau_l = K_m I_a \quad (2)$$

$$RI_a + K_m r^{-1}\dot{q} + \xi = v(t) \quad (3)$$

Where $\xi = L\dot{I}_a + d$, q is the vector of joint positions, v is the vector of motor voltages, I_a is the vector of motor currents and d is a vector of external disturbances. The details are completely explained in [15].

Substituting τ_l from (1) into (2) results in

$$J_m r^{-1}\ddot{q} + B_m r^{-1}\dot{q} + r(D(q)\ddot{q} + C(q,\dot{q})\dot{q} + G(q)) = K_m I_a \quad (4)$$

Using (4), one can calculate I_a as

$$I_a = k_m^{-1}\left((J_m r^{-1} + rD)\ddot{q} + (B_m r^{-1} + rC)\dot{q} + rG\right) \quad (5)$$

Substitution of (5) into (3) yields

$$v = Rk_m^{-1}\left((J_m r^{-1} + rD)\ddot{q} + (B_m r^{-1} + rC)\dot{q} + rG\right) + k_m r^{-1}\dot{q} + \xi \quad (6)$$

Now, (6) can be rewritten as

$$\begin{aligned} v &= \bar{D}\ddot{q} + \bar{C}\dot{q} + \bar{G} + \xi \\ \bar{D} &= Rk_m^{-1}(J_m r^{-1} + rD) \\ \bar{C} &= Rk_m^{-1}(B_m r^{-1} + rC) + k_b r^{-1} \\ \bar{G} &= Rk_m^{-1} rG \end{aligned} \quad (7)$$

We can rewrite (7) as

$$\begin{aligned} v &= \ddot{q} + g \\ g &= \bar{D}\ddot{q} + \bar{C}\dot{q} + \bar{G} + \xi - \ddot{q} \end{aligned} \quad (8)$$

III. The proposed Adaptive Dynamic Sliding Mode Control

The structure of the proposed adaptive controller is shown in Fig. 1. In this block-diagram, error, the first and second sliding surfaces, adaptive rule, and integrating the control signal have been clearly illustrated.

The tracking error (e) and its time derivatives ($\dot{e}, \ddot{e}$) are defined as follows:

$$\begin{aligned} e &= q_d - q \\ \dot{e} &= \dot{q}_d - \dot{q} \\ \ddot{e} &= \ddot{q}_d - \ddot{q} \end{aligned} \quad (9)$$

Now, define a sliding surface as follows:

$$s(t) = \dot{e}(t) + a_1 e(t) + a_2\int_0^t e(\tau)d\tau \quad (10)$$

The time derivative of (10) becomes

$$\dot{s}(t) = \ddot{e} + a_1\dot{e} + a_2 e \quad (11)$$

Substituting $\ddot{e}$ from (9) into (11) results in

$$\dot{s}(t) = \ddot{q}_d - \ddot{q} + a_1\dot{e} + a_2 e \quad (12)$$

Using (8), (12) can be written as

$$\dot{s}(t) = \ddot{q}_d - v + g(t) + a_1\dot{e} + a_2 e \quad (13)$$

The secondary sliding surface is considered as

$$\sigma(t) = \dot{s}(t) + b_1 s(t) + b_2\int_0^t s(\tau)d\tau \quad (14)$$

The time derivative of (14) becomes

$$\dot{\sigma}(t) = \ddot{s}(t) + b_1\dot{s}(t) + b_2 s(t) \quad (15)$$

Using (10) and (13), (15) can be written as

$$\begin{aligned} \dot{\sigma}(t) = {} & (\dddot{q}_d - \dot{v} + \dot{g}(t) + a_1\ddot{e} + a_2\dot{e}) + b_1(\ddot{q}_d - v + g(t) + \\ & a_1\dot{e} + a_2 e) + b_2(\dot{e}(t) + a_1 e(t) + a_2\int_0^t e(\tau)d\tau) \end{aligned} \quad (16)$$

Using (8) and (9), we have

$$\ddot{e} = \ddot{q}_d - v + g \quad (17)$$

Substitution of (17) into (16) yields

$$\dot{\sigma}(t)=\ddot{q}_d-\dot{v}+\dot{g}(t)+a_1(\dot{q}_d-v+g)+a_2\dot{e}+b_1\ddot{q}_d$$
$$-b_1v+b_1g(t)+a_1b_1\dot{e}+a_2b_1e+b_2\dot{e}(t)+a_1b_2e(t)$$
$$+a_2b_2\int_0^t e(\tau)d\tau=\ddot{q}_d-\dot{v}+(a_1+b_2)(\dot{q}_d-v) \quad (18)$$
$$+(a_1+b_2)g(t)+\dot{g}(t)+(a_2+a_1b_1+b_2)\dot{e}$$
$$+(a_2b_1+a_1b_2)e+a_2b_2\int_0^t e(\tau)d\tau$$

we can rewrite (18) as

$$\dot{\sigma}(t)=\ddot{q}_d-\dot{v}+\mu_1\Upsilon(t)+f(t)+\mu_2\dot{e}+\mu_3e+\mu_4\int_0^t e(\tau)d\tau \quad (19)$$

Where $\Upsilon(t)=\dot{q}_d-v$, $f(t)=\mu_1g+\dot{g}$, $\mu_1=a_1+b_2$, $\mu_2=a_2+a_1b_1+b_2$, $\mu_3=a_2b_1+a_1b_2$ and $\mu_4=a_2b_2$. The control law in adaptive DSMC is proposed by

$$\dot{v}_{ADSMC}=\ddot{q}_d+\mu_1\Upsilon(t)+\mu_2\dot{e}+\mu_3e+$$
$$\mu_4\int_0^t e(\tau)d\tau+\hat{f}+v_r \quad (20)$$
$$v_{ADSMC}(t)=\int_0^t\dot{v}_{ADSMC}(\tau)d\tau$$

where $\hat{f}$ is the estimation of f and v_r is the robust control term which will be calculated in the next section. It follows from (19) and (20) that

$$\dot{\sigma}=\tilde{f}-v_r$$
$$\tilde{f}=f-\hat{f} \quad (21)$$

The sampling interval in the experiment is short enough as compared with the variation of f, thus, the term f is also assumed to be a constant during the estimation (i.e. $\tilde{f}=f-\hat{f}\rightarrow\dot{\tilde{f}}=-\dot{\hat{f}}$) [25-28].

$$\dot{V}=\sigma\dot{\sigma}-\frac{1}{\gamma}\tilde{f}\dot{\hat{f}} \quad (23)$$

Using $\dot{\sigma}$ defined in (21) we have

$$\dot{V}=\sigma(\tilde{f}-v_r)-\frac{1}{\gamma}\tilde{f}\dot{\hat{f}} \quad (24)$$

The adaptive law can be proposed as follows:

$$\dot{\hat{f}}=\gamma\sigma \quad (25)$$

Using (25), one can easily conclude that

$$\dot{V}=-\sigma v_r \quad (26)$$

where the robust control term is selected as follows:

$$v_r=k\sigma \quad (27)$$

Substituting (27) into (26), we have

$$\dot{V}=-k\sigma^2 \quad (28)$$

Therefore, it has been guaranteed that $\dot{V}\le 0$. Using Barbalat's lemma [29], it can be found the tracking error asymptotically converges to zero.

Remark: The final Lyapunov function for the total robotic system is the sum of Lyapunov function as defined in (22).

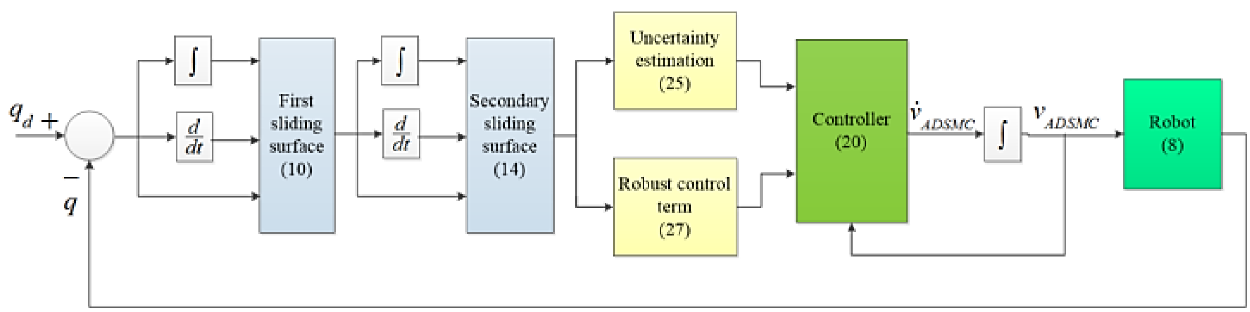

Fig.1. The configuration of the proposed control system

IV. STABILITY ANALYSIS

Consider a Lyapunov function candidate:

$$V=\frac{1}{2}\sigma^2+\frac{1}{2\gamma}\tilde{f}^2 \quad (22)$$

Differentiating the Lyapunov function, we have

V. SIMULATION RESULTS

In order to demonstrate the performance of the proposed controller, an articulated robot is considered, with a symbolic representation given in Fig. 2. The parameters of the robotic system are presented in [30]. The Denavit–Hartenberg (DH) parameters of the robot and the parameters of permanent magnet dc motors are given in Table 1 and Table 2, respectively. The external disturbance d is a step function with the amplitude of 2 volts which is inserted into the system at $t = 6\sec$. The maximum voltage of each motor is set to $v_{\max} = 40V$. The desired position for each joint is formulated by

$$q_d = 1 - \cos(\pi t / 7) \tag{29}$$

This desired trajectory is shown in Fig. 3 .The sliding surface parameters have been selected as $a_1 = 10, a_2 = 0.1, b_1 = 20, b_2 = 0.2$. The parameters γ and k have been set to 3000 and 10, respectively.

TABLE I

The Denavit–Hartenberg parameters

Link	θ	d	a	α
1	θ_1	$d_1 = 0.28$	0	$\frac{\pi}{2}$
2	θ_2	0	$a_2 = 0.76$	0
3	θ_3	0	$a_3 = 0.93$	0

TABLE II

The motor parameters

Motor	R	J_m	B_m	K_m	r	L
1,2,3	1.26	0.0002	0.001	0.26	0.01	0.001

Fig. 4 shows the tracking performance of ADSMC. According to Fig. 4, it can be found that the proposed controller design procedure performs well and has fast tracking performance. Also, the control inputs are depicted in Fig. 5. As shown in this figure, these signals are smooth and do not exceed the allowable values. From Figs. 4 and 5, the simulation results indicate that the favorable tracking performance is obtained.

Now, the proposed method is compared with the DSMC method. In the DSMC, the control signal is as follows:

$$\dot v_{DSMC} = \dddot{q}_d + \mu_1 \Upsilon(t) + \mu_2 \dot e + \mu_3 e + \mu_4 \int_0^t e(\tau) d\tau + \rho \,\mathrm{sgn}(\sigma), \quad |f| < \rho$$
$$v_{DSMC}(t) = \int_0^t \dot v_{DSMC}(\tau) d\tau \tag{30}$$

The value of ρ is selected as 20. In the DSMC method, the sliding surface parameters are chosen as the proposed method, i.e. $a_1 = 10,\ a_2 = 0.1,\ b_1 = 20,\ b_2 = 0.2$. The tracking performance and control signals of the DSMC method are shown in Figs. 6 and 7, respectively. According to Fig. 6, it is observed that the tracking performance of the DSMC method is very weak in comparison with the proposed method, and this method cannot track the specified trajectory with the given initial conditions. In order to achieve better performance, the sliding surface parameters are selected as $a_1 = 100,\ a_2 = 400,\ b_1 = 200,\ b_2 = 600$ in the DSMC. The corresponding tracking errors and control efforts are shown in Figs. 8 and 9, respectively. As illustrated in Fig. 8, the tracking performance of the DSMC is improved, but it is still weak comparing to the proposed ADSMC method. Consequently, according to Figs. 4-9, it is concluded that the suggested ADSMC method has a significant advantage over the DSMC method regarding the tracking performance.

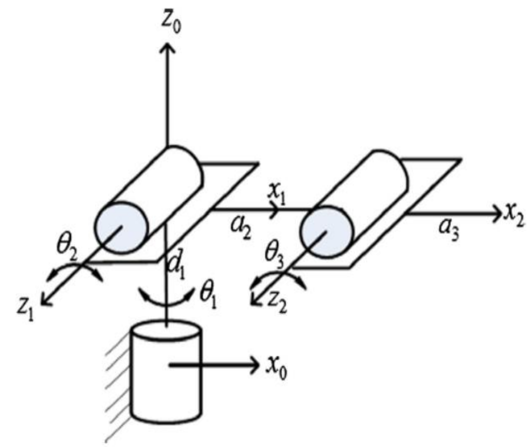

Fig. 2. The symbolic representation of the articulated robot

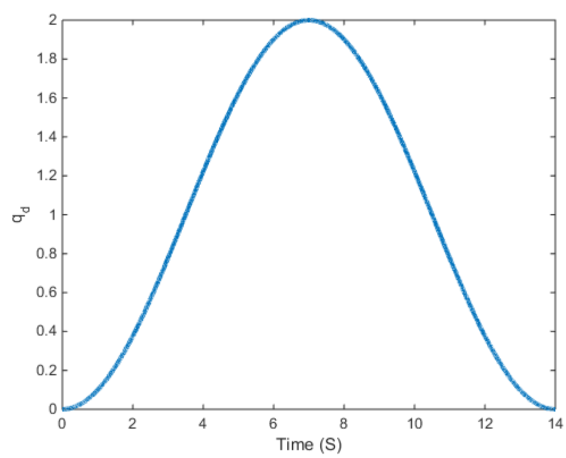

Fig. 3. The desired trajectory

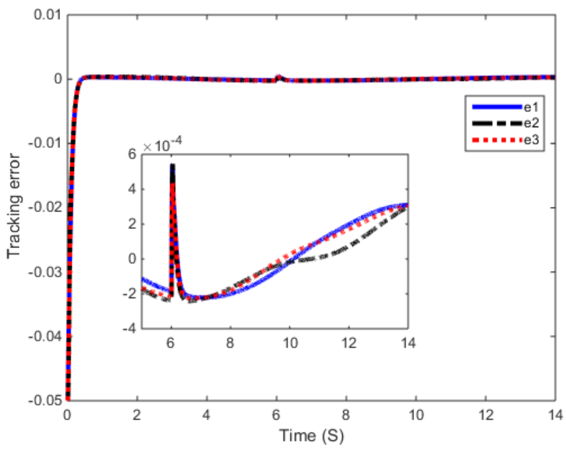

Fig.4. The tracking errors of Adaptive DSMC

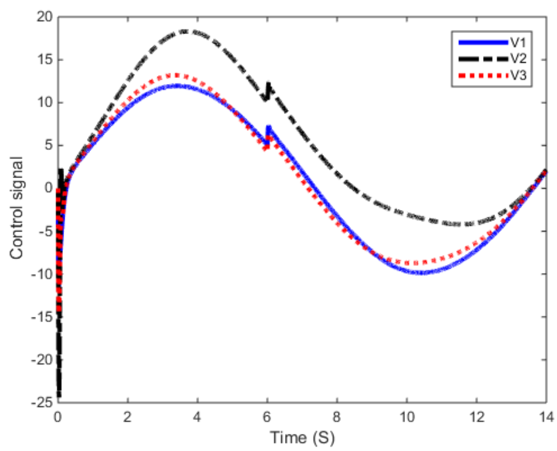

Fig.5. The voltages of motors in the proposed method

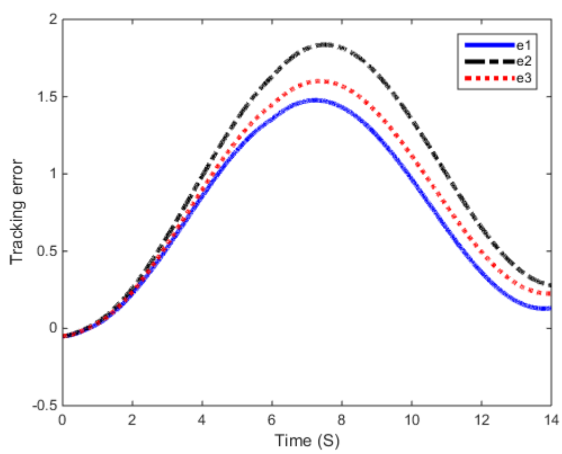

Fig. 6. The tracking errors using DSMC

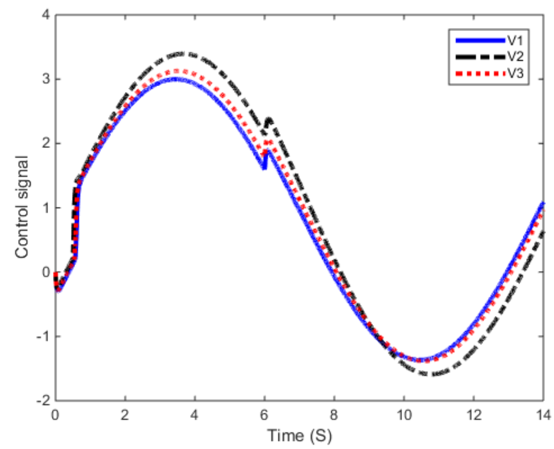

Fig. 7. The voltages of motors using DSMC

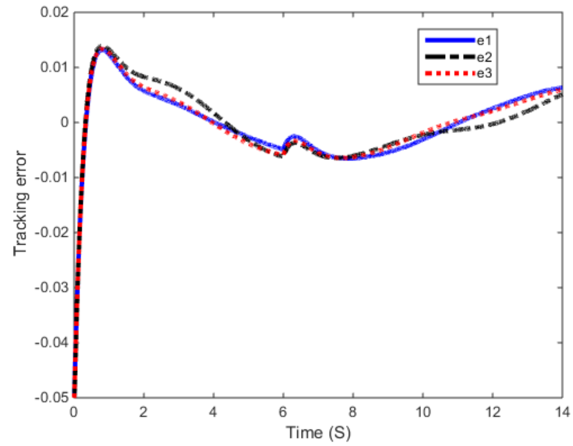

Fig.8. The tracking errors using DSMC

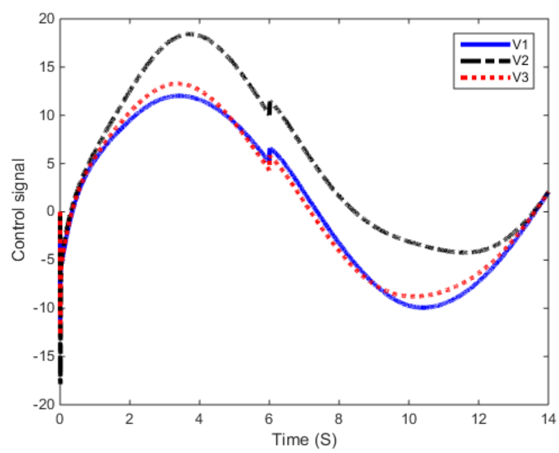

Fig. 9. The voltages of motors using DSMC

Remark: Increasing the parameter k will increase the amplitude of the control signal and actuator saturation will occur. For example if $k = 100$, the control signal will exceed the permitted range. For the sliding surface parameters a_1 and b_1, small values such as 1 or 2 will result in poor tracking performance and the tracking errors cannot converge to zero. For the sliding surface parameters a_2 and b_2, large values will increase the overshoot in the tracking error profile. Due to these issues, the controller parameters have been adjusted using the trial and error process. Also, optimization algorithms such as PSO, BA, ILCOA, GA, OSA, WOA or GPEA [31-44] can be used for tuning the controller parameters.

Finally, in order to show the efficiency of using the second sliding surface, the performance of the proposed method is compared with that of the conventional sliding mode control [40] in which the control signal is designed as:

$$v_{SMC} = \ddot{q}_d + a_1\dot{e} + a_2 e + \rho\,\mathrm{sgn}(\sigma), \quad |g| < \rho_1 \tag{31}$$

Where $\rho_1 = 10$, $a_1 = 100$ and $a_2 = 400$.

The tracking errors and control signals related to the conventional sliding mode control are illustrated in Fig. 10 and Fig. 11, respectively. As it can be seen the control signals are affected by the chattering phenomenon which is not desirable. In fact, in conventional sliding mode control, we are faced with the chattering problem. In order to overcome this problem, dynamic sliding mode control can be used. Moreover, in order to reduce the tracking error, adaptive dynamic sliding mode control is proposed in this paper. These comparisons reveal the superiority of the proposed method.

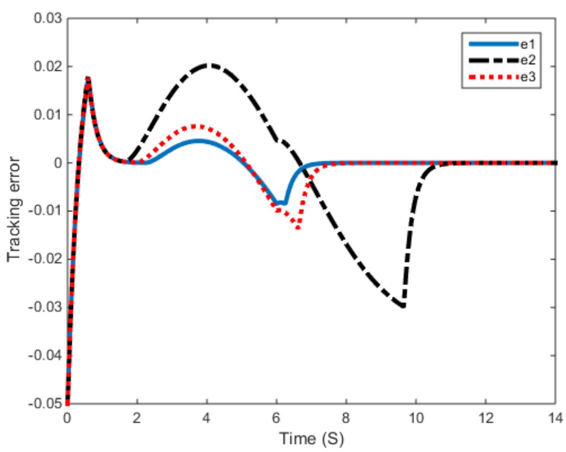

Fig.10. The tracking errors in conventional sliding mode control

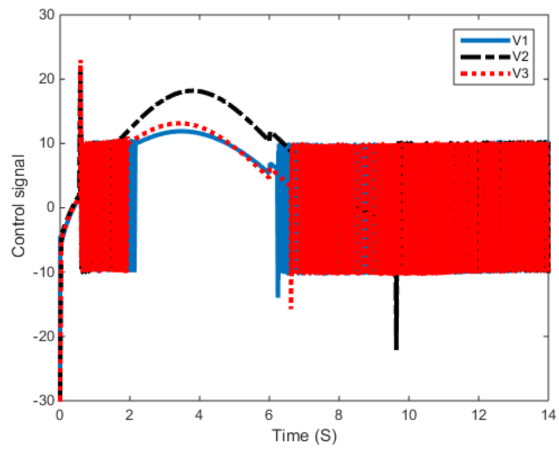

Fig. 11. The control signals in conventional sliding mode control

VI. Conclusion

A new approach based on an adaptive dynamic sliding mode control and VCS has been developed for tracking control of robotic systems. First, a Dynamic sliding mode control scheme has been designed properly. Then, in order to reduce the chattering, an adaptive mechanism has also been developed. The control signal is designed using voltage control strategy. The stability of the robotic system has been proven based on the Lyapunov criteria. The computer simulation results show that the voltage-based adaptive dynamic sliding mode controller can perform successful control and achieve desired tracking performance.

REFERENCES

[1] Y. Su, , C. Zheng, and P. Mercorelli, "Robust approximate fixed-time tracking control for uncertain robot manipulators", Mechanical Systems and Signal Processing, Vol. 135, (2020) p.106379.

[2] R. Gholipour, M.M. Fateh, "Robust Control of Robotic Manipulators in the Task-Space Using an Adaptive Observer Based on Chebyshev Polynomials", Journal of Systems Science and Complexity, (2020). https://doi.org/10.1007/s11424-020-8186-0.

[3] M. Bekrani, M. Heydari, and S.T. Behrooz, "An Adaptive Control Method Based on Interval Fuzzy Sliding Mode for Direct Matrix Converters", International Journal of Industrial Electronics, Control and Optimization, Vol. 3, No. 2, (2020), 159-171.

[4] S.H. Shahalami, and F. Rajab Nejad, "Design of Adaptive Back-Stepping Controller for Chaos Control in Boost Converter and Controller Coefficients Optimization Using CHPSO Algorithm", International Journal of Industrial Electronics, Control and Optimization. Vol. 3, No.3, (2020), 249-257.

[5] A. Haqshenas M, M.M. Fateh, and S.M. Ahmadi, "Adaptive control of electrically-driven nonholonomic wheeled mobile robots: Taylor series-based approach with guaranteed asymptotic stability", International Journal of

Adaptive Control and Signal Processing, (2020), https://doi.org/10.1002/acs.3104.

[6] S.M. Ahmadi, and M.M. Fateh, "Task-space control of robots using an adaptive Taylor series uncertainty estimator", International Journal of Control, Vol. 92, No. 9, (2019), 2159-2169.

[7] M. Van, S.S. Ge and H. Ren, "Finite time fault tolerant control for robot manipulators using time delay estimation and continuous nonsingular fast terminal sliding mode control", IEEE transactions on cybernetics, Vol. 47, No. 7, (2017), 1681-1693.

[8] R. Gholipour, A. Khosravi and H. Mojallali, "Multi-objective optimal backstepping controller design for chaos control in a rod-type plasma torch system using Bees Algorithm", Applied Mathematical Modelling, Vol. 39, No. 15, (2015), 4432-4444.

[9] S. Park and S. Rahmdel, "A new fuzzy sliding mode controller with auto-adjustable saturation boundary layers implemented on vehicle suspension", International Journal of Engineering-Transactions C: Aspects, Vol. 26, No. 12, (2013), 1401-1410.

[10] Y. Zhao, P. Huang and F. Zhang, "Dynamic modeling and Super-Twisting Sliding Mode Control for Tethered Space Robot", Acta Astronautica, Vol. 143, (2018), 310-321.

[11] G. Chen, B. Jin, Y. Chen, "Nonsingular fast terminal sliding mode posture control for six-legged walking robots with redundant actuation", Mechatronics, Vol. 50, (2018), 1-15.

[12] F.J. Lin, S.Y. Chen K.K. Shyu, "Robust dynamic sliding-mode control using adaptive RENN for magnetic levitation system", IEEE Transactions on Neural Networks, Vol. 20, No. 6, (2009), 938-951.

[13] S.Y. Chen, S.S. Gong, "Speed tracking control of pneumatic motor servo systems using observation-based adaptive dynamic sliding-mode control", Mechanical Systems and Signal Processing, Vol. 94, (2017) , 111-128.

[14] S. Wen, M.Z. Chen, Z. Zeng, X. Yu and T. Huang, "Fuzzy control for uncertain vehicle active suspension systems via dynamic sliding-mode approach", IEEE Transactions on Systems, Man, and Cybernetics: Systems, Vol. 47, No. 1, (2017), 24-32.

[15] S. Khorashadizadeh and M.M. Fateh, "Uncertainty estimation in robust tracking control of robot manipulators using the Fourier series expansion", Robotica, Vol. 35, No. 2, (2017), 310-336.

[16] S. Khorashadizadeh and M.H. Majidi, "Chaos synchronization using the Fourier series expansion with application to secure communications", AEU-International Journal of Electronics and Communications, Vol. 82, (2017), 37-44.

[17] R. Gholipour and M.M. Fateh, "Adaptive task-space control of robot manipulators using the Fourier series expansion without task-space velocity measurements", Measurement, Vol. 123, (2018), 285-292.

[18] M.R. Shokoohinia and M.M. Fateh, "Robust dynamic sliding mode control of robot manipulators using the Fourier series expansion", Transactions of the Institute of Measurement and Control, https://doi.org/10.1177/0142331218802357, 2018.

[19] M.R.Shokoohinia, M.M. Fateh, and R. Gholipour, "Design of an adaptive dynamic sliding mode control approach for robotic systems via uncertainty estimators with exponential convergence rate", SN Applied Sciences, Vol. 2, No. 2, (2020), 1-11.

[20] M.M. Fateh and M. Sadeghijaleh, "Voltage control strategy for direct-drive robots driven by permanent magnet synchronous motors", International Journal of Engineering-Transactions B: Applications, Vol. 28, No. 5, (2015), 709-716.

[21] M.M. Fateh and A. Arab, "Robust control of a wheeled mobile robot by voltage control strategy", Nonlinear Dynamics, Vol. 79, No. 1, (2015), 335-348.

[22] S. Khorashadizadeh and M.M. Fateh, "Robust task-space control of robot manipulators using Legendre polynomials for uncertainty estimation", Nonlinear Dynamics, Vol. 79, No. 2, (2015), 1151-1161.

[23] R. Gholipour and M.M. Fateh, "Observer-based robust task-space control of robot manipulators using Legendre polynomial", In Electrical Engineering (ICEE), 2017 Iranian Conference on (pp. 766-771). IEEE, (2017).

[24] M.W. Spong, S. Hutchinson and M. Vidyasagar, "Robot modeling and control", (Vol. 3, pp. 187-227). New York: Wiley, (2006).

[25] F.J. Lin, S.G. Chen and I.F. Sun, "Intelligent sliding-mode position control using recurrent wavelet fuzzy neural network for electrical power steering system" International journal of fuzzy systems, Vol. 19, No. 5, (2017), 1344-1361.

[26] F.J. Lin, S.G. Chen and I.F. Sun, "Adaptive backstepping control of six-phase PMSM using functional link radial basis function network uncertainty observer", Asian Journal of Control, Vol. 19, No. 6, (2017), 2255-2269.

[27] R. Gholipour and M.M. Fateh, "Designing a Robust Control Scheme for Robotic Systems with an Adaptive Observer", International Journal of Engineering, Transactions B: Applications, Vol. 32, No. 2, (2019), 270-276.

[28] F. Lin, S. Chen and C. Hsu, , "Intelligent Backstepping Control Using Recurrent Feature Selection Fuzzy Neural Network for Synchronous Reluctance Motor Position Servo Drive System", IEEE Transactions on Fuzzy Systems, Vol. 27, No. 3, (2019), 413-427.

[29] J.J.E. Slotine and W. Li, "Applied nonlinear control", (Vol. 199, No. 1). Englewood Cliffs, NJ: Prentice hall, (1991).

[30] M.M. Fateh and S. Khorashadizadeh, "Robust control of electrically driven robots by adaptive fuzzy estimation of uncertainty", Nonlinear Dynamics, Vol. 69, No. 3, (2012), 1465-1477.

[31] E. Salahshour, M. Malekzadeh, R. Gholipour, and S.Khorashadizadeh, "Designing multi-layer quantum neural network controller for chaos control of rod-type plasma torch system using improved particle swarm optimization", Evolving Systems, Vol. 10, No. 3, (2019), 317-331.

[32] R. Gholipour, J. Addeh, H. Mojallali, and A. Khosravi, "Multi-objective evolutionary optimization of PID controller by chaotic particle swarm optimization", International Journal of Computer and Electrical Engineering, Vol. 4, No. 6, (2012), 833-838.

[33] R. Gholipour, , H. Mojallali, and S.M.K., Akhlaghi, "A Novel Particle Swarm Optimization with Passive Congregation via Chaotic Sequences", International Journal of Computer and Electrical Engineering, Vol. 4, No. 6, (2012), 809-815.

[34] R. Gholipour, A. Khosravi, and H. Mojallali, "Suppression of chaotic behavior in duffing-holmes system using back-stepping controller optimized by unified particle swarm optimization algorithm", International Journal of

Engineering, Transactions B: Applications, Vol. 26, No. 11, (2013), 1299-1306.

[35] R. Gholipour, A. Khosravi, and H. Mojallali, "Parameter estimation of loranz chaotic dynamic system using bees algorithm", International Journal of Engineering, Transactions C: Aspects, Vol. 26, No. 3, (2013), 257-262.

[36] N. Pourmousa, S.M. Ebrahimi, M. Malekzadeh, and M. Alizadeh, "Parameter estimation of photovoltaic cells using improved Lozi map based chaotic optimization Algorithm", Solar Energy, Vol. 180, (2019), 180-191.

[37] J. Farzaneh, , R. Keypour, and A. Karsaz, "A novel fast maximum power point tracking for a PV system using hybrid PSO-ANFIS algorithm under partial shading conditions", International Journal of Industrial Electronics, Control and Optimization, Vol. 2, No. 1, (2019), 47-58.

[38] H. Moradi CheshmehBeigi, and A. Mohamadi, "Torque Ripple Minimization in SRM Based on Advanced Torque Sharing Function Modified by Genetic Algorithm Combined with Fuzzy PSO", International Journal of Industrial Electronics, Control and Optimization, Vol. 1, No. 1, (2018), 71-80.

[39] M. Dehghani, Z. Montazeri, O.P. Malik, A. Ehsanifar, and A. Dehghani, "OSA: Orientation Search Algorithm", International Journal of Industrial Electronics, Control and Optimization, Vol. 2, No. 2, (2019), 99-112.

[40] N. Ghaffarzadeh, and H. Faramarzi, "A new whale optimization algorithm based fault location method by focusing on dispersed model of the transmission line", International Journal of Industrial Electronics, Control and Optimization, (2020), doi: 10.22111/ieco.2020.32027.1218.

[41] M.E.B. Aguilar, D.V. Coury, R. Reginatto, and R.M. Monaro, "Multi-objective PSO applied to PI control of DFIG wind turbine under electrical fault conditions", Electric Power Systems Research, Vol. 180, (2020), p.106081, https://doi.org/10.1016/j.epsr.2019.106081.

[42] Z. Hu, , X. Xu, , Q. Su, , H. Zhu, and J. Guo, "Grey prediction evolution algorithm for global optimization", Applied Mathematical Modelling, Vol. 79, (2020), 145-160.

[43] M. Kohler, M.M. Vellasco, and R. Tanscheit, "PSO+: A new particle swarm optimization algorithm for constrained problems", Applied Soft Computing, Vol. 85, (2019), p.105865, https://doi.org/10.1016/j.asoc.2019.105865.

[44] A. Taheri, and N. Asgari, "Sliding Mode Control of LLC Resonant DC-DC Converter for Wide Output Voltage Range in Battery Charging", International Journal of Industrial Electronics, Control and Optimization, Vol. 2, No. 2, (2019), 127-136.

Mohammad Reza Shokoohinia received his M. Sc. degree in Control engineering at Garmsar University, Iran in 2012. He is now a Ph. D. candidate in Control engineering at Shahrood University of Technology. His research interests include Dynamic Sliding Mode Control, Robotics and Intelligent Systems.
E-mail: mshokoohinia@yahoo.com (Corresponding author).

Mohammad Mehdi Fateh received his M. Sc. degree in electrical engineering from Tar-biat Modares University, Iran in 1991. He received his Ph. D. degree in robotic Engineering from Southampton University,UK in 2001. He is a full professor with the Department of Electrical and Robotic Engineering at Shahrood University of Technology, Iran. His research interests include nonlinear, robust and fuzzy control,robotics and intelligent systems.
E-mail: mmfateh@shahroodut.ac.ir

International Journal of Industrial Electronics, Control and Optimization
Vol. 3, No. 4, pp. 439-445, Sep (2020)

Quantization Noise Reduction Using Random Dither in Direct Torque Control of an Induction Motor

Amir Ghasemian[1] and Asghar Taheri [2,†]
[1,2]Department of Electrical and Computer Engineering, University of Zanjan, Zanjan, Iran

ABSTRACT

A direct torque control (DTC) induction motor drive is presented in this paper. Quantization errors of current and voltage measurements are simulated and considered. To reduce the average quantization error and other offset errors of current and voltage measurement and eliminating the increasing integrator errors, a random dither signal is added to the truncating analog to digital converter (ADC) outputs. In this method, the ADC mean error is reduced to zero and therefore, integrator output error is mitigated. The proposed quantization method can improve the digital converter result; thus, this method can decrease the current measurement result. Thus, the torque and flux rippleswere be decreased. The proposed dither injection method can be used in Digital signal processor (DSP) or FPGA implemented applications. Experimental results show the performance of the proposed method.

Article Info

Keywords:
Direct torque control, Dither Injection, Induction Motor Drive, Quantization

Article History:
Received 2019-10-28
Accepted 2020-05-19

I. INTRODUCTION

Digital control systems need ananalog to digital converter (ADC) to measure physical data. ADC operation can be modeled by two sub-processes called sampling and quantization [1-4]. The sampling operation incurs no loss of information as long as the input is band-limited in accordance with the sampling theorem [5]. But during quantization, truncating or rounding of the analog signal to a digital signal level, always result in signal degradation [5]. Also, offset error is important where the digital signal must be integrated. Integrating a signal with a small offset error causes the output error to increase linearly by time. In direct torque control (DTC) of an induction motor, estimation of the flux needs integration of the motor current [1,6,7]. Therefore, if a small offset error flaws in the current measurement then the flux estimation error will increase linearly.

The signal dithering is a method to overcome these errors; this method has many applications in digital audio and image processing [5,8]. In control systems, the dithering has not been used commonly as a method to reduce input noises, but it is used as a method by which high-frequency disturbances is introduced to a slow dynamic system to suppress problems like static friction and squeal [9-11]. In this paper, the dithering is used to reduce the mean error of measuring stator currents to zero and suppress the integration of the torque and the flux calculation errors. The DTC method controls both the stator flux and the electrical torque decupled without using any current feedback, PWM algorithm, or rotary coordinate conversion module. Therefore, compared with the field-oriented control method, the DTC technique has a

[†]Corresponding Author: taheri@znu.ac.ir
Tel: +98-24-33054066,Fax: +98-2433052617, University of Zanjan
Faculty of Electrical and Computer Engineering, University of Zanjan, Zanjan, Iran

simpler structure, faster torque response, and better robustness against parameters changes [12]. However, the basic switching-table-based DTC method has some outstanding drawbacks such as variable switching frequency due to the presence of the hysteresis controllers. Also, this method has high torque and flux ripples due to the low number of inverter switching states, and high sampling requirement [13-15].

A suitable look-up table for DTC of three-level dual voltage source inverter fed open-ended winding IM drive is proposed [15], where the VVs selection for lower hysteresis boundary conditions of torque and flux are restructured with null voltage states.

Two simple control methods with a fixed frequency are proposed for improving DTC of induction machines, which is named as CFTC-DTC in [16]. The CFTC-DTC was initially introduced to reduce torque ripple and achieve constant switching frequency in inverters. However, when compared to the original DTC, the CFTC-DTC algorithm suffers from slow torque dynamic response owing to the selection of zero-voltage vectors during torque transient [16].

A suitable duty cycle control technique to reduce torque,flux ripples, and harmonic loss in DTC of six-phase induction machine is proposed in [4]. Three different methods are proposed to improve the performance of DTC Switching Table of machine. The quantization noise cancellation method is used in other applications [17 and 18]. Using of the dither injection method can be used any application with ADC to decrease the error of digital converter. According to these technical points, the quantization noise reduction of the DTC of an induction motor is very important.

II. Direct Torque Control

In a two-level inverter, a DC voltage is inverted to a three-phase output, by means of two switches for each output phase. These six switches can be commanded in six different ways. For each value of the motor torque and the vector form of the stator flux, a suitable switching state can be selected to excite the motor to simultaneously control the flux and torque. This is the basic principle of the DTC scheme.

Figure (1) shows theDTC diagram. The torque and flux vectors must be estimated or calculated from measurable motor parameters. Estimated torque and flux are compared with their desired values and the error signals go to hysteresis blocks to determine the desired changes of the flux and torque. For torque error signal, the hysteresis block is a tree-level hysteresis block. But for flux error, it is a two-level block. Then the suitable switching states are determined by a switching table. Also, the appropriate switching states depend on the angle of the stator flux in the vector space.

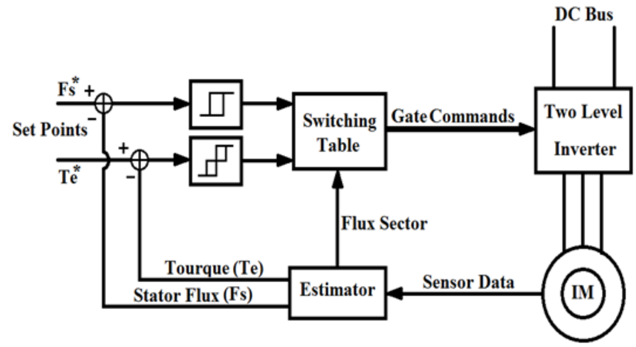

Fig. 1. Used DTC method diagram

If the vector space is divided into six different sectors, as shown in figure (2), each sector has its own suitable switching states depending on the hysteresis block outputs.

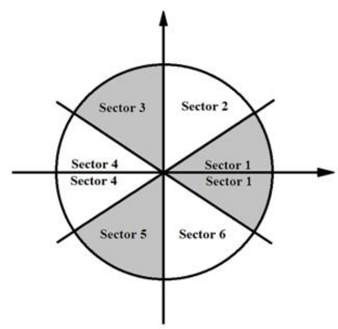

Fig. 2. Two-level inverter switching vectors and stator flux sector

Table (1) shows a switching table for a two-level inverter DTC system. In this way, the torque and flux of the induction motor can remain with a suitable hysteresis band around their desired values, and therefore can be controlled directly by changing the switches.

TABLE I
DTC SWITCHING TABLE

		Sector					
Flux	Torque	1	2	3	4	5	6
Increase	Increase	V2	V3	V4	V5	V6	V1
	No Change	V0	V7	V0	V7	V0	V7
	Decrease	V6	V1	V2	V3	V4	V5
Decrease	Increase	V3	V4	V5	V6	V1	V2
	No Change	V7	V0	V7	V0	V7	V0
	Decrease	V5	V6	V1	V2	V3	V4

III. Quantization and Offset Errors

The process of converting an analog signal to a digital value in ADCs consists of two stages; one is the sampling, and the other is the quantization (figure 3). During the sampling stage, the input analog signal periodically is held to give enough time to the next stage to measure and convert the analog signal. During the quantization stage, the held analog signal is truncated or rounded to a digital neighbor level and then converted to a binary digital number.

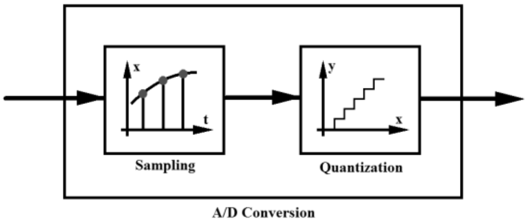

Fig. 3. The quantization model

An ideal ADC uses arounding method; therefore, the mean output error will be zero. If the ADC uses thetruncation method, a mean offset error of value 1/2LSB, will be added to the actual mean value of the original signal. Today many ADCs use therounding method to eliminate this offset error because if this digitized signal needs to be integrated, this small offset error will produce serious problems.

Earlier airplanes with mechanical computers were working more accurately, during fly, because of high-frequency vibrations. This high-frequency vibration was called dither [12]. After that, dither as a technique found many applications in mechanical and electromechanical systems and digital signal processing [5]. In the mechanical and the electromechanical systems, dither means superposition of high-frequency vibration to stabilize a low-frequency vibration [10]. Suppressing squeal in car wiper system [10] or brake system, [11], are two examples of these applications. However, in digital signal processing, it has a little different meaning. In this area, dithering is an intentionally applied form of noise to reduce quantization errors [5].

IV. DTC Simulation

The DTC of an induction motor is simulated in MATLAB Simulink. In this simulation, the induction motor is modeled in d-q coordinate system. A simple PID controller measures the motor speed and determines a suitable torque set point for the DTC measures the motor currents and voltages and estimates its torque and flux vectors. Then, the appropriate switching state is calculated to keep the motor torque and flux in their determined boundaries. Figure (4) shows the Simulink block diagram of this simulation. The motor fluxes magnitude is shown in figure 5(a). As we see, the flux is controlled around its desired value. As mentioned in previous sections, the DTC will control the stator flux vector to rotate around a circle in d-q coordinate system. This circular stator flux graph is shown in figure 5(b). The motor torque is controlled around the load torque to overcome the load torque. The motor Torque is shown in figure 6(a). The desired suitable PID controller controls the speed of the motor shaft by determining suitable torque setpoints. The motor speed is shown in figure 6(b). Compared with the motor frequency response, the DTC outputs are high-frequency switching signals applied to power electronics switches. Therefore, the voltages applied to three-phase motor inputs have high-frequency pulsating voltages. Because of the low-frequency response of the motor, the average power of these pulsating voltages determines the motor response.

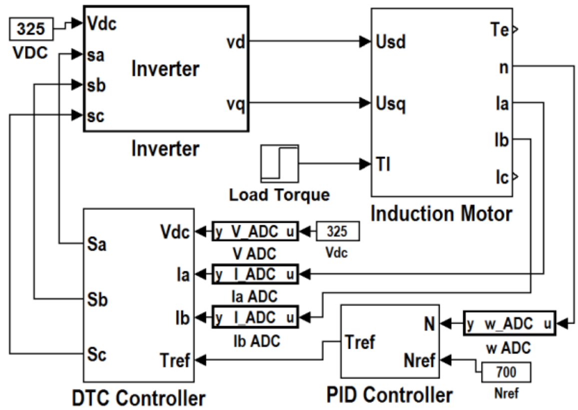

Fig. 4. DTC system simulation in MATLAB Simulink

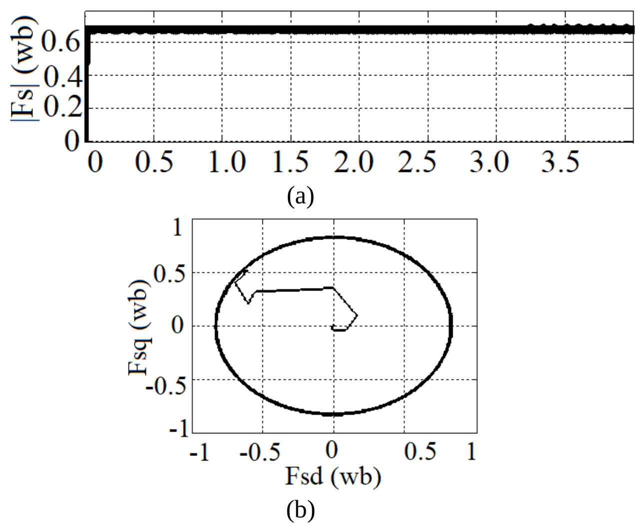

Fig. 5. (a) Stator flux magnitude, (b) Stator flux vector in d-q coordinate

In figure 7(a), averaged voltages are shown. This figure shows that the averaged voltages which are applied to the motor are three phase sinusoidal voltages. The motor current in phase (a) is shown in figure 7 (b). In the experimental setup, two phases of these currents are measured with ADCs and the third phase current is calculated.

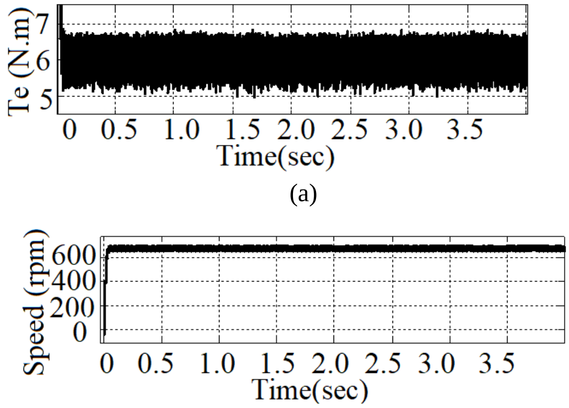

(a)

(b)

Fig. 6. (a) Electromagnetic torque, (b) Motor speed

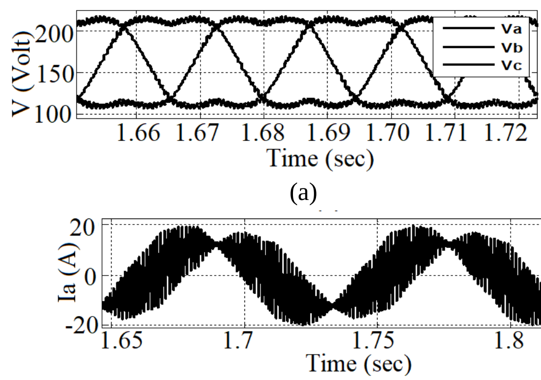

(a)

(b)

Fig. 7. (a) Averaged motor voltage, (b) current phase.

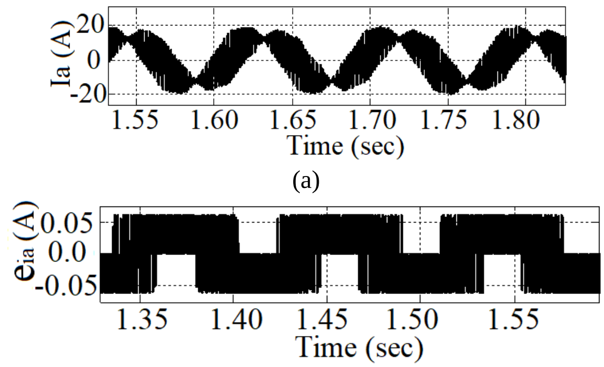

(a)

(b)

Fig. 8. (a) Phase a current, (b) Ia measurement error, (Ideal ADC)

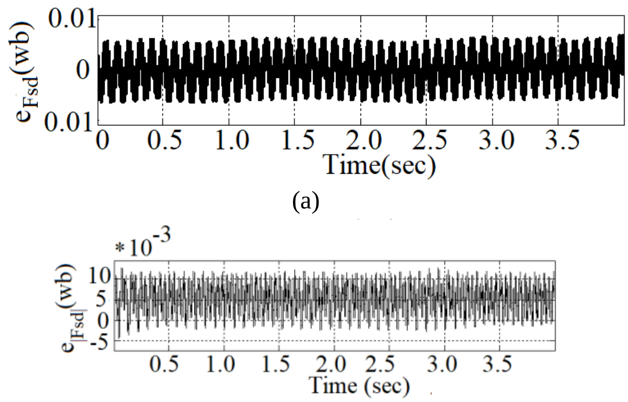

(a)

(b)

Fig. 9. (a) Fsd estimation error, (b) |Fs| estimation error, (Ideal ADC)

V. SIMULATION OF THE QUANTIZATION ERROR

To consider ADC error, small ADC blocks designed in the model. To model ADC, firstly, the transfer function of an ideal ADC [5] is used. In theused DTC system, the controller measures the currents of two phases of the motor using hall effect sensors, and then the third phase current is calculated using these two measurements.

Therefore two current sensors are sufficient for this controller. Figure 8(a) shows the current measurement of phase a, using this ideal ADC that uses arounding method for the quantization. Since three-phase currents are dependent on each other, Ia and Ib are measured by two ADCs and Ic is calculated. The quantization error of measurement Ia is shown in figure 8(b). As it is shown in this figures, the average quantization error of ideal ADCs over a sufficient period of time will be zero.

Zero average ADC errors help the integration carried out properly. Also, integrator blocks do not increase errors. The resulting motor direct component (d-axis) of flux estimation error, and the total flux magnitude error, using ideal ADC models are shown in figures 9 (a) and (b), respectively.

These flux errors are small enough and do not increase with time. Therefore, the motor flux is estimated in a suitable range around its actual value.

VI. SIMULATING WITH OFFSET ERRORS

Although manyof today's ADCs removed truncation offset errors, they still have other sources of offset errors. These offset errors are calculated during thefabrication process, and they are mentioned in the ADC datasheets. Therefore compensating these offset errors is a problem when long interval integrations are carried out. To model ADCs with thetruncation method, a constant offset is added to the ideal ADC model prepared in the previous section. This way the truncating ADC offset error is simulated by setting the offset equal to 0.5 LSB. Also, other offset errors can be simulated by changing this value. Measured phase a current is shown in figure10 (a). As mentioned above,the mean quantization error is not zero in this case. The average quantization error for this ADC has a negative value as shown in figure 10 (b).

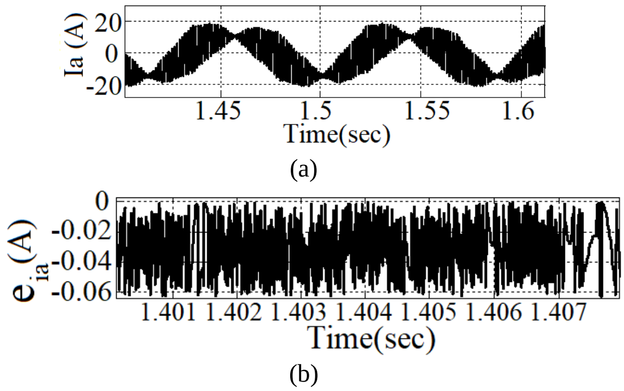

Fig. 10. (a) Phase a current, (b) Ia measurement error, (non-Ideal ADC)

According to figure 11 (a), the current measurement errors resulted inincreasing errors in the direct flux component. Figure 11(b) shows theincreasing fluctuation in the flux magnitude. As it is shown in figure 12 (a), the actual flux magnitude has gone away from its estimated value; and it is not close to the estimated flux magnitude. The circular graph of the actual stator flux vector is shown in figure 12 (b). According to that, the controller controls its estimated flux around its desired values, but the actual flux goes away from its desired value, as the error increases.

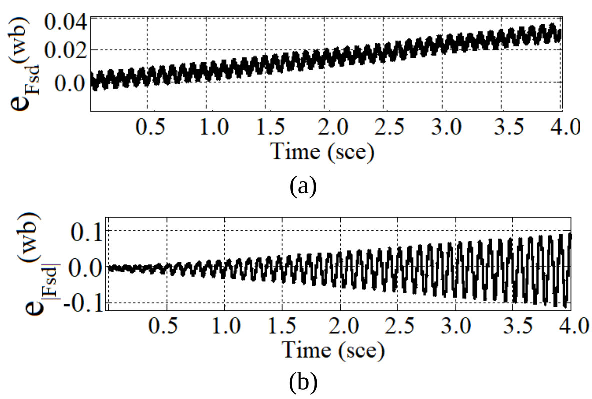

Fig. 11. (a) Fsd estimation error, (b) |Fs| estimation error, (non-ideal ADC)

In d-q coordinate system, the increasing error appears as a shift of circular flux graph with respect to the estimated circular flux graph. In figure 12 (b), the actual and estimated fluxes are shown. The estimated flux vector (red) rotates properly around a circle, but the actual flux shifts in a direction which is shown by the black arrow.

VII. Ditter Injection

To eliminate the current measurement offset error, we cannot add a constant to the ADC output. Because the ADC offset error is 0.5 LSB and this error will be vital if it is integrated.

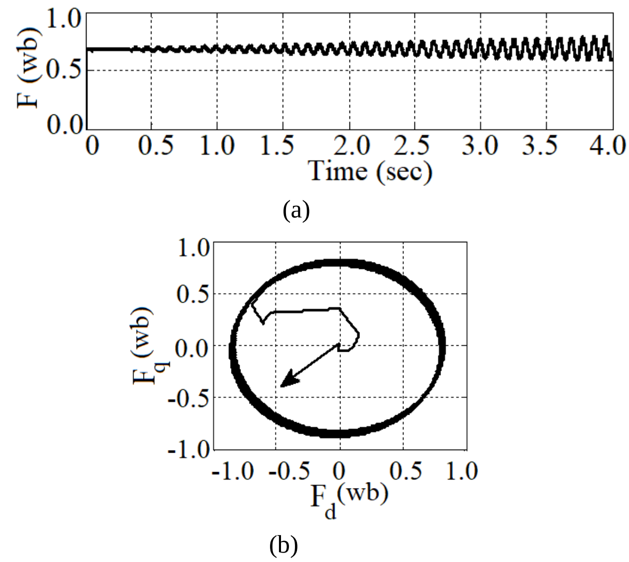

Fig. 12. Non-ideal ADC, (a) Actual stator flux magnitude, (b) Flux vectors in d-q axis

To resolve this problem, a random one-bit signal is added to the ADC output.

The mean value of this random signal eliminates the mean offset error of the ADC. The resulting measured phase a current is shown in figure 13 (a). Quantization errors, in this case, are similar to the previous section. Figures 13 (b) shows the phase a current quantization error.

A random dither signal is added to the ADC output to zero the mean ADC error, which was smaller than one bit in our digital control system. The current measurement error after dither injection is shown in figure 13 (c).

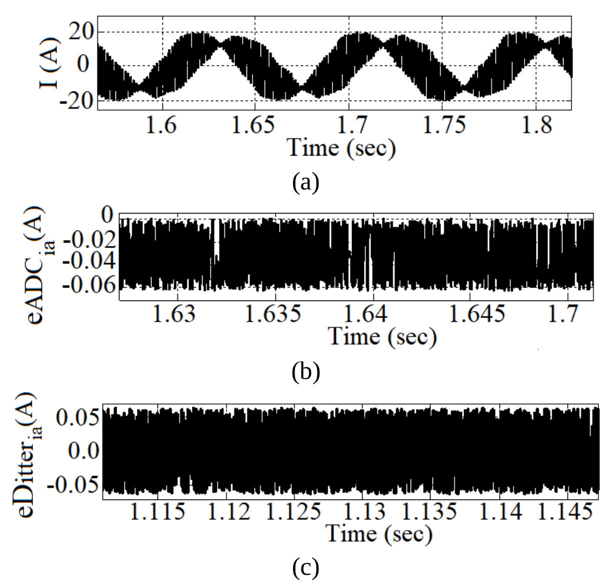

Fig. 13. Ditter injection results, (a) Phase A current, (b) Ia measurement error, (c) Ia measurement error

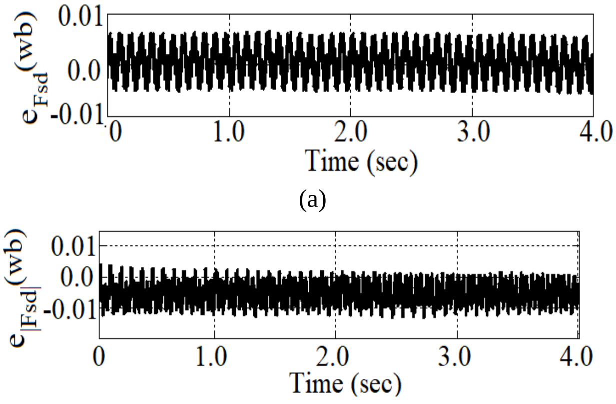

Fig. 14. Ditter injection results in flux estimation, (a) Fsd estimation error, (b) |Fs| estimation error

As it is shown, adding dither changed the mean error back to zero. Again, by decreasing the mean errors to zero, the increasing flux estimation errors are disappeared. The resulting motor direct component of flux estimation error, and the total flux magnitude error, using dither injection are shown in figures 14 (a) and (b), respectively.

Experimental results were added to the manuscript. The experimental results are shown below. The proposed methods is developed and tested in the experimentalsetup. The proposed techniques in DTC of IM are implemented on a Tms320f28337 board. Experimental results of the proposed techniques in DTC IM are shown in Figure.15. Figure 15 shows experimental results of load torque, motor speed, stator flux of d axis according to q axis, phase current, and flux amplitude.

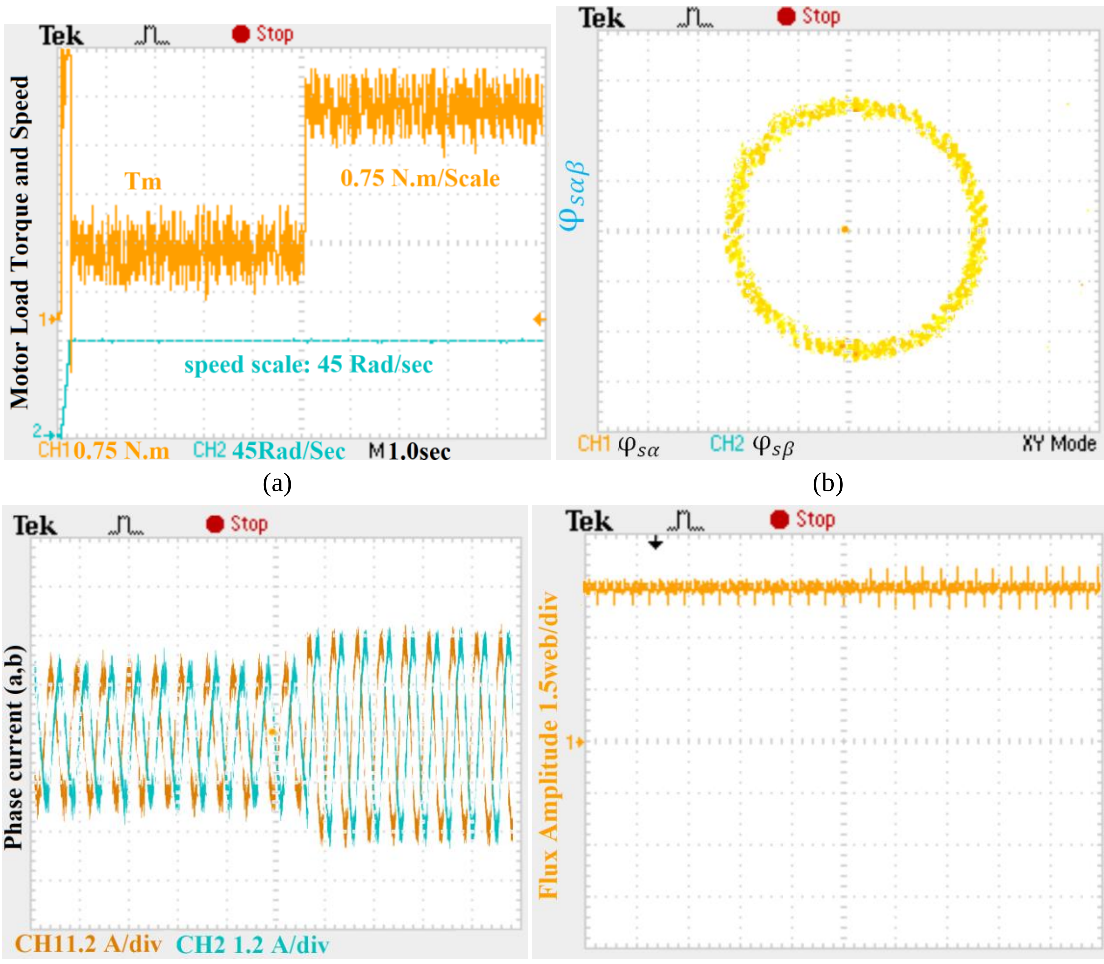

Figure 15 . Experimental results of DTC method, a) motor load torque and speed, b) stator flux of d axis according to q axis, c) phase current, and d) flux amplitude

VIII. CONCLUSION

A random digital dither signal is used to reduce the mean offset error of the motor current measurement to zero. Simulation results show that the increasing integration errors eliminated, and the motor torque and flux controlled properly as the case where an ideal ADC without offset errors is used. According to results, theproposed method decreases the ADC error in DTC of induction motor and improve motor performance.

REFERENCES

[1] Toh Ch. Ling, Implementation of Direct Torque Control of Induction Machines using Digital Signal Processor (DSP) and Field Programmable Gate Arrays (FPGA), Ph.D. dissertation, Faculty of Elect. Eng., UniversitiTeknologi Malaysia, Skudai, 81300, Malaysia, 2005.

[2] T. Sutikno, N. R. N. Idris, A. Jidin and M. N. Cirstea, "An Improved FPGA Implementation of Direct Torque Control for Induction Machines," in IEEE Transactions on Industrial Informatics, vol. 9, no. 3, pp. 1280-1290, Aug. 2013.

[3] A. Taheri, Abdolrezarahmati, and ShahriyarKaboli, Energy Optimization of Field Oriented Six-Phase Induction Motor Drive, Advanced in Electrical and Computer Engineering, May 2011.

[4] H. Masoumkhani and A. Taheri, "PI regulator-Based Duty Cycle Control to Reduce Torque and Flux Ripples in DTC of Six-phase Induction Motor," in IEEE Journal of Emerging and Selected Topics in Power Electronics 2020.

[5] Henrik F. Lundin, Characterization and Correction of Analog-to-Digital Converters , Ph.D. dissertation, KTH School of Electrical Engineering, Stockholm, Sweden 2005.

[6] A. Taheri, Abdolrezarahmati, and ShahriyarKaboli, Efficiency Improvement in DTC of Six-Phase Induction Machine by Adaptive Gradient Descent of Flux, IEEE Transaction on power electronics, 2012.

[7] A. Taheri, Abdolrezarahmati, and ShahriyarKaboli, Compression of Efficiency in Different Switching Tables in Six-Phase Induction Motor DTC Drive, Journal of Power Electronic , 2012.

[8] R.A. Wannamaker , The Theory of Dithered Quantization , Ph.D. dissertation, University of Waterloo, Waterloo, Ontario, Canada, 2003.

[9] R. K. Behera and S. P. DAS, Improved direct torque control of induction motor with dither injection, S¯adhan¯a Vol. 33, Part 5, October 2008.

[10] B. Stallaert, F. Doucet, J. Rys, A. Diallo, S. Chaigne, J. Swevers, P. Sas, Application of dither control for automotive wiper squeal, ISMA, 2006.

[11] M. Dzirasa, K. Cunefare, M. Montbrun, and V. Rastelli, Burst Mode Dither Control of Automotive Brake Squel,, INCE Conference, Vol. 111, 2002.

[12] Ken C. Pohlmann, Principles of Digital Audio, (McGraw-Hill Professional, 2005).

[13] M. H. Holakooie, M. Ojaghi and A. Taheri, "Direct Torque Control of Six-Phase Induction Motor With a Novel MRAS-Based Stator Resistance Estimator," in IEEE Transactions on Industrial Electronics, vol. 65, no. 10, pp. 7685-7696, Oct. 2018.

[14] R. H. Kumar, A. Iqbal and N. C. Lenin, "Review of recent advancements of direct torque control in induction motor drives – a decade of progress," in IET Power Electronics, vol. 11, no. 1, pp. 1-15, 1 12 2018.

[15] R. E. KodumurMeesala and V. K. Thippiripati, "An Improved Direct Torque Control of Three-Level Dual Inverter Fed Open-Ended Winding Induction Motor Drive Based on Modified Look-Up Table," in IEEE Transactions on Power Electronics, vol. 35, no. 4, pp. 3906-3917, April 2020.

[16] I. M. Alsofyani, Y. Bak and K. Lee, "Fast Torque Control and Minimized Sector-Flux Droop for Constant Frequency Torque Controller Based DTC of Induction Machines," in IEEE Transactions on Power Electronics, vol. 34, no. 12, pp. 12141-12153, Dec. 2019.

[17] Alireza shamsi, "A new Mismatch cancelation for Quadrature Delta Sigma Modulator," International Journal of Industrial Electronics, Control and Optimization, early Access, 10.22111/ieco.2019.29632.1167.

[18] A. Taheri and N. asgari, "Sliding Mode Control of LLC Resonant DC-DC Converter for Wide output voltage Range in Battery Charging Applications," International Journal of Industrial Electronics, Control and Optimization, Vol. 2, No. 2, pp. 127-136, 2019.

Amir Ghasemian was born in Mazandaran, Iran, in 1984. He received the B.Sc. degree from Iran University of Science and Technology,Tehran, Iran, in 2007 and the M.Sc. degree in 2010, and Ph.D. degree with theFaculty of Electrical and Computer Engineering, University of Zanjan, Zanjan, Iran all in electrical engineering. His current research interests include modeling,analysis, and control of power converters,digital control of dc–dc converters, switched and hybrid dynamicalsystems, and power electronic systems for renewable energy sources.

Asghar Taheri was born in Zanjan, Iran, in 1977.He received the B.S., M.S., and Ph.D. degrees in electrical and electronics engineering from Amirkabir University of Technology, Tehran, Iran, and Iran University of Science and Technology, Tehran, in 1999, 2001, and 2011, respectively. Since 2010, he has been a Faculty Member with the University of Zanjan, where he was an Assistant Professor from 2011 to 2016 and has been an Associate Professor since 2016. His current research interests include modeling, analysis, and control of power converters, motor drives and control, and multiphase machine drives, multilevel inverter, Z-source inverter, power electronic systems for renewable energy sources, process control, DSP and FPGA based system designs, hardware in the loop, and computer aided control.

IECO

This page intentionally left blank.

International Journal of Industrial Electronics, Control and Optimization © 2020 IECO
Vol. 3, No. 4, pp. 447-457, Sep (2020)

A Novel Complete Dynamic and Static Model of 48-Pulse VSC-based GUPFC for Parallel Transmission Lines

Mahyar Abasi[1], Mahmood Joorabian[2,†], Alireza Saffarian[3], and Seyyed Ghodratollah Seifossadat[4]

[1,2,3,4] Department of Electrical Engineering, Faculty of Engineering, Shahid Chamran University of Ahvaz, Ahvaz, Iran

ABSTRACT

Generalized Unified Power Flow Controller (GUPFC) is a member of the flexible alternating current transmission system (FACTS) devices family that operates based on voltage source converter (VSC) and is known as the most efficient FACTS device. GUPFC can control the voltage of one bus and the active and reactive power flows on at least two transmission lines with equal voltage levels. This paper presents the mathematical modeling of power injection by GUPFC for the first time. Besides, the accurate design and details of the control system for series and shunt converters of a GUPFC, along with a new mathematical function for pulse generation based on a 48-pulse VSC when the GUPFC is placed in the middle point of a parallel transmission line, are presented in this study. The power injection modeling introduced in this paper is very useful and efficient in Newton-Raphson power flow studies and in modeling different parts of the control system and power electronics converter in dynamic and transient studies. The modeling is implemented in MATLAB/Simulink for a 400 km, 230 kV, and 60 Hz nominal frequency double-circuit transmission line. The satisfactory results provided in the simulations section of the paper verify the validity and accurate performance of the proposed model.

Article Info

Keywords:
Active and Reactive Power Control, FACTS, GUPFC, 48-pulse VSC

Article History:
Received 2019-12-05
Accepted 2020-03-15

I. Introduction

Various solutions have so far been proposed for solving the problems caused by electrical energy transmission. One of the most significant and efficient solutions is the application of FACTS devices. Advances in the manufacturing of power electronics converters with high-speed switching [1] and the improved technology of control processors have led to a dramatic growth of novel ideas in designing FACTS devices [2]. To date, 10 types of compensators from the FACTS family have virtually been introduced in terms of theory as well as the experimental and practical manufacturing processes [3]. In 2000, Fardanesh et al. introduced, for the first time, a new concept of the most complete and advanced type of multi-converter FACTS, called GUPFC. Fig. 1 shows the various topologies of GUPFC in the power system. Generally speaking, this device consists of n ($n \geq 2$) series and shunt converters [4].

†Corresponding Author : mjoorabian@scu.ac.ir
Tel: +98-9161183017, Department of Electrical Engineering, Faculty of Engineering, Shahid Chamran University of Ahvaz, Ahvaz, Iran

Once the GUPFC was introduced, similar FACTS devices including GIPFC and MUPFC were also presented [5-6]. These devices have two major common features. First, they can be placed on more than one single transmission line; second, regarding their special topology, each of them contains both series and shunt converters. The main difference between GUPFC and GIPFC is that GUPFC can be used on at least two parallel transmission lines with the same voltage level. However, GIPFC is placed on at least two transmission lines with different voltage levels. The major difference between GUPFC and MUPFC is in the number of shunt converters. GUPFC has only one shunt converter while the number of shunt converters in MUPFC is equal to the number of its series converters. Furthermore, MUPFC can be employed in transmission lines with equal or different voltage levels. After the publication of the first paper in the field of GUPFC, building and installing a GUPFC device was practically proposed in Xinjiang, China, due to several reasons including numerous problems in power transmission to long distances, huge economic loss, and inappropriate power flow distribution which posed a risk to the system safety [7].

Basically, we can classify the literature on GUPFC into several main categories. A number of papers associated with GUPFC have focused specifically on the GUPFC modeling problem in the realm of power flow studies [8-14]. The mathematical modeling of GUPFC using the rating method, and a specific device for Newton-Raphson power flow studies have been presented for power systems [8]. The GUPFC modeling is discussed in the optimal power flow in the nonlinear internal point [9]. The authors in [10] provide the results obtained from utilizing GUPFC in a 28-bus, 330 kV in Nigeria for optimal power flow and voltage drop reduction. Ref. [11] argues the optimal location of GUPFC, the optimal power flow, and the modification of the Jacobian matrix in the presence of GUPFC. The developed model of GUPFC in the analysis of the Newton-Raphson power flow is given in [12] using the combined non-conformity method. Also, the development of GUPFC in Newton-Raphson method without modifying the Jacobian matrix and considering the power flow constraints is discussed in [13]. In another study, an impedance compensation method is used to solve numerical instability problems of power flow analysis in power systems equipped with the GUPFC [14].

The second category includes the dynamic studies and the analysis of various types of stabilities in the presence of GUPFC [15-20]. A control algorithm based on a fuzzy-neural network controller is presented in [15] to improve transient stability. A new algorithm for calculating the power quality index under steady-state and transient conditions is introduced in [16] using the harmonics technique in the presence of GUPFC. To study small-signal stability, a dynamic modeling based on the Heffron-Phillips model of a power system equipped with a GUPFC along with a PSS is proposed in [17]. An algorithm for enhancing the performance of GUPFC using a fuzzy logic-based controller is presented in [18]. Ref. [19] deals with the effect of GUPFC on small-signal stability of power systems. Also, the authors in [20] discuss the sub-synchronous resonance phenomenon in transmission lines compensated by GUPFC.

Still another group of studies concentrate on the operation and economic analyses of the presence of GUPFC in power systems [21-26]. A sensitivity-based approach for deciding on the proper location of GUPFC to perform an optimal power flow and its effect on power generation and transmission costs is suggested in [21]. Furthermore, a novel optimization algorithm for solving the economic problem of emissions and loss reduction in a power system equipped with GUPFC is presented in [22]. A new optimization method based on the PSO algorithm is given in [23] to optimize the generation cost objectives subject to various practical constraints in a power system equipped with GUPFC. The authors in [24] use a nonlinear internal point optimization method to calculate the transmission capability of a power system equipped with GUPFC. The increase in the loading capability of power system through the optimal placement of GUPFC based on PSO is presented in [25]. Line congestion management algorithm based on demand management for a combination of bilateral pool electricity market in a power system equipped with GUPFC is suggested in [26].

A different body of research deals with power quality assessment in power systems with GUPFC [27-28]. Ref. [27] studies the effect of GUPFC on the improvement of power quality and the total harmonic distortion (THD) level. Also, the concept of using GUPFC for reducing voltage flicker phenomenon and improving power quality is proposed in [28]. Finally, in the last group, Ref. [29] analyzes the positive effects of GUPFC on the distance relaying operation in transmission lines.

A thorough scrutiny of the literature shows that all power flow modeling studies performed in the presence of GUPFC for models given in Figs. 1 (a) and (b). Moreover, a major part of literature deals with the impact of GUPFC on power systems and discusses the accurate modeling of different control parts while related power electronics have rarely been investigated.

The topology given in Fig. 1(a) is used when the goal is to control the near-end bus voltage of the double-circuit line and to control power at a double-circuit line with distinctive remote-end buses with different voltages. The two circuits in the topology may differ in terms of distance. The topology given in Fig. 1(b) is employed when the goal is to regulate the near-end bus voltage and control power on one of the double-circuit lines with a common remote-end bus. The distances of both circuits in this topology are equal. The topology given in Fig. 1(c) is utilized when the aim is to regulate voltage along the path on the double-circuit line, especially in the middle of the line. The near and remote-end buses of both circuits in this topology are the same. According to the mentioned differences in different topologies provided in Fig. 1, the GUPFC modeling is different in Newton-Raphson power flow equations and in building the Jacobian matrix. Furthermore, control parameters in the series and shunt converters of the GUPFC in different topologies given in Fig. 1 are different because of power system stabilization in the presence of GUPFC, satisfying different constraints of power flow, and bus voltage control.

The main contributions of the present study are: 1) the accurate mathematical modeling of active and reactive power injections by GUPFC based on the topology given in Fig. 1 (c), which is exclusive for Newton-Raphson power flow studies, 2) the accurate modeling of different parts of the control system of the 48-pulse VSC-based GUPFC, and 3) the presentation of a new mathematical function to generate a 48-pulse signal required in the GUPFC, instead of using the classic 48-pulse signal generator system. The logic used in this block generates the firing angle signals of the 48-pulse VSC's gate turn-off thyristor (GTO).

Using harmonic filters along with FACTS devices to remove harmonics produced by voltage source inverters embedded within the filters leads to increased installation and operation costs of FACTS devices in the power system. Hence, to solve the power quality problem and reduce the harmonic distortions level in output voltage of the converters used in the FACTS devices, the paper presents 48-pulse voltage source inverters. The application of 48-pulse converters within the GUPFC helps reduce the harmonic level of the output voltage so that there is no need to use harmonic elimination filters, making it really cost-effective.

The paper is organized as follows. The mathematical modeling of the active and reactive power injection by the GUPFC is presented in Section 2 of the paper, which is exclusive to Newton-Raphson power flow studies. Section 3 describes the accurate design of the GUPFC's controller system. Section 4 discusses the inverter modeling of the 48-pulse VSC-based GUPFC using a new mathematical function for the pulse generator. Software simulations and the obtained results are provided in Section 5. Section 6 presents conclusions, and finally, the Appendixes include the test system data.

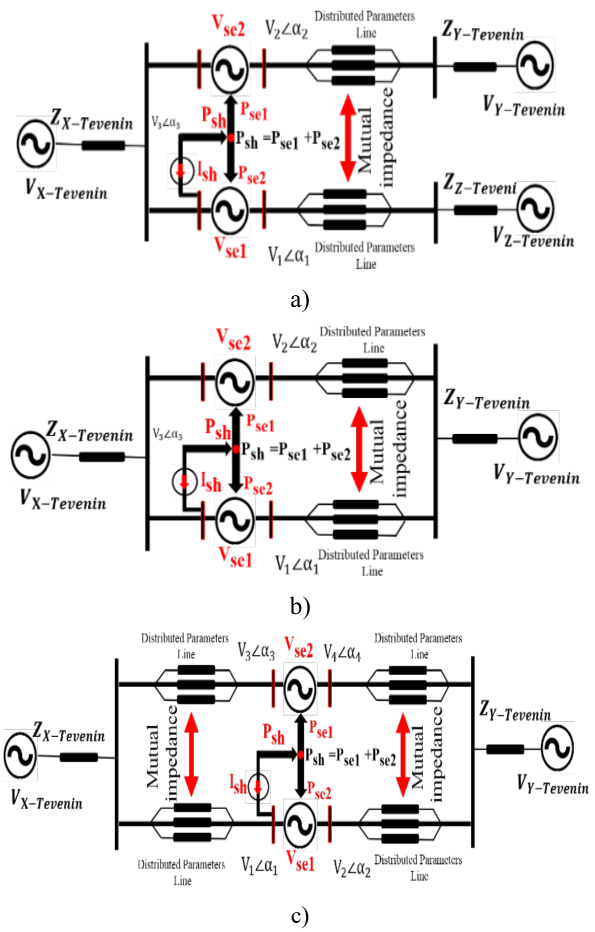

Fig. 1. Various topologies of GUPFC [9,17,29].

II. MATHEMATICAL MODELING OF ACTIVE AND REACTIVE POWER INJECTIONS BY THE GUPFC

For mathematical modeling of the power equations of GUPF, Thevenin and Norton equivalent circuits are used. Fig. 2 shows such circuits for a GUPFC installed on a double-circuit line.

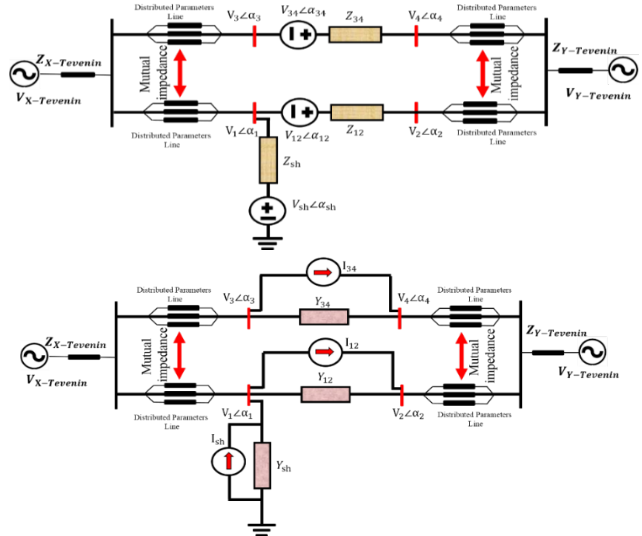

Fig. 2. (a) Thevenin equivalent circuit of a GUPFC, (b) Norton equivalent circuit of a GUPFC.

First, the current of the Norton equivalent circuit of GUPFC is calculated for the two series converters:

$$\vec{I}_{12} = \frac{\vec{V}_{12}}{Z_{12}} = \frac{\vec{V}_{12}}{R_{12}+jX_{12}} = \frac{V_{12}}{\sqrt{{R_{12}}^2+{X_{12}}^2}}\angle\alpha_{12} - tan^{-1}(\frac{X_{12}}{R_{12}}) \quad (1)$$

$$\vec{I}_{34} = \frac{\vec{V}_{34}}{Z_{34}} = \frac{\vec{V}_{34}}{R_{34}+jX_{34}} = \frac{V_{34}}{\sqrt{{R_{34}}^2+{X_{34}}^2}}\angle\alpha_{34} - tan^{-1}(\frac{X_{34}}{R_{34}}) \quad (2)$$

In the remaining, using the currents calculated in (1) and (2), we can find complex powers of buses based on power injection by series converters:

$$S_1 = \vec{V}_1(-\vec{I}_{12})^* \quad (3)$$

$$S_2 = \vec{V}_2(\vec{I}_{12})^* \quad (4)$$

$$S_3 = \vec{V}_3(-\vec{I}_{34})^* \quad (5)$$

$$S_4 = \vec{V}_4(\vec{I}_{34})^* \quad (6)$$

Replacing (1) in (3) and (4) and substituting (2) in (5) and (6) help separate (3) and (4) and express them in the form of active and reactive power equations as given in (7) to (10).

$$P_1 = \frac{V_1V_{12}}{|Z_{12}|^2}(X_{12}\,sin(\alpha_1-\alpha_{12}) - R_{12}\,sin(\alpha_1-\alpha_{12})) \quad (7\text{-a})$$

$$Q_1 = -\frac{V_1V_{12}}{|Z_{12}|^2}(X_{12}\,cos(\alpha_1-\alpha_{12}) + R_{12}\,sin(\alpha_1-\alpha_{12})) \quad (7\text{-b})$$

$$P_2 = \frac{V_2V_{12}}{|Z_{12}|^2}(\text{-}X_{12}\text{sin}(\alpha_2-\alpha_{12}) + R_{12}\text{sin}(\alpha_2-\alpha_{12})) \quad (8\text{-a})$$

$$Q_2 = \frac{V_2V_{12}}{|Z_{12}|^2}(X_{12}\text{cos}(\alpha_2\text{-}\alpha_{12}) + R_{12}\text{sin}(\alpha_2\text{-}\alpha_{12})) \quad (8\text{-b})$$

$$P_3 = \frac{V_3V_{34}}{|Z_{34}|^2}(X_{34}\,sin(\alpha_3-\alpha_{34}) - R_{34}\,sin(\alpha_3-\alpha_{34})) \quad (9\text{-a})$$

$$Q_3 = -\frac{V_3V_{34}}{|Z_{34}|^2}(X_{34}\text{cos}(\alpha_3-\alpha_{34}) + R_{34}\text{sin}(\alpha_3-\alpha_{34})) \quad (9\text{-b})$$

$$P_4 = \frac{V_4V_{34}}{|Z_{34}|^2}(\text{-}X_{34}\text{sin}(\alpha_4-\alpha_{34}) + R_{34}\text{sin}(\alpha_4-\alpha_{34})) \quad (10\text{-a})$$

$$Q_4 = \frac{V_4V_{34}}{|Z_{34}|^2}(X_{34}\,cos(\alpha_4-\alpha_{34}) + R_{34}\,sin(\alpha_4-\alpha_{34})) \quad (10\text{-b})$$

In addition, the complex power lost in $Z_{12}$and $Z_{34}$is defined according to (11).

$$S_{imp12} = \vec{V}_{12}(\vec{I}_{12})^* = \frac{V_{12}{}^2}{|Z_{12}|^2}(R_{12} + j\,X_{12}) \qquad (11\text{-a})$$

$$S_{imp34} = \vec{V}_{34}(\vec{I}_{34})^* = \frac{V_{34}{}^2}{|Z_{34}|^2}(R_{34} + j\,X_{34}) \qquad (11\text{-b})$$

The exchanged active power of the shunt compensator is calculated in Eq. (12) with regard to the active power balance condition of the GUPFC:

$$P_{\text{sh}} = -(P_{12}+P_{34}) \qquad (12)$$

where P_{12} and P_{34} are found from (13-a) and (13-b):

$$P_{12} = P_1 + P_2 - \frac{V_{12}{}^2}{|Z_{12}|^2}R_{12} \qquad (13\text{-a})$$

$$P_{34} = P_3 + P_4 - \frac{V_{34}{}^2}{|Z_{34}|^2}R_{34} \qquad (13\text{-b})$$

Moreover, to calculate reactive power of the shunt converter, the same calculations as used for finding reactive power of the series converter is utilized in this step. Finally, (14) helps obtain the reactive power of the shunt converter.

$$Q_{sh} = \frac{V_1 V_{\text{sh}}}{|Z_{\text{sh}}|^2}(X_{\text{sh}}\cos(\alpha_1\text{-}\alpha_{\text{sh}}) + R_{\text{sh}}\sin(\alpha_1\text{-}\alpha_{\text{sh}})) \qquad (14)$$

The complex powers injected to buses 1 to 4 are calculated using (15) to (18).

$$S_{1,GUPFC} = P_{1,GUPFC} + jQ_{1,GUPFC} = (P_1 + P_{sh}) + j(Q_1 + Q_{sh}) \qquad (15)$$

$$S_{2,GUPFC} = P_{2,GUPFC} + jQ_{2,GUPFC} = P_2 + jQ_2 \qquad (16)$$

$$S_{3,GUPFC} = P_{3,GUPFC} + jQ_{3,GUPFC} = P_3 + jQ_3 \qquad (17)$$

$$S_{4,GUPFC} = P_{4,GUPFC} + jQ_{4,GUPFC} = P_4 + jQ_4 \qquad (18)$$

As a result, the equivalent circuit of the double-circuit line compensated by GUPFC is represented in terms of complex powers injected to buses 1 to 4, as shown in Fig. 3.

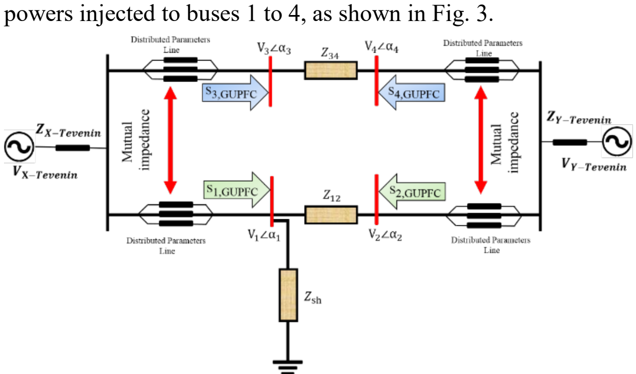

Fig. 3. Equivalent circuit of the double-circuit line compensated by GUPFC in terms of the injected complex power.

Once the steady-state model of GUPFC shown in Fig. 3 is extracted, a modification is applied to the Jacobian matrix and Newton-Raphson power flow equations based on the extracted model and power flow studies are carried out regarding the new model.

III. ACCURATE DESIGN OF THE GUPFC'S CONTROLLER SYSTEM

Referring to Fig. 4, the shunt converter controls the voltage of bus 1. This is performed through exchanging reactive power with the grid, i.e. via controlling the voltage of the DC-link. To realize this, at first, the proper angle ωt for synchronization of voltage and current is calculated using a phase-locked loop (PLL). Then, using the abc-dq0 transform, the three-phase voltage and current components fed to the shunt converter are transformed into active and reactive components. Next, the measured voltage of the bus connected to the shunt converter is instantaneously compared with the reference voltage and is injected to the PI controller so that the error signal is calculated to generate the reference reactive current. In the next step, a comparison is made between the reference reactive current calculated in the previous step and the reactive power of the shunt converter-connected bus. The difference between these two quantities is used as the input in the proportional-integral (PI) controller to generate the phase angle alpha of the inverter voltage. D-alpha is another component used in this converter which is generated by applying the average DC-link voltage values and the reactive power to the PI controller. The last component required for pulse generation by the firing pulse generation system is sigma. Put differently, Sigma is the same modulation index that impacts the amplitude of the converter's output voltage and its value is 172.5. Based on Fig. 1 (c), a GUPFC has two series converters with similar control systems. In this section, we investigate only one series converter knowing that the second one is identical. As per Fig. 5, the series converter is employed to automatically control power flow and adjust the current flowing from the transmission line. In this converter, similar to the shunt converter, the three-phase voltage measured from the bus is connected to one side of the series converter and the PLL calculates the proper angle, ωt, to synchronize voltage and current components. Then, the active and reactive components related to three-phase currents and voltages of the buses are calculated using the abc-dq0 transform. According to Fig. 5, the reference active and reactive currents can be found using the reference active power, the reference reactive power, the active voltage, and the reactive voltage. The calculated reference active and reactive currents are compared with their counterparts from the bus. After that, the error signal is fed to the proportional-integral-differential (PID) controller to calculate the reference active and reactive voltages. Next, a limiter controls the reference active and reactive voltages to prevent any possible system instability. Finally, the output of the real and imaginary voltage limiters is employed for calculating Alpha and Sigma. As the value of D_Alpha is obtained from the shunt converter, it is set zero in this section of the paper.

Coefficients ki and kp used in the series and shunt controllers of the GUPFC are calculated first by using the closed-loop Ziegler-Nichols method and then by trial and error to stabilize the test power system, achieve the balance among constraints, reach ideal operation conditions, and achieve power and power quality control.

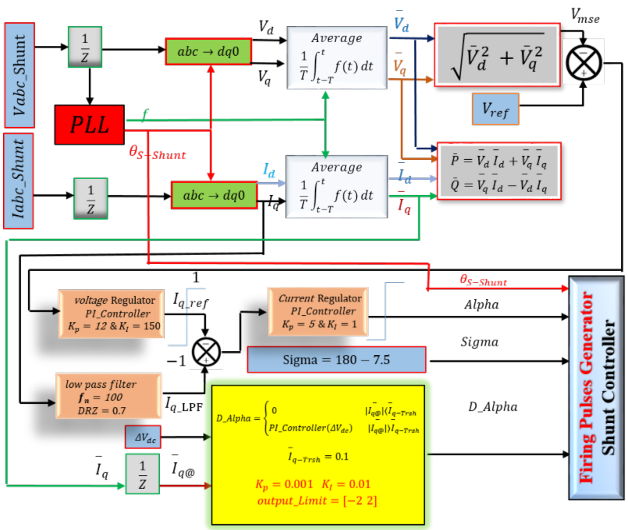

Fig. 4. Control system of the GUPFC's shunt converter.

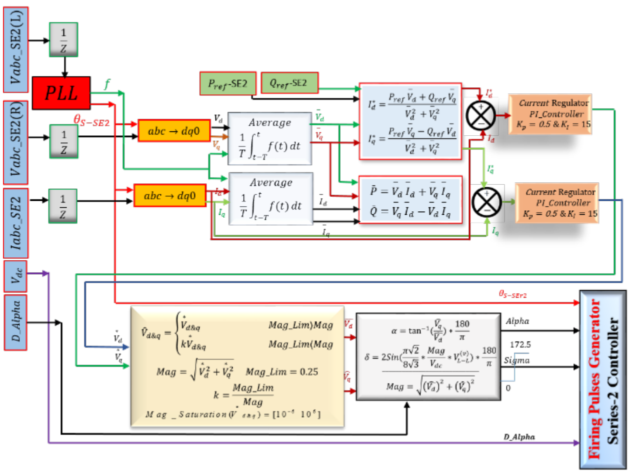

Fig. 5. Control system of the GUPFC's series converter.

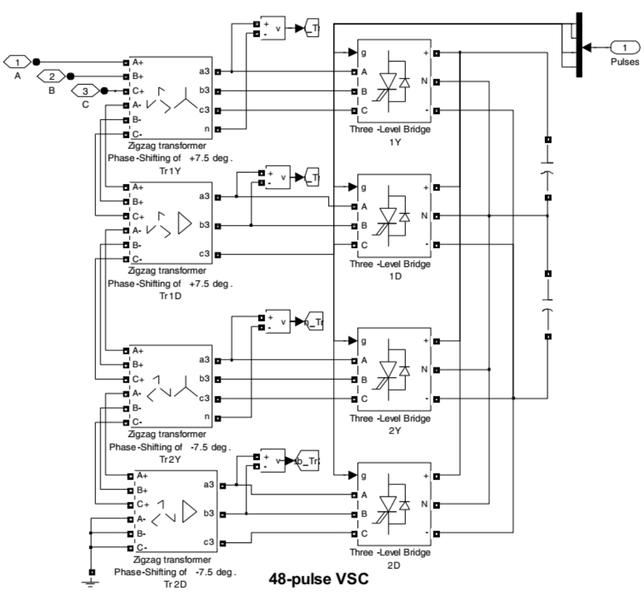

Fig. 6. Model of the GUPFC's voltage source inverter for the shunt converter.

IV. Modeling of the 48-Pulse VSC-Based GUPFC's Inverter

Fig. 6 illustrates the inverter system considered for this compensator, which is a 48-pulse GTO voltage source converter and includes four three-level inverters and four phase-shifting transformers. All inverters considered for this converter can generate a three-phase square semi-sine voltage waveform using the three-level GTO bridge inverter. The secondary winding of the phase-shifting transformer uses three phase sequences of the series voltage wave series with the primary winding to generate a virtually sine voltage waveform. The amplitude of the voltage waveform can adopt one of these values: the DC-link voltage, the minus value of the DC-link voltage, or zero. Period of the zero voltage at each quarter-cycle can be defined as a dead-time with a value between 0 to 90°.

A. Analysis of 48-pulse VSC inverters

Two 24-pulse converters with a 7.5° phase shift with respect to each other form a 48-pulse converter. Using symmetry, a -3.75° phase-shift on the transformer connections of one of the 24-pulse converters and a +3.75° phase-shift on the other transformer create the required 7.5° phase-shift. Hence, the firing pulse needs +3.75° and -3.75° phase-shifts, respectively. Four 12-pulse converters that are interconnected using four 12-pulse transformers with phase-shifting windings are used to form a 48-pulse converter. Thanks to its perfect performance and low harmonic rate on the AC side, this converter, needless of AC filters, can be used for applications that demand high power. The output voltage contains harmonic orders of $n = 48r \pm 1$, where $r = 0, 1, 2, \ldots$, meaning that harmonics of orders 47th, 49th, 95th, 97th, ... have amplitudes of 0.47, 0.49, 0.95, … per unit on the base of the fundamental component. Also on the DC side, the lower flowing harmonic current will be considered as the 48th order harmonic component. The phase-shifting pattern for individual 12-pulse converters will be as follows [30]:

- Analysis of the first converter

The output voltage produced by the first converter is:

$$v_{ab_{12}}(t)_1 = 2[V_{ab_1} sin(\omega t + 30°) + V_{ab_{11}} sin(11\omega t + 195°) + V_{ab_{13}} sin(13\omega t + 255°) + V_{ab_{23}} sin(23\omega t + 60°) + V_{ab25} sin(25\omega t + 120°) + \ldots] \quad (19)$$

- Analysis of the second converter

The output voltage produced by the second converter is:

$$v_{ab_{12}}(t)_2 = 2[V_{ab_1} sin(\omega t + 30°) + V_{ab_{11}} sin(11\omega t + 15°) + V_{ab_{13}} sin(13\omega t + 75°) + V_{ab_{23}} sin(23\omega t + 60°) + V_{ab25} sin(25\omega t + 120°) + \ldots] \quad (20)$$

- Analysis of the third converter

The output voltage produced by the third converter is:

$$v_{ab_{12}}(t)_3 = 2[V_{ab_1} sin(\omega t + 30°) + V_{ab_{11}} sin(11\omega t + 285°) + V_{ab_{13}} sin(13\omega t + 345°) + V_{ab_{23}} sin(23\omega t + 240°) +$$

$$V_{ab25}\,sin(25\omega t + 300°) + \ldots] \quad (21)$$

- Analysis of the fourth converter

The output voltage produced by the fourth converter is:

$$v_{ab_{12}}(t)_4 = 2[V_{ab_1}\,sin(\omega t + 30°) + V_{ab_{11}}\,sin(11\omega t + 105°) + V_{ab_{13}}\,sin(13\omega t + 165°) + V_{ab_{23}}\,sin(23\omega t + 240°) + V_{ab25}\,sin(25\omega t + 300°) + \ldots] \quad (22)$$

These four AC output voltages, given by (19) to (22), are added to the series connection of secondary windings of the transformers. The following expresses the 48-pulse output AC voltage:

$$v_{ab_{48}}(t) = v_{ab_{12}}(t)_1 + v_{ab_{12}}(t)_2 + v_{ab_{12}}(t)_3 + v_{ab_{12}}(t)_4 \quad (23)$$

$$v_{ab_{48}}(t) = 8[V_{ab_1}\,sin(\omega t + 30°) + V_{ab_{47}}\,sin(47\omega t + 150°) + V_{ab_{49}}\,sin(49\omega t + 210°) + V_{ab_{95}}\,sin(95\omega t + 330°) + V_{ab_{97}}\,sin(97\omega t + 30°) + \ldots] \quad (24)$$

The general representation for the 12-pulse AC output voltage is:

$$v_{ab_{12}}(t) = 2\sum_{n=1}^{\infty} V_{ab_n}\,sin(n\omega t + 30°n) \quad \forall n = 12r \pm 1, r = 0,1,2,\ldots \quad (25)$$

Applying an 11.25° phase-shift to (25) using a PST:

$$v_{ab_{12}}(t) = 2\sum_{n=1}^{\infty} V_{ab_n}\,sin(n\omega t + 30°n + 11/25°i) \quad \forall n = 12r \pm 1, r = 0,1,2,\ldots \quad (26)$$

In the above equation, i = 1 for the positive-sequence harmonics is the *abc* sequence and i = −1 for negative-sequence harmonics is the *cba* sequence. The line-to-neutral voltage of phase *a* is as follows.

Now, by lagging the firing pulse by 11.25°, we have:

$$v_{ab_{12}}(t) = 2\sum_{n=1}^{\infty} V_{ab_n}\,sin(n\omega t + 18/75°n + 11/25°i) \quad \forall n = 12r \pm 1, r = 0,1,2,\ldots \quad (27)$$

As a result, the general term for the line-to-line voltage of a 48-pulse converter is given by (28):

$$v_{ab_{48}}(t) = 8\sum_{n=1}^{\infty} V_{ab_n}\,sin(n\omega t + 18/75°n + 11/25°i) \quad \forall n = 48r \pm 1, r = 0,1,2,\ldots \quad (28)$$

The line-to-neutral voltage is:

$$v_{an_{48}}(t) = \frac{8}{\sqrt{3}}[V_{ab_1}\,sin(\omega t) - V_{ab_{47}}\,sin(47\omega t) - V_{ab_{49}}\,sin(49\omega t) + V_{ab_{95}}\,sin(95\omega t) + V_{ab_{97}}\,sin(97\omega t) + \ldots] \quad (29)$$

Rewriting (29) gives:

$$v_{an_{48}}(t) = \frac{8}{\sqrt{3}}\sum_{n=1}^{\infty} V_{ab_n}\,sin(n\omega t + 18/75°n - 18/75°i) \quad \forall n = 48r \pm 1, r = 0,1,2,\ldots \quad (30)$$

Voltages $v_{cn_{48}}(t), v_{bn_{48}}(t)$ have similar patterns except with 120° and 240° phase-shift with respect to $v_{an_{48}}(t)$.

B. Modeling the 48-pulse generator mathematical function

Various methods have so far been introduced for modulations in the power electronics industry, the most popular one of which is pulse width modulation (PWM). PWM methods are characterized by fixed-amplitude pulses where the pulse widths are modulated for controlling the modulator output voltage and reducing its harmonic content. Different methods of PWM include single-pulse modulation, multi-pulse modulation, and sine modulation, each of which differs from others in terms of the harmonic content in the output voltage. For PWM implementation, a digital IC such as a microcontroller or timer 555 can be used. The generated signal is a train of pulses forming a square waveform. In the related literature, various schemes have been introduced for the design of PWM's switching algorithm. The most well-known scheme is a design that compares wave and triangular waveforms. Fig. 7 shows a new mathematical function for describing pulse generation operations in a 48-pulse VSC. There are four switches at each leg of the inverter, with an overall number of 12 switches embedded for each inverter.

As mentioned in the control system design of the GUPFC, the inputs to the pulse generator function are δ, D_Alpha, Alpha, and$\omega t = \theta$. Function mod is used with angular values of $2\pi$and $\beta$for pulse generation. Angle β is influenced by half of the switch-off duration of switch Q1 in the half cycle ($(\pi - \delta)/2$), D_Alpha, $\omega t = \theta$, and the angle of the beginning of each half-cycle, which can be zero orπ. Then the output of the mod function is fed to the step function with a magnitude of one, the output of which is zero or one. Next, the values produced by step functions are sent as switching signals of GTOs. Finally, the operation of the two sets of switches (Q1 and Q3) and (Q2 and Q4) at each leg reverse each other. In this modeling, with no need for complex comparators of various waveforms and complicated pulse generation hardware and using only one simple mathematical function, the signals required for switching GTOs on and off are generated.

V. SOFTWARE SIMULATIONS AND RESULTS

Fig. 1 (c) provides the system under study in this paper. The system consists of one coupled double-circuit line with characteristics of 400 km, 230 kV, and 60 Hz representing the distributed model. Both ends of the system are modeled using a Thevenin equivalent circuit. The Appendix provides the detailed data related to the simulated system. The GUPFC employed in this study is placed in the middle of the coupled double-circuit line and its main task is to control active and reactive power flows between the two lines. The shunt converter considered for the GUPFC has a rated power of 200 MVA so that it can supply the power required by each series converter up to 100 MVA.

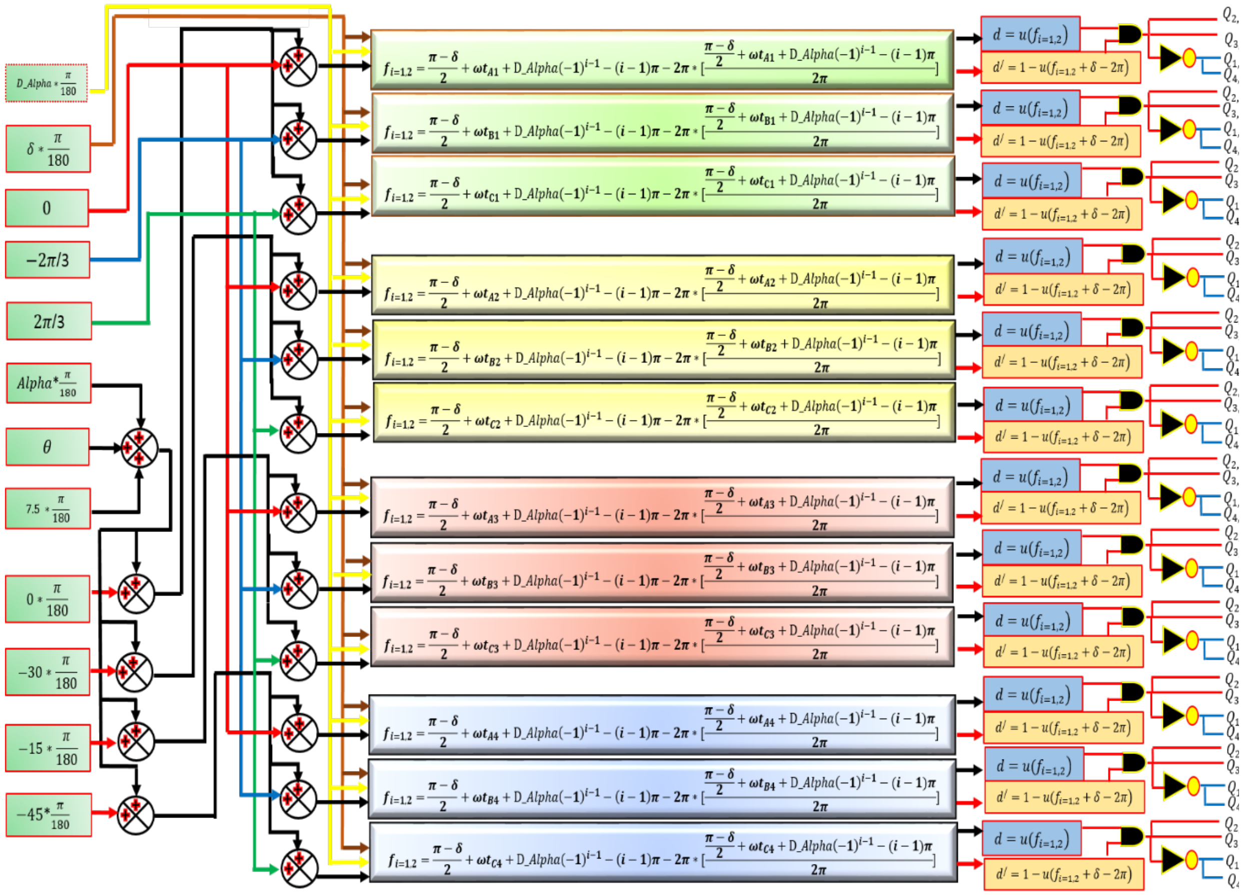

Fig. 7. New mathematical function for generating 48 pulses.

A. Simulation results for the output of the GUPFC's shunt converter

Fig. 8 (a) illustrates the diagram of phase A's secondary voltage for a shunt converter during one cycle. As is seen, the output voltage is a pure 48-pulse signal. Also, Fig. 8 (b) shows the FFT diagram of the output voltage and its THD value (= 4.35%). As expected, the values of the 47th and 49th harmonics are the greatest after the fundamental harmonic value.

Moreover, Fig. 9 shows the voltage of the secondary side and voltage and current of the primary side of the transformer connected to the shunt converter.

Fig. 10 illustrates the active and reactive powers measured at the shunt converter bus. The depicted powers in these diagrams are calculated using three-phase currents and voltages measured from the bus connected to the shunt converter. As is clear, the active and reactive power exchanges between the shunt converter and the grid are positive and negative, respectively. This means that the shunt converter receives active power from the grid to supply the internal loss power and charge the DC-link capacitor, and injects reactive power to the line to maintain the voltage of the bus connected to the shunt converter.

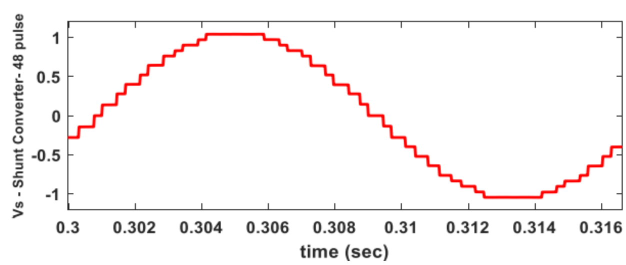

(a)

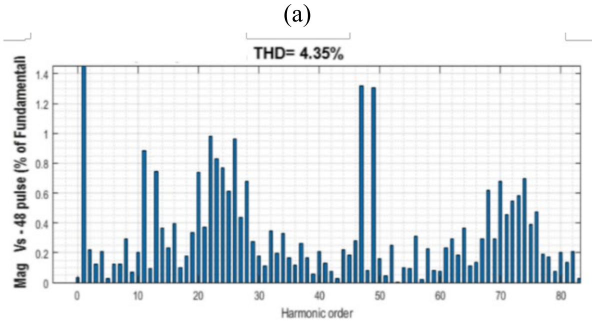

(b)

Fig. 8 .a) The output voltage of the 48-pulse VSC-based inverter for the parallel converter within a single periodic cycle .b) Harmonic analysis diagram of the output voltage of the 48-pulse VSC-based inverter for the parallel converter within a

single periodic cycle.

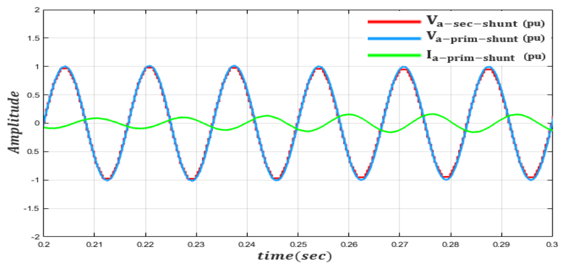

Fig. 9. The voltage of the secondary side and voltage and current of the primary side of the transformer connected to the shunt converter.

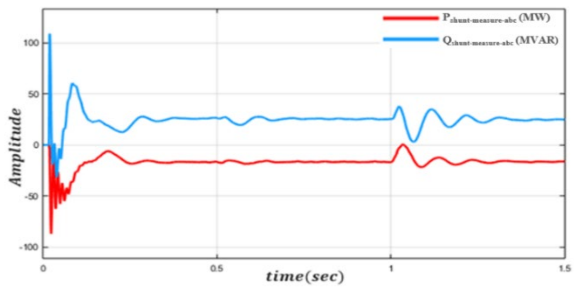

Fig. 10. The active and reactive power diagram for the shunt converter.

Fig. 11 shows the voltage of the bus connected to the shunt converter. Based on the control constraints of the GUPFC, a task of GUPFC is to control the voltage of the bus. In other words, the shunt converter controls the voltage of the middle point of the line. As from Fig. 11 illustrates, the shunt converter suitably maintains the voltage of the middle point of the line close to the reference voltage.

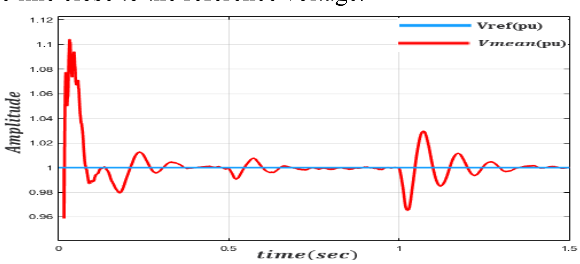

Fig. 11. Diagram of the voltage of the bus connected to the shunt converter.

As is observed in Figs. 10 and 11, an oscillation is seen in the active and reactive power and shunt converter bus voltage 1 s after the start of the simulation. The reason behind this is the great variations in the value of the reference active power at both series converters (converter 1 and converter 2). This change in the power for series converter 1 from a value of 1 to 1.2 and for series converter 2 from 0.9 to -1.2 within 1 s causes changes in the operating mode of the GUPFC besides creating oscillation and transients in the active and reactive powers and voltage of the shunt converter because of satisfying power flow and voltage balance constraints. The established transient and oscillatory state, when the operating mode of the GUPFC changes is utmost two cycles, as shown in Figs. 10 and 11. It is rapidly damped and the system returns to the steady state.

Fig. 12 presents the voltage of the DC-link connected to three converters. As is observed, the voltage magnitude is maintained almost fixed. As discussed in the section related to the design of the control system, the main aim of controlling D_Alpha is to adjust and balance the capacitor voltages of the DC-link common among all converters. According to Fig. 12, the control of D_Alpha in the control system is performed acceptably.

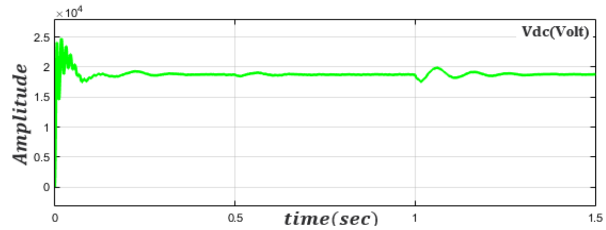

Fig. 12. Voltage of the DC-link common among GUPFC's converters.

B. Simulation results for the output of the GUPFC's series converter 1

Figs. 13 and 14 present the results of active and reactive powers calculated by the control system and the dq reference frame for series converter 1. In these diagrams, active and reactive powers are calculated using the block diagrams provided in Fig. 5.

It is clearly seen that the values of reference active power for the series converter 1 during the time intervals of 0-0.5 s, 0.5-1 s, and 1-1.5 are 1 p.u., 1.1 p.u., and 1.2 p.u., respectively. Additionally, the reference reactive power for the series converter 1 during the whole period is considered -0.3 p.u. As seen in Figs. 13 and 14, series converter 1 is successful in controlling the active and reactive powers.

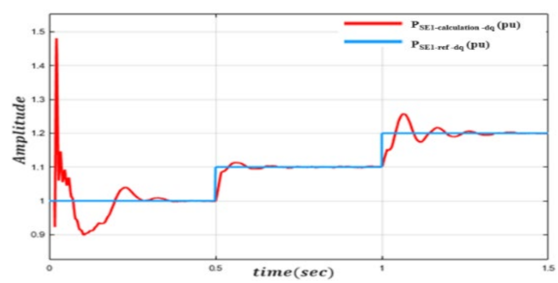

Fig. 13. Active power diagram of series converter 1.

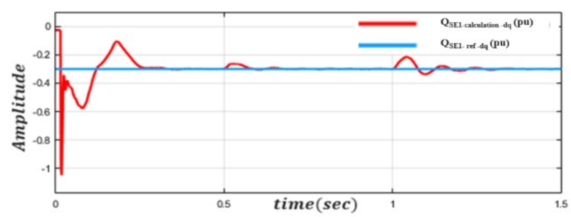

Fig. 14. Reactive power diagram of series converter 1.

C. Simulation results for the output of the GUPFC's series converter 2

Figs. 15 and 16 present the results of active and reactive powers calculated by the control system and the dq reference frame for series converter 2. In these diagrams, active and reactive powers are calculated using the block diagrams provided in Fig. 5.

It is clearly seen that the values of reference active power for the series converter 2 during the time intervals of 0-0.5 s, 0.5-1 s, and 1-1.5 are 1 p.u., 0.9 p.u., and 1.2 p.u., respectively. Moreover, the reference reactive power for the series converter 2 during the entire period is considered −0.4 p.u. As seen in Figs. 15 and 16, series converter 2 is successful in controlling the active and reactive powers.

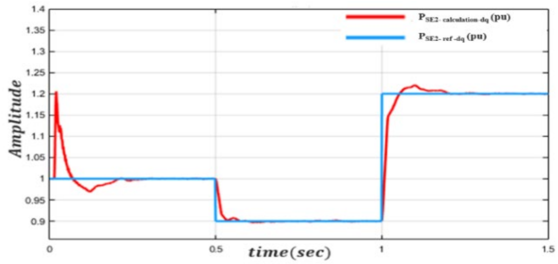

Fig. 15. Active power diagram of series converter 2.

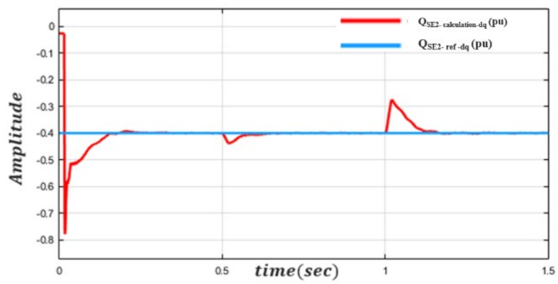

Fig. 16. Reactive power diagram of series converter 2.

D. Simulation results for the active power balance of the GUPFC's three converters

Figs. 17 and 18 present active power diagrams calculated by three-phase voltage and currents measured from buses located at the two ends of series converters 1 and 2. Fig. 19 shows the active power diagram of the shunt converter (Fig. 12) and the sum of active powers of series converters 1 and 2 (Figs. 17 and 18). As is seen from Fig. 19, the active power balance equation for the GUPFC is met.

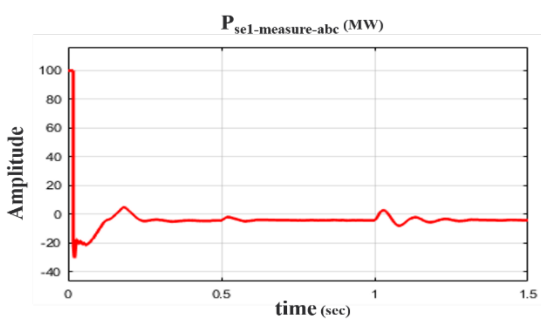

Fig. 17. The measured active power from the transformer of series converter 1.

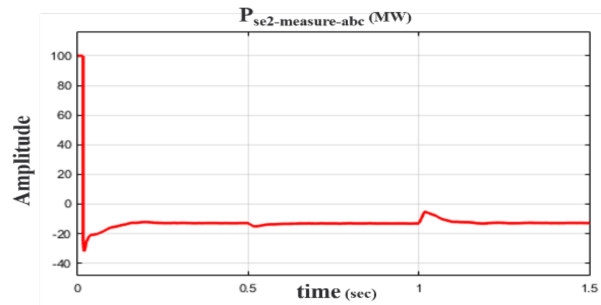

Fig. 18. The measured active power from the transformer of series converter 2.

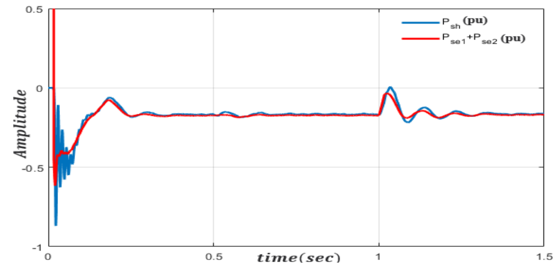

Fig. 19. Active power of the shunt converter along with the sum of active powers of the GUPFC's two series converters.

VI. Conclusion

This paper presents the accurate modeling of power injection by a GUPFC placed in the middle of a double-circuit line for the first time. The proposed model is very efficient in static studies such as the power flow. Moreover, accurate modeling of the control system and inverter of the 48-pulse VSC-based GUPFC, specific to dynamic studies, is provided. The control circuit utilized in the current study relies on the *dq* theory. A new mathematical function that operates based on the PWM theory is presented for the pulse generation system to turn on/off the GTOs of the GUPFC's inverter, where 48 pulses required for turning the GTOs on/off are produced. The suggested technique is robust against noise and can be implemented in various programmable ICs. Furthermore, according to the simulation results, the designed GUPFC can successfully satisfy control constraints and is very effective in terms of improving power quality and reducing harmonic levels.

Appendix

The detailed data of the double-circuit transmission line, Thevenin equivalent circuit of both sides of the line, the control system of the GUPFC, power electronic inverter of the GUPFC, and transformers placed between the GUPFC and the transmission line are listed in Table 1.

Table I

Detailed data of the test system.

Line and Source data					
Parameter	Line		Source1		Source 2
V	230 kV		230 ∠ -20.8° kV		230 ∠ 9.2° kV
X/R	--------------		10		10
r_1	0.02546 Ohm/km		0.8716 Ohm		1.7431 Ohm
r_0	0.3864 Ohm/km		1.3074 Ohm		2.6147 Ohm
r_{0m}	0.1732 Ohm/km		0 Ohm		0 Ohm
l_1	0.9337e-3 H/km		0.02576 H		0.05154 H
l_0	4.1264e-3 H/km		0.00648 H		0.0129 H
l_{0m}	2.01264e-3 H/km		0 H		0 H
c_1	12.74e-9 F/km		info		info
c_0	7.751e-9 F/km		info		info
c_{0m}	0.575e-9 F/km		info		info
GUPFC data					
Control system					
Shunt Converter			Series Converter		
Nominal power (VA)	200e6		Nominal power (VA)		100e6
Voltage regulator	Kp	12	Current regulator1	Kp	0.5
	K_I	150		K_I	15
Current regulator	Kp	5	Current regulator2	Kp	0.5
	K_I	1		K_I	15
Low pass filter	f_n	100	Mag_Limit		0.25
	DRZ	0.7			
D_Alpha Blok	Kp	0.001	D_Alpha		0
	K_I	0.01			
Three level bridge					
Snubber resistance Rs (ohm)			1e5		
Snubber capacitance Cs (f)			info		
Internal resistance Ron (ohm)			1e-4		
Power electronic device			GTO		
Zigzag transformer phase shifting					
Nominal power (VA)			25e6		
Nominal frequency (Hz)			60		
Primary nominal voltage (Volt-rms)			12.5e3		
Secondary nom voltage phase shift (Volt-rms)			12.5e3		
Resistance winding 1 zig-zig (pu)			0.05/30		
Inductance winding 1 zig-zig (pu)			0.05		
Resistance winding 2 zig-zig (pu)			0.05/30		
Inductance winding 2 zig-zig (pu)			0.05		
Resistance winding 3 zig-zig (pu)			0.05/30		
Inductance winding 3 zig-zig (pu)			0.05		

REFERENCES

[1] A.Rasulkhani and A.Taheri , “A New Multilevel Inverter Topology with Component Count Reduction”, International Journal of Industrial Electronics, Control and Optimization, Vol. 2, No. 4, pp. 355-364, Oct .2019.

[2] F. Sedaghati , S. H.Latifi Majareh and H. Dolati , “A Single-Phase Extendable Topology for Multilevel Inverters”, International Journal of Industrial Electronics, Control and Optimization, Vol. 2, No. 3, pp. 207-220, July .2019.

[3] A. Masood, Qadeer-ul-Hassan, A. Mahmood, “Flexible AC Transmission System Controllers: A Review”, In Proc. Conference: IMTIC 2015’ 02, 2015.

[4] B. Fardanesh, B. Shperling, E. Uzunovic, and S. Zelingher, “Multi-Converter FACTS Devices: The Generalized Unified Power Flow Controller (GUPFC)”, 2000 Power Engineering Society Summer Meeting, IEEE, Seattle, USA, July 16-20, 2000.

[5] R.L Vasquez Arnez, and L. Cera Zanetta Jr., “Operational Analysis and Limitations of the GIPFC (Generalized Interline Power Flow Controller),” Power Tech, June 2005, pp. 1–6.

[6] S. Shojaeian, J. Soltani and G. Arab Markadeh, “Damping of Low Frequency Oscillations of Multi-Machine Multi-UPFC Power Systems, Based on Adaptive Input-Output Feedback Linearization Control,”IEEE Transactions on Power Systems, vol. 27, no. 4, pp. 1831-1840, Nov. 2012.

[7] L. Sun, S. Mei, Q. Lu, and J. Ma, “Application of GUPFC in China's Sichuan Power Grid-Modeling, Control Strategy and Case Study” 2003 IEEE Power Engineering Society General Meeting, IEEE ,Toronto, Canada, July 13-17, 2003.

[8] C. Suresh and S. Raju, “Mathematical Modeling and Analysis of a Generalized Unified Power Flow Controller with Device Rating Methodology”, International Journal on Electrical Engineering and Informatics, Vol. 7, no. 1, pp. 59-78, March 2015.

[9] X. Zhang, E. Handschin, and M. Yao, “Modeling of the Generalized Unified Power Flow Controller (GUPFC) in a Nonlinear Interior Point OPF”, IEEE Transactions on Power Systems, vol. 16, no. 3, pp. 367-373, August 2001.

[10] A. Abiola, A. Ayorinde, and O. Oladosu, “Power Flow Analysis of Longitudinal Electrical Power System Incorporating Generalized Unified Power Flow Controller (GUPFC)”, American Journal of Electrical Power and Energy Systems, Vol. 5, no. 6, pp. 59-66, October 2016.

[11] J. Singh, S. Singh and V. Pant, “Modeling of Generalized Unified Power Flow Controller For Suitable Location And Power Flow Control”, Iranian Journal Of Electrical And Computer Engineering, Vol. 3, no. 2, pp.103-110, November 2004.

[12] S. Kamel, F. Jurado, Z. Chen, M. AbdelAkher, and M. Ebeed, “Developed Generalized Unified Power Flow Controller Model in the Newton–Raphson Power-Flow Analysis Using Combined Mismatches Method”, IET Generation, Transmission & Distribution, Vol. 10, no. 9, pp. 2177-2184, June 2016.

[13] M. Ebeed, S. Kamel, and F. Jurado, “Constraints violation handling of GUPFC in Newton-Raphson power flow”, Electric Power Components and Systems, Vol. 45, no. 9, pp. 925-936, May 2017.

[14] X. Zhang, “Robust Modeling of the Interline Power Flow Controller and the Generalized Unified Power Flow Controller with Small Impedances in Power Flow Analysis”, Electrical Engineering, Vol. 89, no. 1, pp. 1-9, December 2006.

[15] A.N.Shirazi, B.Mozafari and S.Soleymani , “Transient stability improvement with neuro-fuzzy control of GUPFC in multi machine system” , Journal of Intelligent & Fuzzy Systems, Vol. 37, no. 1, pp. 611-623, July 2019.

[16] B. Vyakaranam and F. Villaseca, “Dynamic Modeling and Analysis of Generalized Unified Power Flow Controller”, Electric Power Systems Research, Vol. 106, no.1, pp. 1-11, January 2014.

[17] R.Lubis, S.Hadi and Tumiran, “Dynamic simulation of GUPFC in Multi-Machine Power System”, International

Journal of Electrical & Computer Sciences,Vol. 12, no. 3, pp.75-85, June 2012.
[18] J. Singh, P. Tripathy, S. Singh, and S. Srivastava, “Development of a Fuzzy Rule-Based Generalized Unified Power Flow Controller”, European Transactions on Electrical Power, Vol. 19, no. 5, pp. 702-717, July 2009.
[19] V. Azbe and R. Mihalic, “Damping of Power-System Oscillations with the Application of a GUPFC”, 2009 IEEE Bucharest Power Tech, IEEE, Bucharest, Romania ,28 June-2 July ,2009.
[20] R. Thirumalaivasan, N. Prabhu, M. Janaki, and D. Kothari, “Analysis of Sub Synchronous Resonance with Generalized Unified Power Flow Controller”, International Journal of Electrical Power & Energy Systems, Vol. 53, no. 2, pp. 623-631, December 2013.
[21] J. Singh, S. Singh, and S. Srivastava, “A Sensitivity-Based Approach for Optimal Location of Multi-Converter Unified Power Flow Controller Considering its Impact on Generation and Wheeling Costs”, International Journal of Energy Technology and Policy, Vol. 4, no. 3, pp. 394-409, February 2006.
[22] C. Suresh, S. Sivanagaraju, and J. Rao, “Multi-Area Multi-Fuel Economic–Emission Dispatch Using a Generalized Unified Power Flow Controller Under Practical Constraints”, Arabian Journal for Science and Engineering, Vol. 40, no. 2, pp. 531-549, December 2015.
[23] C. Suresh, S. Sivanagaraju, and P. Reddy, “Economic Concerns in Optimal Power Dispatch in the Presence of a Generalized Unified Power Flow Controller under Practical Constraints”, Journal of The Institution of Engineers (India), Vol. 97, no. 3, pp. 319-331, May 2015.
[24] X. Zhang and E. Handschin, “Transfer Capability Computation of Power Systems With Comprehensive Modelling of FACTS Controllers”, 14th Power System Computation Conference (PSCC), Sevilla, Spain, June 24-28, 2002.
[25] C. Suresh and S. Sivanagaraju, “Increasing the Load Ability of Power System Through Optimal Placement of GUPFC Using UDTPSO”, Journal of Electrical Systems, Vol .11, no. 1, pp. 61-75, February 2015.
[26] A. Kumar and C. Sekhar, “Congestion Management-Based on Demand Management and impact of GUPFC”, 2012 International Conference on Power, Signals, Controls and Computation, IEEE ,Thrissur, Kerala, India, January 3-6, 2012.
[27] D. Valle and P. Araujo, “The Influence of GUPFC FACTS Device on Small Signal Stability of the Electrical Power Systems”, International Journal of Electrical Power & Energy Systems, Vol. 65, no. 2, pp. 299-306, February 2015.
[28] S. Ra, T. Prakashb, and L. Sureshc, “Two Neuron Model for Voltage Flicker Mitigation Using Generalized Unified Power Flow Controller”, International Journal of Current Engineering and Technology ,Vol.2, no.2, pp 244-250, June 2012.
[29] M. Khederzadeh and A. Ghorbani, “Impact of VSC-Based Multiline FACTS controllers on Distance Protection of Transmission Lines”, IEEE Transactions on Power Delivery ,Vol. 27, no. 1, pp. 32-39, June 2012.
[30] Sahoo, Ashwin Kumar, K. Murugesan, and T. Thygarajan. "Modeling and simulation of 48-pulse VSC based STATCOM using simulink’s power system blockset." 2006 India International Conference on Power Electronics. IEEE, 2006.

Mahyar Abasi was born in 1989 in Malayer, Iran. He received the B.Sc. degree in electrical power engineering from the Islamic Azad University of Arak Branch, Arak, Iran, in 2012, and the M.Sc. degree in electrical power engineering from Shahid Chamran University of Ahvaz, Ahvaz, Iran, in 2015. He is currently working towards his PhD degree in the Department of Electrical Engineering, Shahid Chamran University of Ahvaz, Ahvaz, Iran. His research interests are fault location, power system protection, FACTS devices, and power quality assessment.

Mahmood Joorabian was born in Shooshtar, Iran, in 1961. He received his B.E.E degree from University of New Haven, CT, USA, M.Sc. degree in Electrical Power Engineering from Rensselaer Polytechnic Institute, NY, USA and Ph.D. degree in Electrical Engineering from University of Bath, Bath, UK in 1983, 1985 and 1996, respectively. He has been with the Department of Electrical Engineering at Shahid Chamran University of Ahvaz as Senior Lecturer (1985), Assistant Professor (1996), Associate Professor (2004) and Professor (2009). His main research interests are faut location, FACTS devices , power system protection, applications of intelligence techniquein power systems, operation and planning of deregulated power system, load and energy management, renewable energy, microgrid, smart grids, and power quality assessment.

Alireza Saffarian was born in 1981 in Ahvaz, Iran. He received the B.Sc. and M.Sc. degrees in electrical engineering from Amirkabir University of Technology, Tehran, Iran, in 2003 and 2005, respectively, and the Ph.D. degree from University of Tehran, Tehran, Iran, in 2011. Currently, he is an Assistant Professor with the Department of Electrical Engineering, Shahid Chamran University of Ahvaz, Ahvaz, Iran. His research interests include power system protection, power system stability, and power quality assessment.

Seyyed Ghodratollah Seifossadat was born in Ahvaz, Iran, on August 28, 1963 and received the B.Sc. degree in electrical engineering from the Iran University of Science and Technology (IUST), Tehran, in 1989 and the M.Sc. degree in electrical engineering from the Ferdosi University of Mashhad, Mashhad, Iran, in 1992 and the Ph.D. degree from IUST in 2006. Currently, he is a Professor with the Department of Electrical Engineering, Shahid Chamran University of Ahvaz, Iran, where he has been since 1992. His research interests are power system protection, fault location, power electronics, electric machinery, FACTS devices, and power quality assessment.

IECO

This page intentionally left blank.

International Journal of Industrial Electronics, Control and Optimization © 2020 IECO
Vol. 3, No. 4, pp. 459-468, Sep (2020)

Improving Quality of Movement in a Linear Switched Reluctance Motor Using a Fuzzy Logic System

Allahverdi Azadrou[1], Siamak Masoudi [2†], Reza Ghanizadeh[3] and Payam Alemi[4]

Department of Electrical Engineering, Urmia Branch, Islamic Azad University, Urmia, Iran.

ABSTRACT

This work deals with minimizing fluctuations of propulsion force and improving the motion quality in a linear switched reluctance motor. In order to minimize the jerks in the moving part of the motor, a new profile has been used to generate an appropriate reference speed profile. The results indicate that at speed 0.5 m/s, the motor reaches its command speed at the proposed time while, using conventional speed profile it takes almost 1.4 times the desired time. In order to control the speed and incease the motion quality, a simple fuzzy logic system has been used which is able to overcome the uncertainties problem in nonlinear systems. The fuzzy control system can regulate the motor performance so that it tracks the reference speed with minimum error and fluctuation. To illustrate the performance of the fuzzy method, a conventional PI method along with a model reference adaptive control (MRAC) strategy have been applied to the motor and the obtained results for three control methods have been compared. Speed overshoot using conventional PI method is about 20 percent of the final speed while this is about 6 percent for fuzzy and MRAC methods. The system is designed and its efficiency is shown through simulation and experimental tests in different performance situations . The obtained results confirm that the fuzzy strategy outperforms other methods.

Article Info

Keywords:
Force Ripple, Fuzzy Logic System, Linear Motor, Speed Control, Switched Reluctance Motor.

Article History:
Received2020-01-06
Accepted 2020-04-18

I. INTRODUCTION

Switched reluctance motors (SRMs) have very interesting characteristics over electrical motors. They are very robust, low price, simple in structure, and fault tolerant with fewer thermal problems compared to other electrical motors. The linear type of these motors has all the above-mentioned benefits along with the ability of direct motion. They do not need any mechanical rotational to linear motion converters making them more suitable in special direct motion applications such as elevators, transport systems, etc. Different types of linear switched reluctance motors (LSRMs) have been presented by researchers previously which can be used in different industries [1]. These motors have inherently nonlinear dynamics with some uncertainties cause to be complicated their analysis and control.

Generally, these motors generate a force with high ripples and so, low quality which again complicates their application. Various speed regulation strategies have been suggested by researchers to improve the motor performance and to solve the torque (or force) fluctuation problem in SRMs. Generated force in LSRMs can be controlled by an appropriate force distribution function (FDF) [2]–[4]. In order to minimize the torque ripple in a rotational switched reluctance motor, an advanced torque sharing function has been proposed in [5] which has used combination of the genetic algorithm and fuzzy PSO methods. An appropriate FDF has been presented in [6] which could noticeably reduce the force fluctuations in a LSRM. We know that considerable force fluctuation can occur

† Siamak Masoudi: s.masoudi@tabrizu.ac.ir
Tel: +98-9141246770, Fax: +98-9141246770, Islamic Azad University. Department of Electrical Engineering, Urmia Branch, Islamic Azad University, Urmia, Iran.

in the phase commutation period. In recent papers, many efforts have been made to decrease the force (or torque) pulsations. In conventional control methods, it is possible to optimize the conduction angles in order to reach a flat force, but it has been shown that under higher loading conditions, noticeable force fluctuation is unavoidable [7]. Some interesting techniques for force (or torque) fluctuation reduction have been presented by researchers in recent years. In [8], dynamic equations of a SRM have been shown and the generated torque has been studied considering the contribution of the mutual inductances. Another current profile analysis has been done in [9] which cause to minimization of the torque pulsation over a wide range of speeds. Other current profile-based optimization methods have been suggested in [10]. In the methods, the current profile has been optimized to produce less ripple in the output current and torque. Destructive interference is the other method which has been used in [11] for improving the torque fluctuation in a SRM. Optimization of the SRM is another method to lower the force or torque pulsation. We have used a seeker optimization algorithm to optimize the LSRM construction in [12]. The obtained results indicated that the optimized structure generates better force with fewer ripples. In [13] and [14], new structures of SRMs have been proposed generating a torque with significantly low ripples. It is obvious that the fluctuated force will affect the speed of the translator; consequently, the actual speed would be different from the command value leading to disturbance in the LSRM performance. Accordingly, an appropriate speed controller can regulate the motor performance accurately. Fuzzy control is a practical alternative for a variety of challenging control applications as it provides a convenient method for constructing nonlinear controllers via heuristic information [15] – [18]. An interesting approach to the analysis of continuous time Takagi-Sugeno fuzzy systems using fuzzy Lyapunov functions has been presented in [16] which is independent of normalized fuzzy weighting functions. Some special systems such as nontriangular structural system have some problems complicating their analysis. In [17], an adaptive fuzzy switched control strategy has been investigated which solved the system problems. Another combined fuzzy control strategy has been proposed for a nonlinear system in [18]. Using Nussbaum function method, an adaptive output feedback control strategy has baan proposed in [19] which is appropriate for nonlinear systems with output constraints. Fuzzy control strategy has the advantage of independence of the system parameters; thus, the method can be used for systems with unknown variables [20] and [21].

In this work, we have been used a fuzzy control strategy to smooth the output actual speed of the moving part of the LSRM. The controller has been implemented to the motor as a speed regulator. The proposed linear motor structure and its dynamic equations have been discussed in section 2. In section 3, block diagram of the control system along with the fuzzy control method have been investigated. Also, a new speed profile to reach a smooth motion quality has been introduced in section 3. In order to have a comparison between the proposed control methods, a new model reference adaptive control strategy has been demonstrated in section 4 and finally, simulation results and experimental results for three control strategies have been demonstrated and discussed in section 5 and 6.

II. PROPOSED SYSTEM

A. The linear motor and its characteristics

Control of a four-phase double-sided linear switched reluctance motor (DLSRM) is proposed in this work. The motor has a moving part with eight winding sets located on it along with two stators on both sides of it [6]. Because of two stators located on both sides of a translator, two same electromagnetic forces are applied to the common translator between them. So, this double sided construction yields high propulsion force density thus making the motor appropriate for applications requiring strong drivers. It is obvious that DLSRMs inherently have complete nonlinear characteristics complicating their performance control over electrical motors. Achieving an appropriate model for the DLSRM with a complete and accurate data of the motor inductance and force is very useful in the motor analysis. This can be done by a precise 3-D finite element analysis. The obtained data of the selected DLSRM are shown in Fig. 1.

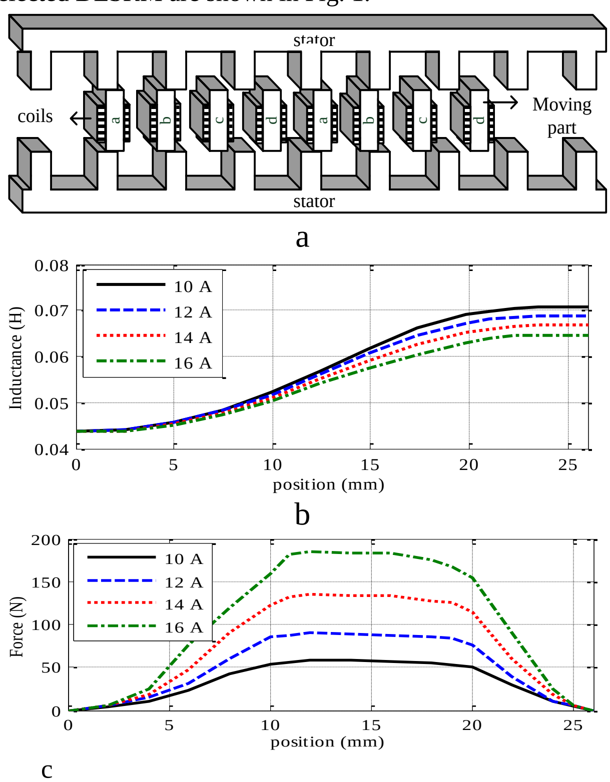

Fig. 1. Selected DLSRM and data from FEM, (a) Selected DLSRM, (b) inductance, (c) force

The dimensions of the proposed DLSRM are shown in

Table 1.

TABLE I
SELECTED DLSRM DIMENSIONS

Parameter	Value	Unit
Air gap length	2	mm
Stator pole width	21	mm
Stator slot width	31	mm
Stator pole height	30	mm
Translator pole width	13	Mm
Translator pole height	26	Mm
Translator height	220	Mm
Turns per phase	200	Turn
Rated current	10	A
Rated voltage	150	V
Friction coefficient (*C*)	10	N/m/s
Translator mass (*M*)	5	kg
Phase resistance	2.5	Ω

B. *Electromagnetic Equation*

Voltage balancing equation for any one phase can be represented as:

$$v_k = R.i_k + \frac{d\lambda_k}{dt}, \qquad \lambda_k = L_k(i_k, x).i_k \tag{1}$$

$$\frac{d\lambda_k}{dt} = L_k(i_k, x).\frac{d\lambda_k}{dt} + g_k.v_x.i_k \tag{2}$$

where, v_k, i_k, λ_k, R and L_k are voltage, current, linkage flux, winding resistance, and inductance of the k-th phase, respectively where k denotes the phases a, b, c, and d. In addition, $v_x = dx/dt$ and $g_k(x) = dL_k/dx$ are linear motion velocity and the force function respectively, in which $g_k(x)$ is defined as the rate of change of phase inductance according to position. Force of each phase (F_k) can be obtained from the phase current and translator position. The resultant propulsion force, Fe is the sum of the phase forces. SRM mathematical analysis has been carried out in [18]. The generated propulsion force in the LSRM can be written as:

$$F_e = M\frac{dv}{dt} + Cv + F_L \tag{3}$$

$$F_e = F_a + F_b + F_c + F_d \tag{4}$$

$$F_L = k_p v \tag{5}$$

where F_e and F_L show the propulsion and output load forces, respectively while F_k with k = a, b, c, and d denotes force of each phase. v, M and C are the speed of the moving part (m/s), moving part total mass and frictional coefficient, respectively. k_p is a constant factor.

Phase currents can be used to express an output force equation. To express the output force in terms of phase currents and translator position, the output force equation is derived from the coenergy W_c. From the definition of the coenergy and assuming that two "*x*" and "*y*" phases are on simultaneously, then according to $\lambda_x = L_x i_x$ and $\lambda_y = L_y i_y$, the differential coenergy is expressed as:

$$dW_c(i_x, i_y, x) = \lambda_x di_x + \lambda_y di_y + F_e dx$$
$$= (L_x i_x)di_x + (L_y i_y)di_x + F_e dx \tag{6}$$

The coenergy can be found by integrating (6) along a path of integration. The most convenient integration path is to integrate over x holding i_x and i_y fixed at zero, integrate over i_y by holding i_x fixe at zero, and finally integrate over i_x. In the first part of the integration, the integral is zero because F_e is zero when both i_x and i_y are zero. Thus, the coenergy is calculated as

$$W_c(i_x, i_y, x) = \int_0^{i_y} \lambda_y(0, \varepsilon, x)d\varepsilon + \int_0^{i_x} \lambda_x(\varepsilon, i_y, x)d\varepsilon =$$
$$\int_0^{i_y}(L_y\varepsilon)d\varepsilon + \int_0^{i_x}(L_x\varepsilon)d\varepsilon = \frac{1}{2}L_x i_x^2 + \frac{1}{2}L_y i_y^2 \tag{7}$$

where ε is an integration variable. Then, the propulsion force F_e is calculated as

$$F_e = \left.\frac{\partial W_c(i_x, i_y, x)}{\partial x}\right|_{i_x, i_y\ fixed} = \frac{1}{2}g_x i_x^2 + \frac{1}{2}g_y i_y^2 \tag{8}$$

Now F_e is expressed in terms of variables, i_x and i_y, an the rate of change of phase inductance, g_x and g_y. After calculating the propulsion force, using (3) and (4), we can write:

$$\dot{v} = -\frac{k_p}{M}v + \frac{1}{M}[-Cv + F_e] \tag{9}$$

III. FUZZY CONTROL SYSTEM DESIGN

The block diagram of the system composis of the LSRM and its control system is demonstrated in Fig. 2. In this study, the speed of the motor has been controlled by the fuzzy logic control approach. The fuzzy system has two inputs: the speed error e and change in the speed error Δe. The output of the controller is the reference current of each phase.

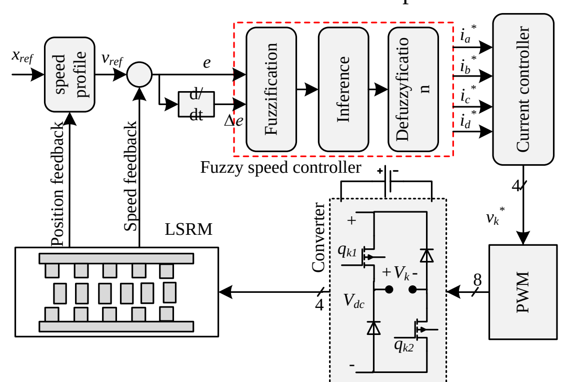

Fig. 2. Block diagram of the proposed control system

A. *Jerk Minimization-Based Speed Profile*

At the first step and after defining the desired position of the translator, it is necessary to produce a speed profile. An appropriate speed profile can reduce the jerks of the motion noticeably, and so it can enhance the motion quality [22]. Assuming that *x*(t) indicates the position of the translator and t_d is the final time of motion,we can write the objective function as follows which should be minimized.

$$j = \int_0^{td} \left(\frac{d^3x(t)}{dt^3}\right)^2 dt \quad (10)$$

If x(t) be the response of the Euler-Poisson problem, then the function 'j' will have an extremum value. According this, we can write the obtained equation as:

$$\frac{d^6x(t)}{dt^6} = 0 \quad (11)$$

This means the minimum jerk profile x(t) is a polynominal like (12).

$$x(t) = \alpha_5 t^5 + \alpha_4 t^4 + \alpha_3 t^3 + \alpha_2 t^2 + \alpha_1 t + \alpha_0 \quad (12)$$

Consequently, the reference speed profile of the system is obtained as:

$$v_{ref}(t) = 5\alpha_5 t^4 + 4\alpha_4 t^3 + 3\alpha_3 t^2 + 2\alpha_2 t \quad + \alpha_1 \quad (13)$$

In order to solve the equation (13), five boundary conditions are required which are $x(0) = 0$, $x(t_d) = x_d$, $\dot{x}(0) = v_0 = 0$, $\dot{x}(t_d) = v_d$, $\ddot{x}(0) = \alpha_0$, and $\ddot{x}(t_d) = 0$. Subscript 'd' indicates the parameters at the end of the motion period. Finally, the reference speed is obtained as:

$$\begin{aligned} v_{ref}(t) &= \left(-\frac{a_0}{2t_d^3} - 3\frac{v_0}{t_d^4} - 3\frac{v_d}{t_d^4} - 6\frac{x_0}{t_d^5} + 6\frac{x_d}{t_d^5}\right).t^4 \\ &+ \left(3\frac{a_0}{2t_d^2} + 8\frac{v_0}{t_d^3} + 7\frac{v_d}{t_d^3} + 15\frac{x_0}{t_d^4} - 15\frac{x_d}{t_d^4}\right).t^3 \\ &+ \left(-3\frac{a_0}{2t_d} - 6\frac{v_0}{t_d^2} - 4\frac{v_d}{t_d^2} - 10\frac{x_0}{t_d^3} + 10\frac{x_d}{t_d^3}\right).t^2 \\ &+ \alpha_0 t + v_0 \end{aligned} \quad (14)$$

The proposed speed profile was applied to the system and the obtained results were compared with the conventional trapezoidal approach findings. At speed 0.5 m/s and using a conventional trapezoidal profile, speed of the motor reaches its command value at t=0.17 s while this time is less than t=0.12 s using the proposed speed profile. This can be seen at speed 2.5 m/s in Fig. 3 (b). It can be seen from Fig. 3 that the proposed method has a better performance in reference speed tracking.

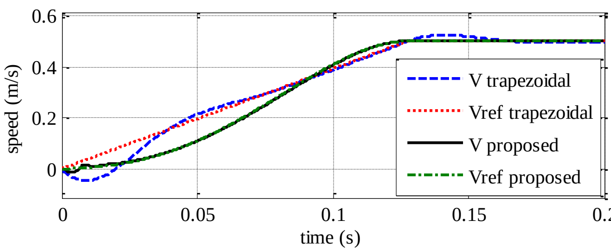

Fig. 3. a

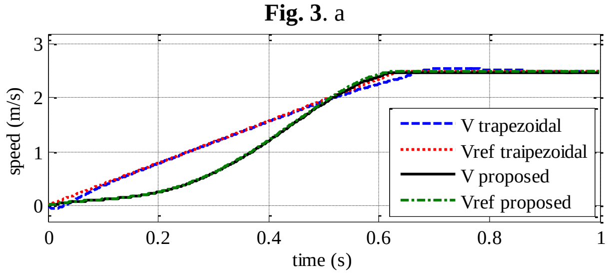

Fig. 3. b

Fig. 3. Speed profile comparison, (a) 0.5 m/s, (b) 2.5 m/s

B. *Fuzzy Control Strategy*

A zero order Takagi-Sugeno fuzzy system is selected to be applied to the DLSRM. The system is able to approximate the nonlinear characteristics of the motor. The proposed fuzzy system elements are shown in Fig. 2. The inference part consists of inference mechanism unit, database unit, and fuzzy rule base unit. The database unit includes all required data such as linguistic variables of input signals, membership function of each linguistic variable, and a set of fuzzy rules. The system consists of a mapping from an input vector $z = [z_1, \dots, z_m]^T \in \Omega_z \subset R^m$ to a scalar output variable $y_f \in R$, where $\Omega_z = \Omega_{z_1} \times \dots \times \Omega_{z_m}$ and $\Omega_{z_i} \subset R$. Assuming that each variable z_k has fuzzy sets $G_k^j, j = 1, \dots, M_k$, the TS fuzzy system can be introduced by a set of if-then rules such as the following:

$$R^{(i)}: If\ z_1 = G_1^i\ and\ z_2 = G_2^i, \text{Then}$$

$$y_f = y_f^i = q_0^i + q_1^i z_1 + q_2^i z_2 = \boldsymbol{\theta}_i^T [1\ \mathbf{z}^T]^T \quad (15)$$

where G_k^i indicate fuzzy sets, k=1, 2, $i = 1, \dots, N_r$, $\mathbf{z}^T = [z_1\ z_2]$ is the input vector, $\theta_i^T = [q_0^k\ q_1^k\ q_2^k]$ shows a vector of the adjustable parameters, y_f^i is the scalar output of the i-th rule, and N_r is the total number of fuzzy rules. By using the central average defuzzifier and product inference, the output of the TS fuzzy system can be expressed as:

$$y_f(z) = \frac{\mu_1 y_f^1 + \dots + \mu_{N_r} y_f^{N_r}}{\mu_1 + \dots + \mu_{N_r}} = \frac{\sum_{i=1}^{N_r} \mu_i\, y_f^i}{\sum_{i=1}^{N_r} \mu_i} \quad (16)$$

$$\mu_i = \prod_{k=1}^{2} \mu_{G_k^i}(z_k) \quad (17)$$

where $\mu_{G_k^i}$ denotes the membership function of the fuzzy set G_k^i. We can rewrite the output of the fuzzy system expressed in (9) as follows:

$$y_f(z) = w^T(z)\theta \quad (18)$$

where $\theta = \left[y_f^1, \dots, y_f^{N_r}\right]^T$ is a vector grouping all consequent parameters, and $w(z) = \left[w_1(z), \dots, w_{N_r}(z)\right]^T$ indicates a set of fuzzy basis functions defined as

$$w_i(z) = \frac{\mu_i(z)}{\sum_{j=1}^{N_r} \mu_j}, \quad i = 1, \dots, N_r \quad (19)$$

Defining enough fuzzy rules, the fuzzy logic system (19) can be used for approximating any real continuous function. The speed error and change of the speed error represent the inputs of the fuzzy system. Each input and output variable have fuzzy sets as shown in Fig. 4. According to Fig. 4 (a), seven triangular fuzzy sets were used to introduce each input variable with fuzzy sets having 50% overlap with each other. For the output variable, a fuzzy inference mechanism was calculated using a singleton membership function shown in Fig. 4 (b). In this work, we have selected singleton membership function for the output of the system. this cause to fast response of the controller.

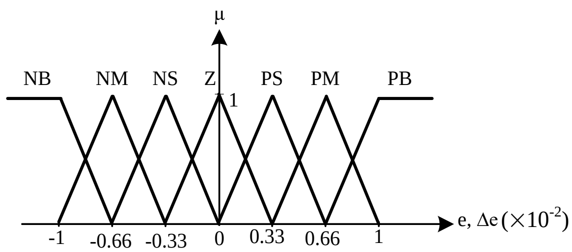

Fig. 4. a

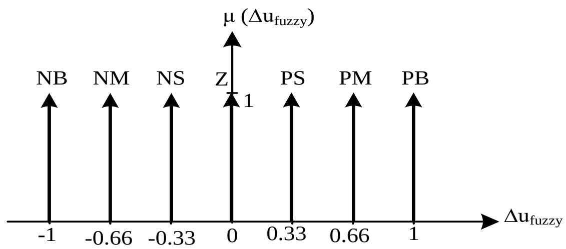

Fig. 4. b

Fig. 4. fuzzy sets (a) Input variables, (b) Output variables

The main advantage of the fuzzy control system is that it does not need lots of data to control the LSRM performance. Totally the used fuzzy controller has the following advantages over the other control strategies:

- Simplicity and flexibility
- Can handle problems with imprecise and incomplete data
- Can model nonlinear structure of the LSRM
- Cheaper and need very low memory in implementation
- Cover a wide range of operation conditions.

The fuzzy rules are listed in TABLE II.

TABLE II
Rules Of Proposed Fuzzy Controller

Δe \ e	NB	NM	NS	Z	PS	PM	PB
NB	NB	NB	NB	NB	NM	NS	Z
NM	NB	NB	NB	NM	NS	Z	PS
NS	NB	NB	NM	NS	Z	PS	PM
Z	NB	NM	NS	Z	PS	PM	PB
PS	NM	NS	Z	PS	PM	PB	PB
PM	NS	Z	PS	PM	PB	PB	PB
PB	Z	PS	PM	PB	PB	PB	PB

IV. Model Reference Adaptive Control (MRAC)

A new MRAC system has been proposed in [23] which can be used for speed control of the electrical motors. Implementation of this control strategy needs state equation of the system same as [23]:

$$\dot{x} = f(x) + G(x)u \tag{20}$$

where $\dot{\boldsymbol{x}} \in \boldsymbol{R}^{\boldsymbol{n}}$ are state variables and $\boldsymbol{u} \in \boldsymbol{R}^{\boldsymbol{m}}$ is the input of the system. This equation can be written as

$$\dot{x} = A(x)x + B(x)u \tag{21}$$

where $\boldsymbol{f}(\boldsymbol{x}) = \boldsymbol{A}(\boldsymbol{x})\boldsymbol{x}$ and $\boldsymbol{G}(\boldsymbol{x}) = \boldsymbol{B}(\boldsymbol{x})$. The speed is the time derivative of the position i.e:

$$\dot{x} = v \tag{22}$$

Using (6), we can write:

$$\dot{v} = -\frac{C+k_p}{M}v + \frac{1}{M}F_e \tag{23}$$

The matrix form of (22) and (23) is written as follows:

$$\begin{bmatrix}\dot{x}_1\\ \dot{x}_2\end{bmatrix} = \begin{bmatrix}\dot{x}\\ \dot{v}\end{bmatrix} = \begin{bmatrix}0 & 1\\ 0 & -\frac{C+k_p}{M}\end{bmatrix}\begin{bmatrix}x_1\\ x_2\end{bmatrix} + \begin{bmatrix}0\\ \frac{1}{M}\end{bmatrix}[F_e] \tag{24}$$

$$u(t) = F_e \tag{25}$$

In the proposed system, position speed $\boldsymbol{x_1} = \boldsymbol{v}$ and derivative of the speed $\boldsymbol{x_2} = \dot{\boldsymbol{v}}$ are state variables while, according to (25), propulsion force $\boldsymbol{F_e}$ is the output. In (10), $\boldsymbol{A}(\boldsymbol{x})$ and $\boldsymbol{B}(\boldsymbol{x})$ are the state-dependent coefficient matrices that represent the nonlinear system in the form (20) in a pseudo-linear form. In this work we examine the controllability of the LSRM system using the equation (3) discussed in the [23]. Using the state-dependent Riccati equation, all atate variables should reach zero by minimizing the following integral quadratic cost function:

$$J = \frac{1}{2}\int_0^{\infty}(x^T Q(x) + u^T R(x)u)dt \tag{26}$$

where $\boldsymbol{Q}(\boldsymbol{x}) \in \boldsymbol{R}^{\boldsymbol{n}\times\boldsymbol{n}}$ and $\boldsymbol{R}(\boldsymbol{x}) \in \boldsymbol{R}^{\boldsymbol{n}\times\boldsymbol{m}}$ are the state-dependent weight matrices. For any x, it is assumed that

$$Q(x) \geq 0\ ,\quad R(x) > 0 \tag{27}$$

Briefly description of the method has been demonstrated in [23]. This control strategy was implemented to the LSRM system and simulation results along with experiments results were obtained.

V. Simulation Results

We use Matlab/Simulink to simulate the DLSRM along with the proposed control strategy. After generating the reference speed by the presented speed profile, the reference speed was compared with the actual value. Then, the error was introduced into the proposed fuzzy speed controller. Four phase currents were the output of the speed controller, which entered the PI current controller after comparison with the corresponding actual values. The proportional and integral parameters of the applied PI controller extracted by a trial and error approach were set to 0.05 and 2.2, respectively. In order to compare the performance of the proposed fuzzy system, a conventional PI controller along with a MRAC strategy discussed in [23] were applied to the motor and the obtained results have been shown under all conditions. The proportional and integral gains of the PI speed controller were set to 1.3 and 3.2, respectively.

The simulation results including the speed, speed error, and total propulsion force for three control strategies are shown in Fig. 5. According to Fig. 5 (a), the profiles of the speed and position are same for all control methods, so only one curve is shown in the figure. In Fig. 5 (b), propulsion forces obtained from three control strategies are demonstrated. Generally, the figures are same and reach their final value in a same time. Pick value of force in MRAC and PI controllers are about 20 N.m while this is lower in the proposed fuzzy control method. Current of phase "a" is depicted in Fig. 5 (c). According to these figures, the current is high at starting while it reduces to a lower value in steady state. According to figures, proposed fuzzy control method has better performance than the conventional PI method while has the same performance as modern MRAC strategy discussed in [23].

The advantage of the fuzzy method is that it does not require accurate information about the nonlinear LSRM structure and is easier to implement. Comparison of the speed between three control methods obtained by simulation and experimental have been shown in Fig. 9. There are some effective methods for evaluating the performance of control strategies which can be useful in comparing different systems. A useful method discussed in [12] introduces the critical parameters of the results including the percentage of overshoot, rising time, settling time, the criteria encompassing integral of absolute error (IAE) along with integral of time absolute error (ITAE). The parameters for the simulation test have been obtained and reported in Table 3. In order to study the performance of the system under load variations, an 8 kg load was added to the translator when it was moved at a constant speed. Then, the above-mentioned parameters were measured again and written in Table 3. The data confirm that the proposed control strategy has outperformed the conventional PI method in both no load and full load conditions, while it is approximately same as MRAC method. Considering the simple structure and implementation of the proposed fuzzy control method, it seems to be more appropriate than two other control strategies.

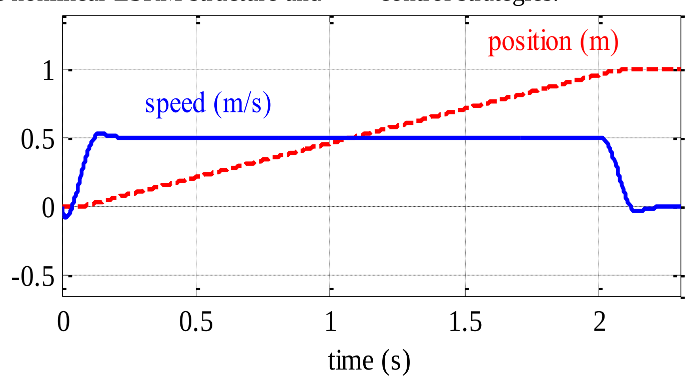

Fig. 5. a

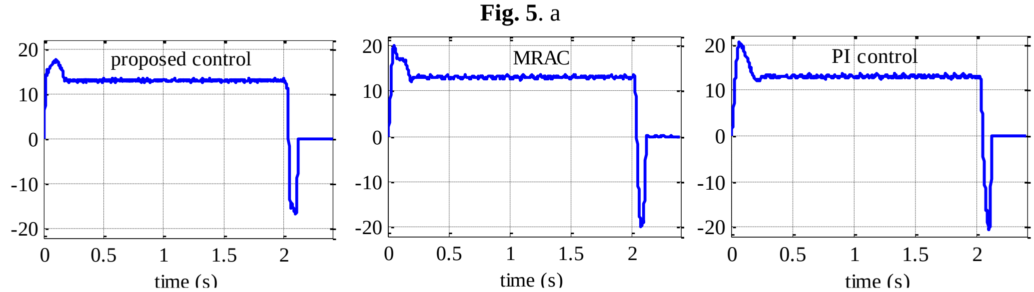

Fig. 5. b

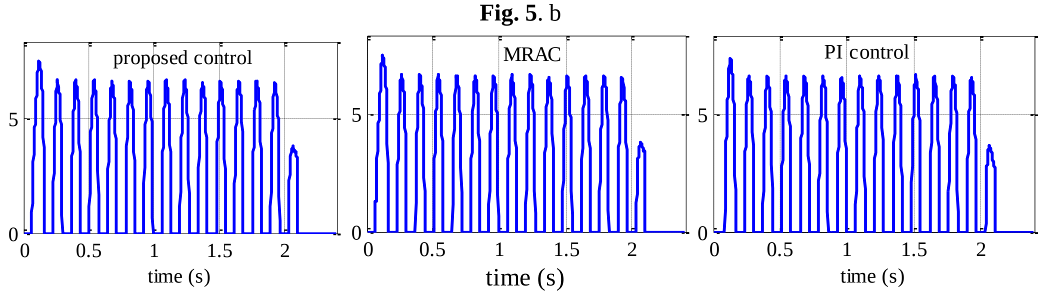

Fig. 5. c

Fig. 5. Comparison of simulation results, (a) speed and position, (b) force (N), (c) phase current (A)

TABLE III. Critical Parameters

	No load			Full load		
Parameter	proposed	MRAC	PI	proposed	MRAC	PI
Overshoot (%)	0.87	0.88	1.5	2.8	3	6
Rising time	0.014	0.013	0.018	0.004	0.003	0.006
Setteling time	0.016	0.017	0.031	0.009	0.010	0.026
IAE	0.01	0.01	0.015	0.014	0.014	0.025
ITAE	0.001	0.001	0.004	0.001	0.001	0.006

VI. EXPERIMENTAL RESULTS

In this study, a DLSRM with dimensions and parameters outlined in Table 1 was selected. Then the proposed control strategy along with a conventional PI controller was applied to regulate the motor performance. The motor and its experimental drive are shown in Fig. 6. Steel sheets with 0.5 mm thickness were used to construct the stator poles and yoke. For creating the translator, nonlaminated iron was used which coils of AWG#15 wire placed on translator poles. In order to implement the control system, an ARM Cortex-M4 microcontroller STM32f407 was used with 72 MHz processing frequency. Four Hall sensors sensed the actual phase currents and sent them to the current control unit. All signals were stored in a flash memory. Also, the propulsion force was calculated by the corresponding equations and finite element analysis information. A magnetic sensor strip with 10 µm resolution runs alongside the stator giving the position feedback signal. The speed information was also obtained through a capture channel of the timer inside the microcontroller.

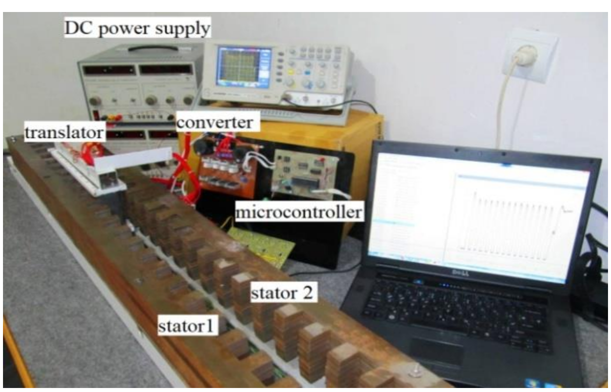

Fig. 6. Experimental setup

The results measured in the experimental test for three control strategies are shown in Fig. 7. The test conduct under the same conditions as the simulation in Fig. 5. According Fig. 7, force in the steady state condition is 12 N. At start and to overcome the moment of inertia, the generated force is higher. The pick start force is 17 N, 20 N, and 20.5 N for proposed fuzzy method, MRAC, and PI method, respectively. This also happens during braking.

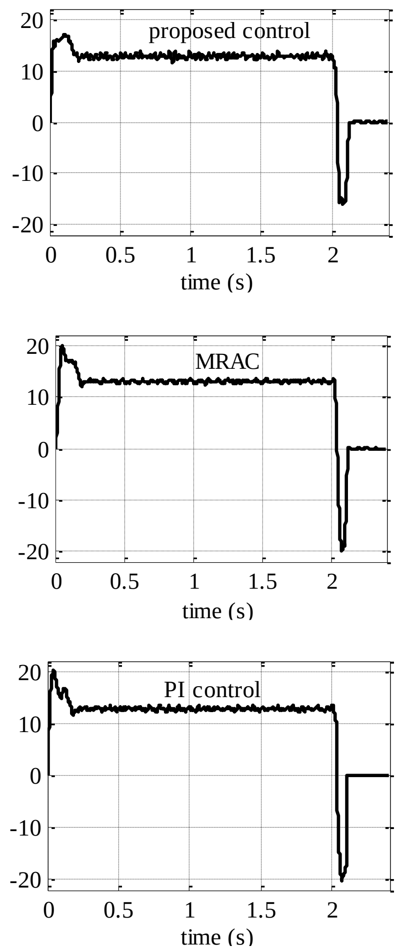

Fig. 7. Force comparison of three methods

The currents of a phase obtained from the experimental test for three control methods are demonstrated in Fig. 8. In order to have a better realization, the current is shown in all of the moving periods along with in a limited interval. Current profile in three strategies are approximately same, so only one profile is demonstrated.

The speed error for three control strategies obtained from simulation and experimental tests are shown together in Fig. 9. The figuers indicate that the experimental results are approximately same as the simulation results. According to

Fig. 9, the speed error in proposed fuzzy control strategy and MRAC method has same overshoot about 0.03 m/s while this exceeds 0.1 m/s in the conventional PI controller. So, the proposed fuzzy control method and MRAC strategy have almost the same performance but fuzzy control method has some benefits explained in section 3.

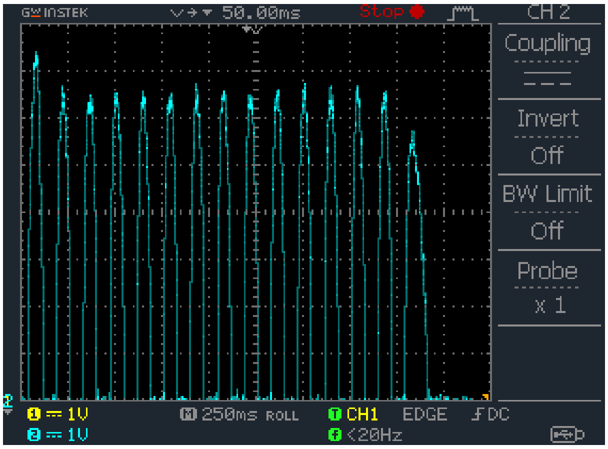

Fig. 8. a

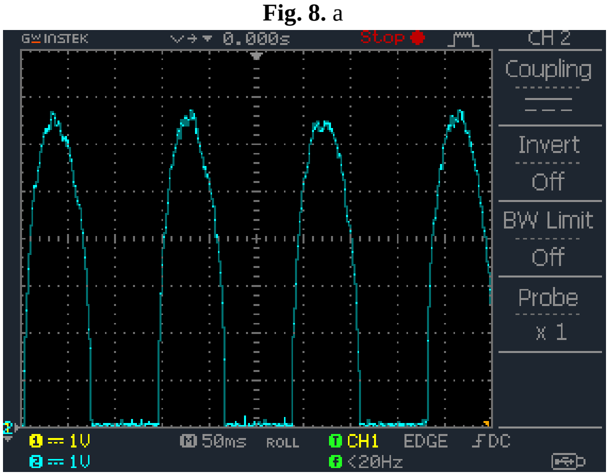

Fig. 8. b

Fig. 8. Experimental results, phase current, (a) total current, (b) current in a limited interval

VII. Conclusion

This work proposed the control of a double-sided linear switched reluctance motor by a simple fuzzy logic-based system. Linear switched reluctance motors are inherently non-linear systems with some unknown parameters such as saturation and end effect phenomena complicating their precise control. The proposed control strategy was applied to a motor along with a conventional PI and a modern MRAC strategies. The controller was able to control the position, speed, force and current of the motor simultaneously. To make the study more robust, simulation and experimental tests were performed and the obtained results were compared for three methods. The results confirmed that the fuzzy control approach outperformed the other methods. In addition, the proposed method was very simple requiring to additional information about the system when compared with the other methods.

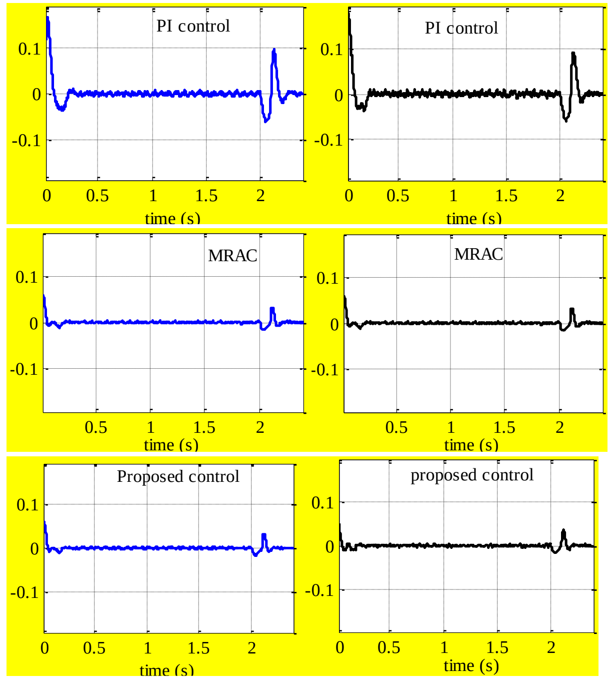

Fig. 9. a **Fig. 9.** b

Fig. 9. Speed error comparison, (a) simulation, (b) experimental

References

[1] Lobo, N.S., Lim, H.S., Krishnan, R.: *'Comparison of linear switched reluctance machines for vertical propulsion application: analysis, design and experimental correlation'*, IEEE Trans. Ind. Appl., 2008, 44, (4), pp 1134-1142.

[2] Ye, J., Bilgin, B., Emadi, A., *'An Offline Torque Sharing Function for Torque Ripple Reduction in Switched Reluctance Motor Drives'*, IEEE Trans. On Energy Convers., 2015, 30, (2), pp. 726–735.

[3] Shin, H.-U., Park, K., Lee, K.-B., '*A Non-Unity Torque Sharing Function for Torque Ripple Minimization of Switched Reluctance Generators in Wind Power Systems'*, Energies, 2015, 8, (10), pp. 11685–11701.

[4] Li, H., Bilgin, B., Emadi, A., '*An Improved Torque Sharing Function for Torque Ripple Reduction in Switched Reluctance Machines'*, IEEE Trans. On Power Electron., 2019, 34, (2), pp. 1635-1644.

[5] Moradi Cheshmehbeigi, H., and Mohamadi Amidi, A., '*Torque ripple minimization in SRM based on advanced torque sharing function modified by genetic algorithm combined with fuzzy PSO'*, International Journal of Industrial Electronics, Control and Optimization, 2018, 1, (1), pp. 71-80.

[6] Masoudi. S., Feyzi, M. R., Sharifian, M. B. B.: *'Force*

ripple and jerk minimization in double sided linear switched reluctance motor used in elevator application', IET, Electric Power Appl., 2016, 10, (6), pp. 508-516.

[7] Luis, O., Costa, B.: '*Proposition of an off-line learning current modulation for torque-ripple reduction in switched reluctance motors: design and experimental evaluation'*, IEEE Trans. On Ind. Electron., 2002, 49, (3), pp. 665-676.

[8] Sanches, E.S., Santisteban, J.A., '*Mutual Inductances Effect on the Torque of an Axial Magnetic Flux Switched Reluctance Motor*', IEEE Trans. On Lat. Am., 2015, 13, pp. 2239–2244.

[9] Mikail, R., Husain, I., Islam, M.S., Sozer, Y. Sebastian, T., 'Four-Quadrant Torque Ripple Minimization of Switched Reluctance Machine Through Current Profiling with Mitigation of Rotor Eccentricity Problem and Sensor Errors', IEEE Trans. On Ind. Appl. 2015, 51, pp. 2097–2104.

[10] Shaked, N.T., Rabinovici, R., 'New procedures for minimizing the torque ripple in switched reluctance motors by optimizing the phase-current profile', IEEE Trans. On Magn., 2005, 41, pp. 1184–1192.

[11] Labiod, C., Srairi, K., Mahdad, B., Benbouzid, M.E.H., '*A novel control technique for torque ripple minimization in switched reluctance motor through destructive interference'*, Electr. Eng. 2017, 100, pp. 1–10.

[12] Soltanpour, M, Abdollahi, H., and Masoudi, S., '*Optimization of double sided linear switched reluctance motor for mass and force ripple minimization', IET Science Measurement and Technology*, 2019, 13, (4), pp. 509-517.

[13] Jin, W.L., Hong S.K., Byung I.K., Byung T.K., '*New rotor shape design for minimum torque ripple of SRM using FEM*', IEEE Trans. On Magn. 2004, 40, (2), pp. 754–757.

[14] Kermanipour, M.J., Ganji, B., *'Modification in Geometric Structure of Double-Sided Axial Flux Switched Reluctance Motor for Mitigating Torque Ripple'*, Canadian Journal of Elect. Comput. Eng., 2015, 38, (4), pp. 318–322.

[15] Keramat, R., Ershadi, M. H., and Shojaeian, S., *'A comparison of fuzzy and brain emotional learning-based intelligent control approaches for a full bridge DC-DC converter*', International Journal of Industrial Electronics, Control and Optimization, 2019, 2, (3), pp. 197-206.

[16] Liu, Y., Wu, F., and Ban, X., *'Dynamic output feedback control for continuous-time T-S fuzzy systems using fuzzy lyapunov functions*', IEEE Trans. On Fuzzy Systems, 2017, 25, (5), pp. 1155-1167.

[17] Sun, K., Mou, S., Qiu, J., Wang, T., Gao, H., '*Adaptive fuzzy control for nontriangular structural stochastic switched nonlinear systems with full state constraints'*, IEEE Trans. On Fuzzy Systems, 2018, 27, (8), pp. 1587-1601.

[18] Masoudi, S., Soltanpour, M., Abdollahi, H., '*Adaptive fuzzy control method for a linear switched reluctance motor*', IET Electric Power Appl., 2018, 12, (9), pp. 1328-1336.

[19] Liu, Z., Lai, G.Y., and Chen, C.L.P., '*Adaptive neural output feedback control of output constrained nonlinear systems with unknown output nonlinearity'*, IEEE Trans., on Neural Netw. Learn Syst., 2015, 26, (8), pp. 1789-1802.

[20] Zhang, L., and Jia, M., *'Robust controller design for switched fuzzy system with uncertain input'*, 4th International Conf. On Information, Cybernetics and Computational Social Systems, 2017, Dalian, Chaina.

[21] Xu, J., Du, Y., Chan, Y.H., Guo, H., *'Optimal robust control design for constrained uncertain systems: a fuzzy set theoretic approach',* IEEE Trans. On Fuzzy Systems, 2018, 26, (6), pp. 3494-3505.

[22] Lambrechts, P., Boerlage, M., Steinbuch, M., '*Trajectory planning and feedforward design for high performance motion systems'*, Proceedings of the 2004 American Control Conference, 2005, Boston, USA.

[23] Rahideh, M., Ketabi, A., and Halvaei Niasar, A., '*Maximum power point tracking using a state dependent riccati equation-based model reference adaptive control'*, International Journal of Industrial Electronics, Control and Optimization, 2020, 3, (2), pp. 115-124.

Allahverdi Azadrou was born in Salmas, Iran, in 1983. He received his B.S. degree in electrical engineering from Islamic Azad University, Abhar Branch, Abhar, Iran, and M.S. degree from Dezful Branch, Dezful, Iran. He is a member of science in Islamic Azad University, Salmas Branch, Iran since 2012. Currently he is Ph.D student in Islamic Azad University, Urmia Branch, Urmia, Iran.

Siamak Masoudi was born in Miyaneh, Iran. He received his B.S. degree in power engineering from Tarbiat Moallem Tabriz University, Tabriz, Iran, in 2006, and his M.S. and Ph.D. degrees in Electrical Machines and Drives from University of Tabriz, Tabriz, Iran, in 2009 and 2016, respectively. From 2010, he is a member of science in Islamic Azad University, Abhar Branch, Zanjan, Iran. His current research interests include Electrical machines design and control and linear motors/generators.

Reza Ghanizadeh received the B.S. degree in electrical engineering from the Ardabil Branch-Islamic Azad University (Ardabil), Iran, in 2009. He received the M.S. and the Ph.D. degrees from University of Birjand (Birjand), Iran, in 2013 and 2017, respectively. He is currently an assistance professor in faculty of electrical engineering at Urmia Branch, Islamic Azad University (Urmia), Iran. His research interests include power quality, microgridscontrol, power electronics, high voltage studies,power systems stability and Fact devices.

Payam Alemi was born in Tabriz, Iran, in 1982. He received his B.S. degree from the University of Tabriz, Tabriz, Iran, in 2005, and his M.S. degree from the Science and Research Branch, Islamic Azad University, Tehran, Iran, in 2008, and Ph.D. degree in Electrical Engineering, from Yeungnam University, Gyeongsan, Korea, in 2014. Then he joined Simon Fraser University, BC, Canada for his Post-doctoral program until 2016. Currently he is an assistant professor in the department of electrical engineering, Islamic Azad University, Urmia Branch, Urmia, Iran. His current research interests include the control of multilevel power converters, power loss analysis for converters, LCL filters and machine drives, DC- DC converters.

International Journal of Industrial Electronics, Control and Optimization © 2020 IECO
Vol. 3, No. 4, pp. 469-474, Sep (2020)

Solving Economic Load Dispatch by a New Hybrid Optimization Method

Hossein Sharifzadeh[1,†]

[1] Department of Electrical and Computer Engineering, Hakim Sabzevari University, Sabzevar, Iran.

ABSTRACT

This paper presents a new solution method to efficiently handle non-convexity stemmed from valve points in the economic load dispatch problem. The proposed solution technique integrates both the advantage of fast solution algorithms of linear programming and powerful solution techniques of nonlinear programming to find the global solution. In the first step of the proposed solution framework, non-convex terms are replaced by some linear segments and the new linear model solved by modern fats algorithms. In the second step, a nonlinear programming algorithm as a powerful local search algorithm solves the original non-convex model to improve the solution obtained in the previous step. By exploiting the main strength of linear and nonlinear programming algorithms, the proposed solution approach can quickly converge to nearly the global solution method. By experimental results on three test cases with different sizes, we show that the presented method outperforms the other algorithms published in the literature in the quality of the solution.

Article Info

Keywords:
Branch and bound, Economic load dispatch, Hybrid optimization method

Article History:
Received 2020-01-08
Accepted 2020-02-03

I. Introduction

Among different operational tools provided to efficiently operate power systems in dispatch centers, economic load dispatch (ELD) has special importance as it determines final generation levels of generators. Economic dispatch optimally assigns output power of generators while satisfies power system demand. To this end, an optimization problem with a cost function, as the objective function, and a set of practical constraints is defined [1]. The cost function shows the operational or just fuel cost of power plants and usually models as a quadratic term.

Nonetheless, it is shown that the cost function can better be represented by taking a rectified sine into account as it more precisely models the effect of opening several valves, in a power plant, on cost function [2]. However, from an optimization viewpoint, the considered rectified sinusoidal term changes the ELD problem into a non-smooth non-convex optimization problem. A wide range of solution algorithms has been published in the literature to tackle the optimization problem and can be categorized into two gradient and artificial intelligence-based (AI) methods. The gradient-based methods can include Lagrangian relaxation [3], modified lambda-iteration [4], linear programming [5], and quadratic programming [6]. The traditional gradient-based methods rely on derivatives of objective and constraints in optimization problems and as a result, they can not effectively manage the non-differentiable absolute function induced by rectified sinusoidal term. Moreover, they are local optimizer in nature and their performances dramatically depend on the starting point. Therefore, they have poor performances in the no-convex problem with multiple local minimums [7].

†Corresponding Author: h.sharifzade@hsu.ac.ir
(or: h.sharifzade@gmail.com)
Tel: +98-440129678,Fax: +98-44012821, Hakim Sabzevari University
Department of Electrical and Computer Engineering, , Hakim Sabzevari University, Sabzevar, Iran

Applications of AI algorithms have demonstrated in some studies [8]-[10]. AI based algorithms particularly in the ELD subject may consist of bat algorithm [11], gravitational search algorithm [12], symbiotic organisms search algorithm [13], firefly algorithm [14], cuckoo search algorithm [15], cooperative search algorithm [16], phasor particle swarm optimization [17], hybrid optimization framework [18], hybrid PSO–SQP [19], and hybrid GA–PS–SQP [20]. The algorithms do not require a differentiable search space. Moreover, they work with a set of solutions, so-called population, swarm, etc., compared to the gradient-based methods use a single solution. Hence, they may find the global solution using the parallel search. However, the computation burdens of these algorithms are high. Moreover, the performances of these methods severely depend on algorithm parameters limiting their application in practice.

In this paper, a new hybrid solution method is employed to tackle with the non-convexity of economic load dispatch accommodating the valve point effects. In the first step, the proposed method decomposes the non-convex problem to the set of linear problem method. The best solution among these linear problem methods can be found by a strong branch and bound algorithm. In the second step of the presented approach, the original problem is solved using a nonlinear programming (NLP) algorithm considering non-convex terms using the starting point, obtained in the first step, most likely located near the global solution depending on the quality of the linear segments approximation. Thus, NLP may converge to the global solution by providing an effective starting point.

The rest of the paper is organized as follows. The economic load dispatch problem formulation accounting for valve loading points is modeled in section II. Section III presents the proposed solution framework for solving non-convex ELD. Experimental results to show the effectiveness of the proposed solution technique is provided in section IV. Section V concludes the paper.

II. PROBLEM STATEMENT

The economic load dispatch tool aims to minimize total operation cost considering the physical and operational limits of power systems. From a formulation point of view, the aims and the limits can be represented by an objective function and set of equality and inequality constraints in an optimization model as follows [2]:

$$Minimize \sum_{j=1}^{n}\left(a_j P_j^2 + b_j P + c_j + \left|e_j \sin\left(f_j\left(P_j^{\min} - P_j\right)\right)\right|\right) \quad (1)$$

$$P_j^{\min} \le P_j \le P_j^{\max}, \quad j = 1, 2, ..., n \quad (2)$$

$$\sum_{j=1}^{m} P_j = D \quad (3)$$

In the formulation, j shows an index of generators from 1 to n (number of generators). a_j, b_j, c_j, e_j, f_j are the coefficient cost of generator j. The decision variable P_j stands for the generation level of generator j. The minimum and maximum power limits of generator j are represented by $P_j^{\min}$ and $P_j^{\max}$ respectively. The power system demand is shown by D.

The objective function in (1) indicating the total cost of generators includes two convex and non-convex components. The quadratic term $a_j P_j^2 + b_j P + c_j$ is a convex function while the term $\left|e_j \sin\left(f_j\left(P_j^{\min} - P_j\right)\right)\right|$ is a non-convex and non-smooth function added due to valve loading effects. The non-nonconvex term changes the ELD problem to non-convex one with many local optimal solutions.

In the next section, a two layers method is proposed to cope with the non-convex and non-smooth space of the presented ELD problem.

III. THE PROPOSED ELD SOLUTION METHOD

As mentioned before, the ELD accommodating valve point effects is a non-convex problem. Here, to tackle with the non-convexity, the non-convex cost functions replaced with some of the linear segments finally producing a mixed integer linear problem. Subsequently, a mixed integer programming (MIP) solution technique is used to solve the new model. As the mixed inter algorithms are very powerful at present, the new model can be solved very fast. The obtained solution of mixed inter then used as the starting solution of the original non-convex ELD problem solved by a nonlinear programming (NLP) approach. The NLP can remove the approximation error and converge to the nearly global solution as it currently uses the high- quality starting point obtained in the first step. The mixed integer problems usually solved by powerful branch and bound (B&B) algorithms [21]. In the B&B algorithm, firstly, all integer values relaxed and they can adopt fractional values. The resulting relaxed LP model is solved. In the B&B algorithm, a so-called tree is generated composed of a root (the first LP model) with some branches, nodes, and leaves as shown in figure 1. Nodes Correspond to some integer variables that have fractional values in the solution of the LP model. In each node, a decision is made about rounding up or down the fractional values of the integer variable shown by corresponding branches. Subsequently, two new nodes in two branches ending of the node show the two new models with fixing the fractional to integer values. The nodes that have been not branched yet called leaves. The two new models may be solved in two new nodes and other new nodes can be generated. The procedure continues until some stopping criteria satisfied. Consequently, the solution space of the original non-convex model is approximated by some probably smaller linear models with a more efficient solution algorithm.

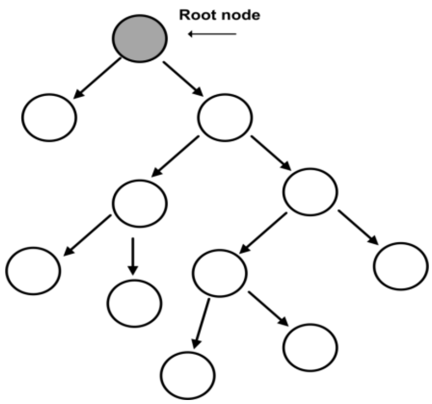

Fig.1. The tree generated by B&B algorithm

A mixed integer linear model of a nonlinear function can be found as described below.

Consider that the *B+1* breakpoints or equivalently *B* segments are used to linearly approximate a nonlinear function and $x^{\min} = x_0 \prec x_1 \prec, ..., \prec x_B = x^{\max}$ stand for the breakpoints.

Let us show the non-convex function with its kth linear segment approximation as follows:

$$y_k = m_k \hat{x}_k + d_k \,, \; x_{k-1} \le \hat{x}_k \le x_k \qquad (4)$$

Where x_{k-1} and x_k show the beginning and ending points of the segments respectively. Here, in the ELD problem, $\hat{x}_k$ and y_k can be interpreted as the generation level and associated cost in the kth interval. The slope and y-intercept of the linear segments (in kth linear segment) are represented by m_k and d_k respectively. Then the whole piecewise linear approximation can be modeled using binary variables z_k as follows [22]:

$$x = \sum_{k=1}^{B} \hat{x}_k \qquad (5)$$

$$y = \sum_{k=1}^{B} (m_k \hat{x}_k + d_k) \qquad (6)$$

$$x_{k-1} z_k \le \hat{x}_k \le x_k z_k \quad \forall k = 1, 2, ..., B \qquad (7)$$

$$\sum_{k=1}^{B} z_k = 1 \qquad (8)$$

$$z_k \in \{0,1\} \quad \forall k = 1, 2, ..., B \qquad (9)$$

In this modeling method, z_k activates the segment *k* and its associated variable $\hat{x}_k$. Based on (7) and (8) only one continuous variable $\hat{x}_k$ can be non-zero that is determined based on the corresponding non-zero binary variable z_k. Relying on the technique, the MIP model for ELD problem can be described as follows:

$$Minimize \; \sum_{j=1}^{n} F_j \qquad (10)$$

$$P_j^{\min} \le P_j \le P_j^{\max}, \quad j = 1, 2, ..., n \qquad (11)$$

$$\sum_{j=1}^{m} P_j = D \qquad (12)$$

$$F_j = \sum_{k=1}^{B_j} (m_{j,k} \hat{p}_{j,k} + d_{j,k}), \quad j = 1, 2, ..., n \qquad (13)$$

$$P_j = \sum_{k=1}^{B_j} \hat{p}_{j,k} \,, \quad j = 1, 2, ..., n \qquad (14)$$

$$p^{d}_{j,k} z_{j,k} \le \hat{p}_{j,k} \le p^{u}_{j,k} z_{j,k} \;\; k = 1, 2, ..., B_j \,, and \;\; j = 1, 2, ..., n \qquad (15)$$

$$\sum_{k=1}^{B_j} z_{j,k} = 1, \quad j = 1, 2, ..., n \qquad (16)$$

$$z_{j,k} \in \{0,1\} \quad \forall k = 1, 2, ..., B_j \,, and \;\; j = 1, 2, ..., n \qquad (17)$$

Where $\hat{p}_{j,k}$ is the generation level of generator *j* in segment *k* and limited to up and down breakpoints of the segment i.e. $p^{u}_{j,k}$ and $p^{d}_{j,k}$ respectively. The linear cost of generator *j* is shown by F_j. Other symbol denotations are straightforward as they are a formulation extension of single function approximation in (5)-(9) to multi-function cost approximation of *n* generators in ELD problem.

The solution obtained from the MIP model of ELD (10)-(17) can be used as the starting point of nonlinear ELD model (1)-(3) to converge to the nearly global solution.

IV. Numerical results

This section deals with performance evaluation of the proposed solution technique for solving non-convex non-smooth economic load dispatch. To show the efficiency of the presented method three case studies with different size are selected as follows:

Case I: A small scale 3 unit test system.
Case II: A medium scale 13 unit test system.
Case III: A large scale 40 unit test system.

The proposed solution technique is implemented using

GAMS software. We used a laptop with CPU Core i3, 2.4GHZ clock frequency and 4 GB RAM in all simulations. The mixed integer model is solved by CPLEX and the nonlinear model using CONOPT. It is noted that the optimality of obtained results is not sensitive to the selected solver.

Application results of the proposed hybrid approach on these case studies are reported in the following. Moreover, the performance of the presented technique is compared with other solution algorithms in the literature to evaluate the capabilities of the proposed method more precisely.

Case I: 3 unit case study

The load demand of the three units test case is 850MW. All of its units have vale loading effects in their cost function. The required data for the test case can be found in [23].

For Case I, result of the presented algorithm and other ELD solution techniques, which are adopted from their published paper, are provided in Table I. As the table shows, different algorithms nearly have the same optimal solutions due to relatively a simple ELD problem in this small test case.

Nonetheless, most of the solution techniques present a noticeable fluctuation in results among different algorithms runs shown by best, average and worst costs. However, the proposed solution method always converges to a unique solution showing its robustness in solving the nonconvex ELD problem. Note that the optimal cost obtained by the proposed method is lower than the mean cost and worst costs of all the reported algorithms in table I illustrating its merit in solving the ELD problem in practice. Table II demonstrates the generation levels of units of case I for the optimal solution of the proposed method.

The outcome of MIP, i.e. the approximate objective function as (9), for the case I is 8233.64$. The solution of MIP is employed as the initial point of the nonlinear programming solver to solve the original non-convex model, here CONOPT solver. The final solution achieved by the CONOPT is 8234.07$ showing that the main part of the provided solution method is actually the presented MIP model.

TABLE I: Comparison Of Solution Algorithms For Solving Eld In Case I

Methods	Best cost ($)	Mean cost ($)	Worst cost ($)
MFEP[23]	8234.08	8234.71	8241.80
CEP[23]	8234.07	8235.97	8241.83
FEP[23]	8234.07	8234.24	8241.78
IFEP[23]	8234.07	8234.16	8234.54
FA[24]	8234.07	8234.08	8241.23
PS*[25]	8234.05	8453.00	8352.41
Proposed hybrid algorithm	8234.07	8234.07	8234.07

*Violation of demand constraint

TABLE II: Generation Levels, And Associated Cost In Optimal Solution Of Case I

Unit	Generation (MW)
1	300.2669
2	149.73310
3	400.0000
Cost ($)	8234.07173

Case II: 13 unit case study

The generator characteristics of thirteen test system are adopted from [23]. The demand for this test case is D=1800MW. The cost functions of all 13 units test case have vale loading effects. Table III shows the outcome pertaining to the application of the proposed hybrid solution method and results taken from other published approaches in the literature to solve the economic load dispatch problem for case II. The presented method outperforms most of the other methods in finding the better optimal solution, as the table III shows. Again, while the solution of the proposed piecewise technique is unique, dissimilar final solutions of other techniques challenge their applicability in real-word problems. Table IV illustrates the unit dispatch as the solution of the suggested method in solving ELD in test system II. For the case II, the output of the MIP solver is 17959.455$ finally reaches to 17960.366$ by the nonlinear solver.

TABLE III: Comparison Of Solution Algorithms For Solving Eld In Case I

Methods	Best cost ($)	Mean cost ($)	Worst cost ($)
CEP [23]	18048.21	18190.32	18404.04
MFEP [23]	18028.09	18192.00	18416.89
FEP [23]	18018.00	18200.79	18453.82
IFEP [23]	17994.07	18127.06	18267.42
SOMA [26]	17967.42	17985.32	18017.62
MDE [2]	17960.39	17967.19	17969.09
CSOMA [26]	17960.366	17967.87	17970.83
Proposed hybrid algorithm	17960.366	17960.366	17960.366

TABLE IV: Generation Levels, And Associated Cost In Optimal Solution Of Case Ii

Unit	Generation (MW)	Unit	Generation (MW)
1	628.319	8	109.867
2	149.6	9	109.867
3	222.749	10	40
4	109.867	11	40
5	109.867	12	55
6	60	13	55
7	109.867	-	
Cost ($)		17960.366	

Case III: 40 unit case study

The forty unit test case demand is 10500MW. The valve loading effects appear in the cost function of all of its units. The data for the test case are taken from [23].

Table V compares the obtained results of the proposed solution technique and reported outcomes of other methods in the literature in solution quality of case III. The first point that should be highlighted is the considerable difference between reported solutions due to the large scale nonconvex ELD problem in this test case. For the same reason, more solution oscillations can be seen in multiple runs of the reported algorithms. Nevertheless, the proposed method converges to the best solution and without any change showing its ability to solve the large scale nonconvex ELD problem. Optimal dispatch for test case III found by the proposed algorithm is illustrated in Table VI. While the returned cost by the MIP solver in the case III is 121413.57$, the final optimal solution is 121412.53$ given by the CONOPT nonlinear solver.

TABLE V: Comparison Of Solution Algorithms For Solving Eld In Case I

Methods	Best cost ($)	Mean cost ($)	Worst cost ($)
FEP [23]	122679.71	124119.37	127245.59
MFEP[23]	122647.57	123489.74	124356.47
IFEP[23]	122624.35	123382.00	125740.63
ESO [27]	122122.16	122558.45	123143.07
MDE [2]	121414.79	121418.44	121466.04
HS [28]	121544.51	121761.01	122113.96
HIS [28]	121560.53	121796.49	121963.31
GHS [28]	121624.32	121870.96	122272.68
SAHS [28]	121516.94	121694.49	121900.42
ACHS [28]	121414.85	121510.50	121655.66
Θ-MBA [29]	121412.53	121412.79	121412.95
Proposed hybrid algorithm	121412.53	121412.53	121412.53

TABLE VI :Generation Levels, And Associated Cost In Optimal Solution Of Case Iii

Unit	Generation (MW)	Unit	Generation (MW)	Unit	Generation (MW)	Unit	Generation (MW)
1	110. 8	11	94	21	523.3	31	190
2	110. 8	12	94	22	523.3	32	190
3	97.4	13	214. 8	23	523.3	33	190
4	179.7	14	394.3	24	523.3	34	164.8
5	87.8	15	394.3	25	523.3	35	194.48
6	140	16	394.3	26	523.3	36	200
7	259.6	17	489.3	27	10	37	110
8	284.6	18	489.3	28	10	38	110
9	284.6	19	511.3	29	10	39	110
10	130	20	511.3	30	87.8	40	511.3
Cost ($)				121412.5355			

Although the presented hybrid technique establishes a nearly global solution and virtually outperforms the other ELD solution methods published in the literature, its computational burden also should be evaluated for the practical application. Because of the different software and hardware used in this paper compared with other techniques presented in the literature, comparisons of computation times are fairly invalid. However, to illuminate the application of the hybrid method, the elapsed time of the suggested technique for each experiment, for all the three test cases, are shown in Table VII. As can be seen from Table VII, the computation times of the presented hybrid algorithm in all the three experiments are less than 2 seconds showing the fast convergence of the method and its application for practical test cases.

TABLE VII: The Computation Burden Of The Proposed Technique In All The Three Test Cases

Test case	Computation time (Sec)
Case I: 3 units test system	0.41
Case II: 13 units test system	1.18
Case III: 40 units test system	1.35

V. CONCLUSIONS

To handle the nonconvexity appears in the ELD problem with valve point effects, we propose a hybrid solution method of powerful local and global searching ability. We describe how the solution method exploits both the branch and bound algorithm as the global search technique and NLP solvers as the local search algorithm to converge to unique high-quality solutions. Comparison results of solution algorithms of the nonconvex ELD problem show the considerable advantage of the presented hybrid technique concerning the other algorithms published in the literature both in the solution quality and robustness of the solution in the multiple algorithms runs. It is noticed that the performance of the AI-based algorithms highly depends on their parameters. However, the proposed technique outperforms the other methods without a trial and error parameter tuning mechanism. Another crucial factor the presented solution method is the low computational burden allowing to be used in practical applications.

REFERENCES

[1] Conejo, Antonio J., and Luis Baringo, *Power system operations*, Springer, 2018.

[2] Amjady N, Sharifzadeh H. *Solution of non-convex economic dispatch problem considering valve loading effect by a new modified differential evolution algorithm*. Int J Electr Power Energy Syst 2010; 32(8):893–903.

[3] Hindi KS, Ghani MRA. *Dynamic economic dispatch for large scale power systems: a Lagrangian relaxation approach.* Int J Elect Power Energy Syst ,1991;13(1):51–6.

[4] Dike DO, Adinfono MI, Ogu G. *Economic dispatch of generated power using modified lambda-iteration method.* IOSR J Electr Electron Eng (IOSR-JEEE) 2013;3331:49–54 e-ISSN: 2278-1676, p-ISSN: 2320.

[5] Parikh J, Chattopadhyay D. *A multi-area linear programming approach for analysis of economic operation of the Indian power system*. IEEE Trans Power Syst 1996;11(February (1)):52–8.

[6] Reid GF, Hasdorff L. *Economic dispatch using quadratic programming.* IEEE Trans Power Apparat Syst 1973; 6:2015–23.

[7] Amjady N, Sharifzadeh H., *Security constrained optimal power flow considering detailed generator model by a new robust differential evolution algorithm*, Electr Power Syst Res, 2011, 81(2), 740-749.

[8] Farzaneh J, Keypour R, Ali Karsaz A, *A novel fast maximum power point tracking for a PV system using hybrid PSO-ANFIS algorithm under partial shading conditions*, International Journal of Industrial Electronics, Control and Optimization (IECO), 2019, 2(1), 47-58.

[9] Barati H, Shahsavari M, *Simultaneous Optimal placement and sizing of distributed generation resources and shunt capacitors in radial distribution systems using Crow Search Algorithm*, International Journal of Industrial Electronics, Control and Optimization (IECO), 2018, 1(1), 24-40.

[10] Bikdeli Sh, Farshad M, *Allocation of Fault Current Limiters in Power Systems Considering Fault Current, Cost, and Lost Power Indices Using Imperialist Competitive Algorithm*, International Journal of Industrial Electronics, Control and Optimization (IECO), 2020, 3(1), 91-102

[11] B.R.Adarsh, T.Raghunathan, T.Jayabarathi, Xin-SheYang, Economic dispatch using chaotic bat algorithm, Energy, 2016, 96(1), 666-675.

[12] Derafshi Beigvand S, Abdia H, La Scala M, *Combined heat and power economic dispatch problem using gravitational search algorithm*, Electr Power Syst Res, 2016, 133(1), 160-172.

[13] CalinSecui. D, *A modified Symbiotic Organisms Search algorithm for large scale economic dispatch problem with valve-point effects*, Energy, 2016, 113(1), 366-384.

[14] Chen G, Ding X, *Optimal economic dispatch with valve loading effect using self-adaptive firefly algorithm*, Applied Intelligence, 2015, 42(2), 276-288.

[15] Basu M, Chowdhury A, *Cuckoo search algorithm for economic dispatch*, Energy, 2013, 60(1), 99-108.

[16] AghayKabolia Abdullah S. Hr, Alqallafb. K, *Solving non-convex economic load dispatch problem via artificial cooperative search algorithm, Expert Systems with Applications*, 2019, 128r(1), 14-27

[17] Gholamghasemi.M, Akbari E, Asadpoor M.B,Ghasemi M, *A new solution to the non-convex economic load dispatch problems using phasor particle swarm optimization*, Applied Soft Computing, 2019, 79(1), 111-124.

[18] Silva Chavez J.C., Zamora-Mendez A, Yrena Heredia J.F, Cardenas-Javier. R, *A hybrid optimization framework for the non-convex economic dispatch problem via meta-heuristic algorithms*, Electr Power Syst Res,2019, 77(1), 1-10.

[19] Victoire, T. Aruldoss Albert, and A. Ebenezer Jeyakumar. "Hybrid PSO–SQP for economic dispatch with valve-point effect." Electric Power Systems Research 71.1 (2004): 51-59.

[20] Alsumait, J. S., J. K. Sykulski, and A. K. Al-Othman. "*A hybrid GA–PS–SQP method to solve power system valve-point economic dispatch problems*." Applied Energy 87.5 (2010): 1773-1781.

[21] https://www.gurobi.com/resource/mip-basics/

[22] Jeroslow, R. and Lowe, J., *Modelling with integer variables. Mathematical Programming Studies*, 1984, 22,167–84.

[23] N. Sinha,R.Chakrabarti,P.K.Chattopadhyay, *Evolutionary programming techniques for economic load dispatch*, IEEETrans.Evol.Comput.,2003, 7(1), 83–94.

[24] Yanga XY, Sadat Hosseini S.S, Gandomi AH, *Firefly Algorithm for solving non-convex economic dispatch problems with valve loading effect, Applied Soft Computing* , 2012, 12(1) ,1180–1186.

[25] Alsumait JS, Al-Othman AK, Sykulski JK, *Application of PS method to power system valve-point ELD*, Electr Power Energy Syst, 2007, 29(1),720–30.

[26] Dos Santos Coelho L,*, Cocco Mariani V, *An efficient cultural self-organizing migrating strategy for economic dispatch optimization with valve-point effect, Energy conversion and management*, 2010, 51(1), 2580–2587.

[27] Pereira-Neto A, Unsihuay C, Saavedra OR, *Efficient evolutionary strategy optimization procedure to solve the nonconvex economic dispatch problem with generator constraints*. IEE Proc Gen Transm Distrib 2005;152(5):653–60.

[28] Niu Q, Zhang H, Wanga X, Li K, Irwin G.B, *A hybrid harmony search with arithmetic crossover operation for economic dispatch*, . Int J Electr Power Energy Syst 2014; 62(1), 237–257.

[29] Kavousi-Fard A, Khosravi A, *An intelligent θ-Modified Bat Algorithm to solve the non-convex economic dispatch problem considering practical constraints*, Int J Electr Power Energy Syst 2016; 82(1), 189–196.

Hossein Sharifzadeh is an assistant professor of electrical engineering at Hakim Sabzevari University (HSU). He mainly works on application of modern optimization techniques and uncertainty handling on power systems operation. His current research interest is application of global optimization techniques on power system problems.

International Journal of Industrial Electronics, Control and Optimization © 2020 IECO
Vol. 3, No. 4, pp. 475-482, Sep (2020)

Novel Stability Criteria for Piecewise Affine Systems with Time-Varying Delay

Salehe Afsharian[1], Hussein Eliasi[2,†]

[1,2] Faculty of Electrical and Computer Engineering, University of Birjand, Birjand, Iran

ABSTRACT

This article aims to derive new sufficient conditions to guarantee the stability of piecewise affine systems with time-varying delay (PWA-TVD). The set of delay-dependent linear matrix inequality (LMI) describes the novel stability criteria. This approach considers the PWA-TVD system with a time-delayed state-dependent switching signal. The newly suggested Lyapunov-Krasovskii functional (L-K-F) and improved estimation of its derivative have a crucial role in decreasing the complexity and conservatism of the proposed stability results. The suggested L-K-F belongs to the current and time-delayed states, the integral of the states over the time-varying delay, and time derivation of the states. A new inequality was used to obtain an upper bound (UB) for the time derivation of the Lyapunov functional. Then based on this UB, less conservative results are achieved. The theoretical results are applied to the numerical examples. The results confirm the effectiveness of the presented method. The conservative index is the maximum admissible UB of time delay.

Article Info

Keywords:
Linear matrix inequality (LMI),Lyapunov-krasovskii functional, PWA systems, Stability analysis, Time-varying delay,

Article History:
Received 2020-01-19
Accepted 2020-04-19

I. Introduction

A piecewise affine (PWA) system is a dynamical system that contains multiple affine subsystems and a switching signal that allows switching between various subsystems. These systems have broad applications in a range of science and engineering. This type of system constructs a robust structure for to model a wide variety of hybrid and nonlinear systems in that nonlinearities are estimated by a set of linear-affine models around different operating points. [1].

A time delay is inevitable in the real world. It exists in industrial processes, control systems, energy systems, and so on. The time-delay may cause unsatisfactory efficiency, undesired oscillation, and also system instability. So, it is imperative to analyze the stability criterion of systems with time-delay [2].

The PWA systems with time-delay have a key role in the modeling of such systems as communication networks, highway transportation systems, automotive clutch systems, etc. Delay is an outstanding design and performance characteristic of these systems and cannot be ignored.

To study the stability of switching systems and PWA systems, the primary approach is to obtain a common Lyapunov function for the system under arbitrary switching [3]. For less conservative results, multiple Lyapunov functions have been proposed [4] - [7]. LyapunovKrasovskii functional and Lyapunov-Razumikhin functional techniques are used for time-delay systems to obtain stability criteria [8]. A critical goal in the delay-dependent stability analyses is to improve conditions in which one guarantees the stability for the allowable UB of time delay as large as possible. The conservativeness of the results depends on two points. The first one is the choice of proper Lyapunov functional. In order to improve the results, an augmented vector has been used to make a Lyapunov functional. Augmented state variables contain information about current and delayed states, their integral and their derivative. The stability of time-delay systems depends on the current states and their history, so the

†Corresponding Author: h_eliasi@birjand.ac.ir, Tel: +98-9122454027, Faculty of Electrical and Computer Engineering, University of Birjand, Birjand, Iran

use more states information in Lyapunov functional can be a less conservative way for stability analysis [9-12]. In all of these work, the novel augmented L-K-F are proposed, and according to this selection, the results will be less conservative. The other one is to estimate the bound of integral that appears in the time derivation of the Lyapunov functional. Several remarkable approaches have been reported to estimate a tighter bound of integral terms such as Wirtinger's inequality [13], free-weighting matrix [14], Jensen's inequality [2], double integral inequality [15], delay-dependent-matrix based (DDMB) reciprocally convex inequality [16], and etc.

The first time the PWA with time-delay systems to stability analysis has been discussed in [17]. Then the sufficient conditions that guarantee the stability of the PWA-TVD system have been investigated in [18-19]. In which, switching law is based on only the current states, and the results are more conservative. In [20-21], the state-dependent switching condition depends on the delayed states that are considered, but the delay is constant. In [22], stability conditions are derived for PWA-TVD systems with the switching law, which is dependent on the statesdependent delay and the delayed-states. Then a switching signal that is independent of the timedelayed states for the Lyapunov function is designed. In all of these works, LMIs depend only on the bound of delay and bound of its derivative, and therefore, the results are more conservative.

In the present work, the PWA-TVD systems with switching law, which is based on both the states and delayed states, are considered. We aim at improving the existing results by proposing a proper L-K-F and developing a new inequality used to derive a more accurate estimation of the lower bound of the integral, which appears in the time derivation of the L-K-F. The proposed L-K-F contains more information about the states. This Lyapunov functional depends on the current and delayed states, the integral of the states across the time-delay, and the time derivative of the states. Integral terms with time-varying delay intervals are considered in the suggested Lyapunov functional, and new stability conditions are presented, which depend on time-varying delay, and its derivative does not depend only on the bound of these. Also, we use new inequality to find the bound for the derivative of the Lyapunov functional, and we then propose stability criteria, which enhance the feasible region of stability, for the TVD-PWA system. The new stability results for the TVD-PWA system are formulated in terms of LMIs. These LMIs depend on time-varying delay and derivative of delay.

The paper is organized as below. The preliminaries and problem formulation are defined in in Section II. The main stability theorem is proposed in Section III. Section IV is dedicated to numerical examples. The paper is terminated with a conclusion paragraph in Section V.

Notation: $\mathbb{R}^{q\times r}$ is the set of all q×r real matrices. $\mathbb{S}^r$ denotes a set of symmetric r×r matrices. In addition Q > 0, for $Q\in\mathbb{R}^{n\times n}$, means that Q is positive definite. We describe $\mathrm{Sym}(X) = X + X^T$, for any square matrix $X\in\mathbb{R}^{n\times n}$. The notation I_d represents the appropriate unit matrix. The symbol * represents the symmetric structure. $K^{\perp}$ denotes the matrix basis for the null space of $K\in\mathbb{R}^{n\times m}$.

II. PROBLEM FORMULATION

The following formulation represents the PWA-TVD system:

$$S_1:\begin{Bmatrix}\dot{x}=A_ix(t)+A_i^dx_d(t)+a_i;\ \ x(t)=\sigma(t),\ t\epsilon[-h_d,0]\\ \forall\begin{bmatrix}x\\x_d\end{bmatrix}\epsilon\chi_i\ ,\ i\in I\end{Bmatrix}\tag{1}$$

where $x(t)\in\mathbb{R}^{n\times 1}$ is the system current states, $x_d(t)=x(t-d_h(t))$ is the delayed-states, $A_i, A_i^d\in\mathbb{R}^{n\times n}$ are the current state and time-delayed state matrices respectively, $a_i\in\mathbb{R}^{n\times 1}$ is the affine terms, and $\sigma(t)$ is an initial condition. The state space is partitioned to a number of polyhedral cell that are shown with $\chi_i=\left\{(a,b)\in R^n\times R^n\,\middle|\,\bar{E}_i\begin{bmatrix}a\\1\end{bmatrix}\geq 0,\ \bar{E}_i^d\begin{bmatrix}b\\1\end{bmatrix}\geq 0\right\}$, where $\bar{E}_i=[E_i\ \ e_i]$, $\bar{E}_i^d=[E_i^d\ \ e_i^d]$ are the cell boundaries matrices. $I=\{1,\ldots,\Xi\}$ shows the index of the subsystems. $d_h(t)$ is a time-varying delay, which value and its rate are bounded:

$$0\leq d_h(t)\leq h_d,\ -\mu\leq\dot{d}_h(t)\leq\mu\tag{2}$$

The state space can be partitioned as below:

$$\begin{bmatrix}\bar{E}_i & \bar{E}_i^d\end{bmatrix}\begin{bmatrix}\bar{x}(t)\\ \bar{x}_d(t)\end{bmatrix}\geq 0;\ \forall\begin{bmatrix}x\\x_d\end{bmatrix}\epsilon\chi_i\ ,\ i\in I\tag{3}$$

where $\bar{x}(t)\triangleq[x(t)\ \ 1]^T$, and $\bar{x}_d(t)\triangleq[x_d(t)\ \ 1]^T$.

The continuity matrices $\bar{F}_i=[F_i\ \ f_i]$, $\bar{F}_i^d=[F_i^d\ \ f_i^d]$, satisfying:

$$\begin{gathered}[\bar{F}_i\ \ \bar{F}_i^d][\bar{x}(t)\ \ \bar{x}_d(t)]^T=[\bar{F}_j\ \ \bar{F}_j^d][\bar{x}(t)\ \ \bar{x}_d(t)]^T\\ \forall\begin{bmatrix}x\\x_d\end{bmatrix}\epsilon\chi_i\cap\chi_j,\ i,j\ \epsilon I\end{gathered}\tag{4}$$

The following in [23] can construct these matrices.

Define the following augmented matrices; $\bar{A}_i=\begin{bmatrix}A_i & a_i\\0 & 0\end{bmatrix}$, $\bar{A}_i^d=\begin{bmatrix}A_i^d & o\\0 & 0\end{bmatrix}$, thus the system (1) is formulated as:

$$S_2:\left\{\dot{\bar{x}}(t)=\bar{A}_i\bar{x}(t)+\bar{A}_i^d\bar{x}_d(t);\ \forall\begin{bmatrix}x\\x_d\end{bmatrix}\epsilon\chi_i\ ,\ i\in I\right\}\tag{5}$$

The subsystems that contain the origin is expressed by I_0, and other subsystems are denoted by I_1.

III. MAIN RESULT

In this section, the set of delay-dependent LMI-based sufficient conditions is extracted to analyze the stability of the PWA-TVD. We introduce the following lemmas that will be used in the extraction of the stability criteria. Then, the main theorem is presented.

Lemma 1 [24]: If y is a differentiable function:$[\vartheta_1,\vartheta_2]\rightarrow R^n$, for any matrices $M_2\in\mathbb{R}^{3n\times 3n}$and $V_1, V_2\in\mathbb{R}^{3n\times n}$and symmetric matrices $M_1, M_3\in\mathbb{R}^{3n\times 3n}$, and $Q\in\mathbb{R}^{n\times n}$, and satisfying:

$$\begin{bmatrix} M_1 & M_2 & V_1 \\ * & M_3 & V_2 \\ * & * & Q \end{bmatrix}\geq 0 \tag{6}$$

the following inequality holds:

$$-\int_{\vartheta_1}^{\vartheta_2}\dot{y}^T(s)Q\dot{y}(s)ds\leq\varpi_1^T(\vartheta_1,\vartheta_2)\psi_1\varpi_1(\vartheta_1,\vartheta_2) \tag{7}$$

Where

$$\varpi_1(\vartheta_1,\vartheta_2)=\begin{bmatrix} y^T(\vartheta_1) & y^T(\vartheta_2) & \frac{1}{\vartheta_1-\vartheta_2}\int_{\vartheta_1}^{\vartheta_2}y^T(s)ds \end{bmatrix}$$

$$\psi_1=(\vartheta_2-\vartheta_1)\left(M_1+\frac{1}{3}M_3\right)+ \mathrm{Sym}\{V_1[I_d \quad -I_d \quad 0]+V_2[-I_d \quad -I_d \quad 2I_d]\}$$

Lemma 2 [25]: (Finsler's Lemma) Let $W\in\mathbb{R}^n$, $S\in\mathbb{S}^n$, and $K\in\mathbb{R}^{m\times n}$ so that Rank (K) < n. The statements (1) and (2) are equivalent to:

(1) $W^TS\,W<0, \forall KW=0, x\neq 0$

(2) $K^{\perp T}S\,K^{\perp}<0$;

Finsler's lemma can be used to give novel linear matrix inequality characterizations to stability and control problems.

We now present novel stability criteria for the PWA-TVD system, which conditions are dependent of time-delay.

Theorem 1: For positive constants h_d and μ, the system (1), in the absence of sliding behavior, is asymptotically stable, if there exist, positive symmetric matrices $R, S, Q, Z, Z_1, Z_2, Z_3, Z_4 (\forall i\in I_0)$, $\bar{R}, \bar{S}, \bar{Q}, \bar{Z}, \bar{Z}_1, \bar{Z}_2, \bar{Z}_3, \bar{Z}_4 (\forall i\in I_1)$, any matrices$Y_1, Y_2$ $(\forall i\in I_0)$, $\bar{Y}_1, \bar{Y}_2$ $(\forall i\in I_1)$, N_1, N_2, N_3, N_4 $(\forall i\in I_0)$, $\bar{N}_1, \bar{N}_2, \bar{N}_3, \bar{N}_4$ $(\forall i\in I_1)$, symmetric matrices $L_1\in\mathbb{R}^{m\times m}$, $H_i\in\mathbb{R}^{n\times n}$ $(i\in I)$ such that H_i have nonnegative entries, where:

$$P_i=\begin{bmatrix} F_i^TL_1F_i & F_i^TL_1F_i^d \\ F_i^{dT}L_1F_i & F_i^{dT}L_1F_i^d \end{bmatrix}, \forall i\in I_0;$$

$$\bar{P}_i=\begin{bmatrix} \bar{F}_i^TL_1\bar{F}_i & \bar{F}_i^TL_1\bar{F}_i^d \\ \bar{F}_i^{dT}L_1\bar{F}_i & \bar{F}_i^{dT}L_1\bar{F}_i^d \end{bmatrix}, \forall i\in I_1$$

,which satisfy the following LMIs for every region and for $\forall d_h(t)\in\{0,h_d\}$, $\dot{d}_h(t)\in\{-\mu,\mu\}$.

For $\forall i\in I_0$

$$\begin{bmatrix} Z_1 & Y_1 & N_1 \\ * & Z_2 & N_2 \\ * & * & R \end{bmatrix}\geq 0, \begin{bmatrix} Z_3 & Y_2 & N_3 \\ * & Z_4 & N_4 \\ * & * & R \end{bmatrix}\geq 0; \quad Z_{1,2,3,4}\in\mathbb{R}^{3n\times 3n}, N_{1,2,3,4}\in\mathbb{R}^{3n\times n}, Y_{1,2}\in R^{3n\times 3n}, R\in\mathbb{R}^{n\times n} \tag{8}$$

$$P_i-\begin{bmatrix} E_i^TH_iE_i & E_i^TH_iE_i^d \\ E_i^{dT}H_iE_i & E_i^{dT}H_iE_i^d \end{bmatrix}>0 \tag{9}$$

$$(B_i^{\perp})^T\psi_i(B_i^{\perp})<0 \tag{10}$$

where

$B_i=[A_i \quad A_i^d \quad 0 \quad -I_d \quad 0 \quad 0 \quad 0 \quad 0]$; $h_t(t)=1-\dot{d}_h(t)$,

$b_j(j=1,\ldots,8)\in R^{8n\times n}$:block entry matrices, $b_0=0_{8n\times n}$;

$\psi_i=\mathrm{Sym}\{E_1P_iE_2^T\}+\mathrm{Sym}\{E_3SE_4^T\}+\Omega_1+\Omega_2+h_de_4Re_4^T+\Phi_1+\Phi_2$

$\Omega_1=E_5QE_5^T-h_tE_6QE_6^T+\mathrm{Sym}\{E_7QE_8^T\}$;

$\Omega_2=h_tE_9ZE_9^T-E_{10}ZE_{10}^T+\mathrm{Sym}\{E_{11}ZE_{12}^T\}$

$E_1=[b_1 \quad b_2]$, $E_2=[b_4 \quad h_tb_5]$, $E_3=[b_3 \quad d_h(t)b_7 \quad (h_d-d_h(t))b_8]$,

$E_4=[b_6 \quad b_1-h_tb_2 \quad h_tb_2-b_3]$,

$E_5=[b_1 \quad b_4 \quad b_0]$, $E_6=[b_2 \quad b_5 \quad b_1-b_2]$,

$E_7=[d_h(t)b_7 \quad b_1-b_2 \quad d_h(t)(b_1-b_7)]$,

$E_8=[b_0 \quad b_0 \quad b_4]$, $E_9=[b_2 \quad b_5 \quad b_0]$, $E_{10}=[b_3 \quad b_6 \quad b_2-b_3]$,

$E_{11}=[(h_d-d_h(t))b_8 \quad b_2-b_3 \quad (h_d-d_h(t))(b_2-b_8)]$,

$E_{12}=[b_0 \quad b_0 \quad h_tb_5]$, $E_{13}=[b_1 \quad b_2 \quad b_7]$, $E_{14}=[b_2 \quad b_3 \quad b_8]$

$$\Phi_1=d_h(t)E_{13}\left(Z_1+\frac{1}{3}Z_2\right)E_{13}^T+ \mathrm{Sym}\{E_{13}(N_1(b_1-b_2)^T+N_2(2b_7-b_1-b_2)^T\}$$

$$\Phi_2=(h_d-d_h(t))E_{14}\left(Z_3+\frac{1}{3}Z_4\right)E_{14}^T+ \mathrm{Sym}\{E_{14}(N_3(b_2-b_3)^T+N_4(2b_8-b_2-b_3)^T\}$$

$$S=\begin{bmatrix} S_{11} & S_{12} & S_{13} \\ S_{12}^T & S_{22} & S_{23} \\ S_{13}^T & S_{23}^T & S_{33} \end{bmatrix}, Q=\begin{bmatrix} Q_{11} & Q_{12} & Q_{13} \\ Q_{12}^T & Q_{22} & Q_{23} \\ Q_{13}^T & Q_{23}^T & Q_{33} \end{bmatrix},$$

$$Z=\begin{bmatrix} Z_{11} & Z_{12} & Z_{13} \\ Z_{12}^T & Z_{22} & Z_{23} \\ Z_{13}^T & Z_{23}^T & Z_{33} \end{bmatrix}$$

$R\in\mathbb{R}^{n\times n}$, $S\in\mathbb{R}^{3n\times 3n}$,$Q\in R^{3n\times 3n}$, $Z\in\mathbb{R}^{3n\times 3n}$

For $\forall i\in I_1$

$$\begin{bmatrix} \bar{Z}_1 & \bar{Y}_1 & \bar{N}_1 \\ * & \bar{Z}_2 & \bar{N}_2 \\ * & * & \bar{R} \end{bmatrix}\geq 0, \begin{bmatrix} \bar{Z}_3 & \bar{Y}_2 & \bar{N}_3 \\ * & \bar{Z}_4 & \bar{N}_4 \\ * & * & \bar{R} \end{bmatrix}\geq 0 \quad \bar{Z}_{1,2,3,4}\in\mathbb{R}^{3(n+1)\times 3(n+1)}, \bar{N}_{1,2,3,4}\in\mathbb{R}^{3(n+1)\times(n+1)}, \bar{Y}_{1,2}\in\mathbb{R}^{3(n+1)\times 3(n+1)}, \bar{R}\in\mathbb{R}^{(n+1)\times(n+1)} \tag{11}$$

$$\bar{P}_i-\begin{bmatrix} \bar{E}_i^TH_i\bar{E}_i & \bar{E}_i^TH_i\bar{E}_i^d \\ \bar{E}_i^{dT}H_i\bar{E}_i & \bar{E}_i^{dT}H_i\bar{E}_i^d \end{bmatrix}>0 \tag{12}$$

$$(\bar{B}_i^{\perp})^T\bar{\psi}_i(\bar{B}_i^{\perp})<0 \tag{13}$$

where

$\bar{B}_i=[\bar{A}_i \quad \bar{A}_i^d \quad 0 \quad -I_d \quad 0 \quad 0 \quad 0 \quad 0]$,

$\bar{b}_j(j=1,2,\ldots,8)\in R^{8(n+1)\times(n+1)}$, $\bar{b}_0=0_{8(n+1)\times(n+1)}$

$\bar{\psi}_i=\mathrm{Sym}\left\{\bar{E}_1\bar{P}_i\bar{E}_2^T\right\}+\mathrm{Sym}\left\{\bar{E}_3\bar{S}\,\bar{E}_4^T\right\}+\bar{\Omega}_1+\bar{\Omega}_2+h_d\bar{e}_4\bar{R}\bar{e}_4^T+\bar{\Phi}_1+\bar{\Phi}_2$

$$\bar{\Omega}_1=\bar{E}_5\bar{Q}\bar{E}_5^T-h_t\bar{E}_6\bar{Q}\,\bar{E}_6^T+\mathrm{Sym}\left\{\bar{E}_7\bar{Q}\,\bar{E}_8^T\right\}$$
$$\bar{\Omega}_2=h_t\bar{E}_9\bar{Z}\,\bar{E}_9^T-\bar{E}_{10}\bar{Z}\bar{E}_{10}^T+\mathrm{Sym}\left\{\bar{E}_{11}\bar{Z}\,\bar{E}_{12}^T\right\}$$
$$\bar{E}_1=[\bar{b}_1 \quad \bar{b}_2],\ \bar{E}_2=[\bar{b}_4 \quad h_t\bar{b}_5],$$
$$\bar{E}_3=[\bar{b}_3 \quad d_h(t)\bar{b}_7 \quad (h_d-d_h(t))\bar{b}_8],\ \bar{E}_4=[\bar{b}_6 \quad \bar{b}_1-h_t\bar{b}_2 \quad h_t\bar{b}_2-\bar{b}_3],$$
$$\bar{E}_5=[\bar{b}_1 \quad \bar{b}_4 \quad \bar{b}_0],\ \bar{E}_6=[\bar{b}_2 \quad \bar{b}_5 \quad \bar{b}_1-\bar{b}_2]$$
$$\bar{E}_7=[d_h(t)\bar{b}_7 \quad \bar{b}_1-\bar{b}_2 \quad d_h(t)(\bar{b}_1-\bar{b}_7)]$$
$$\bar{E}_8=[\bar{b}_0 \quad \bar{b}_0 \quad \bar{b}_4],\ \bar{E}_9=[\bar{b}_2 \quad \bar{b}_5 \quad \bar{b}_0],\ \bar{E}_{10}=[\bar{b}_3 \quad \bar{b}_6 \quad \bar{b}_2-\bar{b}_3]$$
$$\bar{E}_{11}=[(h_d-d_h(t))\bar{b}_8 \quad \bar{b}_2-\bar{b}_3 \quad (h_d-d_h(t))(\bar{b}_2-\bar{b}_8)],$$
$$\bar{E}_{12}=[\bar{b}_0 \quad \bar{b}_0 \quad h_t\bar{b}_5],$$
$$\bar{E}_{13}=[\bar{b}_1 \quad \bar{b}_2 \quad \bar{b}_7],\ \bar{E}_{14}=[\bar{b}_2 \quad \bar{b}_3 \quad \bar{b}_8]$$
$$\bar{\Phi}_1=d_h(t)\bar{E}_{13}\left(\bar{Z}_1+\frac{1}{3}\bar{Z}_2\right)\bar{E}_{13}^T+$$
$$\mathrm{Sym}\{\bar{E}_{13}(\bar{N}_1(\bar{b}_1-\bar{b}_2)^T+\bar{N}_2(2\bar{b}_7-\bar{b}_1-\bar{b}_2)^T\}$$
$$\bar{\Phi}_2=(h_d-d_h(t))\bar{E}_{14}\left(\bar{Z}_3+\frac{1}{3}\bar{Z}_4\right)\bar{E}_{14}^T+$$
$$\mathrm{Sym}\{\bar{E}_{14}(\bar{N}_3(\bar{b}_2-\bar{b}_3)^T+\bar{N}_4(2\bar{b}_8-\bar{b}_2-\bar{b}_3)^T\}$$

$$\bar{R}=\begin{bmatrix} R & R_{12} \\ R_{12}^T & R_{22}\end{bmatrix}>0,\ \bar{S}=\begin{bmatrix} S_{11} & 0 & S_{12} & 0 & S_{13} & 0 \\ * & 0 & 0 & 0 & 0 & 0 \\ * & * & S_{22} & 0 & S_{23} & 0 \\ * & * & * & 0 & 0 & 0 \\ * & * & * & * & S_{33} & 0 \\ * & * & * & * & * & 0 \end{bmatrix}>0$$

$$\bar{Q}=\begin{bmatrix} Q_{11} & 0 & Q_{12} & Q_{121} & Q_{13} & Q_{131} \\ * & 0 & 0 & 0 & 0 & 0 \\ * & * & Q_{22} & Q_{221} & Q_{23} & Q_{213} \\ * & * & * & Q_{222} & Q_{231}^T & Q_{232} \\ * & * & * & * & Q_{33} & Q_{331} \\ * & * & * & * & * & Q_{332} \end{bmatrix},$$

$$\bar{Z}=\begin{bmatrix} Z_{11} & 0 & Z_{12} & Z_{121} & Z_{13} & Z_{131} \\ * & 0 & 0 & 0 & 0 & 0 \\ * & * & Z_{22} & Z_{221} & Z_{23} & Z_{231} \\ * & * & * & Z_{222} & Z_{231}^T & Z_{232} \\ * & * & * & * & Z_{33} & Z_{331} \\ * & * & * & * & * & Z_{332} \end{bmatrix}$$

$$\bar{S}\in\mathbb{R}^{3(n+1)\times 3(n+1)},\bar{Q}\in\mathbb{R}^{3(n+1)\times 3(n+1)},\ \bar{Z}\in\mathbb{R}^{3(n+1)\times 3(n+1)}$$

Proof: For $\forall i\in I_0$, the L-K-F is proposed as follow:

$$V_i(t,x,\dot{x})=V_{1i}(t,x)+\sum_{g=2}^{5}V_g(t,x,\dot{x})$$
$$V_{1i}(t,x)=\eta_1^T(t)P_i\eta_1(t),\ \ V_2(t,x)=\eta_2^T(t)S\eta_2(t),$$
$$V_3(t,x,\dot{x})=\int_{t-d_h(t)}^{t}\eta_3^T(y)Q\eta_3(y)dy,$$
$$V_4(t,x,\dot{x})=\int_{t-d_h(t)}^{t}\eta_4^T(y)Z\eta_4(y)dy,$$
$$V_5(t,x,\dot{x})=\int_{t-h_d}^{t}\int_{y}^{t}\dot{x}^T(w)R\dot{x}(w)dw\,dy$$
$$\eta_1(t)\triangleq[x^T(t) \quad x_d{}^T(t)]^T$$
$$\eta_2(t)\triangleq\left[x^T(t-h_d) \quad \int_{t-d_h(t)}^{t}x^T(w)dw \quad \int_{t-h_d}^{t-d_h(t)}x^T(w)dw\right]^T$$
$$\eta_3(y)\triangleq\left[x^T(y) \quad \dot{x}^T(y) \quad \int_y^t\dot{x}^T(w)dw\right]^T,$$
$$\eta_4(y)\triangleq\left[x^T(y) \quad \dot{x}^T(y) \quad \int_y^{t-d_h(t)}\dot{x}^T(w)dw\right]^T$$

According to Schur complement and positive definiteness of S, Q, Z, R, the proposed L-K-F is positive definite from LMI (9)

Define:

$$\xi^T(t)\triangleq[x^T(t) \quad x_d{}^T(t) \quad x^T(t-h_d) \quad \dot{x}^T(t) \quad \dot{x}_d{}^T(t) \quad \dot{x}^T(t-h_d)$$
$$\frac{1}{d_h(t)}\int_{t-h_d}^{t-d_h(t)}x^T(w)dw \quad \frac{1}{h_d-d_h(t)}\int_{t-h_d}^{t-d_h(t)}x^T(w)dw\,]$$

Calculating the time derivative of V_i gives:

$$\frac{\partial v_i}{\partial t}=\frac{\partial v_{1i}}{\partial t}+\sum_{v=2}^{5}\frac{\partial v_v}{\partial t}$$

where

$$\frac{\partial v_{1i}}{\partial t}=\xi^T(t)\ \mathrm{Sym}\{E_1P_iE_2^T\}\xi(t),$$
$$\frac{\partial v_2}{\partial t}=\xi^T(t)\ \mathrm{Sym}\{E_3SE_4^T\}\xi(t),\ \frac{\partial v_3}{\partial t}=\xi^T(t)\Omega_1\xi(t),$$
$$\frac{\partial v_4}{\partial t}=\xi^T(t)\Omega_2\xi(t),\ \frac{\partial v_5}{\partial t}=\xi^T(t)h_de_4Re_4^T\xi(t)-$$
$$\int_{t-h_d}^{t-d_h(t)}\dot{x}^T(w)R\dot{x}(w)dw-\int_{t-d_h(t)}^{t}\dot{x}^T(w)R\dot{x}(w)dw$$

By applying Lemma (1) with LMI (8), the UB of the derivative can be estimated as:

$$\frac{\partial v_i}{\partial t}\leq\xi^T(t)\psi_i\xi(t) \tag{14}$$

According to Lemma (2), it is clear that if LMI (10) holds, then inequality (14) is satisfied.

For $i\in I_1$ consider the L-K-F as bellow:

$$\bar{V}_i(t,x,\dot{x})=\bar{V}_{1i}(t,x)+\bar{V}_2(t,x)+\bar{V}_3(t,x,\dot{x})+\bar{V}_4(t,x,\dot{x})+\bar{V}_5(t,x,\dot{x})$$
$$\bar{V}_{1i}(t,x)=\bar{\eta}_1^T(t)\bar{P}_i\bar{\eta}_1(t),\ \bar{V}_2(t,x)=\bar{\eta}_2^T(t)\bar{S}\bar{\eta}_2(t),$$
$$\bar{V}_3(t,x,\dot{x})=\int_{t-d_h(t)}^{t}\bar{\eta}_3^T(y)\bar{Q}\bar{\eta}_3(y)dy,$$
$$\bar{V}_4(t,x,\dot{x})=\int_{t-d_h(t)}^{t}\bar{\eta}_4^T(y)\bar{Z}\bar{\eta}_4(y)dy,$$
$$\bar{V}_5(t,x,\dot{x})=\int_{t-h_d}^{t}\int_{y}^{t}\dot{\bar{x}}^T(w)\bar{R}\dot{\bar{x}}(w)dw\,dy$$
$$\bar{\eta}_1(t)=[\bar{x}^T(t) \quad \bar{x}_d{}^T(t)]^T,$$
$$\bar{\eta}_2(t)=\left[\bar{x}^T(t-h_d) \quad \int_{t-d_h(t)}^{t}\bar{x}^T(w)dw \quad \int_{t-h_d}^{t-d_h(t)}\bar{x}^T(w)dw\right]^T$$
$$\bar{\eta}_3(y)=\left[\bar{x}^T(y) \quad \dot{\bar{x}}^T(y) \quad \int_y^t\dot{\bar{x}}^T(w)dw\right]^T$$
$$\bar{\eta}_4(y)=\left[\bar{x}^t(y) \quad \dot{\bar{x}}^T(y) \quad \int_y^{t-d_h(t)}\dot{\bar{x}}^T(w)dw\right]^T$$

A similar approach to $\forall i\in I_0$ can be repeated for this case.

According to LMI (12) and positive definiteness of $\bar{R}$, $\bar{S}$, $\bar{Q}$, $\bar{Z}$, the Lyapunov functional is positive definite. LMI (13) with respect to LMI (11) guarantees that the derivative of Lyapunov functional decreases over time.

Note that $V_2=\bar{V}_2$, $V_3=\bar{V}_3$, $V_4=\bar{V}_4$, $V_5=\bar{V}_5$, and the condition that guarantees the continuity of V_1 and $\bar{V}_1$ at the boundaries can be obtained by using the appropriate continuity matrices.☐

The suggested Lyapunov functional is continuous, but its derivative is not continuous at all points of the state space, so Theorem 1 is confirmed if sliding behavior does not occur at the boundaries. It is necessary to study of the appearance of the charming sliding modes at the boundaries for the PWA systems. An analysis to recognize this sliding mode according to the Filippov solution is discussed in [23].

IV. NUMERICAL EXAMPLES

This section, presents three numerical examples to illustrate the effectiveness of the proposed stability conditions. In the first example, it is considered a switched linear time-delay system. In this system, the delay is constant and switching law depends on the current states. In the second example, it is considered the equation of the water level changes in a tank. In this example, the delay is time-varying and switching law depends on the current states. The third example is about the equation of motion of a simple pendulum. In this example, the delay is constant and switching law depends on the delayed states as well as the current states. The characteristics of these examples are given in Table 1. The conservatism of delay-dependent stability conditions is checked by computing the maximum allowable UB of time delay.

Table I
The characteristics of the studied systems

	Type of delay	Dependence type of switching law
Example 1	Constant	Current states
Example 2	Time-varying	Current states
Example 3	Constant	Current states and delayed states

Example 1: Suppose the switched linear time-delay system $\dot{x}=A_i x(t)+A_{di}x(t-d_h)$ with the system matrices given by:

$$A_1=\begin{bmatrix}-0.1 & 0\\ 0 & -0.1\end{bmatrix},$$

$$A_2=\begin{bmatrix}-0.1 & 0\\ 0 & -0.1\end{bmatrix}, A_3=\begin{bmatrix}-0.1 & 0\\ 0 & -0.1\end{bmatrix}, A_4=\begin{bmatrix}-0.1 & 0\\ 0 & -0.1\end{bmatrix};$$

$$A_1^d=\begin{bmatrix}0 & 5\\ -1 & 0\end{bmatrix}, A_2^d=\begin{bmatrix}0 & 1\\ -5 & 0\end{bmatrix} A_3^d=\begin{bmatrix}0 & 5\\ -1 & 0\end{bmatrix} A_4^d=\begin{bmatrix}0 & 1\\ -5 & 0\end{bmatrix};$$

and the cell partition:

$$E_1=\begin{bmatrix}-1 & 1\\ -1 & -1\end{bmatrix}, E_2=\begin{bmatrix}-1 & 1\\ 1 & 1\end{bmatrix}, E_3=\begin{bmatrix}1 & -1\\ 1 & 1\end{bmatrix}, E_4=\begin{bmatrix}1 & -1\\ -1 & -1\end{bmatrix};$$

In this system, the time-delay is constant (d_h), and the switching law depends on the current states. Table 2 shows the maximum allowable time delay obtained by Theorem 1 (h_d) and existing methods [17-21]. As shown in this table, the results obtained by Theorem 1 are less conservative than the currently existing ones.

Table II
Comparison of UB of delay for example 1

Methods	Feasible UB for delay (h_d)
[17]	0.0142
[18,19]	0.0142
[20,21]	0.0168
Theorem 1	0.0193

The state trajectories of the system with initial conditions $[-2,0]^T$ are shown in Fig.1. As shown in this figure, the system is stable for $d_h = 0.02$ and unstable for $d_h = 0.021$. According to this, the theoretical maximum UB for time-delay in the system is between 0.02 and 0.021. Therefore, the simulation results confirm less conservatism in Theorem 1.

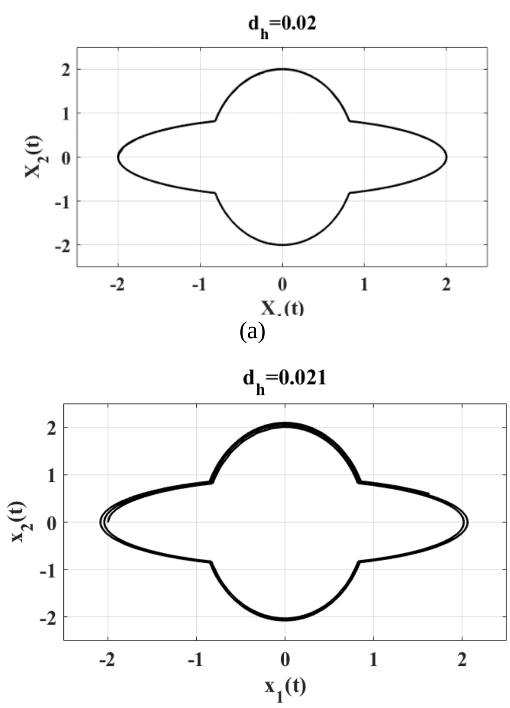

Fig.1: The state trajectories of the system in Example 1 with (a) $d_h = 0.02$ and (b) $d_h = 0.021$

Example 2: Fig.2 shows a water tank and a pipe with length of *L*. In this example, a water tank system with a nonlinear model has the following statement [18]:

$$\dot{x}(t)=\frac{1}{A\varphi}\left(-\frac{1}{H}\sqrt{\varphi g x(t)}+u_{in}\left(t-d_h(t)\right)\right) \quad (15)$$

where $g=9.8\ ms^{-2}$, $\varphi=1000\ kgm^{-3}$, $H=11.3882\ m^{-1/2}kg^{-1/2}$ and $A=10\ m^2$. The pipe length L makes a time-varying delay ($d_h(t)$) in the water inflow to the tank. The goal is to keep the water level at x=0.5cm. We obtained a PWA model of the system with linearization around two operating point x_0=0.25 cm, x_0=0.75 cm, as follow as:

$$\dot{x}(t)=\frac{-gx(t)}{2AH\sqrt{0.25\varphi g}}+\frac{1}{A\varphi}u_{in}(t-d(t)) + \left(\frac{0.25g}{2AH\sqrt{0.25\varphi g}}-\frac{\sqrt{0.25\varphi g}}{\varphi AH}\right);\quad 0\leq x(t)<0.5$$

$$\dot{x}(t)=\frac{-gx(t)}{2AH\sqrt{0.75\varphi g}}+\frac{1}{A\varphi}u_{in}(t-d(t))+ \left(\frac{0.75g}{2AH\sqrt{0.75\varphi g}}-\frac{\sqrt{0.75\varphi g}}{\varphi AH}\right);\quad 0.5\leq x(t)<1$$

and the cell partition is obtained:

$$E_1=\begin{bmatrix}-1 & 0.5\\ 0 & 1\end{bmatrix},\ E_2=\begin{bmatrix}1 & -0.5\\ 0 & 1\end{bmatrix}$$

The switching law is based on the current states.

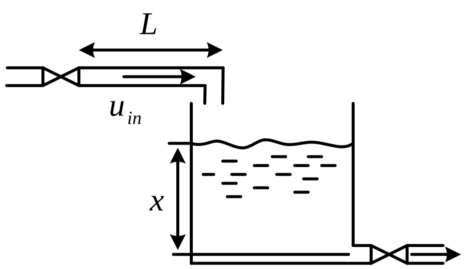

Fig.2: Water tank

Suppose a control input denoted as below:

$u_{in}(t)=0.2A\varphi x(t),\qquad 0\leq x(t)<0.5$

$u_{in}(t)=-0.1A\varphi x(t),\qquad 0.5\leq x(t)<1$

Fig.3 shows the level of water for the system without delay. As shown in this figure, the system without delay is stable. But in practice the system should be considered with delay. Incrasing the delay can cause closed-loop instability. Therefore, it is necessary to found the maximum allowable upper bound of the time-delay for which the stability of the closed loop system is guaranteed.

Table 3 shows the results for the maximum allowable time-varying delay for various bounds of the time derivative of the time delay obtained by Theorem 1. In Table 3, μ is the UB of the derivative of time delay, as shown in (2). It can be verified with the simulation that the nonlinear system is marginal stable for constant delay d_h=6.53 as shown in Fig. 4 and the system is unstable for d_h=6.54. The maximum allowable constant delay obtained with Theorem 1 for the equivalence PWA system is h_d=6.265.

Table III

The maximum allowable time-varying delay for several of μ

μ	0.1	0.3	0.6
Maximum allowable delay	6.09	4.94	0.02

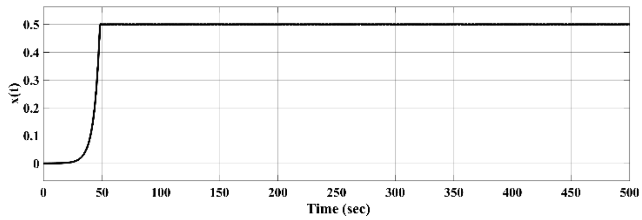

Fig. 3: The water level in the tank without delay

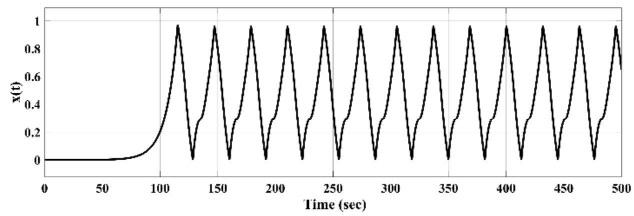

Fig. 4: The water level in the tank with constant input delay d_h=6.53

Example 3: In this example, a simple pendulum motion model with constant time delay (d_h) between the sensor and the controller is considered as bellow [20]:

$$M_pL_p^2\ddot{\vartheta}(t)=-M_pgL_p\sin(\vartheta(t))+T(t-d_h)\tag{16}$$

where M_p=1kg is the mass of pendulum, L_p=9.8m is the length of pendulum, g is the gravity of earth, and T is the input torque. A PWA model of this system with time delay and the switching conditions, which depend on both the states and the delayed states, is obtained in [20]:

$$\begin{bmatrix}\dot{\vartheta}(t)\\ \ddot{\vartheta}(t)\end{bmatrix}=\begin{bmatrix}0 & 1\\ -0.825 & 0\end{bmatrix}\begin{bmatrix}\vartheta(t)\\ \dot{\vartheta}(t)\end{bmatrix}+\begin{bmatrix}0 & 0\\ -1 & -1\end{bmatrix}\begin{bmatrix}\vartheta(t-d_h)\\ \dot{\vartheta}(t-d_h)\end{bmatrix};\ \forall\begin{bmatrix}\vartheta(t-d_h)\\ \dot{\vartheta}(t-d_h)\end{bmatrix}\in\Psi1$$

$$\begin{bmatrix}\dot{\vartheta}(t)\\ \ddot{\vartheta}(t)\end{bmatrix}=\begin{bmatrix}0 & 1\\ -0.825 & 0\end{bmatrix}\begin{bmatrix}\vartheta(t)\\ \dot{\vartheta}(t)\end{bmatrix}+\begin{bmatrix}0 & 0\\ -5 & -5\end{bmatrix}\begin{bmatrix}\vartheta(t-d_h)\\ \dot{\vartheta}(t-d_h)\end{bmatrix};\ \forall\begin{bmatrix}\vartheta(t-d_h)\\ \dot{\vartheta}(t-d_h)\end{bmatrix}\in\Psi2$$

$$\begin{bmatrix}\dot{\vartheta}(t)\\ \ddot{\vartheta}(t)\end{bmatrix}=\begin{bmatrix}0 & 1\\ -0.4875 & 0\end{bmatrix}\begin{bmatrix}\vartheta(t)\\ \dot{\vartheta}(t)\end{bmatrix}+\begin{bmatrix}0 & 0\\ -1 & -1\end{bmatrix}\begin{bmatrix}\vartheta(t-d_h)\\ \dot{\vartheta}(t-d_h)\end{bmatrix};\ \forall\begin{bmatrix}\vartheta(t-d_h)\\ \dot{\vartheta}(t-d_h)\end{bmatrix}\in\Psi3$$

$$\begin{bmatrix}\dot{\vartheta}(t)\\ \ddot{\vartheta}(t)\end{bmatrix}=\begin{bmatrix}0 & 1\\ -0.4875 & 0\end{bmatrix}\begin{bmatrix}\vartheta(t)\\ \dot{\vartheta}(t)\end{bmatrix}+\begin{bmatrix}0 & 0\\ -5 & -5\end{bmatrix}\begin{bmatrix}\vartheta(t-d_h)\\ \dot{\vartheta}(t-d_h)\end{bmatrix};\ \forall\begin{bmatrix}\vartheta(t-d_h)\\ \dot{\vartheta}(t-d_h)\end{bmatrix}\in\Psi4$$

with partitions:

$\Psi1:\{-0.7854\leq\vartheta(t)\leq0,\ -0.7854\leq\vartheta(t-d_h)\leq0\}$;

$\Psi2:\{-0.7854\leq\vartheta(t)\leq0,\ 0\leq\vartheta(t-d_h)\leq0.7854\}$;

$\Psi3:\{0\leq\vartheta(t)\leq0.7854,\ -0.7854\leq\vartheta(t-d_h)\leq0\}$;

$\Psi4:\{0\leq\vartheta(t)\leq0.7854,\ 0\leq\vartheta(t-d_h)\leq0.7854\}$;

The simulation results are given in Fig. 5, and 6 and show that the system is stable with d_h=0.19, but becomes unstable when d_h=0.196, which implies that the theoretical UB of the delay is between 0.19 and 0.196. The maximum allowable delay obtained with Theorem 1 for this system is h_d=0.18. Due to switching based on delayed-states, the methods proposed in

[17-19] cannot deal with this example and the maximum upper bound that is obtained in [20], is h_d=0.161. As a result, the proposed approach can achieve less conservative estimate of the UB for the delay in this system.

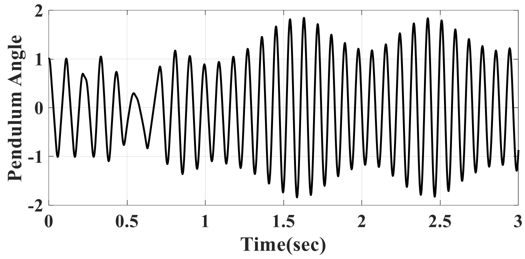

Fig. 5: The pendulum angle for d_h=0.19

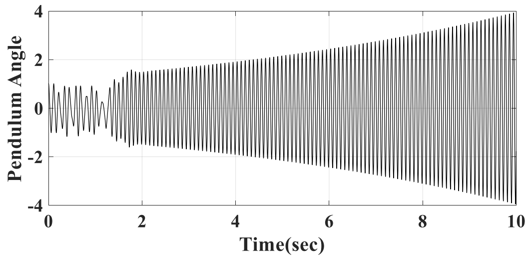

Fig. 6: The pendulum angle for d_h=0.196

V. CONCLUSIONS

This paper introduced novel stability conditions for the PWA-TVD system. It is considered that the system switches are based on both the states and the delayed states. The stability criteria for the PWA-TVD system have been established in terms of LMIs. By choosing the improved L-K-F and using new inequality for the estimation of its derivative, the derived results are less complex and conservative. Future research can focus on several extensions such as stability condition for uncertain PWA systems, the use of different Lyapunov functional to obtain less conservative results, and the use of the presented theorem to stabilize PWA systems with time delay and uncertainty.

APPENDIX

The following algorithm is used to find the maximum allowable upper bound for delay:

Step1: Select the positive constants h_d and μ.

Step2: Solve LMIs (8)-(13) and then check the feasibility of LMIs for $\forall d_h(t)\in\{0,h_d\}$, $\dot{d}_h(t)\in\{-\mu,\mu\}$.

Step3: If LMIs will be feasible, increase h_d ,and then solve LMIs (8)-(13) again (step2), else if LMIs will be infeasible, exit the algorithm.

REFERENCES

[1] M. S. Branicky, "Studies in hybrid systems: Modeling, analysis, and control," Sc.D. dissertation, Dept. of Electrical Engineering and Computer Science, MIT, Cambridge, MA, June 1995.

[2] J. P. Richard, "Time-delay systems: An overview of some recent advances and open problems," *Automatica*, vol. 39, no. 10, pp. 1667–1694, 2003.

[3] H. Ye, A. N. Michel, and L. Hou, "Stability theory for hybrid dynamical systems," *in Proc. IEEE Decision and Control Conference*, New Orleans, LA, Dec. 1995.

[4] M. Johansson and A. Rantzer, "*Computation of piecewise quadratic Lyapunov functions for hybrid systems*," Dept. Automatic Control, Lund Institute of Technology, Tech Rep. TFRT-7549, June 1996.

[5] M. S. Branicky, "Multiple lyapunov functions and other analysis tools for switched and hybrid systems," *IEEE Transaction on Automatic Control*, vol. 43, no. 4, pp. 475–482, April 1998.

[6] A. Hassibi, and S. Boyd, "Quadratic stabilization and control of piecewise-linear systems," *Proceedings of the American Control Conference, Philadelphia*, PA, vol. 6, pp. 3659–3664, June 1998.

[7] A. Bemporad, G. Ferrari-Trecate, and M. Morari, "Observability and controllability of piecewise affine and hybrid systems," *IEEE Transaction on Automatic Control*, vol. 45, no. 10, pp. 1864–1876, Oct. 2000.

[8] K. Gu, V. L. Kharitonov, and J. Chen, "Stability of Time-Delay Systems, " *Springer Science & Business Media*, 2003.

[9] H. B. Zeng, Y. He, M. Wu, and S. P. Xiao, "Less conservative results on stability for linear systems with a time-varying delay," *Optimal control, application and Method*., vol. 34, no. 6, pp. 670–679, 2013.

[10] W. kwon, B. Koo, and S. M. Lee, "Novel Lyapunov–Krasovskii functional with delay-dependent matrix for stability of time-varying delay systems", *Applied Mathematics and Computation*, vol. 320, pp.149-157, 2018.

[11] F. Long, L. Jiang, Y. He, and M. Wu, "Stability analysis of systems with time-varying delay via novel augmented Lyapunov–Krasovskii functionals and an improved integral inequality", *Applied Mathematics and Computation*, vol. 357, pp.325-337, 2019.

[12] T. H. Lee, and J. H. Park, "Improved stability conditions of time-varying delay systems based on new Lyapunov functionals", *Journal of the Franklin Institute*, vol. 355, no.3, pp.1176-1191, 2018.

[13] A. Seuret and F. Gouaisbaut, "Wirtinger-based integral inequality: Application to time-delay systems," *Automatica*, vol. 49, no. 9, pp. 2860–2866, 2013.

[14] H. Zeng, Y. He, M. Wu, and J. She, "Free-Matrix-Based integral inequality for stability analysis of systems with time-varying delay," *IEEE Transaction on Automatic Control*, vol. 60, no. 10, pp. 2768–2772, 2015.

[15] R. Datta, R. Dey, B. Bhattacharya, R. Saravanakumar, and C. K. Ahn, "New double integral inequality with application to stability analysis for linear retarded systems", *IET Control Theory & Applications*, vol. 13, no. 10, pp.1514-1524,2019.

[16] R. Zhang, D. Zeng, J. H. Park, S. Zhong, Y. Liu, and X. Zhou, "New approaches to stability analysis for time-varying delay systems", *Journal of the Franklin Institute*, vol. 356, no.7, pp. 4174-4189, 2019.

[17] V. Kulkarni, M. Jun, and J. Hespanha, "Piecewise quadratic Lyapunov functions for piecewise affine time-delay systems," *Proceedings of the American Control Conference*, vol. 5, no.30, pp. 3885- 3889, 2004.

[18] K. Moezzi, L. Rodrigues, and A. G Aghdam, "Stability of Uncertain Piecewise Affine Systems with Time Delay:

Delay-Dependent Lyapunov Approach," *International Journal of Control*, vol. 82, no. 8, pp. 1423-1434, 2009.

[19] K. Moezzi, L. Rodrigues, and A. G. Aghdam, "Stability of uncertain piecewise affine systems with time-delay," American Control Conference, pp. 2373-2378, 2009.

[20] S. Duan, J. Ni, and A. G. Ulsoy, "An improved LMI-based approach for stability of piecewise affine time-delay systems with uncertainty," *International Journal of Control*, vol. 85, no. 9, pp. 1218-1234, 2012.

[21] S. Duan, J. Ni, and A. G. Ulsoy, "Stability criteria for uncertain piecewise affine time-delay systems," *American Control Conference (ACC)*, pp. 5460-5465, 2012.

[22] C. Fiter and E. Fridman, "Stability of piecewise affine systems with state-dependent delay, and application to congestion control," *in 52nd IEEE conference on decision and control*, pp. 1572-1577, 2013.

[23] M. Johansson, "Piecewise Linear Control Systems," *Springer-Verlag*, 2003.

[24] T. H. Lee, H. Ju, and S. Xu, "Relaxed conditions for stability of time-varying delay systems," *Automatica*, vol. 75, pp. 11-15, 2017.

[25] R. E. Skelton, T. Iwasaki, and K. M. Grigoradis, "A unified algebraic approach to linear control," *design. New York: Taylor and Francis*, 1997.

Salehe Afsharian received the B.S. and M.S. degree in control engineering from the Ferdowsi University of Mashhad (FUM), Iran, in 2009 and 2012, respectively. Since 2014, she is doing a PhD dissertation in Control Engineering at Department of Electrical and Computer Engineering, University of Birjand, Iran. Her research interests include Hybrid System, Time-delay Systems, Stability Analysis, Model Predictive Control, Modeling and Simulation, Renewable and Sustainable Energy, and Control.

Hussein Eliasi received the B.S. degree in electrical engineering from the Ferdowsi University of Mashhad (FUM), Iran, in 2001. He received the M.S. and the Ph.D. degrees from Amirkabir University of technology (Tehran), Iran, in 2005 and 2011, respectively. He is currently an assistance professor in faculty of electrical engineering at University of Birjand, Iran. His research interests include Constrained Nonlinear Dynamics Systems, Robust Control, Parameter Optimization of Model Predictive Control, Transient Stability in Power Systems and Load Following by Nuclear Power Plants.

International Journal of Industrial Electronics, Control and Optimization © 2020 IECO
Vol. 3, No. 4, pp. 483-490, Sep (2020)

Optimal Impedance Voltage-Controller for Electrically Driven Robots

Mohsen Jalaeian F. [1,†], Mohammad Mehdi Fateh[2], and Morteza Rahimiyan[3],

[1,2,3] Department of Electrical and Robotic Engineering, Shahrood University of Technology, Shahrood, Iran,

ABSTRACT

This paper presents a novel optimal impedance voltage-controller for Electrically Driven Lower Limb Rehabilitation Robots (EDLR). To overcome the dynamical complexities, and handle the uncertainties, the proposed method employs an expected forward model of the actuator. The existing value of lamped uncertainty is represented by the output difference of the model and system. A voltage-controller, which compensates for the uncertainties, is designed based on this uncertainty estimator. Parameters of the controller are optimized using genetic algorithms. Key contributions of this paper are I) uncertainty estimation through the expected model's output, II) overcoming the changes in motors' parameters, III) introducing a class of closed-loop system termed as "Repeatable", and IV) designing an optimal impedance voltage-controller that is non-sensitive to the parameter variations. Significant merits of the approach are swift calculations, efficiency, robustness, and guaranteed stability. Furthermore, the simplicity of design, ease of implementation and model-free independent joint structure of the approach are noticeable. The method is compared with an adaptive robust sub-controller and a Taylor-series-based adaptive robust controller, through simulations in passive range of motion and active assistive rehabilitation exercises. The results show the superiority of the proposed method in tracking performance and the time of calculations.

Article Info

Keywords:
Electrically Driven Robots (EDR), Impedance control, Model-free tracking control, Rehabilitation robots, Voltage-based control,

Article History:
Received: 2020-02-03
Accepted: 2020-04-19

I. INTRODUCTION

The human lower limb's dysfunctionality has significant effects on daily life quality [1]. Nowadays, patients suffering from such diseases may improve their lower limb motor function through robotic rehabilitation programs [2]. Robots provide several benefits for the therapeutic process, namely reducing the costs [3], speeding up the process [4], reducing pain [5], as well as being user-friendly [6]. However, control of rehabilitation robots is a difficult complex problem, due to the lack of an accurate model for the human body, and the high sensitivity to interconnection forces [7]. In addition, the Electrically Driven Robots (EDR), has coupled third-order nonlinear differential equations [8]. Moreover, since the robot may be powered by batteries, energy consumption is another important issue.

Over the last decade, in the field of therapeutic robots' control, several scientific articles such as a PID [9], adaptive robust controller [10], as well as voltage-based adaptive control [11] are presented.

In terms of using system equations, robot control methods are divided into four categories: (i) Model Free Controllers (MFC) [9], (ii) Computed Torque Control (CTC) [12], (iii) Integrated Dynamics Methods (IDM) [8], and (iv) Voltage Control Strategy (VCS) [11,13,14]. Although the robot control signal is applied through the actuators, they are not considered in the MFC and CTC methods. The IDMs have heavy time-consuming calculations, whereas the dynamic effects of the complex coupled nonlinear dynamics of the robot, environment, and the mechanical part of the motor, altogether are observable in the motor current. Thus, the VCS methods design the controller using the electrical portion of

[†]Corresponding Author: m.jalaeian@yahoo.com
Faculty of Electrical and Robotic Engineering, Shahrood University of Technology, Shahrood, Iran

the actuator's dynamics [13]. However, the electrical current's derivative is hard to be measured [15,16], and actuator parameters may vary due to heat [17]. The VCS strategies try to approximate, estimate, or predict the unmeasurable parts of the equation using different types of observers or approximators. To do so, an adaptive uncertainty estimator [8], an adaptive impedance approach [11], fuzzy approximators [14,18,19], an estimator based on Fourier series expansion [16], a FAT-based robust adaptive approximator [20], and a Taylor series approximator [21] are introduced.

To the best of our knowledge, the variation of motor parameters is neglected in the literature. To overcome these challenges, a novel voltage-controller is proposed in this research that uses the known part of the system to estimate the model imperfection. In [22], a forward internal model is used to control a lower extremity exoskeleton; however, since it utilizes the dynamical model of the robot, the final control law is a complex highly nonlinear coupled system. In this paper, we employ the VCS to reach a simple final controller. The advantages of the approach are swift calculations, fast response, efficiency, guaranteed closed-loop stability, simplicity of design, ease of implementation, and independent joint structure.

This paper includes the following sections: Section 2 is allocated to detail the dynamical model of the EDLR. The proposed method is described in Section 3 while the analysis of its stability is expressed in Section 4. Then, the description and analysis of the simulations and comparisons are detailed in Section 5. Finally, the paper is concluded in the last section.

II. MODEL OF AN EDLR

The EDLR (Fig. 1) is a robot, with two degrees of freedom, which is used to provide rehabilitation exercises for the human lower limb in the sagittal plane [2,4].

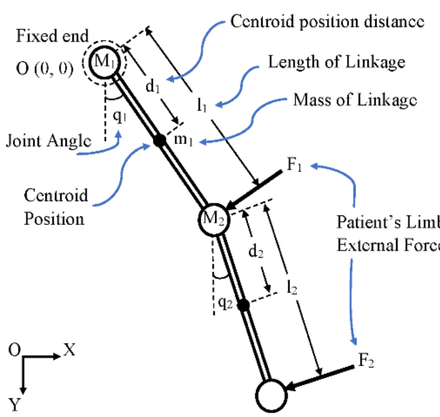

Fig. 1. The EDLR, assembly drawing.

The equations of motion of an EDLR can be written as Equ. (1), [10]. In this paper, the matrices and vectors are written in bold characters while the scalars are written in narrow fonts.

$$\boldsymbol{M}(\boldsymbol{q})\ddot{\boldsymbol{q}} + \boldsymbol{H}(\boldsymbol{q},\dot{\boldsymbol{q}}) + \boldsymbol{J}(\boldsymbol{q})^T\boldsymbol{F_e} + \boldsymbol{d} = \boldsymbol{T_r} \tag{1}$$

in which, $\boldsymbol{q} = [q_1, q_2, \dots, q_n]^T$ is the vector of joints angles, where n is the robot's degree of freedom, $\boldsymbol{M}(\boldsymbol{q}) \in \mathbb{R}^{n\times n}$ is inertia matrix, $\boldsymbol{H}(\boldsymbol{q},\dot{\boldsymbol{q}}) \in \mathbb{R}^{n\times 1}$ is a vector containing the centripetal, Coriolis, and gravity forces, $\boldsymbol{J}(\boldsymbol{q})$ is the Jacobian matrix of the robot, $\boldsymbol{F_e} \in \mathbb{R}^{n\times 1}$ is a vector representing the patient-exerted-forces, $\boldsymbol{T_r}$ is the joints torques vector, and $\boldsymbol{d}$ is the lumped bounded uncertainty. The torque of i^{th} joint is produced by an electrical DC motor through a gearbox with the speed transmission ratio of r_i , that means:

$$\dot{q}_i = r_i\dot{\theta}_i \tag{2}$$

in which, $\dot{\theta}_i$ is the angular speed of the motor shaft. The dynamic equations of each DC motor consist of two parts, namely a mechanical portion and an electrical equation.

$$J_{m,i}\ddot{\theta}_i + B_{m,i}\dot{\theta}_i + r_iT_{r,i} = K_{m,i}I_i \tag{3}$$

$$L_i\dot{I}_i + R_iI_i + K_{b,i}\dot{\theta}_i = V_i \tag{4}$$

where, $J_{m,i}$ and $B_{m,i}$ are the inertia and friction of the motor. V_i , I_i, and $T_{r,i}$ are the motor's terminal voltage, armature current, and joint torque, respectively. $K_{m,i}$ and $K_{b,i}$ are the motor torque transmission and back-EMF constants. L_i, and R_i are the actuator inductance and resistance.

The block diagram of a robotic-assisted lower limb rehabilitation process is depicted in Fig. 2.

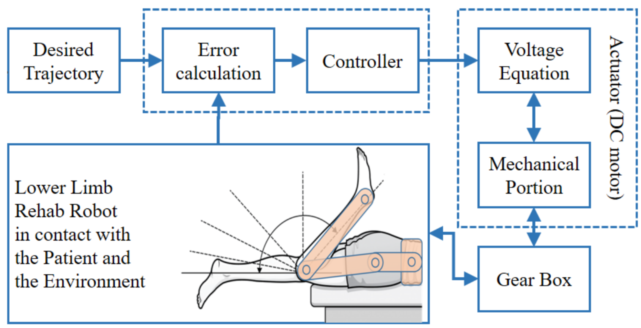

Fig. 2. Block-diagram of robotic rehabilitation.

Substituting Equs. (1)-(2) in Equ. (3), the integrated mechanical portion is obtained:

$$\begin{aligned}&(\boldsymbol{r_M}\boldsymbol{M}(\boldsymbol{q}) + \boldsymbol{r_M}^{-1}\boldsymbol{J_M})\ddot{\boldsymbol{q}} + \boldsymbol{r_M}^{-1}\boldsymbol{B_M}\dot{\boldsymbol{q}} + \boldsymbol{r_M}\boldsymbol{H}(\boldsymbol{q},\dot{\boldsymbol{q}})\\ &+\boldsymbol{r_M}\boldsymbol{J}(\boldsymbol{q})^T\boldsymbol{F_e} + \boldsymbol{r_M}\boldsymbol{d} = \boldsymbol{K_M}\boldsymbol{I}\end{aligned} \tag{5}$$

in which, $\boldsymbol{J_M}, \boldsymbol{B_M}, \boldsymbol{K_M}$, and $\boldsymbol{r_M}$, are the diagonal matrices of the mechanical parameters of all motors.

Property 1 (Inertia Matrix Invertibility):

The $\boldsymbol{M}(\boldsymbol{q})$, is a symmetric positive definite matrix, which is bounded even if $\boldsymbol{q}$ is not bounded. Therefore, $\bar{\boldsymbol{M}}(\boldsymbol{q}) = (\boldsymbol{r_M}\boldsymbol{M}(\boldsymbol{q}) + \boldsymbol{r_M}^{-1}\boldsymbol{J_M})$ is a positive definite bounded matrix, and its inverse exists and remains non-zero and bounded [23].

Considering property 1, one can rewrite the dynamics of mechanical portion as:

$$\ddot{\boldsymbol{q}} = \overline{\boldsymbol{M}}(\boldsymbol{q})^{-1}\big(\boldsymbol{K_M I} - (\boldsymbol{r_M}^{-1}\boldsymbol{B_M}\dot{\boldsymbol{q}} + \boldsymbol{r_M H}(\boldsymbol{q},\dot{\boldsymbol{q}}) + \boldsymbol{r_M J}(\boldsymbol{q})^T\boldsymbol{F_e} + \boldsymbol{r_M d})\big) \quad (6)$$

Assumption 1 (Desired Trajectory):

The desired angular position ($\boldsymbol{q_d}$), velocity ($\dot{\boldsymbol{q}}_{\boldsymbol{d}}$), and acceleration ($\ddot{\boldsymbol{q}}_{\boldsymbol{d}}$) are given bounded.

Assumption 2 (Voltage Supplier):

The input voltage, which is produced by a real supplier, is bounded because of factual limits.

$$|\boldsymbol{V}| \le \boldsymbol{V_{max}} \quad (7)$$

Assumption 3 (Measurement Noises):

It is assumed that each measured signal is passed through a low-pass filter; thus, the measurement noise is not considered in the course of this paper.

III. The Proposed Position Controller

The voltage equation of each actuator is considered independently without losing generality. The subscript i is omitted, and $\alpha \triangleq K_b r^{-1}$ is defined for the sake of simplicity, hence, Equ. (4) can be rewritten as:

$$\alpha\dot{q} + L\dot{I} + RI = V \quad (8)$$

Based on Equ. (5), the motor current represents the dynamical effect of the entire mechanical parts of the system [13]. Therefore, Equ. (8) can be used to design the controller in an independent joint structure.

A. Case 1: Expected-Model Voltage Control with fixed known parameters:

Here, we consider a simple forward model of the system defined as:

$$\dot{\hat{q}}(t) = \alpha^{-1}\big(V(t-\varepsilon) - RI(t)\big) \quad (9)$$

The unknown portion of the system can be computed by attention to Equs. (8) and (9) as:

$$\psi(t) \triangleq \dot{\hat{q}}(t) - \dot{q}(t) \equiv \alpha^{-1}\left(L\dot{I}(t) - \delta(t)\right) \quad (10)$$

in which, $\delta(t) = \big(V(t) - V(t-\varepsilon)\big)$, and ε is a very small positive value as a time delay. Then, the control law can be designed as:

$$V = RI + \alpha(\dot{q}_d + \lambda e + \psi) \quad (11)$$

where, $e \triangleq q_d - q$, is the error of the joint angle, and λ is a real positive scalar. The tracking error dynamics, which is discussed later in details, is equivalent to $\dot{e} + \lambda e = \alpha^{-1}\delta(t)$.

B. Case 2: Extended-Model Voltage Control with parameters variations:

Motor parameters may vary during the runtime owing to the motor heat and temperature changes [17]. Hence, the parameters R and α are supposed to be unknown, and two suggested design parameters, $\hat{R}$ and $\hat{\alpha}$, are utilized, instead. The new model can be proposed as:

$$\dot{\hat{q}}(t) = \hat{\alpha}^{-1}\left(V(t-\varepsilon) - \hat{R}I(t)\right) \quad (12)$$

Using the new model, Equ. (12), total imperfection can be measured as:

$$\psi(t) \triangleq \dot{\hat{q}}(t) - \dot{q}(t) \quad (13)$$

Analytically, the imperfection term (ψ) equivalents:

$$\psi \equiv \alpha^{-1}\big(L\dot{I} + RI\big) - \hat{\alpha}^{-1}\hat{R}I - \xi \quad (14)$$

in which, $\xi = \big(\alpha^{-1}V(t) - \hat{\alpha}^{-1}V(t-\varepsilon)\big)$. Accordingly, a new control law is proposed as:

$$V(t) = \hat{R}I + \hat{\alpha}(\dot{q}_d + \lambda e + \psi) \quad (15)$$

Applying the proposed control law, Equ. (15), to the electrical equation of the actuator, Equ. (8), yields:

$$\dot{q} = \alpha^{-1}\left(\left(\hat{R}I + \hat{\alpha}(\dot{q}_d + \lambda e + \psi)\right) - L\dot{I} - RI\right) \quad (16)$$

For analyzing the closed-loop system, the imperfection term, ψ, can be substituted with its analytical equivalence, Equ. (14):

$$\alpha\dot{q} = \hat{\alpha}(\dot{q}_d + \lambda e) + \hat{R}I - \big(L\dot{I} + RI\big) + \hat{\alpha}\big(\alpha^{-1}\big(L\dot{I} + RI\big) - \hat{\alpha}^{-1}\hat{R}I - \xi\big) \quad (17)$$

That yields:

$$(\dot{e} + \lambda e) = (\hat{\alpha}^{-1}\alpha - 1)\dot{q} + (\hat{\alpha}^{-1} - \alpha^{-1})\big(L\dot{I} + RI\big) + \xi \quad (18)$$

Apply some manipulations and exchanging ξ, we obtain:

$$(\dot{e} + \lambda e) = (\hat{\alpha}^{-1} - \alpha^{-1})\big(\alpha\dot{q} + L\dot{I} + RI\big) + \big(\alpha^{-1}V(t) - \hat{\alpha}^{-1}V(t-\varepsilon)\big) \quad (19)$$

Considering Equ. (8), we have:

$$(\dot{e} + \lambda e) = \hat{\alpha}^{-1}\big(V(t) - V(t-\varepsilon)\big) \quad (20)$$

Thus, the closed-loop system can be represented by:

$$(\dot{e} + \lambda e) = \hat{\alpha}^{-1}\delta(t) \quad (21)$$

Note that, although $\hat{\alpha}$ is noticed in Equ. (21), the estimation errors, $\tilde{R} \triangleq \big(R - \hat{R}\big)$ and $\tilde{\alpha} \triangleq (\alpha - \hat{\alpha})$, do not play any role in the closed-loop system. The pseudo-code of the proposed algorithm is detailed in Fig. 3.

- Initialize the control parameters ($\hat{R}$ *and* $\hat{\alpha}$)
- Initialize the imperfection indicator ($\psi = 0$)
- While (time < final_time)
  - Compute the control signal (V)
  - Apply recent control signal into the system
  - Measure the feedback variables (I *and* $\dot{q}$)
  - Compute the forward model output ($\dot{\hat{q}}$)
  - Compute the imperfection indicator (ψ)
- End While

Fig. 3. The proposed controller pseudo-code.

In a rehabilitation robot with revolute joints driven by DC motors with bounded terminal voltages, the electrical current, its derivative, and the angular velocity remain bounded [11]. The closed-loop system stability is studied here. According to assumption 2, $V(t)$ is bounded. When voltage is saturated, $|V| = V_{max}$, it can be concluded that $\delta(t) = 0$, and it leads the Equ. (21) to become $\dot{e} + \lambda e = 0$. If the voltage is not saturated, $|V| < V_{max}$, then $|\delta(t)| < 2V_{max}$, and consequently, the input value of Equ. (21) is bounded.

Therefore, the boundedness of error, e, and its derivative, $\dot{e}$, are guaranteed [24]. Thus, according to assumption 1, the actual position and velocity of the joint, (q, and $\dot{q}$), and of the motor, (θ, and $\dot{\theta}$), remain bounded as well. Having assumption 2 and equation (8), the following is gained:

$$L\dot{I} + RI = \nu \tag{22}$$

in which $\nu = (V - \alpha\dot{q})$ is a bounded value as proved. Since Equ. (22) is a first-order linear differential equation with positive-constant coefficients, it is stable based on the Routh-Hurwitz criterion. With bounded input, ν, the responses (I, and $\dot{I}$) are bounded [24]. Although the motor parameters vary during time, they are always positive and bounded due to physical constraints. Ergo, Equs. (12) and (13) claim that $\hat{q}$ and ψ are bounded. In addition, Equ. (3) shows that the produced joints torque, $\boldsymbol{T_r}$, is bounded. So, the closed-loop system is stable. □

IV. Proposed Impedance Control, Design, and Optimization

The main idea of mechanical impedance control is to enhance the desirability of dynamical interactions between a robot and its environment [25,26]. The desired impedance law for each joint is defined as a second order equation [7].

$$M_d(\ddot{q}_d - \ddot{q}_r) + B_d(\dot{q}_d - \dot{q}_r) + K_d(q_d - q_r) = J(q)^T F_e \tag{23}$$

in which, $M_d, B_d,$ and K_d are the desired inertia, damping, and stiffness, respectively, and q_d is the desired trajectory. In addition, q_r is a regenerated trajectory for the joint angle based on the desired impedance law, which is obtained as:

$$\ddot{q}_r = \ddot{q}_d + {M_d}^{-1}[B_d(\dot{q}_d - \dot{q}_r) + K_d(q_d - q_r) - J(q)^T F_e] \tag{24}$$

Since $F_e, q_d, \dot{q}_d$ and $\ddot{q}_d$ are bounded, and the desired impedance coefficients are positive, the q_r is bounded. The block diagram of the proposed impedance control is presented in Fig. 4.

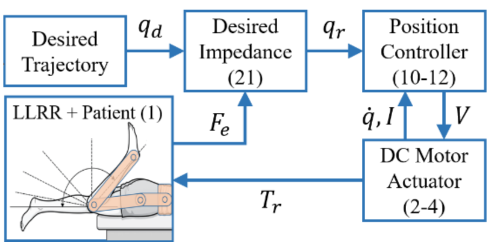

Fig. 4. The block-diagram of using impedance controller in rehabilitation.

Successful uncertainty handling is one of the main advantages of the proposed method, which enables the designer to tune the controller parameters using an offline optimization algorithm, like Genetic Algorithms (GAs) or Particle Swarm Optimization (PSO) [15,23]. Here, this characteristic is termed as "repeatability" of the closed-loop control system.

Definition 1: Repeatable closed-loop system

A closed-loop system is termed "*Repeatable*" if a fixed set of controller-parameters leads to a repetitive closed-loop response, even in the presence of uncertainty and external disturbances. In other words, in a repeatable closed-loop system:

$$\int_0^t \left(e(\tau) - e(\tau|\langle\phi, d\rangle)\right)^2 d\tau \ll \int_0^t \left(e(\tau)\right)^2 d\tau \tag{25}$$

where, $e(\tau)$ is the tracking error of the closed-loop system without uncertainty or external disturbances, and $e(\tau|\langle\phi, d\rangle)$ is the tracking error of the closed-loop system in the presence of model uncertainty, (ϕ), and external disturbances, (d), and $\langle . \rangle$ is used to denote the expectation value of the variables.

Remark 1:

Offline techniques are not being able to optimize the controller-parameters, due to the erratic essence of the system response, in the case of the unrepeatable system. However, if a system is repeatable, the offline optimization algorithm can be used to optimize its parameters; while uncertainties and unknown external disturbances have neglectable impacts on the results.

Remark 2:

The EDR with the proposed controller is repeatable, thus, the offline techniques may be utilized to optimize its parameters, without any worries about the exposure to uncertainty and external disturbances.

V. Simulations

In this section, two simulation scenarios (comparative position control, and optimized impedance control) of the LLRR are studied, in which, MATLAB® 2018a software is utilized within an ASUS laptop powered by Windows 10, and an Intel® Core™ i7-2.6GH CPU.

A. *Position Control:*

The proposed controller is applied to a 2-DoF EDLR for hip and knee therapeutic exercises. Human joints have a certain Range of Motion (ROM), which are considered inside the interval of (-30˚, +120˚) for hip and (-90˚,0˚) for knee, [10,28,29]. In addition, Maximum Angular Speeds (MAS) of hip and knee joints are considered equal to 30 degrees per second. The parameters of motor and robot are detailed in Table 1. Interested readers can find full details of the dynamic equations in [10]. The proposed controller is applied to the position control in comparison with two other controllers, namely an adaptive robust sub-controller (ARSC) [10], and a Taylor-series-based adaptive robust controller (TSARC) [8].

TABLE I
PARAMETERS OF ELECTRICALLY DRIVEN LLRR

Parameter	Dimension	Joint 1	Joint 2
$\boldsymbol{m_i}$	kg	5.5	5
$\boldsymbol{l_i}$	m	0.5	0.45
$\boldsymbol{d_i}$	m	0.45	0.4
$\boldsymbol{I_i}$	$kg.m^2$	0.25	0.2
$\boldsymbol{F_s}$	$N.m$	0.9	0.9
$\boldsymbol{F_c}$	$N.m$	0.8	0.8
σ_i	$N.m/rad.s^{-1}$	1.2	1.2
K_m	$N.m/A$	4.32	4.32
R_i	Ω	4	4
L_m	H	2.5e-3	2.5e-3
K_v	$v/rad.s^{-1}$	0.287	0.287
$K_g = r^{-1}$	-	16	16

Remark 3:

In order to perform a Passive ROM exercise for lower limb rehabilitation in the joint training practice, previous scientific works set the desired joint trajectory as a four-part piecewise linear periodic path, which is very simple but not smooth [9,10], or as a sinusoidal trajectory, which has not enough rest in each period for the patient. This study proposes an adjustable smooth and continuous trajectory whose derivative is computable analytically. Thus, the angular position and speed are desirably adjustable. Since the exercises are periodic, the time inside each period is defined as $\eta = Rem\left(\frac{time}{T_{prd}}\right)$, in which T_{prd} is a pregiven cycle-time that is determined by the physiotherapist, and $Rem(.)$ computes the reminder value of the division. Afterward, the desired trajectory is proposed based on the η.

$$q_d(\eta) = \big(max(ROM) - min(ROM)\big) \times \big(y(\eta,\eta_1) - y(\eta,\eta_2)\big) + min(ROM) \qquad (26)$$

where $y(\eta,\eta_i) = \left(1 + \exp\left(-\frac{\eta-\eta_i}{a}\right)\right)^{-1}$, and a is a setting parameter for maximum angular speed.

The desired trajectory, which is introduced in remark 3, is applied to the proposed position control method. The tracking performances of hip and knee joints are shown in Fig. 5.

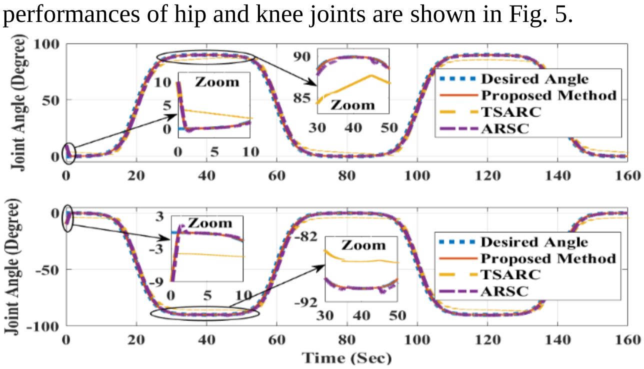

Fig. 5. PROM tracking performance of hip and knee joints.

According to Fig. 5, the proposed controller shows better tracking performance due to the smaller error and zero overshoot. There is an initial angle error that the controller overcomes it by nearly two seconds, (First zoomed areas in Fig. 5). To study the control performance, an external disturbance ($d = 2N$) is applied to the robot between the 35sec and 45sec, which the controller succeeds to damp its effects completely (Second zoomed areas in Fig. 5). Tracking errors are depicted in Fig. 6, where its value is small with the proposed controller, and the external disturbances do not affect the closed-loop errors (repeatability).

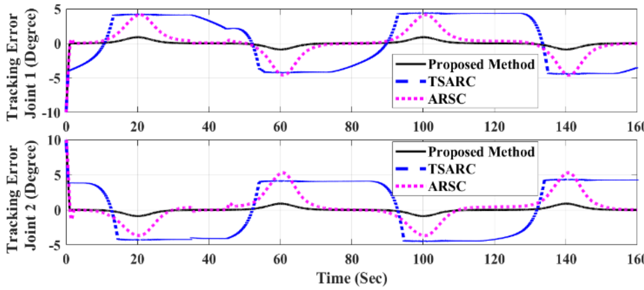

Fig. 6. PROM tracking error of hip and knee joints (comparison).

Based on Fig. 6, the proposed method proves superiority since its error magnitude is smaller than the other two, while no oscillation is observed in its response. To have a numerical comparison, several indices are studied in Table 2.

TABLE II
NUMERICAL COMPARISON

	Proposed Method		TSARC		ARSC	
Joint	**1**	**2**	**1**	**2**	**1**	**2**
ACT	1.22e-5		3.78e-5		1.60e-4	
MCT	2.21e-4		2.90e-3		4.2e-3	
MAV	2.778	2.785	3.956	3.973	2.850	3.100
MAC	0.66	0.26	0.82	0.49	0.68	0.28
SAE	8.68e2	8.78e2	5.8e4	6.1e4	1.9e4	2.1e4
MSE	0.21	0.21	7.39	7.61	3.53	4.01

ACT=Average cycle time, MCT=Max cycle time, MAV=Mean Absolute Voltage, MAC=Mean Absolute Current, SAE=Sum Absolute Error, MSE=Mean Square Error,

From the performance point of view, the tracking error of the proposed controller in both indices (Sum Absolute Error and Mean Square Error) is smaller than the other two. In addition, from the efficiency point of view, Mean Absolute Voltage, Mean Absolute Current and Average Cycle Time of the controller computation are studied while the proposed controller is better in those features. The proposed controller is superior in efficiency and performance, in spite of its great simplicity in design and implementation. Furthermore, the proposed structure is not sensitive to parameters estimation error. The controller has a few design parameters which should be set once in the first run. In contrast with a majority of controllers that have many design parameters and are sensitive to their setting values, which must be readjusted for each new trajectory. Control signals, the terminal voltages of motors, are illustrated in Fig. 7. As seen, the voltages are saturated when the error is big; however, the controller overcomes and becomes unsaturated as fast as possible. The effect of external disturbance on voltages can be seen in the zoomed area in Fig. 7. Motors currents are displayed in Fig. 8 as well. Fig. 8 shows that the current is small and smooth. Based on the aforementioned principle, the dynamical behaviors of mechanical parts can be observed in the currents, as seen in Fig. 8.

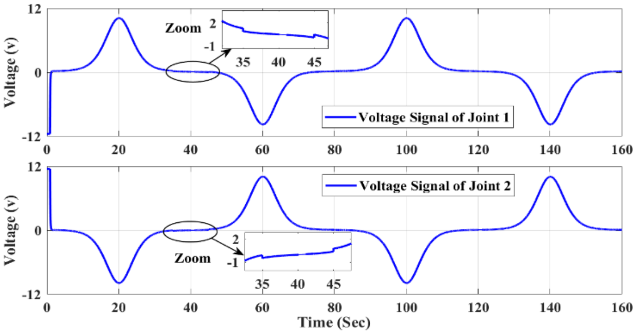

Fig. 7. motors voltages (control signals) of hip and knee joints.

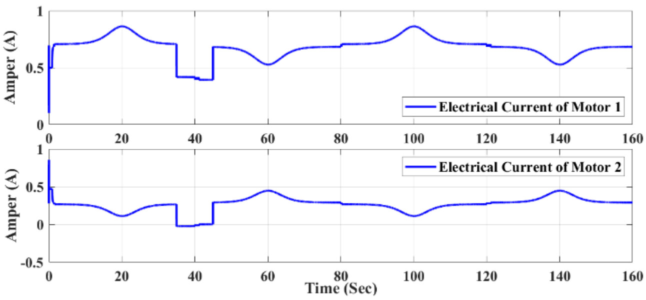

Fig. 8. DC motors currents.

B. *Optimized Impedance Control:*

The proposed scheme is utilized in impedance control of the LLRR in the presence of uncertainty and external disturbance. Based on remarks 1 and 2, GA is used to minimize the Mean Square Error (MSE) of tracking performance. Note that, the cost function for optimization can be selected based on error and energy [30], or one of them.

As expected, changes on $\hat{R}$ do not affect system performance. Nevertheless, the effect of changing in $\hat{\alpha}$ should be taken into account. Fig. 9 illustrates the impact of changes in $\hat{\alpha}$. The optimized $\hat{\alpha}$ is used, to minimize the error. Fig. 10 illustrates the patient's exerted force.

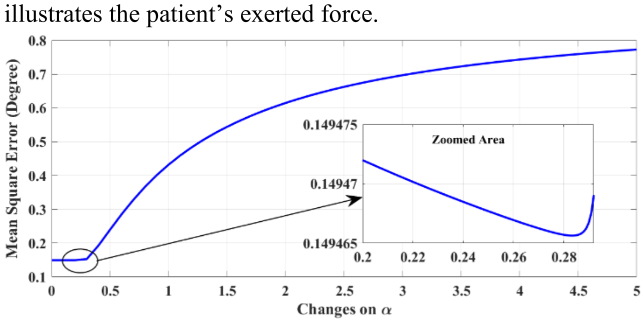

Fig. 9. The impact of changes in $\hat{\alpha}$ on impedance error.

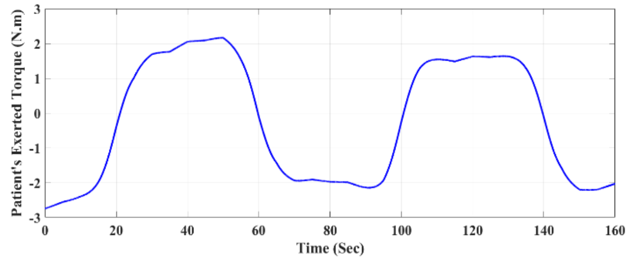

Fig. 10. Patient's exerted force.

The tracking performance is also depicted in Fig. 11, where the regenerated and actual trajectories are shown.

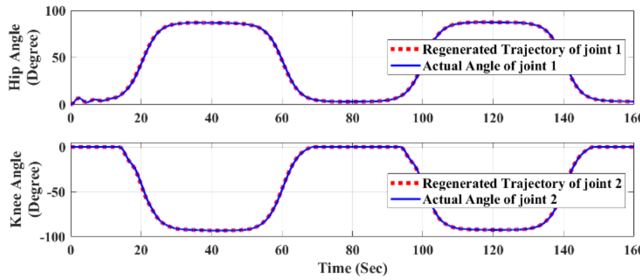

Fig. 11. Tracking performance (regenerated and actual trajectories).

Fig. 11 shows that the actual joints angles track the regenerated trajectories. However, the difference between them is shown in Fig. 12, as the impedance tracking error, with less than a few degrees which is neglectable in the context of rehabilitation.

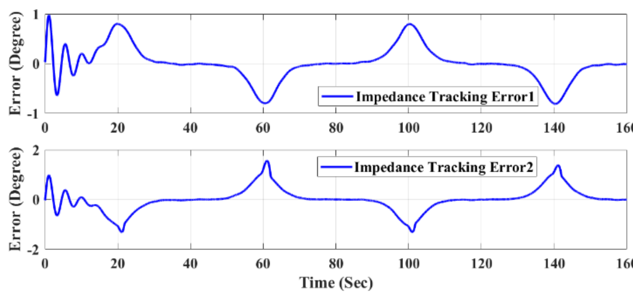

Fig. 12. The difference between the measured and commanded errors.

Applied voltages to the actuators are shown in Fig. 13.

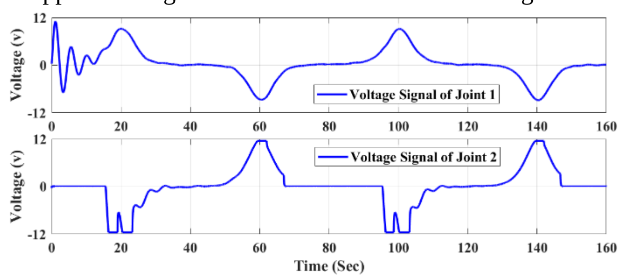

Fig. 13. Actuators' voltages (control signal).

These voltages provide the joints torques, which are depicted in Fig. 14.

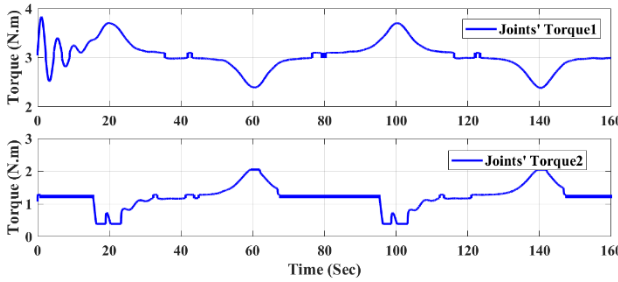

Fig. 14. Joint Torque.

It can be seen that the actuators' voltages are smooth and bounded. In other words, the closed-loop system that contains the robot, patient, and the environment, altogether behaves as the reference desired impedance rule.

In the future studies, authors going to utilize model predictive compensator or dynamic-growing fuzzy-neural acceleration-based compensator, which are first introduced by the authors in [31,32], to compensate for the effects of $\delta(t)$.

VI. Conclusions

The EDLRs can be controlled through the terminal voltage of their actuators in an independent joint manner. However, the parameters of actuators may vary over time and the value of the motor current derivative is unmeasurable. In this paper, a novel approach has been proposed to overcome these challenges. The proposed control method, which is applied to the position and optimal impedance control of an EDLR, has overcome the uncertainty and complexities in dynamics of the robot. Swift calculations, high performance and efficiency, robustness, and guaranteed stability are the main merits of the proposed method. Comparatively, the higher performance of the method is validated showing less tracking error. At the same time, greater efficiency is achieved through brief calculations, smaller control signal (voltage), and reduced power consumption leading to smaller motor sizing. In addition, the most significant advantages of the method are the independent joint structure, simplicity of design, and ease of implementation. The method has been compared with two others, namely an adaptive robust sub-controller, and a Taylor-series based robust controller through simulations. The results of simulations and comparisons have confirmed the aforementioned merits.

References

[1] F. Molteni, G. Gasperini, G. Cannaviello, and E. Guanziroli, "Exoskeleton and End-Effector Robots for Upper and Lower Limbs Rehabilitation: Narrative Review," PM&R, Vol. 10, No. 9S2, pp. 174-188, Sep. 2018.

[2] JK. Mohanta, S. Mohan, P. Deepasundar, and R . Kiruba-Shankar, "Development and control of a new sitting-type lower limb rehabilitation robot," Comput Electr Eng, Vol. 67, pp. 330-347, Apr. 2017.

[3] SF. Atashzar, M. Shahbazi, and R. V. Patel, "Haptics-enabled Interactive NeuroRehabilitation Mechatronics: Classification, Functionality, Challenges and Ongoing Research," Mechatronics, Vol. 57, pp. 001-019, Feb. 2019.

[4] W. Meng, Q. Liu, Z. Zhou, Q. Ai, B. Sheng, and SS. Xie, "Recent development of mechanisms and control strategies for robot-assisted lower limb rehabilitation," Mechatronics, Vol. 31, pp. 132-145, Oct. 2015.

[5] H. Huang, DL. Crouch, M. Liu, GS. Sawicki, and D. Wang, "A Cyber Expert System for Auto-Tuning Powered Prosthesis Impedance Control Parameters," Ann Biomed Eng, Vol. 44, pp. 1613-1624, Sep. 2015.

[6] H. Erdogan, Y. Palaska, E. Masazade, D. Erol Barkana, and HK. Ekenel, "Vision-based game design and assessment for physical exercise in a robot-assisted rehabilitation system," IET Comput Vis, Vol. 12, No. 1, pp. 059-068, Feb. 2018.

[7] E. Akdoğan, ME. Aktan, AT. Koru, M. Selçuk Arslan, M. Atlıhan, and B. Kuran, "Hybrid impedance control of a robot manipulator for wrist and forearm rehabilitation: Performance analysis and clinical results," Mechatronics, Vol. 49, pp. 077-091, Feb. 2018.

[8] SM. Ahmadi, and M. M. Fateh, "Robust control of electrically driven robots using adaptive uncertainty estimation," Comput Electr Eng, Vol. 56, No. C, Nov. 2016.

[9] E. Akdoğan, and MA. Adli, "The design and control of a therapeutic exercise robot for lower limb rehabilitation: Physiotherabot," Mechatronics, Vol. 21, No. 3, pp. 509-522, Apr. 2011.

[10] J. Wu, J. Gao, R. Song, R. Li, Y. Li, and L. Jiang, "The design and control of a 3DOF lower limb rehabilitation robot," Mechatronics, Vol. 33, pp. 013-022, Feb. 2016.

[11] M. M. Fateh, and V. Khoshdel, "Voltage-based adaptive impedance force control for a lower-limb rehabilitation robot," Adv Robot, Vol. 29, No. 15, pp. 961-971, Apr. 2015.

[12] S. Mohan, JK. Mohanta, S. Kurtenbach, J. Paris, B. Corves, and M. Huesing, "Design, development and control of a 2PRP-2PPR planar parallel manipulator for lower limb rehabilitation therapies," Mech Mach Theory, Vol. 112, pp. 272-294, Jun. 2017.

[13] M.M. Fateh, "On the Voltage-Based Control of Robot Manipulators," Int J Control Autom Syst, Vol. 6, pp. 702-712, 2008.

[14] S. Fateh, and M. M. Fateh, "Adaptive Fuzzy Control of Robot Manipulators with Asymptotic Tracking Performance," J Control Autom Electr Syst, Vol. 31, pp. 052-061, Oct. 2019.

[15] M. M. Fateh, and S. Khorashadizadeh, "Optimal robust voltage control of electrically driven robot manipulators," Nonlinear Dyn, Vol. 70, No. 2, pp. 1445-1458, Oct. 2012.

[16] S. Khorashadizadeh, and M. M. Fateh, "Uncertainty estimation in robust tracking control of robot manipulators using the Fourier series expansion," Robotica, Vol. 35, No. 2, pp. 310-336, Feb. 2017.

[17] R. Shanmugasundram, K. M. Zakaraiah, and N. Yadaiah, "Effect of parameter variations on the performance of direct current (DC) servomotor drives," JVC/Journal Vib Control, Vol. 19, No. 10, pp. 1575-1586, Jul. 2013.

[18] S. Khorashadizadeh, and M. Sadeghijaleh, "Adaptive fuzzy tracking control of robot manipulators actuated by permanent magnet synchronous motors," Comput Electr Eng, Vol. 72, pp. 100-111, Nov. 2018.

[19] M. M. Fateh, and S. Khorashadizadeh, “Robust control of electrically driven robots by adaptive fuzzy estimation of uncertainty,” Nonlinear Dyn, Vol. 69, No. 3, pp. 1465-1477, Aug. 2012.
[20] A. Izadbakhsh, P. Kheirkhahan, and S. Khorashadizadeh, “FAT-Based Robust Adaptive Control of Electrically Driven Robots in Interaction with Environment,” Robotica, Vol. 37, No. 5, pp. 779-800, May. 2019.
[21] S. M. Ahmadi, and M.M. Fateh, “On the Taylor series asymptotic tracking control of robots,” Robotica, Vol. 37, No. 3, pp. 405-427, Mar. 2019.
[22] L. Wang, Z. Du, W. Dong, Y. Shen, and G. Zhao, “Intrinsic sensing and evolving internal model control of compact elastic module for a lower extremity exoskeleton,” Sensors (Switzerland), Vol. 18, No. 3, Mar. 2018.
[23] S. M. Hashem Zadeh, S. Khorashadizadeh, M. M. Fateh, and M. Hadadzarif. “Optimal sliding mode control of a robot manipulator under uncertainty using PSO,” Nonlinear Dyn, Vol. 84, No. 4, Feb. 2016.
[24] M. M. Fateh, “Robust control of flexible-joint robots using voltage control strategy,” Nonlinear Dyn, Vol. 67, pp. 1525–1537, Jan. 2012.
[25] M. Jalaeian-F, M. M. Fateh, and M. Rahimiyan, “Optimal Predictive Impedance Control in the Presence of Uncertainty for a Lower Limb Rehabilitation Robot,” J Syst Sci Complex, Vol. 33, No. 3, Jun. 2020.
[26] M. Jalaeian-F, M. M. Fateh, and M. Rahimiyan, “Bi-Level Adaptive Computed-Current Impedance Controller for Electrically Driven Robots,” Robotica, Published online, 28 May 2020, pp. 1-17.
[27] C. Guo, S. Guo, J. Ji, and F. Xi, “Iterative Learning Impedance for Lower Limb Rehabilitation Robot,” J Healthc Eng, Vol. 2017, Article ID 6732459, 9 pages, Aug. 2017.
[28] J. F. Veneman , R. Kruidhof, E. E. G. Hekman, R. Ekkelenkamp, E. H. F. Van Asseldonk, and H. Van Der Kooij, “Design and evaluation of the LOPES exoskeleton robot for interactive gait rehabilitation,” IEEE Trans Neural Syst Rehabil Eng, Vol. 15, No. 3, pp. 379-386, Sep. 2007.
[29] G. A. Turley, M.A. Williams, R.M. Wellings, and D.R. Griffin, “Evaluation of range of motion restriction within the hip joint,” Med Biol Eng Comput, Vol. 51, No. 4, pp. 467-477, Dec. 2012.
[30] H. Fasih, S. Tavakoli, J. Sadeghi, and H. Torabi, “Kalman Filter-Smoothed Random Walk Based Centralized Controller for Multi-Input Multi-Output Processes,” Int J Ind Electron Control Optim, Vol. 2, No. 2, pp. 155-166, Spr. 2019.
[31] M. Jalaeian-F, M.M. Fateh, and M Rahimiyan, “Internal Model Impedance Control for a Lower Limb Rehabilitation Robot in the Presence of Uncertainty,” 26th Iran. Conf. Electr. Eng. ICEE 2018, Mashhad, Iran: IEEE, Vol. 2018, pp. 930-935, 2018.
[32] M. Jalaeian-F, M. M. Fateh, and M. Rahimiyan, “Dynamic-Growing Fuzzy-Neural Acceleration-Based Impedance Controller for a Lower Limb Rehabilitation Robot,” Electr Eng (ICEE), Iran Conf 2018, Vol. 2018, pp. 1000-1004, 2018.

Mohsen Jalaeian-F received the M.Sc. degree of control engineering from the Ferdowsi University of Mashhad, Iran, in 2012. Currently, he is a Ph.D. candidate at Shahrood University of Technology. He is also with the Center of Excellence on Soft Computing and Intelligent Information Processing (SCIIP). His research interests include robotics, control, optimization, AI/ML (soft-computing), fuzzy logic, and deep reinforcement learning.

Mohammad Mehdi Fateh received his B. Sc. degree from Isfahan University of Technology in 1988. He received his M.Sc. degree in electrical engineering from Tarbiat Modares University, Iran in 1991, and his Ph.D. degree in robotic engineering from Southampton University, the UK in 2001. He is a full professor with the Department of Electrical and Robotic Engineering at Shahrood University of Technology, Iran. His research interests include nonlinear, robust and fuzzy control, robotics and intelligent systems, mechatronics, and automation.

Morteza Rahimiyan received the B.Sc. degree from the Isfahan University of Technology, Isfahan, Iran, in 2003, and the M.Sc. and Ph.D. degrees (with honors) from the Ferdowsi University of Mashhad, Mashhad, Iran in 2006 and 2011, respectively, all in electrical engineering. He is currently an associate professor at Shahrood University of Technology, Shahrood, Iran. His research interests include operation, planning, and economics of power systems, as well as optimization.

International Journal of Industrial Electronics, Control and Optimization © 2020 IECO
Vol. 3, No. 4, pp. 491-501, Sep (2020)

Linear Modelling of Six Pulse Rectifier and Designee of Model Predictive Controller with Stability Analysis

Hamid Radmanesh[1], Masood Saeidi [2†]

[1]Electrical Engineering Department, Shahid Sattari Aeronautical University of Science and Technology, Tehran, Iran
[2]Department of Electrical and Computer Engineering, Iran University of Science and Technology, Tehran, Iran

ABSTRACT

The AC/DC converter is one of the popular power electronic converters in industrial applications such as in the railway, power supply systems and electric vehicle. In this paper, a three-phase controllable rectifier is considered and its linear model is extracted. Because of MPC controllers benefits, the continuous control set model predictive controller (CCs-MPC) is designed for controlling this rectifier output DC voltage. By considering rectifier dynamic response, the suitable criteria to choice the model predictive controller parameters such as sampling time, prediction horizon and control horizon is proposed. In experimental implantation the computing burden of microcontroller is limit therefore the reaching to optimal and minimum complexity in algorithms implantation is vital problem. In other words by using these proposed criteria for selection of sample time, prediction and control horizon the tradeoff between computational burden, system performance and dynamic stability is made. When using designed MPC controller, the rectifier and grid performance such as total harmonic distribution (THD), power factor (PF) and output voltage ripple have acceptable value. This controller can eliminated the effect of heavy load change on rectifier performance which is very common problem in industrial system. Also, this controller stability guaranteed is checked by using the dual-mode method. The simulation results and controllers performance are validated in MATLAB software

Article Info

Keywords:
Linear model, Power Conversion, Predictive control, Rectifier, Stability analysis

Article History:
Received 2020-03-05
Accepted 2020-07-22

I. INTRODUCTION

Once Todays, power electronic converters have become the most important controllable device in power systems [1]. With using of power electronics converter to merge all of the new energy sources, make possible many advantages such as reduced component counts, weight reduction and control simplicity in power utility and microgrids [2]. In the past, due to the low level of semiconductor manufacturing technology, the converters switching speed was low and making using them impossible or very limit [2]. Nowadays, thanks to semiconductor manufacturing improvements, these converters can be used in high switching frequency and high power rating, so today, in the power system and industrial application these converters are used at the scale of Gigawatt and with frequency up to 400 kHz [3] .After this progression, they are widely used in microgrids, hybrid/electric transportation vehicles or hybrid energy systems. Benefit of implementation control methods on power electronic converters have been investigated and different methods for control these converters have been proposed in [4]. The conventional Linear controller is used for controlling the output voltage by appropriate tuning the Kp and Ki values ,however, this control method have some disadvantage as result researcher tried to develop new control method form past years. Due to the existence of uncertainties and nonlinear behavior in the power electronic system, using the linear

†Corresponding Author: masood.saeidi.sbu@gmail.com
Tel: +98-21-77240540, power, electrical engineering, Iran university of science and Theology, Tehran, Iran

controller theory is not recommended [5]. So, researchers have tried to use new control methods that solve the linear controller theory problems and use all capacity of this converter. To overcome these problems, new control methods such as neural networks, fuzzy, and sliding mode control as known an intelligent control methods has been proposed in [5-6] . The nonlinear controller such as MPC, fuzzy and sliding mode controllers have some benefits and advantage with compression of linear controllers such as dynamic speed, low ripple and ability to consider system model nonlinearity effect and etc. Therefore in recent years especially after microprocessor computational power progression, most of the nonlinear controller are implemented in linear control system. In spite of creating computational burden and being complex in both design and implementation procedures, using these controllers can indeed overcome the disadvantage of ordinary linear controllers but linear controllers nowadays still the first priority in power electronic converters in compression with this intelligent methods. In recent years theory of the predictive control methods are presented and this control method has gradually been used in the all fields of industrial application .The initial implementation of model predictive control algorithm has been introduced in the chemical and thermal industry [7] .With the advancement of computer processors, the processing speed has been increased dramatically and providing the ability to implement new control method such as model predictive control algorithms in most industrial system [8].

According to the discrete nature of the power electronic converters, the use of predictive control algorithm in these systems has been suggested in [9, 10]. One of the main reasons for using this method in power electronic converters, is the possibility of considering constraints in the controller design. In [11, 12], designing and implementation of constrained model predictive controller methods in power electronic converters have been investigated. The application of predictive control in various types of power electronic converters are reviewed in [13], which has demonstrated the use of this control algorithm in the distributed generation sources become widespread in last years [13].

Generally, model predictive control can be divided into Continuous Control Set (CCS)-MPC and Finite Control Set (FCS)-MPC [14]. In FCS-MPC, searching and selecting the optimal switching mode from among the number of switching states and after applying it to the system, while in the CCS-MPC, the optimal control signal is produced by optimizing the process according to the system dynamic equations. CCS-MPC requires a modulator to generate control signals, which cause the fixed switching frequency, while in FCS-MPC the switching frequency is variable [15]. In [16], these two control methods in the induction motor drive are compared.

In fact, for designing an appropriated controller, modeling the power electronic converters are necessary. In [17, 18], the modeling of these converters and electrical machines drives are discussed. In these references, the Taylor expansion method for small signal modeling without considering large signal modeling and parameter variation is used. Therefore, using small signal model leads to a significant error conditions such as in fault conditions and severe load change, that it may cause disturb control system. The model predictive controller can reduce uncertainties effects on the system performance hence the use of linear models for designing a prediction controller will lead to satisfactory results. But in some literature, such as [19, 20], designing and using of nonlinear model predictive controllers in power electronic converters is proposed, although it contributes to the better performance than linear MPC but leads to complex design and operation aren't suitable for industrial application.

Today, all controllers are implement digitized, but it is necessary to select the suitable sampling time for these systems. The importance of selecting the appropriate sampling time in the MPC algorithm is discussed in [21]. Some of the most important reasons for choosing the appropriate sampling time in the MPC controller are impacts on the calculations time and the dependence of the controller stability. Design and implementation of constrain MPC is another important topic which is discussed in [22, 23]. In most articles that refer to the use of MPC controller in power electronic converters and electrical drives, the issue of choosing an appropriate sampling time and the prediction and control horizon, aren't considered. In most MPC controller applications in power electronics, have not offer analytical method for designing of MPC parameters such as sampling time, prediction horizon and control horizon while in this article, attempt has been made to set these parameters using a dynamic model and system behavior.

In this paper, CCS-MPC for controlling a three-phase rectifier is designed. According to the system dynamic response, a criterion is proposed for selecting the prediction and control horizon in the MPC controller, and MPC controller stability proof is investigated by use of the dual-mode method. In the some related works in power electronics, the stability proof is not considered for MPC controller or other new control methods .While in this study, the stability of the proposed controller is investigate and proved. In the VI it is shown that the stability of the MPC controller is related to the prediction horizon and sampling time which indicates the importance of the criterion controller parameters designing procedure.

This paper is arranged as follows. The mathematical and linearized model of the three-phase controllable rectifier is presented in Section 2. Model predictive controller design of rectifier is presented in Section 3. Stability analysis of modified CCS-MPC controller with using dual-mode method is illustrated in Section 4. The simulation results are describe in Section 5. Conclusions are given in Section 6.

II. Mathematical Model of Three-Phase Controllable Rectifier

In this section, the three-phase converter (rectifier), which uses the IGBT switches, is investigated. Rectifiers are the oldest and the most used power electronic converters. To use them in high power applications, the input voltage of these converters is usually three phases. To reduce the output voltage fluctuations, a capacitor is usually used as a voltage filter in rectifier structure. Also, a resistive load is used in rectifier structure. The three-phase rectifier topology is shown in Fig. 1.

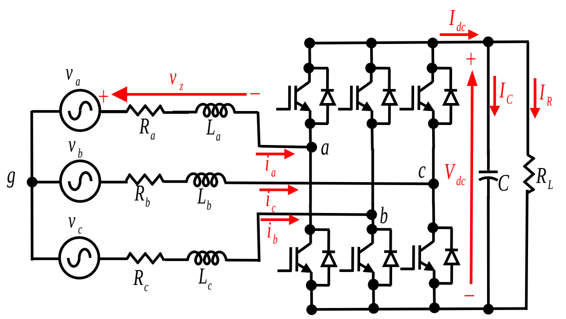

Fig. 1. Studied rectifier structure

The state space method is used to model this converter. Dynamic elements are selected as system state variables; therefore, capacitor voltage and grid current are selected as rectifier system state variables [25]. With this assumption and with using Table 1 the state equations of the system are given as follows:

$$\frac{di_a(t)}{dt} = -\frac{R}{L}i_a - \frac{1}{L}v_{za}(t) + \frac{1}{L}v_{ga}(t) \tag{1}$$

$$\frac{di_b(t)}{dt} = -\frac{R}{L}i_b - \frac{1}{L}v_{zb}(t) + \frac{1}{L}v_{gb}(t) \tag{2}$$

$$\frac{di_c(t)}{dt} = -\frac{R}{L}i_c - \frac{1}{L}v_{zc}(t) + \frac{1}{L}v_{gc}(t) \tag{3}$$

$$I_{dc}(t) = I_{dca}(t) + I_{dcb}(t) + I_{dcc}(t) \tag{4}$$

$$\frac{d}{dt}v_{dc}(t) = \frac{1}{c}I_{dc}(t) - \frac{1}{cR_L}v_{dc}(t) \tag{5}$$

$$v_{rabc} = \frac{1}{2}m_i(t) * v_{dc} \tag{6}$$

$$v_{r_{abc}} = v_{abc} - v_z \tag{7}$$

$$i_{r_{abc}} = \frac{1}{2}m_i(t) * I_{dc} \tag{8}$$

Table.I
Parameter Definition of Studied Rectifier

Parameter	Definition	*Unit*
I_{abc}	Grid three phase current	Amp
$Vabc$	Grid three phase voltage	Volt
V_{dc}	Dc link voltage	Volt
C	Capacitor	F
m_i	modulation index	-
I_{dc}	output dc current	-
R	Grid resistance	Ω
L	Grid inductance	H

With sinusoidal grid voltage assumption and using (4) the above equations are rewritten as follows:

$$\frac{di_a(t)}{dt} = -\frac{R}{L}i_a - \frac{m_i}{2L}v_{dc} + \frac{1}{L}V_{ag} \tag{9}$$

$$\frac{di_b(t)}{dt} = -\frac{R}{L}i_b - \frac{m_i}{2L}v_{dc} + \frac{1}{L}V_{bg} \tag{10}$$

$$\frac{di_c(t)}{dt} = -\frac{R}{L}c - \frac{m_i}{2L}v_{dc} + \frac{1}{L}V_{cg} \tag{11}$$

$$\frac{d}{dt}v_{dc}(t) = \frac{3m_i}{2c}I_{dc}(t) - \frac{1}{cR_L}v_{dc}(t) \tag{12}$$

$$m_i = 2\frac{V_{abcg}\,sin(\omega t) - V'_{abcg}\sin(\omega t + \varphi)}{v_{dc}} \tag{13}$$

$$\varphi = \tan^{-1}\left(\frac{XL}{R}\right) \tag{14}$$

Where V_{ag}, V_{bg}, V_{cg} are the amplitude of grid voltages and v' is amplitude voltage drop on grid impedance. By using the above equations, the model of the system is written as follows:

$$\frac{di_a(t)}{dt} = -\frac{R}{L}i_a - \frac{1}{L}v_{ra}(t) + \frac{1}{L}v_a(t) \tag{15}$$

$$\frac{di_b(t)}{dt} = -\frac{R}{L}i_b - \frac{1}{L}v_{rb}(t) + \frac{1}{L}v_b(t) \tag{16}$$

$$\frac{di_c(t)}{dt} = -\frac{R}{L}i_c - \frac{1}{L}v_{rc}(t) + \frac{1}{L}v_c(t) \tag{17}$$

$$\frac{d}{dt}v_{dc}(t) = \frac{(i_a + i_b + i_c)}{cv_{dc}}\sqrt{v^2{}_g - 2v_g v'\cos(\varphi) + v'^2} - \frac{1}{cR_L}v_{dc} \tag{18}$$

TABLE. II
PARAMETER DEFINITION (8-18)

Parameter	Definition	*Unit*
V_{ag}, V_{bg}, V_{cg}	Grid voltage amplitude	Volt
V'	voltage drop amplitude	Volt
V_{dc}	Dc link voltage	Volt
φ	Power factor	Deg
m_i	modulation index	-
V_g	Phase Voltage	Volt

In (15-18) with considering that grid currents have dependency with together, therefore, one phase current and dc link capacitor voltage are selected as state variables and grid voltages are system input variables respectively. In the state equations, there are some nonlinear term such as $(\frac{I_a+I_b+I_c}{CV_{dc}})$ and $m_i(t)$ therefore for linear analyses, with using 10 kW rectifier parameter (Table I) and using the Taylor expansion method can be linearize of (15-18) around the nominal operation point ($i^{abc} = 26.18, V_{dc} = 400, V' = 19.09$) , transfer function is calculated as:

$$H(s) = \frac{V_{dc}}{m_i}(s) = \frac{2.8286(s+175100)}{(s+51.17)(s+125.7)} \qquad (19)$$

TABLE III
RECTIFIER SYSTEM PARAMETER VALUES

Parameter	Unit	Value
$P_{rectifier}$	Kw	10
V_g	Volt	180
V_{dc}	volt	400
f_{grid}	Hz	60
L_{grid}	mH	1.93
R_{grid}	Ω	0.1
R_L	Ω	16
C	μF	990

III. MODEL PREDICTIVE CONTROL DESIGN

Because of nonlinear behavior and parameter uncertainties in power electronic converters, by using the new controller, the defects of linear controllers are eliminated [25]. The model predictive control algorithm is one of the best options for using in power electronic converter applications.

A. Model Predictive Control Algorithm

Model predictive control algorithm generates a proper control signal to stabilize the rectifier voltage. MPC controller is implemented in 4 forms which are: DMC, AMC, PFC, and GPC [26]. In [26], a full comparison between 4 forms of the MPC controller is taken and its result is that using GPC format for unstable, non-minimum phase and system with very small zero is appropriate. Therefore in this paper, the GPC form for MPC implementation is used. For nonlinear effects minimizing, Using of MPC is recommended [26], therefore in this paper, it is applied to the rectifier system. The rectifier control system is shown in Fig. 2.

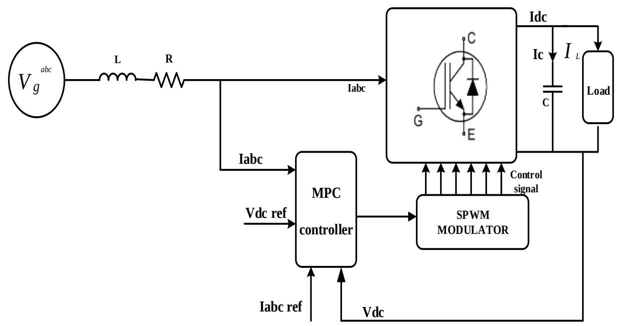

Fig. 2. Rectifier control system.

The MPC is a multivariable control algorithm and the calculation of the optimal control move is based on solving the optimization problem defined by a cost function and the control goal can be prescribed by the quadratic cost function. The MPC controller cost function can be formulated as (20), a control signal can be produced, with minimization of the cost function J:

$$J(N_1, N_p, N_c) = \sum_{j=N_1}^{N_p} \delta(j)\left[\hat{y}(t+j|t) - w(t+j)\right]^2 + \sum_{j=1}^{N_c} \lambda(j)[\Delta u(t+j-1]^2 \qquad (19)$$

where, N_p is prediction horizon, N_c control horizon, N_1 model delayed, Δu control signal, y (t) model output(t) reference set point and δ(t) and λ(t) are the weight factors [18].

B. Tuning of the Model Predictive Controller Parameter

Choosing the appropriate values for the controller parameters in the cost function can be effective in reducing the computation burden. Therefore, with proper selection of these parameters, optimal control signals can be generated which improves the power electronic converters performance and efficiency. The prediction horizon and sample time should be selected according to the system specification [21]. If the cost function doesn't have any constraints, by applying optimization methods, the cost function can be optimized by conventional method but in case of constrained MPC controller design, complex minimization method such as active set and Gauss-Seidel method are applied [22, 23].

The MPC controllers are implemented in both schemes of finite control set (FSC-MPC) and continuous control set (CCS-MPC). The idea of using FCS-MPC is referred as to the natural discrete property of power electronic converter hence by applying the model prediction, the switches finite state is predictable [29]. This method has advantages, such as lack of need for modulators, the simple implementation, and the intuitive understanding algorithm. Having variable switching frequency, system response fluctuations and the steady-state error in the system output response are considered as its disadvantage. Another scheme for implementing the MPC controller is acquired via the CCS approach. In this method, the MPC controller generates an appropriate reference signal which is used in SPWM or SVM modulators. Some of the CCS-MPC advantages are given as constant switching frequency, the possibility of eliminating the steady-state error, less sampling time and designed controller with proof of the possibility of stability moreover using long horizon police and provide MPC with the high degree of robustness [9]. In comparison with FCS-MPC controller, CCS-MPC requires less time for computing and it has a clear design approach otherwise it is vulnerability to noise and external disturbances effects.

In order to calculate CCS-MPC algorithm, use of online and offline methods are recommended. An online method based on calculations of the control law in each sample interval [10]. The offline mode is based on obtaining explicit control signals with consideration of system operation points and keep these explicit signals. Specification all operating point in which the optimal control moves are determined by evaluating a linear function. Explicit MPC controllers require lower computation time than the conventional controller. Therefore it is useful for applications which require small sample time [31]. Principles of determining suitable operation points are under discussion been in [32], further investigation is beyond the scope of this paper. To implement the CCS-MPC controller, selection of the sample time, the predictive horizon and the control horizon is necessary. The volume of computations depends on the choice of these parameters so that they should be precisely selected until lower processing time needed for the algorithm computations. Some criteria for choosing sample time and prediction horizon are given in [33] but, in this reference, the first order system with constant time delay is under discussion, while rectifier system model is two order system with one zero. Therefore, this method will not provide any appropriate responses in the rectifier system. In this paper, it is suggested that the sampling time should be selected based on model dynamic response and theorem of Shannon which is using in continues model discretization process. Based on digital control theorem, for converting S-domain system to Z- domain model, in each oscillation cycle between 8-12 samples is require until the quantization error is ignorable. In this paper, this number is selected 10, and in selecting of the prediction horizon for oscillating systems, it should be noted that the prediction horizon should be able to cover at least one peak or one valley of the wave in order to provide sufficient information about the system model so that the prediction process can be done to produce the control signal properly still, the value of the control horizon should not be taken very high because it diminishes the calculation rate of system.

C. Model Predictive Controller Design

In this paper, the primary prediction and control horizon is given the initial value 11 and 2 respectively but the changes in the prediction and control horizon in the system response are still checked in following simulation and investigate this parameters effect on controller response. The sample time for the system transfer function discretization according to the system dynamic response is selected 0.00083(s). Sample time is selected 0.00083 (s) and using of zero-pole match method for discretization. The discrete transfer function of the system is given as follow:

$$\mathrm{h}\left(Z^{-1}\right)=\frac{.116Z^{-1}+.107Z^{-2}}{1-1.858Z^{-1}+.8622Z^{-2}} \tag{21}$$

Commonly, in GPC technic, controlled autoregressive integrated moving average (CARIMA) model type is used. The equation of CARIMA model can be derived as follows:

$$A\left(Z^{-1}\right)y\left(t\right)=B\left(Z^{-1}\right)u\left(t-1\right)+C\left(Z^{-1}\right)\frac{\xi\left(t\right)}{\Delta} \tag{22}$$

Where for power electronics and drive application, d is considered 1, $\zeta(t)$ represent noise in system and $\Delta=1-\boldsymbol{Z}^{-1}$, Δ is deviation operator. If $\zeta(t)$ is white noise, $C(Z^{-1})$ is set to 1 thus (22) can be simplified as:

$$A\left(Z^{-1}\right)y\left(t\right)=B\left(Z^{-1}\right)u\left(t-1\right)+\frac{\xi\left(t\right)}{\Delta} \tag{23}$$

In order to calculate the prediction step, the following Diophantine equation is considered as following [33]:

$$1=E_j\left(Z^{-1}\right)A\left(Z^{-1}\right)\Delta+Z^{-j}F_j\left(Z^{j}\right) \tag{24}$$

Calculation of F and E terms are described in [33]. The best possible prediction for y is:

$$\mathrm{y}\left(\mathrm{t}+\mathrm{j}\right)=G_j\left(Z^{-1}\right)\Delta U\left(t+j-1\right)+F_j\left(Z^{-1}\right)y\left(t\right) \tag{25}$$

In which: $G_j(t)=E_j(Z^{-1})B(Z^{-1})$. In (25) the term of $G_j(Z^{-1})\Delta U(T+j-1)$ is divide into 2 terms, concerning past and future. Sum of the past output term with $F_j(Z^{-1})$ is named free response (f) and system response to future value is force response. System transfer function $h(Z^{-1})$ is expressed as following:

$$A\left(Z^{-1}\right)V_{dc}\left(t\right)=B\left(Z^{-1}\right)m_i\left(t-1\right) \quad (26)$$

At the first step, assuming that there is no constraint in the system, the control signal is obtained by minimizing as follow:

$$\frac{\partial j}{\partial U}=2\left(G^TG+\lambda I\right)U+2G^T\left(f-w\right)=0 \quad (27)$$

$$U=\left(G^TG+\lambda I\right)^{-1}G^T\left(w-f\right) \quad (28)$$

In MPC controller, receding horizon approach is used and in any optimization one term of control effort (U) is applied to the system [34]. In the above equation, G is system dynamic matrix, f denotes the free response of the system, λ the weighting factor and W the reference trajectory.

IV. Stability Analysis of CCS-MPC Controller with Using Dual Mode Method

To ensure the stability of the controller, it should be demonstrated mathematically. In linear controllers, it is possible to prove the stability through conventional methods, such as an NYQUIST diagram, root locus curve or bode diagram analysis [35]. Stability analysis method of MPC controllers is not as same as linear controllers. In the references such as [36], [37], mathematical methods for proving the stability of MPC controllers have been discussed.

The method examined in this paper is to prove the stability of the MPC controller, known as the Dual Mode method. In (20), if the upper limit of the first summation approach to infinity, the optimization problem is feasible. But in practical and industrial applications, the computation power of microprocessors are limited, therefore, prediction and control horizon are selected on the basis of a specified criteria such as the defined method. Hence MPC controller requires stability investigation. The basis of the Dual Mode method is minimizing the cost function from one until prediction horizon and applying state feedback from the perdition horizon to the infinity. Accordingly, if the conditions of the Dual Mode problem are satisfied, it is strongly claimed that the MPC controller is stable. The rectifier system transfer function in (19) is rewritten as the state space model in below.

$$\begin{bmatrix} x_1(k+1) \\ x_2(k+2) \end{bmatrix}=\begin{bmatrix} 1.83 & -0.83 \\ 1 & 0 \end{bmatrix}\begin{bmatrix} x_1(k) \\ x_2(k) \end{bmatrix}+\begin{bmatrix} 1 \\ 0 \end{bmatrix}\left[v_i(k)\right]$$
$$y(k)=\begin{bmatrix} 0.2383 & 0.218 \end{bmatrix}\begin{bmatrix} x_1(k) \\ x_2(k) \end{bmatrix} \quad (29)$$

The quadratic cost function with an infinite horizon is written as follows:

$$J=\sum_{j=0}^{\infty}\left[x^T\left(k+i\right)Qx\left(k+i\right)+u^T\left(k+i\right)Ru\left(k+i\right)\right] \quad (30)$$

As being as, the (30) until infinite prediction horizon is minimized, it will certainly be stable, however in practice the control horizon is limited, so the (30) is rewritten as following and this is done by choosing the terminal weighting matrix $\bar{Q}$ so that the term $x^T(k+N_p+1)Q\Delta x(k+N_p+1)$ is equal to the cost over the mode 2, which is equivalent to the state feedback effect [34].

$$J=\sum_{i=0}^{N_p}\left[x^T\left(k+i\right)Qx\left(k+i\right)+u^T\left(k+i\right)Ru\left(k+i\right)\right]+ \\ x^T\left(k+N_p+1\right)\bar{Q}x\left(k+N_p+1\right) \quad (31)$$

Terminal weighting matrix is achieved by a solution of the LYAPUNOV equation:

$$\bar{Q}-\left(A+BK\right)^TQ\left(A+BK\right)\geq+K^TRK \quad (32)$$

Where A,B are calculated from the state space model and denotes is stated feedback gain.

The LYAPUNOV equation (32) has a unique solution for $\bar{Q}$ if and only if: 1) the eigenvalues of $A+BK$ are located inside in the unit circle, 2) $Q+K^TRK$ where $Q=C^TC$ positive definite [34] is. For the controllable system, by designing an appropriate K , closed-loop poles can be placed at the specified locations [34]. Using terminal weighting matrix, LYAPUNOV function can be defined as $V(x)=x^T\bar{Q}x$ where $V(x)>x$ and $\dot{V}(x)<0$ and ,which guarantee the MPC controller stability.

In summary, this paper suggests dual-mode receding horizon control method with state feedback controller which is applied inside the attractive region and a receding horizon controller applied outside the terminal region [33]. Dual model method concept is shown in Fig. 3.

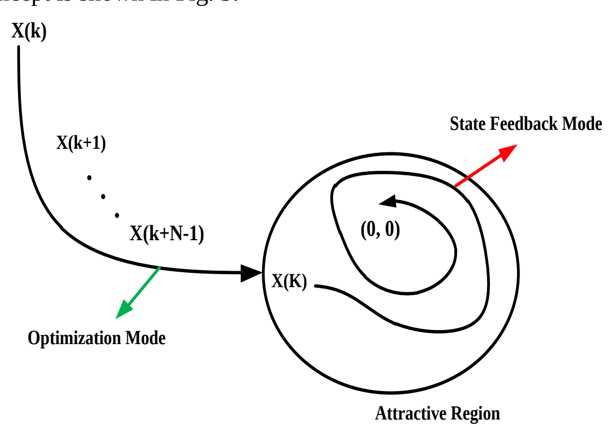

Fig.3. The schematic diagram of the dual-mode method

By using equations of (29) and (32), state feedback gain (K) and terminal weighting matrix ($\bar{Q}$) are defined as follow:

$$K = \begin{bmatrix} 1.833 \,,\, 1.077 \end{bmatrix}$$
$$\overline{Q} = \begin{bmatrix} 5.34 & 1.83 \\ 1.83 & 1 \end{bmatrix} \quad (33)$$

After calculation of $\bar{Q}$ and K, we can claim that designed CCS-MPC controller is stable [38]. In case of power electronic converters and electrical drive applications, stability problem of MPC controller isn't a major issue because their models aren't complex, therefore, using this paper the proposed method for sampling time and prediction horizon selection, don't require for power electronic converters and electrical drive stability evaluate but without using appropriate criteria, stability analysis is needed.

V. SIMULATION RESULTS

Plotting of the time or frequency response is the first step in any controller design. The rectifier system step response is shown in Fig. 4(a). According to Fig. 4(a), the system output voltage without a controller is not appropriate and has 5% steady state error, as well as the system settling time, is not suitable. Therefore a controller should be designed to improve the system output voltage.

Fig. 4(b) depicts the simulation result of the system via the CCS-MPC controller. As can be seen from Fig. 4(b), the use of CCS-MPC controller in the rectifier system has made it possible to provide the fast response with high steady-state precision without having any oscillation or overshoot rectifier output voltage. As a result, the selection of criteria for MPC parameter is acceptable.

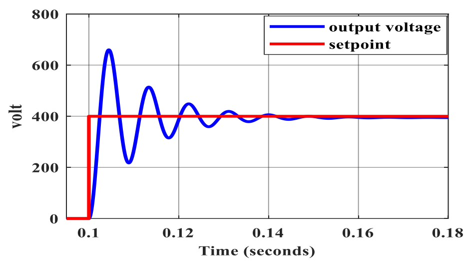

(a)

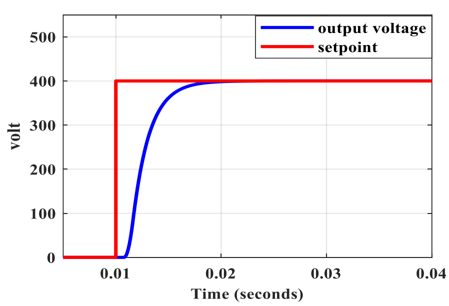

(b)

Fig. 4. The Rectifier output voltage step response; without (a) and with (b) CCS-MPC controller with the prediction horizon 11, and the control horizon 2

The effect of sampling time, prediction and control horizon variation on system performance is discussed in following. Initially, the sampling time will change without altering other parameters. As shown in Fig. 5(a), by increasing the sample time, system dynamic response is also strongly affected and reducing the system speed response. In fact, by increasing the sampling time, a portion of the model is ignored and the signal is not properly recovered and ultimately it reduces system dynamic speed. The effect of reducing the sampling time on the performance of the system has been investigated in Fig. 5(b). The simulation result shown in Fig. 5(b) illustrates the influence on DC side voltage when sampling time is reduced. When the sampling time is set to 0.0002 seconds, the output voltage has a 550V peak in its response, therefore, if sampling time more reduced, it may lead to voltage instability. The system output oscillation reason is related to reduction its sampling time because when the sampling rate is smaller, the little amount of date from the model response is available then the controller cannot be able to generate the optimal signal, that it may even lead to system instability. In other words, in the selection of sampling time, should be established a tradeoff between output response speed, stability, and computational complexity, thus the criterion which is proposed in this paper is an effective solution. The effect of changing the prediction horizon on the system response is investigated in Fig. 5(c). As can be seen from Fig. 5(c), the effect of prediction horizon reduction is approximately equivalent to reducing the sampling time with this difference that decreasing the prediction horizon will reduce the burden of the complexity computations. So, in practice, there will be a relax tradeoff between the system response and facilitates calculation.

Control horizon is another tuning parameter in CCS-MPC controller. In contrast to the two parameters of prediction horizon and sampling time, this parameter has no significant effect on the system stability and it only affects the transient response of the system. The choice of control horizons is important only in constrained systems and its selection is not important for unconstrained systems so that the long control horizon result in more computational volume [12]. Fig. 5(d) shows the variation of the control horizon on the system response.

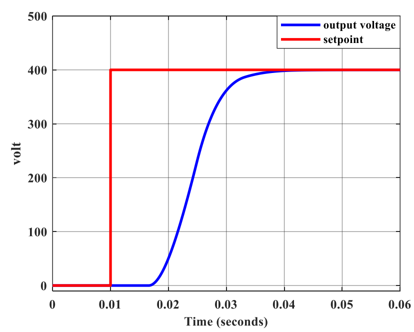

Fig. 5 (a)

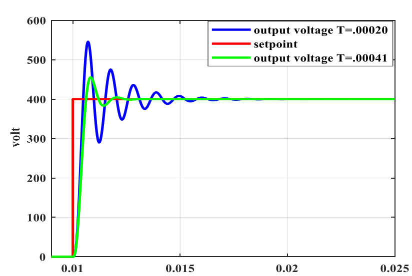

Fig. 5 (b)

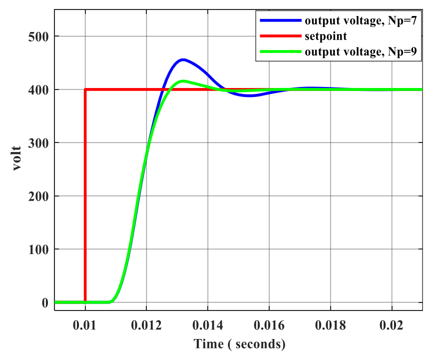

Fig. 5 (c)

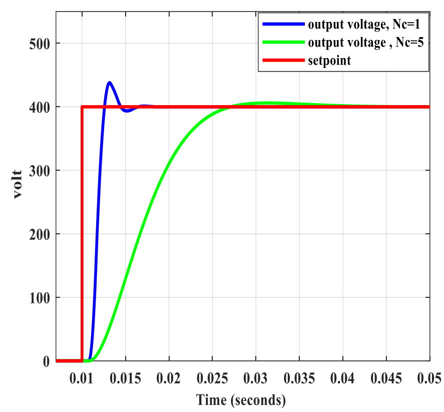

Fig. 5 (d)

Fig. 5. The effect of (a) increasing the sampling time, (b) reducing the sampling time, (c) prediction horizon change, (d) control horizon change on the system response.

A. Analysis of Rectifier Performance with CCS-MPC Controller

In order to show the MPC controller benefits, converter performance when using MPC controller should be investigated. Grid current, PF and THD are very important factors in rectifier converter control, therefore in Fig. 6 is showing these parameters when using the MPC controller. As inferred from Fig. 6, THD and PF parameter in the rectifier system is controlled in the acceptable range, therefore, can be recommended for using this control algorithm in high power rectifier system however in traditional Thyristor rectifier, power quality problem is an open topic of research that requires further attention. In output voltage harmonic spectrum is shown that after the main DC component, harmonics in f=300 Hz and f=600 Hz are other harmonics which is less than IEC61000 3-2 standard values therefore from power quality aspect, this system output voltage is desirable. Following, controller performance has been investigated when the load is increased. Due to the fact, when using the linear model for system behavior representation, this model is valid on system operation point so the system load changes are should be changed around the operation point [28]. In this paper, a modified structure of the MPC controller is used and therefore we expect that this controller can reduce the effect of heavy load change in rectifier performance.

Fig. 8 shows rectifier output DC voltage when the load is increased 20%, 50%, 100% and 150% respectively. As can be noticed, Fig. 8 evidence that when using MPC in the rectifier control system heavy load variations do not distribute output voltage severely because, in the new structure, nonlinearity of system is reduced by selection of appropriate correction factor. From Fig. 7 can be inferred that when load changes, the rectifier output voltage have steady state error that depends on the value of the new load because when load is increased dramatically, system voltage droop in grid impedance is increased therefore rectifier input voltage is reduced and as a result, this effect cause voltage steady state error in output voltage

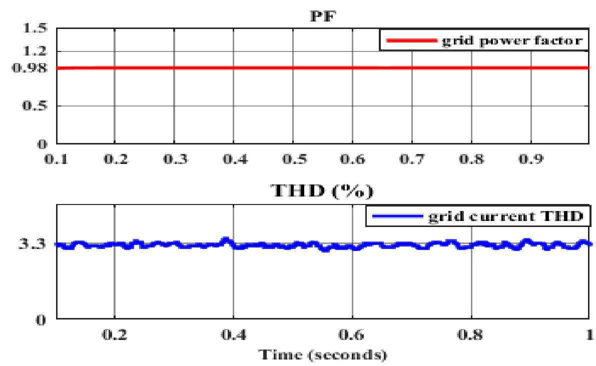

Fig. 6: Grid side current THD and PF when using CCS-MPC controller in Rectifier.

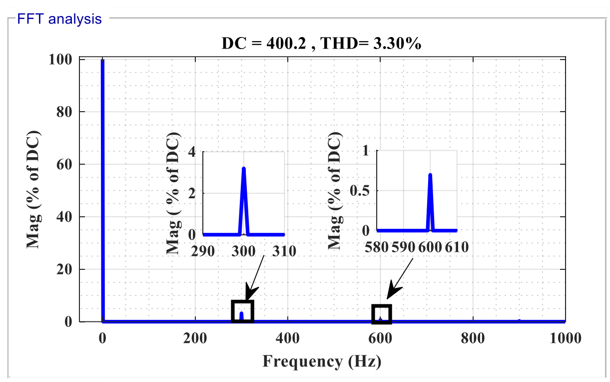

Fig 7: Rectifier output voltage harmonic spectrum

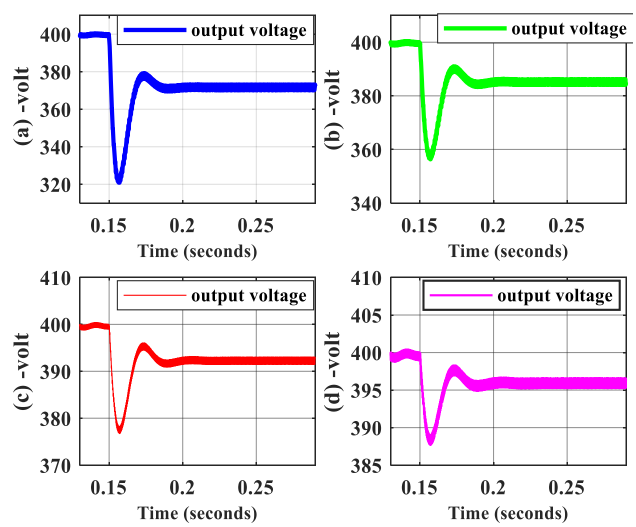

Fig. 8: Rectifier output voltage when load is change in t= .15 (s), (a) 150 %, (b) 100 %, (c) 50 %, (d) 25 %.

In practical applications, overvoltage and lower voltage conditions events are very probable case. This events causes may be related to starting high load system, the transient overvoltage of capacitors or short circuit fault in the system, therefore in this conditions the investigation of the rectifier performance is very necessary. Fig. 8(a) shows the rectifier output voltage when a three-phase 30% overvoltage fault has occurred in t =.25 (s) until t= .4 (s). As shown in Fig. 9(a), at the fault duration event in the grid, the rectifier output voltage is stabilized. In online CCS-MPC, cost function optimization will be done in any sampling time so the differences between the linear model and real system are decreased as result CCS-MPC controller is robustness again external conditions. This MPC algorithm reduces the uncertain effects of the system on the output voltage and it robust the system in front of severe faults such as over or under voltage.

In the final step, should be tested rectifier performance in harmonic condition. In this case, 20% harmonic order 5 is applied to grid voltage and investigate rectifier performance. As shown in Fig. 8(b), with using MPC controller in rectifier voltage harmonic effects are eliminated in output DC voltage. In practical application, the input voltage of the rectifier converter has some harmonic such as 5 and 7 orders so as a result from Fig. 8(b) using of MPC controller is guaranteed rectifier output voltage in the normal range.

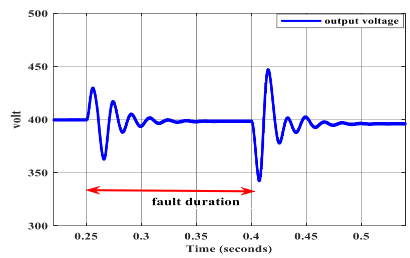

Fig. 9 (a)

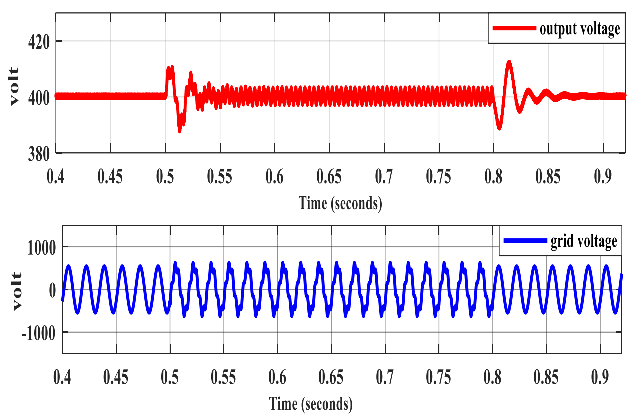

Fig. 9 (b)

Fig. 9: Rectifier output voltage, (a) with three phase overvoltage, (b) in the harmonic condition.

VI. Conclusion

In this paper, the linear model of the controllable rectifier is obtained and the specified transfer function is calculated. The main goal of this paper is designing a CCS-MPC controller for regulating rectifier output DC voltage and investigating its performance in the rectifier converter. The criterion for selecting of CCS-MPC sampling time, prediction and control horizon is proposed. This criterion is the specified procedure for tuning the sampling time and prediction horizon with the consideration system dynamic response and the computing power of the processor. Using of CCS-MPC controller demonstrates that it has the appropriate result in some grid and converter characteristics such as grid PF, THD, and output voltage drop value. In particular, when sever changes or faults and disturbances affects the system, MPC controller has the ability to eliminate this outer disturbance. In this paper, MPC controller stability proof is investigated by using the dual model method. The main result from MPC controller stability procedure, is that, if a valid criterion is used in traditional power electronic converter, the stability analysis won't be a vital problem but if don't regard suitable tuning method in selection of MPC controller parameters, stability analyses and determination of stability margin are vital step in MPC controller design.

References

[1] A. Q. Huang, "Power Semiconductor Devices for Smart Grid and Renewable Energy Systems," in *Proceedings of the IEEE*, vol. 105, no. 11, pp. 2019-2047, Nov. 2017.

[2] T. J. Besselmann, S. Van de moortel, S. Almér, P. Jörg and H. J. Ferreau, "Model Predictive Control in the Multi-Megawatt Range," *in IEEE Transactions on Industrial Electronics*, vol. 63, no. 7, pp. 4641-4648, July 2016.

[3] S. X. She, A. Q. Huang, Ó. Lucía and B. Ozpineci, "Review of Silicon Carbide Power Devices and Their Applications," in *IEEE Transactions on Industrial Electronics*, vol. 64, no. 10, pp. 8193-8205, Oct. 2017, doi: 10.1109/TIE.2017.2652401.

[4] H. L. Ginn, N. Hingorani, J. R. Sullivan and R. Wachal, "Control Architecture for High Power Electronics Converters," *in Proceedings of the IEEE*, vol. 103, no. 12, pp. 2312-2319, Dec. 2015.

[5] N. u. A. Hanif, S. A. R. Kashif and M. A. Saqib, "Multiplexed control strategy for a multi-input converter using fuzzy logic algorithm," *in Electronics Letters*, vol. 52, no. 15, pp. 1327-1329, 7 21 2016.

[6] L. Xiong, J. Wang, X. Mi and M. W. Khan, "Fractional Order Sliding Mode Based Direct Power Control of Grid-Connected DFIG," in *IEEE Transactions on Power Systems*, vol. 33, no. 3, pp. 3087-3096, May 2018.

[7] S. An overview of industrial model predictive control technology", *Proc. Chemical Process Control-V*, pp. 232-256, 1997

[8] D. Hrovat, S. Di Cairano, H. E. Tseng and I. V. Kolmanovsky, "The development of Model Predictive Control in automotive industry: A survey," 2012 *IEEE International Conference on Control Applications*, Dubrovnik, 2012, pp. 295-302.

[9] S. Vazquez, J. Rodriguez, M. Rivera, L. G. Franquelo and M. Norambuena, "Model Predictive Control for Power Converters and Drives: Advances and Trends," *in IEEE Transactions on Industrial Electronics*, vol. 64, no. 2, pp. 935-947, Feb. 2017.

[10] C. Bordons and C. Montero, "Basic Principles of MPC for Power Converters: Bridging the Gap Between Theory and

Practice," *in IEEE Industrial Electronics Magazine*, vol. 9, no. 3, pp. 31-43, Sept. 2015.

[11] M. Féher, O. Straka, V. Šmídl and Š. Janouš, "Constrained time-optimal control of PMSM with continuous control domain," *2017 IEEE International Symposium on Predictive Control of Electrical Drives and Power Electronics (PRECEDE)*, Pilsen, 2017, pp. 42-47.

[12] K. G. Pavlou, M. Vasiladiotis and S. N. Manias, "Constrained model predictive control strategy for single-phase switch-mode rectifiers," *in IET Power Electronics*, vol. 5, no. 1, pp. 31-40, January 2012.

[13] Jose Rodriguez; Patricio Cortes, "Model Predictive Control,*" in Predictive Control of Power Converters and Electrical Drives* , 1, Wiley-IEEE Press, 2012, pp.31-39.

[14] J. Rodriguez et al., "State of the Art of Finite Control Set Model Predictive Control in Power Electronics," in IEEE Transactions on Industrial Informatics, vol. 9, no. 2, pp. 1003-1016, May 2013.

[15] P. Karamanakos, T. Geyer, N. Oikonomou, F. D. Kieferndorf and S. Manias, "Direct Model Predictive Control: A Review of Strategies That Achieve Long Prediction Intervals for Power Electronics," in IEEE Industrial Electronics Magazine, vol. 8, no. 1, pp. 32-43, March 2014.

[16] A. A. Ahmed, B. K. Koh and Y. I. Lee, "A Comparison of Finite Control Set and Continuous Control Set Model Predictive Control Schemes for Speed Control of Induction Motors," *in IEEE Transactions on Industrial Informatics, vol. 14*, no. 4, pp. 1334-1346, April 2018.

[17] A. S. de Morais, F. Lessa Tofoli and I. Barbi, "Modeling, Digital Control, and Implementation of a Three-Phase Four-Wire Power Converter Used as a Power Redistribution Device," *in IEEE Transactions on Industrial Informatics*, vol. 12, no. 3, pp. 1035-1042, June 2016.

[18] Seung-Ki Sul, "Basic Structure and Modeling of Electric Machines and Power Converters," *in Control of Electric Machine Drive Systems*, 1, Wiley-IEEE Press, 2011, pp.36-115.

[19] A.Taheri , N.Asgari "Sliding Mode Control of LLC DCDC Converter for Wide Output Voltage Range i n Battery Charging" International Journal of Industri al Electronics, Control and Optimization (IECO), Vol 2, Issue 2, , PP 127-136 spring 2019.

[20] A. El Kachani, E. M. Chakir, A. A. Laachir, T. Jarou and A. Hadjoudja, "Nonlinear model predictive control applied to a DFIG-based wind turbine with a Shunt APF*," 2016 International Renewable and Sustainable Energy Conference (IRSEC)*, Marrakech, 2016, pp. 369-375.

[21] Mohsen Ehsani1, Masood Saeidi, Hamid Radmanesh, Adib Abrishamifar " Comparisons between Generalized Predictive Control and Linear Controllers in Multi-Input DC-DC Boost Converter ", International Journal of Industrial Electronics, Control and Optimization (IECO), Vol. 1, No. 3, pp. 27-34, Jan 2020.

[22] Thomas, "Particle swarm optimization based model predictive control for constrained nonlinear systems," 2014 11th International Conference on Informatics in Control, Automation and Robotics (ICINCO), Vienna, Austria, 2014, pp. 397-403.

[23] L. Dai, Y. Xia, Y. Gao and M. Cannon, "Distributed Stochastic MPC of Linear Systems With Additive Uncertainty and Coupled Probabilistic Constraints," in *IEEE Transactions on Automatic Control*, vol. 62, no. 7, pp. 3474-3481, July 2017.

[24] M. A. Santoyo Anaya, J. R. Rodriguez-Rodriguez, E. L. Moreno-Goytia, V. Venegas-Rebollar and N. M. Salgado Herrera, "Current-Sensorless VSC-PFC Rectifier Control with enhance response to dynamic and sag conditions using a single PI loop," in IEEE Transactions on Power Electronics, vol. PP, no. 99, pp. 1-1. Sep 2017

[25] S. Vazquez et al., "Model Predictive Control: A Review of Its Applications in Power Electronics," in IEEE Industrial Electronics Magazine, vol. 8, no. 1, pp. 16-31, March 2014.

[26] T. Peterson, E. Hernández, Y. Arkun and F. Schork, "A nonlinear DMC algorithm and its application to a semibatch polymerization reactor", Chemical Engineering Science, vol. 47, no. 4, pp. 737-753, 1992.

[27] M. Haeri, "Improved EDMC for the processes with high variations and/or sign changes in steady-state gain", COMPEL - The international journal for computation and mathematics in electrical and electronic engineering, vol. 23, no. 2, pp. 361-380, 2004.

[28] J. C. Basilio and S. R. Matos, "Design of PI and PID controllers with transient performance specification," in *IEEE Transactions on Education*, vol. 45, no. 4, pp. 364-370, Nov 2002.

[29] R. Mendez, D. Sbarbaro and J. Espinoza, "High dynamic and static performance FCS-MPC strategy for static power converters," 2016 IEEE Energy Conversion Congress and Exposition (ECCE), Milwaukee, WI, 2016, pp. 1-7.

[30] G. Deshmukh, J. Aute and A. Gupta, "Explicit model predictive control for disturbance rejection and tracking control of boost converter," 2016 IEEE 1st International Conference on Power Electronics, Intelligent Control and Energy Systems (ICPEICES), Delhi, 2016, pp. 1-5.

[31] T. Besselmann, J. Lofberg and M. Morari, "Explicit MPC for LPV Systems: Stability and Optimality," in IEEE Transactions on Automatic Control, vol. 57, no. 9, pp. 2322-2332, Sept. 2012.

[32] R. Shridhar and D. Cooper, "A Tuning Strategy for Unconstrained SISO Model Predictive Control", Industrial & Engineering Chemistry Research, vol. 36, no. 3, pp. 729-746, 1997.

[33] A. Linder, R. Kanchan, R. Kennel, and P. Stolze, "Model-Based Predictive Control of Electric Drives" Göttingen, Germany: Cuvillier Verlag, 2010.

[34] D. Clarke, C. Mohtadi and P. Tuffs, "Generalized predictive control—Part I. The basic algorithm", Automatica, vol. 23, no. 2, pp. 137-148, 1987.

[35] C. Rajhans, S. Patwardhan, and H. Pillai, "Discrete Time Formulation of Quasi Infinite Horizon Nonlinear Model Predictive Control Scheme with Guaranteed Stability", IFAC-PapersOnLine, vol. 50, no. 1, pp. 7181-7186, 2017.

[36] Mayne and J. Rawlings, "Correction to "Constrained model predictive control: stability and optimality"", Automatica, vol. 37, no. 3, p. 483, 2001.

[37] Cannon, Mark Clas lecture Topic" Model Predictive Control", C21, department of engineering science University of Oxford, Oxford, 2013.

[38] I. Zaidi, M. Chaabane, F. Tadeo and A. Benzaouia, "Static State-Feedback Controller and Observer Design for Interval Positive Systems With Time Delay," in IEEE Transactions on Circuits and Systems II: Express Briefs, vol. 62, no. 5, pp. 506-510, May 2015.

Hamid Radmanesh was born in 1981. He received the B.Sc. Degree in electrical Engineering from Malek-Ashtar University of Technology, Tehran, Iran, in 2006, the M.Sc. Degree in electrical Engineering from Shahed University, Tehran, in 2009, and the Ph.D. degree in electrical engineering from Amirkabir University of Technology (AUT), Tehran, in 2015. He has authored more than 100 published technical papers and has been involved in several industrial projects and educational programs in the fields of power electronics and power systems. His research interests include transient in power system, renewable energy, power quality, HVdc transmission systems, and more-electrical aircraft.

Masood Saeidi was born in 1994. He received the B.Sc. degree in electrical engineering from Shahid Beheshti University, Tehran, Iran in 2016 and currently, is the M.Sc. Of electrical Engineering in Iran University of Science and Technology, Tehran. Iran since 2016. His main interesting activity is related to power electronic converter modeling, model predictive control applications in power electronics, electrical machine control, power system control and renewable energy

IECO
This page intentionally left blank.

International Journal of Industrial Electronics, Control and Optimization © 2020 IECO
Vol. 3, No. 4, pp. 503-510, Sep (2020)

Robust Congestion Control Using Sliding Mode Control In TCP/IP Computer Networks

Shoorangiz Shams S Farahani[1, †], Narges Masoomabadi[2], Mohammadreza Jahed-Motlagh[3]

[1]Department of Electrical Engineering, Islamshahr branch, Islamic Azad University, Islamshahr, Iran,
[2]Department of Electrical Engineering, Science and Research Branch, Islamic Azad University, Tehran, Iran,
[3]Department of Electrical Engineering, Iran university of Science and Technology, Tehran, Iran

ABSTRACT

Based on the recent Internet advances, congestion control is considered as an important issue and has spurred a significant amount of research. In this study, second-order sliding mode control is used to adjust the average queue length and maintain the closed-loop system performance. The control law is obtained in two steps. First, the nonlinear state-space form of the network is extracted based on state variables as the average queue length and congestion window size. Then, the proportional-Integrator-derivative and proportional- derivative sliding surface are defined according to the tracking error. Also, in order to avoid chattering, the derivative of the sliding surface is considered and the closed-loop system stability is investigated based on Lyapunov theory. The proposed scheme renders good tracking specifications and closed-loop system robustness. The simulation results show that the proposed methods outperform proportional integral (PI) and proportional integral derivative (PID) schemes. Also, robustness to disturbances increases and chattering and transient response degradation are avoided.

Article Info

Keywords:
Chattering, Congestion control, Disturbance, Sliding mode control (SMC), TCP/IP computer network,

Article History:
Received 2020-02-24
Accepted 2020-08-31

I. INTRODUCTION

A set of protocols is defined as TCP/IP reference model to enable end-to-end (E2E) communications over the Internet. The Transmission Control Protocol (TCP) is an Internet standard which is utilized by many applications[1]. In [2], the scalable TCP is established as a Multiplicative Increase Multiplicative Decrease (MIMD) protocol. It explains the conditions where the total multiplicative increase dynamics of window size is transformed to an additive increase one. In [3], a framework is developed for networked TCP applications which supports both congestion avoidance and slow start algorithms. The aforementioned model addresses the router network which supports any Active Queue Management (AQM) techniques.

Congestion control is an important function which motivates wide acceptance of TCP. Congestion of packets at the outgoing queues in routers renders low reliability and network performance degradation. So, more effective congestion control schemes are needed. Since 1990s control theory has been applied to solve congestion problem in communication networks [4].

Recently, there has been a vast amount of research on using sliding mode control in congestion control schemes [5]-[12]. A TCP congestion control mechanism based on a sliding window mechanism where an additive increase multiplicative decrease (AIMD) algorithm is employed to fit the transmission rate to available network resources is

†Corresponding Author: shoorangiz_shams@yahoo.com,
Tel: +98-56363073-7,Department of Electrical Engineering, Islamshahr branch, Islamic Azad University, Islamshahr, Iran

introduced in [5], a TCP congestion control protocol which uses the congestion window growth function as an exponential function and introduces an adaptive increasing factor in the aforementioned function is established in [6], SMC to control congestion in TCP networks where stability analysis is assessed using Lyapunov theorem is assessed in [7], an adaptive generalized minimum variance (AGMV) as a congestion controller for dynamically varying TCP/AQM networks is presented in [8], sliding mode variable structure control (SMVS) is presented as a congestion controller for AQM in [9], an SMC based on TCP input–delayed model for AQM routers supporting TCP data transfer is established in [10], SMC for uncertain time delay TCP/AQM network systems is presented in [11] and an SMC technique to control congestion in differentiated service communication networks is addressed in [12].

Time delay could be found in different fields. In [13], delay and data loss compensation are studied in Internet-based process control systems, and Internet transmission delay is overcome by considering a variable sampling time. In this regard, two compensation elements in feedforward and feedback channels are presented. Delay can lead to epidemic outbreak in complex networks and it must be considered in the analysis of congestion control methods [14]. In [15], decentralized LMI-based strategies are presented in a delayed nonlinear network to control congestion. The schemes are robust to queue size changes and the consequent delay changes. Also, the control problem is solved using linear matrix inequalities (LMIs). The stability of a TCP/RED congestion control model is studied in [16] where delays are state-dependent and Random early detection (RED) is considered for Internet congestion control. However, RED parameters are difficult to study because of model discontinuous terms and delay.

During the last two decades, great attention has been paid to improving TCP congestion performance by considering slow start, congestion avoidance, fast retransmit, and fast recovery as the congestion control scheme modules. In [17], AQM schemes are used to evaluate TCP performance to control congestion where different TCP and AQM variants are studied. The study is conducted by a practical setup and shows the importance of choosing proper TCP and AQM variants. In [18], the bibliography of TCP/IP congestion control schemes in the last two decades is classified and some main results are obtained. In [19], a scalable testing method is presented for congestion control schemes in real-world TCP implementations where the TCP congestion control is either tested at the interface level or it is tested using an equivalence class of test inputs simultaneously.

In this study, second-order sliding mode control is used to adjust the average queue length and maintain the closed-loop system performance. In this strategy, the control law is obtained in two steps. Also, in order to avoid chattering, the sliding surface derivative is considered and the closed-loop system stability is investigated based on Lyapunov theory.

The reminder of this article is organized as follows: Section II summarizes the TCP/IP dynamic model. Sections III and IV present the sliding mode congestion controller for TCP/IP dynamic model based on sliding surface proportional-integrator-derivative (SSPID) and sliding surface proportional-derivative (SSPD), afterwards, in section V, the performance of our approach is assessed by a simulation set up, and finally section VI provides the conclusion of this paper.

II. Tcp/Ip Dynamic Model

Among different dynamic models which are developed for TCP/IP, the model by [20] is one of the most widely used models which incorporates the fluid flow and stochastic differential equations to represent TCP/IP dynamics. In the aforementioned model, the queue size and the congestion window size are considered as state variables. The model is expressed as follows:

$$\begin{aligned} \dot{w}(t) &= \frac{1}{R(t)} - \frac{w(t)}{2}\frac{w(t-R(t))}{R(t-R(t))}p(t-R(t)) \\ \dot{q}(t) &= N\frac{w(t)}{R(t)} - C \end{aligned} \tag{1}$$

where $w(t)$ is the TCP congestion window size (packets), $q(t)$ the queue size (packets), $R(t)$ the round-trip time (RTT) (seconds), C the link capacity (packets / sec), N the traffic load (the TCP session number) and finally $p(t)$ is the packet drop probability. In (1), the congestion window size and the queue size are considered as state variables. Also, the packet drop probability and the queue length are input and output signals, respectively. By considering $x_1(t) = w(t)$ and $x_2(t) = q(t)$ as state variables, $u(t) = p(t-R(t))$ as input signal and $y(t) = q(t)$ as system output, the network nonlinear state-space model is as follows:

$$\begin{aligned} \dot{x}_1(t) &= \frac{1}{R(t)} - \frac{x_1(t)}{2}\frac{x_1(t-R(t))}{R(t-R(t))}u(t) \\ \dot{x}_2(t) &= N\frac{x_1(t)}{R(t)} - C \end{aligned} \tag{2}$$

Also, RTT is the queue length function and we have:

$$R(t) = \frac{q(t)}{C} + \tau_p \tag{3}$$

where τ_p represents the propagation delay (seconds). So, the state-space model (2) can be written as:

$$\dot{x}_1(t) = \frac{1}{\left(\frac{x_2(t)}{C}+\tau_p\right)} - \frac{x_1(t)}{2}\frac{x_1(t-\left(\frac{x_2(t)}{C}+\tau_p\right))}{\left(\frac{x_2(t-\left(\frac{x_2(t)}{C}+\tau_p\right))}{C}+\tau_p\right)}u(t) \tag{4}$$

$$\dot{x}_2(t) = N\frac{x_1(t)}{\left(\frac{x_2(t)}{C}+\tau_p\right)} - C$$

There exist some constraints on the input signal and system states which shall be considered in the controller as a saturation function. The constraints are as follows:

$$0 \le q(t) \le q_{\max}$$
$$0 \le w(t) \le w_{\max} \tag{5}$$
$$0 \le p(t) \le 1$$

where $q_{\max}$ is the queue capacity (packets) and $w_{\max}$ is the maximum congestion window size (packets).

III. Sliding Mode Congestion Controller for Tcp/Ip Dynamic Model

Sliding mode control (SMC) can be considered as an important control scheme which is robust to disturbances and modeling uncertainties. Since there exist uncertainties occurring in TCP/IP computer networks, SMC is suggested for congestion control in this paper. In this scheme, states should reach a sliding surface in a limited period of time and remain there. The queue length tacking error can be written as:

$$e(t) = q(t) - q_d = x_2(t) - x_{2d} \tag{6}$$

where q_d is the optimal average queue size. In this section, the sliding surface is considered as a sliding surface proportional -integrator- derivative (SSPID):

$$s(t) = \dot{e}(t) + \lambda_1 e(t) + \lambda_2 \int_0^t e(t)d(t) \tag{7}$$

The sliding mode control ensures that system states converges to the sliding surface asymptotically in a limited time. The Lyapunov function is considered as:

$$v(t) = \frac{1}{2}s^2(t) \tag{8}$$

By derivating (8), we have

$$\dot{v}(t) = s(t)\dot{s}(t) \tag{9}$$

To ensure the stability of the closed loop system, (9) shall be negative. So, the inequality (10) is used:

$$\dot{v}(t) = s(t)\dot{s}(t) \le -\eta|s(t)| \rightarrow \dot{s}(t) \le -\eta \operatorname{sign}(s(t)) \tag{10}$$

Using (7), the sliding surface derivative is as follows

$$\dot{s}(t) = \ddot{e}(t) + \lambda_1 \dot{e}(t) + \lambda_2 e(t) \tag{11}$$

Considering the tracking error (6), we have

$$\dot{s}(t) = \ddot{x}_2(t) - \ddot{x}_{2d} + \lambda_1\left(\dot{x}_2(t) - \dot{x}_{2d}\right) + \lambda_2\left(x_2(t) - x_{2d}\right) \tag{12}$$

Since we have

$$\ddot{x}_2(t) = N\frac{\dot{x}_1(t)}{\left(\frac{x_2(t)}{C}+\tau_p\right)} - \frac{N}{C}\frac{\dot{x}_2(t)x_1(t)}{\left(\frac{x_2(t)}{C}+\tau_p\right)^2}, \tag{13}$$

By substituting (2), we have

$$\ddot{x}_2(t) = N\frac{\left(\frac{1}{\left(\frac{x_2(t)}{C}+\tau_p\right)} - \frac{x_1(t)}{2}\frac{x_1(t-\left(\frac{x_2(t)}{C}+\tau_p\right))}{\left(\frac{x_2(t-\left(\frac{x_2(t)}{C}+\tau_p\right))}{C}+\tau_p\right)}u(t),\right)}{\left(\frac{x_2(t)}{C}+\tau_p\right)} - \frac{N}{C}\frac{\left(N\frac{x_1(t)}{\left(\frac{x_2(t)}{C}+\tau_p\right)}-C\right)x_1(t)}{\left(\frac{x_2(t)}{C}+\tau_p\right)^2} \tag{14}$$

So

$$\ddot{x}_2(t) = \frac{2N}{\left(\frac{x_2(t)}{C}+\tau_p\right)^2} - N\frac{-\frac{x_1(t)}{2}\frac{x_1(t-\left(\frac{x_2(t)}{C}+\tau_p\right))}{\left(\frac{x_2(t-\left(\frac{x_2(t)}{C}+\tau_p\right))}{C}+\tau_p\right)}u(t),}{\left(\frac{x_2(t)}{C}+\tau_p\right)} - \frac{N^2}{C}\frac{x_1^2(t)}{\left(\frac{x_2(t)}{C}+\tau_p\right)^3} \tag{15}$$

which can be rewritten as

$$\ddot{x}_2(t) = \Phi(x,t) + \Psi(x,t)u(t) \tag{16}$$

where

$$\Phi(x,t) = \frac{2N}{\left(\frac{x_2(t)}{C}+\tau_p\right)^2} - \frac{N^2}{C}\frac{x_1^2(t)}{\left(\frac{x_2(t)}{C}+\tau_p\right)^3}$$
$$\Psi(x,t) = -N \; -\frac{x_1(t)}{2\left(\frac{x_2(t)}{C}+\tau_p\right)} * \frac{x_1(t-\left(\frac{x_2(t)}{C}+\tau_p\right))}{\left(\frac{x_2(t)}{C}+\tau_p\right)\left(\frac{x_2(t-\left(\frac{x_2(t)}{C}+\tau_p\right))}{C}+\tau_p\right)} \tag{17}$$

So, the sliding surface derivative is:

$$\dot{s}(t) = \Phi(x,t) + \Psi(x,t)u(t) - \ddot{x}_{2d} + \lambda_1\left(\dot{x}_2(t) - \dot{x}_{2d}\right) + \lambda_2\left(x_2(t) - x_{2d}\right) \tag{18}$$

Considering (10), we have

$$\Phi(x,t) + \Psi(x,t)u(t) - \ddot{x}_{2d} + \lambda_1\left(\dot{x}_2(t) - \dot{x}_{2d}\right) + \lambda_2\left(x_2(t) - x_{2d}\right) \le -\eta \operatorname{sign}(s(t)) \tag{19}$$

In order to satisfy (18), the control signal is considered as follows

$$u(t)=\frac{1}{\Psi(x,t)} \left(-\Phi(x,t)+\ddot{x}_{2d}-\lambda_1(\dot{x}_2(t)-\dot{x}_{2d})-\lambda_2(x_2(t)-x_{2d})-k\operatorname{sign}(s(t))\right) \tag{20}$$

In (20), k is sliding mode gain and plays a key role in dealing with uncertainties.

IV. Sliding Mode Congestion Controller for Tcp/Ip Dynamic MODEL

In this scheme, the sliding surface is considered as a sliding surface proportional -derivative:

$$s(t)=\dot{e}(t)+\lambda e(t) \tag{21}$$

The sliding surface derivative is defined as:

$$\dot{s}(t)=-k_1 s(t)-k_2\operatorname{sign}(s(t)) \tag{22}$$

There exist two design parameters, namely, k_1, k_2 in (22). SMC suffers from the disadvantage of high frequency oscillations of the control signal which is considered as chattering. In case of using high order sliding mode control, increasing the sliding mode gain ends in chattering decrease in the control signal. By considering k_1, a stable dynamic is obtained for sliding surface derivative where the derivative of the sliding surface tends to be zero. To extract the SMC law, first, the sliding surface derivative is calculated. So, we have:

$$\dot{s}(t)=\ddot{e}(t)+\lambda e(t)=\Phi(x,t)+\Psi(x,t)u(t)-\ddot{x}_{2d}+\lambda(\dot{x}_2(t)-\dot{x}_{2d}) \tag{23}$$

Using Equ. (22), we have

$$\Phi(x,t)+\Psi(x,t)u(t)-\ddot{x}_{2d}+\lambda(\dot{x}_2(t)-\dot{x}_{2d})= -k_1 s(t)-k_2\operatorname{sign}(s(t)) \tag{24}$$

So, the SMC law is as follows:

$$u(t)=\frac{1}{\Psi(x,t)} \left(-k_1 s(t)-k_2\operatorname{sign}(s(t))+\ddot{x}_{2d}-\lambda(\dot{x}_2(t)-\dot{x}_{2d})-\Phi(x,t)\right) \tag{25}$$

In the following, by choosing the sliding surface derivative (22), Lyapunov stability is established. The Lyapunov function is considered as:

$$v(t)=\frac{1}{2}s^2(t) \tag{26}$$

So, we have:

$$\dot{v}(t)=s(t)\dot{s}(t)=s(t)\left(-k_1 s(t)-k_2\operatorname{sign}(s(t))\right) =-k_1 s^2(t)-k_2 s(t)\operatorname{sign}(s(t)) \tag{27}$$

Since

$$\begin{cases} s(t)\geq 0 \rightarrow sign(s(t))=1 \rightarrow s(t)sign(s(t))>0 \\ s(t)<0 \rightarrow sign(s(t))=-1 \rightarrow s(t)sign(s(t))>0 \end{cases} \tag{28}$$

so,

$$\dot{v}(t)=-k_1 s^2(t)-k_2 s(t)\operatorname{sign}(s(t))\leq 0 \tag{29}$$

The above inequality shows that if Equ. (22) is satisfied, the closed-loop system stability is guaranteed. In other words, (29) shows that the sliding surface converges to zero asymptotically. On the other hand, according to Equ. (6), if the sliding surface converges to zero, the tracking error will converge to zero asymptotically.

V. Performance Analysis

In this part, first the performance of SSPID and SSPD is studied. In this regard, changes in queue length, packet loss probability and the congestion window size and RTT are studied. Afterwards, the impact of disturbance is examined on the system performance. Finally, the results of the proposed controller are compared with PI and PID controllers.

A. Performance Analysis of the Proposed Controllers

In this part, the performance of SSPID and SSPD is studied in case of tracking of the desired queue length and packet drop probability. Also, the congestion window size, RTT, the sliding surface and its derivative are shown. The sliding mode controller sets the average queue length such that the system performance is guaranteed in the presence of external disturbances and model uncertainties. The simulations are run for the following network parameters: $N=60,\ C=3750,\ \tau_d=0.2$ .The parameters set in SSPID are $\lambda_1=16, \lambda_2=64, k=5$ and the parameters set in SSPD are $k_1=15,\ k_2=10,\ \lambda=20$. It is worth noting that the state variables and control signal are constrained in TCP-based computer network systems. Fig.1 shows the tracking of the desired queue length in SSPID and SSPD.

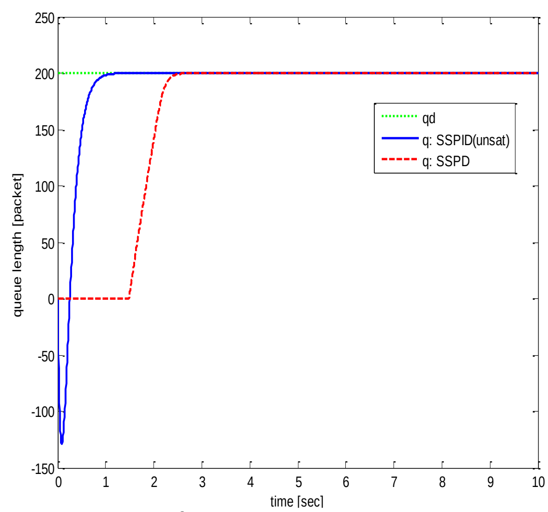

Fig. 1. Tracking of the desired queue size in in SSPD and SSPID

Fig. 1 shows the effect of saturation on the control signal and system states. The output converges to its desired level after the transient time. Fig. 2 shows the control signal.

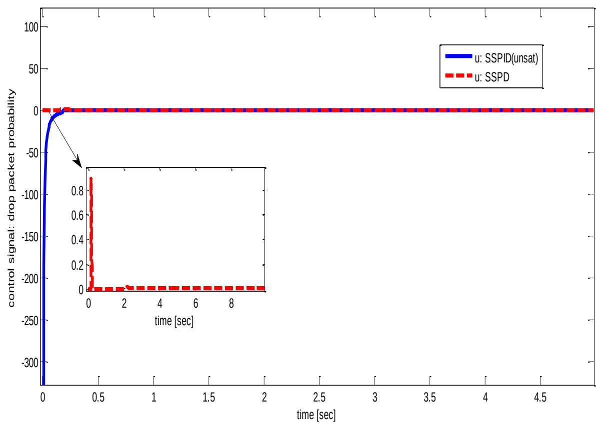

Fig. 2. Packet drop probability in in SSPD and SSPID

The control signal implies that the packet drop probability is high in transient time, however, it is reduced after the transient time. The packet drop probability in SSPD is less than that of in SSPID, so a better control signal is gained in SSPD comparing with SSPID. Fig. 3 shows the congestion window size and RTT in SSPD and SSPID.

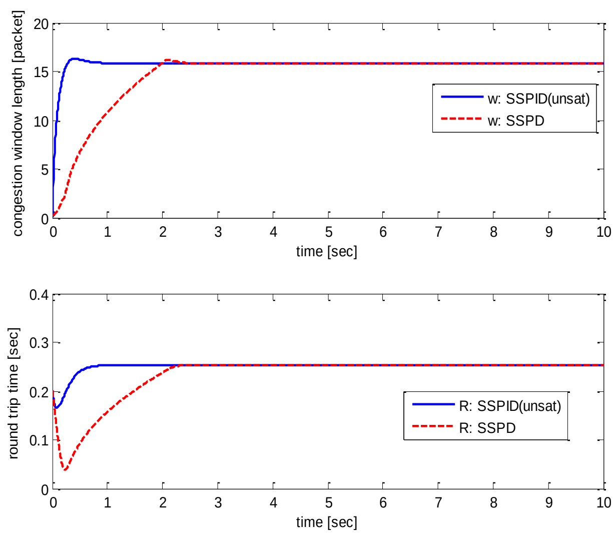

Fig. 3. Congestion window size and RTT in in SSPD and SSPID

The congestion window size in SSPD and SSPID converges to a constant value after a certain period of time which shows the closed-loop system stability. Also, RTT converges to a constant value after the transient time. Fig. 4 shows the sliding surface and its derivative in SSPD and SSPID. It can be seen that the sliding surface and its derivative converge to zero in SSPD. However, the sliding surface in SSPID does not converge to zero.

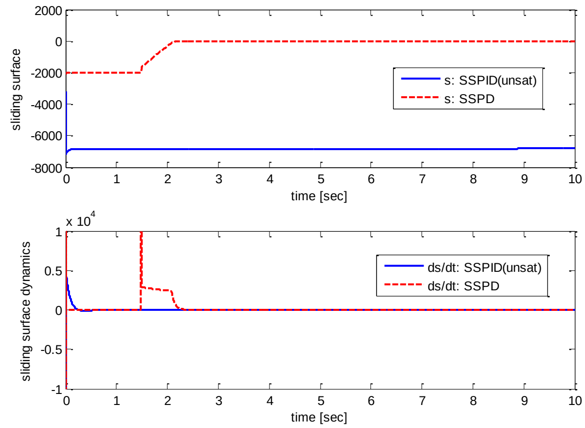

Fig. 4. Sliding surface and its derivative in in SSPD and SSPID

B. Performance Analysis of the Proposed Controllers in the Presence of Disturbance

In this part, the performance of the proposed controller is studied in the presence of disturbance. A step disturbance (value=20, time=10) is applied to the average queue length. Table I shows the performance of the proposed controllers in case of average queue length error, average congestion window size error, average RTT error and average packet drop probability with and without disturbance.

Table I. Performance Of The Proposed Controllers With And Without Disturbance

SSPID (with disturbance)	**SSPID (without disturbance)**	**SSPD (with disturbance)**	**SSPD (without disturbance)**	**Scheme / Performance metrics**
6141.8	4910.5	3895.1	3395.3	Average queue length error
6.7812	5.8491	5.6480	5.1880	Average congestion window size error
0.0616	0.0603	0.0596	0.0591	Average RTT error
5.9184×10^{-4}	5.3271×10^{-4}	3.8958×10^{-4}	3.1167×10^{-4}	Average packet drop probability

Table I shows that SSPD without disturbance outperforms SSPD with disturbance in terms of average queue length error, average congestion window size error, average RTT error and average packet drop probability. Also, SSPID without disturbance outperforms SSPID with disturbance in terms of average queue length error, average congestion window size error, average RTT error and average packet drop probability. Moreover, SSPD without disturbance ends in better performance comparing with SSPD with disturbance, and SSPID with/without disturbance. Also, SSPID with disturbance performs the worst comparing with SSPID without disturbance, and SSPD with/without disturbance.

C. Comparison of the Proposed Controller with PI and PID Controllers

In this part, the performance of the proposed controller (SSPD) is compared with PI [21] and PID [22] controllers. In [21], given that W_0, p_0 and q_0 are the equilibrium points of TCP nonlinear system, the transfer function of δp and δq is determined as follows:

$$G_{pq}(s) = \frac{R_0 C_0 K}{\left(R_0 s + \frac{1}{K}\right)\left(R_0 s + 1\right)} e^{-R_0 s} \tag{30}$$

where

$$\delta p = p(t) - p_0,\ \delta q = q(t) - q_0,\ K = \frac{R_0 C_0}{2N_0},\ R_0 = T_0 + \frac{q_0}{C_0} \tag{31}$$

In [21], the performance of PI controllers is studied in TCP networks. In this paper, Skogestad's method [23] is suggested where the system transfer function as the following first order approximation is taken into consideration:

$$G_{pq}(s) \approx \frac{R_0 C_0 K^2}{\left(K + \frac{1}{2}\right) R_0 s + 1} e^{-\frac{3}{2} R_0 s} \tag{32}$$

The controller parameters are derived as follows:

$$k_p = \frac{1}{C_0 K^2} \frac{K + 0.5}{\tau_c + 1.5 R_0}, \qquad k_i = \frac{k_p}{\min\left\{K R_0 + 0.5 R_0, 4\left(\tau_c + 1.5 R_0\right)\right\}} \tag{33}$$

The following values are obtained as the controller parameters:

$k_p = 4.2196,\ k_i = 3.7056$

Based on the model, a PID controller is as follows [22]:

$$G_c(s) = 2.9067 \times 10^{-5}\left(1 + \frac{1}{5.45 s} + 0.4157 s\right) \tag{34}$$

In this section, the desired average queue length is 120. Fig. 5 shows the tracking of the desired queue length in the proposed controller, PI and PID controllers.

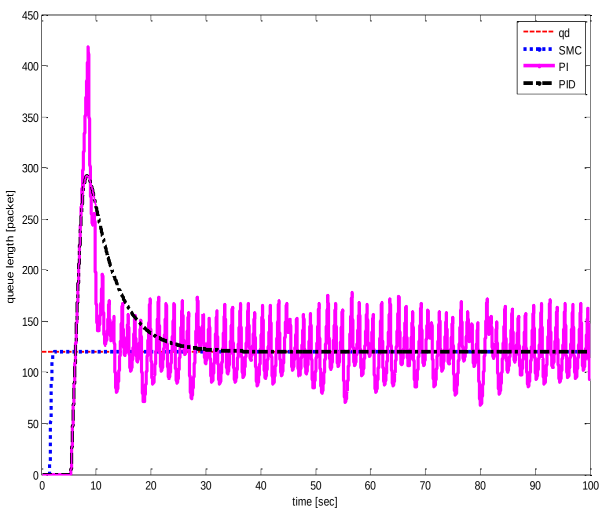

Fig. 5. Tracking of the desired queue length in the proposed controller, PI and PID controllers

Fig. 5 shows that the proposed scheme renders satisfactory tracking of the desired queue length comparing with PI and PID controllers. The PID controller ends in an undesired transient closed-loop response and a very high overshoot. Also, the PI controller renders unsatisfactory performance comparing with the proposed scheme since the desired queue length significantly fluctuates. Fig. 6 shows the packet drop probability in the proposed controller, PI and PID controllers. Also, the congestion window size is shown in Fig. 7.

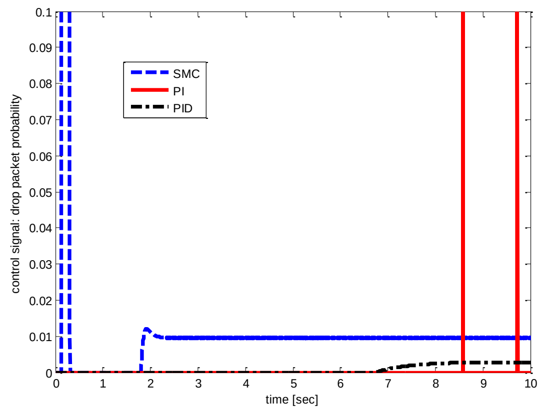

Fig. 6. Packet drop probability in the proposed controller, PI and PID controllers

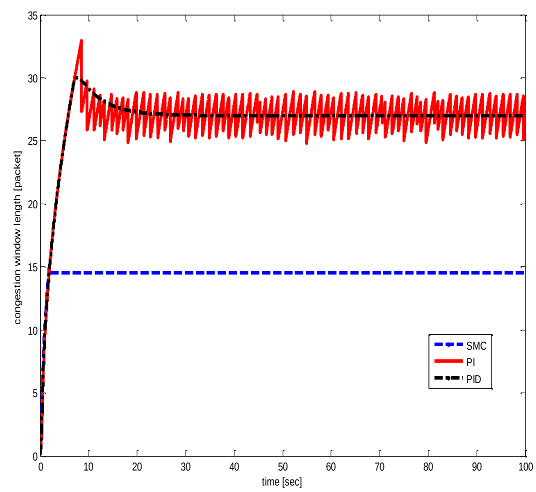

Fig. 7. Congestion window size in the proposed controller, PI and PID controllers

Fig. 6 shows that the PI controller has the worst packet drop probability, however the packet drop probability in the PID controller is less than the proposed controller. Also, Fig. 7 shows that the desired value of congestion window size is gained in the proposed controller, however a fluctuating congestion window size is obtained in the PI controller. So, satisfactory performance is not obtained in the PI controller. Fig. 8 shows the packet round-trip time in the proposed controller, PI and PID controllers.

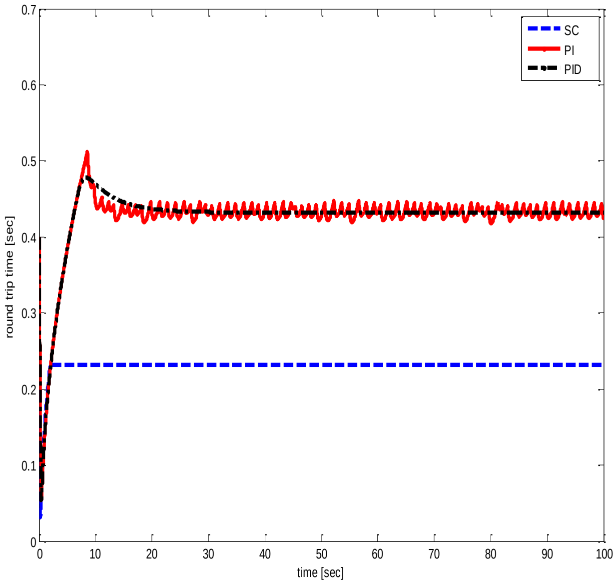

Fig. 8. Packet round-trip time in the proposed controller, PI and PID controllers

The packet round-trip time in the proposed controller is less than that of the PI and PID controllers. The congestion window size in Fig. 7 and RTT in Fig. 8 demonstrate that the proposed method outperforms PI and PID schemes. The performance of the proposed controller, PI and PID controllers are compared in Table II.

TABLE II. Performance of The Proposed Controller, PI And PID Controllers

PI	PID	The proposed controller	Scheme / Performance metrics
5427.2	4160.6	3395.3	Average queue length error
6.2886	5.7190	5.1880	Average congestion window size error
0.0617	0.2360	0.0591	Average RTT error
3.6×10^{-4}	0.594×10^{-4}	3.1167×10^{-4}	Average packet drop probability

Table II demonstrates that the proposed controller outperforms PI and PID controllers. The PI controller has the highest mean queue length error, however, the PID controller outperforms the PI controller with less packet drop probability and less congestion window size. Also, the PID controller has the worst packet round-trip time and the proposed scheme renders the best queue length tracking.

VI. Conclusions

In this study, the sliding mode control scheme is presented for desired queue length tracking in TCP-based computer network. In this regard, the proportional-Integrator-derivative and proportional-derivative sliding surface is defined and the control signal is extracted. Also, the Lyapunov stability conditions are satisfied. The proposed scheme renders satisfactory performance in the presence of disturbance. Also, no chattering occurs in the control signal and satisfactory transient response is gained. The comparison between the proposed method with PI and PID control schemes shows the superiority of sliding mode control comparing with the aforementioned controllers where congestion window size remains unchanged, satisfactory control signal is achieved and less overshoot is obtained.

References

[1] K.R. Sollins, *The TFTP Protocol (REVISION 2).* RFC 783. http://www.rfc-editor.org/info/rfc783, 1981.

[2] R. El Khoury, E. Altman, R.El Azouzi, "Analysis of scalable TCP congestion control algorithm," *Computer Communications*, Vol. 33, No.1, pp. S41–S49, Nov.2010.

[3] M. Barbera, A. Lombardo and G. Schembra, "A fluid-based model of time limited TCP flows," *Computer Networks*, Vol. 44,No.3, pp. 275–288, Feb.2004.

[4] M.A. Ardestani and M.T.H. Beheshti, "A robust discrete-time controller for delay sensitive applications," in *Proc. 7th International Conference on Information, Communications and Signal Processing*, 2009.

[5] V. Jacobson and M.J. Karels, "Congestion avoidance and control," *ACM Sigcomm Computer Communication Review*, Vol. 18, pp. 314-329, Nov.1988.

[6] Z. Wang, X. Zeng, X. Liu, M. Xu, Y. Wen, L. Chen, "TCP congestion control algorithm for heterogeneous Internet," *Journal of Network and Computer Applications,* Vol. 68, pp.56–64, Jun.2016.

[7] R. Barzamini, M. shafiee, "A New Sliding Mode Controller for TCP Congestion Control," *19th Telecommunications forum TELFOR,* 2011.

[8] R. Barzamini, M. Shafiee, A. Dadlani, "Adaptive generalized minimum variance congestion controller for dynamic TCP/AQM networks," *Computer Communications,* Vol.35, No.2, pp. 170–178, Jan.2012.

[9] F. Ren, C. Lin, and X. Yin, "Design a congestion controller based on sliding mode variable structure control," *Computer Communications,* Vol. 28, No.9, pp.1050-1061, Jun.2005.

[10] F. Blanchini, W. Krajewski, S. Miani, U. Viaro, "A sliding mode strategy to control TCP flows," *IFAC Proceedings Volumes*, Vol. 42, No.13, pp. 717-722, 2009.

[11] H. Wang, Y. Jing, Y. Zhou, Z. Chen, and X. Liu, "Sliding mode control for uncertain time delay TCP/AQM network systems," in *Proc. 17th World IFAC Congress*, Seoul, Korea, pp.12013-12018, 2008.

[12] H. Ebrahimirad, M.J. Yazdanpanah, "Sliding Mode Congestion Control in Differentiated Service Communication Networks," *International Conference on Wired/Wireless Internet Communications,* pp. 99-108, 2004.

[13] S.H. Yang, X. Chen, L.S. Tan, L. Yang, "Time delay and data loss compensation for Internet-based process control systems," *Transactions of the Institute of Measurement and Control*, Vol. 27,No.2, pp. 103-118, Apr.2005.

[14] C. Xia, L. Wang, S. Sun, J. Wang, "An SIR model with infection delay and propagation vector in complex networks," *Nonlinear Dynamics,* Vol. 69, pp. 927–934, Jan.2012.

[15] S. Shams Shamsabad Farahani, S. Fakhimi Derakhshan, "LMI-based Congestion Control Algorithms for a Delayed Network," *International Journal of Industrial Electronics, Control and Optimization*, Vol.2, No.2., pp. 91-98, Feb. 2019.

[16] Z. Shu , J. Xu, K. Chung, "On the stability and multi-stability of a TCP/RED congestion control model with state-dependent delay and discontinuous marking function,"

Communications in Nonlinear Science and Numerical Simulation, Vol. 22, No.1-33, pp. 269–284,May 2015.

[17]S. B. Vyakaranal, J. G. Naragund, "Performance Evaluation of TCP using AQM Schemes for Congestion Control," in *Proc. Second International Conference on Advances in Electronics, Computers and Communications (ICAECC)*, 2018.

[18] S. Lar and X. Liao, "An initiative for a classified bibliography on TCP/IP congestion control," *Journal of Network and Computer Applications*, Vol. 36, No.1, pp. 126-133, Jan. 2013.

[19] W. Sun, L. Xu, S. Elbaum, "Scalably Testing Congestion Control Algorithms of Real-World TCP Implementations," in *Proc. IEEE International Conference on Communications (ICC)*, 2018.

[20] V. Misra, W.B. Gong, and D. Towsley, "Fluid-based analysis of a network of AQM routers supporting TCP flows with an application to RED," *ACM SIGCOMM Computer Communication Review*, Vol. 30, pp.151-160, Aug. 2000.

[21] HU. Unal, D. Malchor-Aguilar, D. Ustebay,S.L. Niculescu, H. Özbay, "Comparison of PI controllers designed for the delay model of TCP/AQM networks," *Computer Communications,* Vol. 36, No.10-11, pp. 1225-1234, Jun. 2013.

[22] J. Wang, L. Rong, and Y. Liu, "Design of a stabilizing AQM controller for large-delay networks based on internal model control," *Computer Communications,* Vol. 31, No.10, pp. 1911-1918, Jun. 2008.

[23] S. Skogestad, "Simple analytic rules for model reduction and PID controller tuning," *Journal of Process Control,* Vol.13, No.4, pp. 291–309, Jun.2003.

Shoorangiz Shams Shamsabad Farahani obtained her B.Sc., M.Sc. degrees, and the PhD in Electrical engineering in 2001, 2005 and 2013, respectively. She is an Assistant Professor in Islamic Azad University, Islamshahr branch, Islamshahr, Iran. Her current research interests include switching systems, communication networks, wireless sensor networks, complex systems, stability analysis, fuzzy control, robust control and nonlinear control. She has supervised and co-supervised several graduate students in these areas.

Narges Masoumabadi obtained her B.Sc. and M.Sc. degrees in Electrical engineering in 2010 and 2015, respectively. Her current research interests include complex systems, communication networks, robust control and nonlinear control.

Mohammad Reza Jahed-Motlagh obtained his B.Sc., M.Sc. degrees, and the PhD in Electrical engineering in 1978, 1986 and 1990, respectively. He is a full Professor in Iran University of science and Technology, Tehran Iran. His current research interests include control engineering, complex systems, wireless sensor networks, robust control and nonlinear control. He has supervised and co-supervised several graduate students in these areas.